Improved MAX-DOAS measurements and retrievals focused on the marine boundary layer

Enno Peters

Dissertation

zur Erlangung des Grades

Doktor der Naturwissenschaften

Institut für Umweltphysik
Fachbereich Physik und Elektrotechnik
Universität Bremen

Bremen, den

25.06.2013

Universität Bremen

Dissertation eingereicht am: 25.06.2013

1. Gutachter: Prof. John P. Burrows
2. Gutachter: Prof. Justus Notholt

Abstract

In this work, atmospheric trace gas columns and profiles of NO_2, HCHO and IO were retrieved from ground-based multi-axis differential optical absorption spectroscopy (MAX-DOAS) measurements during different field campaigns focusing on the marine troposphere. The improvement of the existing IUP-Bremen MAX-DOAS instrument was a precondition for this work. Thus, in the scope of this thesis, the existing instrument was modified allowing pointing in any viewing direction and installation during ship-based campaigns (and especially allowing viewing directions towards the water surface). The improved instrument showed excellent performance during an NO_2 intercomparison campaign in June/July 2009 where it was selected as one of the reference instruments.

Although the DOAS method is a well known measurement technique used routinely for trace gas observations from space (e.g. GOME-2, OMI, SCIAMACHY), large uncertainties exist over the vast remote, oceanic regions, where tropospheric trace gas levels are normally small. In addition, a recent discussion within the scientific community proposed the ocean surface to be an inorganic source for iodine monoxide (IO). Iodine monoxide is an ozone depleting substance and may impact Earth's radiation budget (and thus climate) through its potential of forming new particles by condensation of iodine oxides. Thus, the knowledge of its occurrence, concentrations and possible pathways is important. However, satellite observations of IO over the ocean, which makes up 70% of the entire Earth's surface, indicate negative concentrations in some regions which cannot occur by definition. The reason is thought to be retrieval articfacts from spectral effects of liquid water (absorption and inelastic scattering). These can become large in water leaving radiance which is present in nadir satellite observations over the ocean.

This work aims at a clarification of the presence and magnitude of IO amounts in the remote marine environment as well as the estimation of oceanic background concentrations of NO_2 and HCHO. For this purpose, MAX-DOAS measurements were performed during several campaigns, focusing on the ship-based *TransBrom* campaign across the western Pacific in October 2009. MAX-DOAS instruments are more sensitive for tropospheric absorbers than satellite instruments as a consequence of the measurement geometry. Over the remote tropical ocean, IO volume mixing ratios of 0.5 - 2 pptv were retrieved close to the ground (corresponding to a vertical column of $1 - 3 \cdot 10^{12}$ molec/cm^2). For tropospheric NO_2 a background concentration of ≈ 50 ppt ($1.3 \cdot 10^{14}$ molec/cm^2) was derived. Formaldehyde (mainly from methane oxidation) shows a clear diurnal cycle. Maximum HCHO values under clear weather conditions and strong sun irradiance reached up to 1.1 ppbv or $4 \cdot 10^{15}$ molec/cm^2.

In addition, measurements pointing towards the water surface were performed in order to clarify the impact of liquid water spectral effects on the DOAS retrieval. From these measurements, empirical correction spectra for uncertainties of currently available liquid water absorption and VRS cross-sections were retrieved. It is demonstrated that the consideration of these residual correction spectra in MAX-DOAS and satellite DOAS measurements improves the fit quality by up to 20% over clear water surfaces. It could also be shown that the negative IO slant columns derived from satellite measurements are indeed caused by insufficiently removed liquid water structures.

List of publications

1. Journal articles

As first author:

- Peters, E., Wittrock, F., Großmann, K., Frieß, U., Richter, A., and Burrows, J. P.: Formaldehyde and nitrogen dioxide over the remote western Pacific Ocean: SCIAMACHY and GOME-2 validation using ship-based MAX-DOAS observations, Atmos. Chem. Phys., 12, 11179-11197, doi:10.5194/acp-12-11179-2012, 2012.

As co-author:

- Großmann, K., Frieß, U., Peters, E., Wittrock, F., Lampel, J., Yilmaz, S., Tschritter, J., Sommariva, R., Glasow, R. v., Quack, B., Krüger, K., Pfeilsticker, K., and Platt, U.: Iodine monoxide in the Western Pacific marine boundary layer, Atmos. Chem. Phys., 13, 3363-3378, 2013.

- Pinardi, G., Roozendael, M. V., Abuhassan, N., Adams, C., Cede, A., Clèmer, K., Fayt, C., Frieß, U., Gil, M., Herman, J., Hermans, C., Hendrick, F., Irie, H., Merlaud, A., Comas, M. N., Peters, E., Piters, A. J. M., Puentedura, O., Richter, A., Schönhardt, A., Shaiganfar, R., Spinei, E., Strong, K., Takashima, H., Vrekoussis, M., Wagner, T., Wittrock, F., and Yilmaz, S.: MAXDOAS formaldehyde slant column measurements during CINDI: intercomparison and analysis improvement, Atmos. Meas. Tech., 6, 167-185, 2013.

- Piters, A. J. M., Boersma, K. F., Kroon, M., Hains, J. C., Roozendael, M. V., Wittrock, F., Abuhassan, N., Adams, C., Akrami, M., Allaart, M. A. F., Apituley, A., Beirle, S., Bergwerff, J. B., Berkhout, A. J. C., Brunner, D., Cede, A., Chong, J., Clèmer, K., Fayt, C., Frieß, U., Gast, L. F. L., Gil-Ojeda, M., Goutail, F., Graves, R., Griesfeller, A., Großmann, K., Hemerijckx, G., Hendrick, F., Henzing, B., Herman, J., Hermans, C., Hoexum, M., Hoff, G. R. v. d., Irie, H., Johnston, P. V., Kanaya, Y., Kim, Y. J., Baltink, H. K., Kreher, K., Leeuw, G. d., Leigh, R., Merlaud, A., Moerman, M. M., Monks, P. S., Mount, G. H., Navarro-Comas, M., Oetjen, H., Pazmino, A., Perez-Camacho, M., Peters, E., Piesanie, A. d., Pinardi, G., Puentedura, O., Richter, A., Roscoe, H. K., Schönhardt, A., Schwarzenbach, B., Shaiganfar, R., Sluis, W., Spinei, E., Stolk, A. P., Strong, K., Swart, D. P. J., Takashima, H., Vlemmix, T., Vrekoussis, M., Wagner, T., Whyte, C., Wilson, K. M., Yela, M., Yilmaz, S., Zieger, P., and Zhou, Y.: The Cabauw Intercomparison campaign for Nitrogen Dioxide measuring Instruments (CINDI): design, execution, and early results, Atmos. Meas. Tech., 5, 457-485, 2012.

- Roscoe, H. K., Roozendael, M. V., Fayt, C., Piesanie, A. d., Abuhassan, N., Adams, C., Akrami, M., Cede, A., Chong, J., Clèmer, K., Friess, U., Ojeda, M. G., Goutail, F., Graves, R., Griesfeller, A., Grossmann, K., Hemerijckx, G., Hendrick, F., Herman, J., Hermans, C., Irie, H., Johnston, P. V., Kanaya, Y., Kreher, K., Leigh, R., Merlaud, A., Mount, G. H., Navarro, M., Oetjen, H., Pazmino, A., Perez-Camacho, M., Peters, E., Pinardi, G., Puentedura, O., Richter, A., Schönhardt, A., Shaiganfar, R., Spinei, E., Strong, K., Takashima, H., Vlemmix, T., Vrekoussis, M., Wagner, T., Wittrock, F., Yela, M., Yilmaz, S., Boersma, F., Hains, J., Kroon, M., Piters, A., and Kim, Y. J.: Intercomparison of slant column measurements of NO_2 and O_4 by MAX-DOAS and zenith-sky UV and visible spectrometers, Atmos. Meas. Tech., 3, 1629-1646, 2010.

2. Selected oral and poster presentations (only first author)

Oral presentations at conferences and workshops:

- E. Peters, F. Wittrock, A. Schönhardt, M. Vrekoussis, A. Richter, and J. P. Burrows: Comparison of MAX-DOAS and in-situ observations of NO_2 during CINDI, DPG Spring meeting, Hannover, Germany, March 2010.
- E. Peters, K. Großmann, F. Wittrock, U. Frieß, A. Schönhardt, A. Richter, J. P. Burrows, K. Krüger, B. Quack: MAX-DOAS IO and BrO measurements in the western pacific boundary layer, EGU General Assembly 2011, Vienna, Austria, April 2011.
- E. Peters, F. Wittrock, A. Schönhardt, A. Richter, J. P. Burrows, K. Krüger, B. Quack: MAX-DOAS measurements of IO, BrO, HCHO and NO_2 in the western Pacific MBL, DOAS-Workshop 2011, Mainz, Germany, July 2011.

Poster presentations:

- E. Peters, F. Wittrock, K. Großmann, U. Frieß, A. Richter, and J. P. Burrows: Formaldehyde and nitrogen dioxide over the western Pacific: SCIAMACHY and GOME-2 validation, Atmospheric Composition Validation and Evolution Workshop, Frascati, Italy, March 2013.
- E. Peters, F. Wittrock, A. Richter, and J. P. Burrows: Empirical correction spectra for the liquid water absorption and VRS effect in DOAS retrievals, DOAS workshop 2013, Boulder (Colorado), United States, August 2013 (submitted).

Contents

List of Figures

List of Tables

1. Motivation and Objectives

The atmosphere is only a thin film, half of its mass is located below 5 km altitude. This thin film separating Earth's surface from outer space is crucial for the existence of life on Earth: It covers the entire biosphere shielding it from harmful UV radiation (ozone layer), it raises the surface temperature above freezing point (greenhouse effect) and its constituents are needed by most life-forms for their metabolism. Thus, the understanding of the atmosphere, its characteristics, processes and response to anthropogenic influences are vital and one of the most relevant aspects of science.

Measurements of atmospheric constituents and parameters can be performed either locally by in situ techniques (taking samples) or on a larger scale by remote sensing. This thesis focuses on the latter one. Historically, remote sensing originates from military surveillance and reconnaissance purposes (e.g., observation of enemy movements and systematic aerial photography from balloons and airplanes in World War I, etc.) which is unfortunately still an important aspect of this technique today (military reconnaissance satellites). Starting with the detection of the ozone layer by absorption measurements (e.g., Dobson and Harrison, 1926), over time, remote sensing was adopted for scientific purposes extending our knowledge about nature and has become an important tool in environmental science as well as astronomy. Today, spectroscopic observations are performed from ground-based instruments on multiple locations and satellite-based platforms provide a global view of trace gas distributions as well as weather situations.

The remote sensing technique used in this thesis is the well-known Differential Optical Absorption Spectroscopy (DOAS). At the IUP-Bremen ground-based DOAS measurements using UV/Vis scattered sunlight are performed since 1993. In addition, the DOAS technique is applied to retrieve trace gas columns from satellite data (e.g., GOME, SCIAMACHY, GOME-2, OMI).

In general, the focus of tropospheric trace gas retrievals is over continents because here the anthropogenic (and often also natural) sources of many trace gases are located and this is also where most humans live. A prominent example is NO_2 originating predominantly from anthropogenic releases (traffic, industry). Source regions of pollution and trends can be observed from space (e.g. Richter et al., 2005). However, major parts of the Earth's surface are covered by oceans. Thus, although the abundance of trace gases over remote oceanic regions is often small, the potential impact on a global scale can be large. Also, the ocean hosts the majority of life on Earth. Furthermore, some important trace gases are rather emitted by oceanic than continental sources.

One example for this is iodine monoxide (IO). IO is involved in ozone chemistry (ozone depleting potential) and therefore influences the atmosphere's oxidizing capacity (e.g., Saiz-Lopez et al., 2012). In addition, higher iodine oxides I_xO_y can be produced that may grow to cloud condensation nuclei (McFiggans et al., 2004) (possibly impacting on climate). Predominant sources of IO are marine life-forms (macro- and microalgea) emitting organic precursor species (e.g. CH_2I_2). For illustration, Fig. 1.1 is a multi-year average of the global IO distribution retrieved from SCIAMACHY data. In this image, larger IO values are located close to Antarctica, e.g. in the Weddell and Ross sea. Here, under-ice algea are considered to produce iodine compounds. Enhanced IO

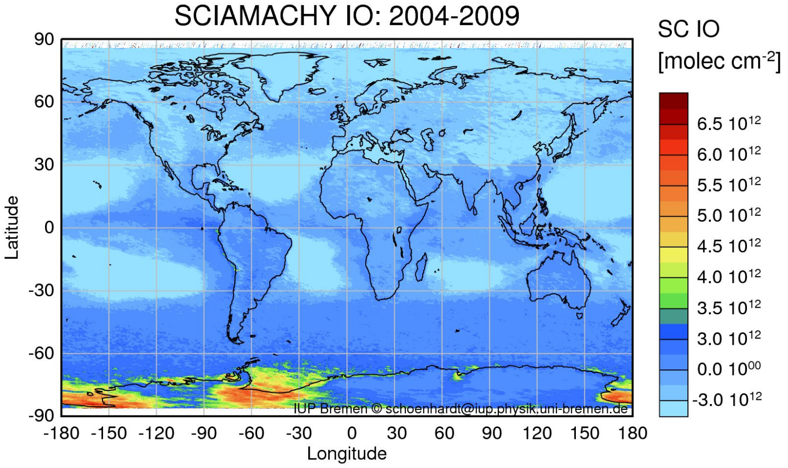

Figure 1.1: Iodine monoxide (IO) as measured from SCIAMACHY for the years 2004-2009 (A. Schönhardt, IUP-Bremen, personal communication 2012).

values occur mostly in Antarctic springtime when the sea ice partly melts and breaks (Schönhardt et al., 2012). Apparently, the IO does not reach comparable levels elsewhere (IO is also enhanced in some coastal regions, but this is too small-scaled to be visible here). A problem in these data is that over large oceanic regions the IO values are even negative. By definition, negative trace gas abundances cannot occur.

Most likely, the observed negative values have two causes: 1) The IO levels are low in remote oceanic regions and subsequently cause only a weak absorption that is hard to detect, especially from space. 2) The light collected by the satellite (in nadir viewing) over ocean surfaces necessarily contains spectral structures of liquid water. This is, because incident sunlight penetrates the water surface and travels some distance inside the water (where it experiences water-related absorption and scattering processes) before it is (partly) backscattered into the atmosphere and finally reaches the satellite. The introduced spectral effects of liquid water are possibly not sufficiently accounted for in the DOAS retrieval. Not perfectly corrected water structures may interfere with the IO spectral structures causing the observed negative IO values.

The second reason is supported by the global distribution of the liquid water absorption strength in the ocean. It is well-known that liquid water has a broad-band absorption spectrum that is small but still present in the visible range. In Fig. 1.2, the liquid water absorption as observed from satellite has been plotted on a global scale. Most positive values indicate regions of very clear water and subsequently largest penetration depths or longest light paths under water, respectively (the values in Fig. 1.2 are the average length of the light path under water). When comparing Figs. 1.1 and 1.2, the similarity between regions of largest liquid water absorption and regions of negative IO columns over the ocean becomes obvious.

This thesis aims at the problem of detecting *small absorbers* (like IO) in the remote marine environment. Therefore, ground-based MAX-DOAS measurements were performed in exactly the regions discussed above where satellite observations are problematic due to water-related spectral effects and trace gas abundances are small. These measurements have been carried out predominantly during the ship-based *TransBrom* campaign across the western Pacific. The results were used to retrieve trace gas profiles and to validate corresponding satellite observations. A MAX-DOAS instrument is well-suited for this purpose as it provides a higher sensitivity for trace gases in the boundary layer than satellite instruments do.

In addition, MAX-DOAS measurements were performed towards the water surface during Trans-

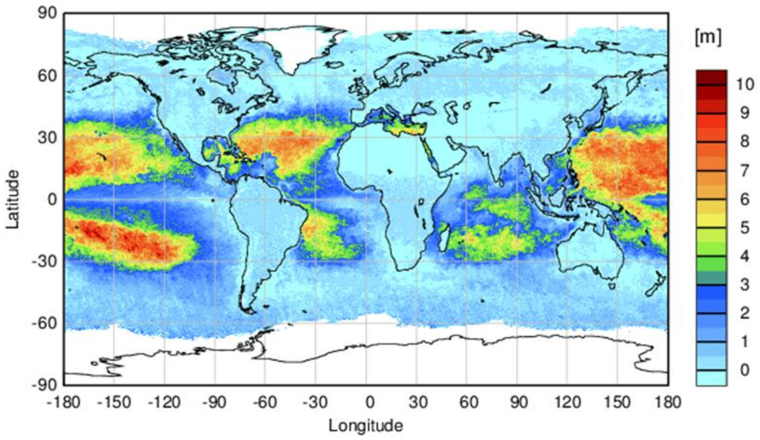

Figure 1.2: Liquid water absorption (average length of the light path under water) as observed from OMI for August 2007.

Brom in order to study spectral effects of liquid water and their impact on the DOAS analysis. These measurements were realized in a way that minimizes atmospheric contributions to the recorded spectra while at the same time the light path inside the water was estimated to be ≈ 5 times larger than in strongest water-affected satellite measurements. The final aim was to retrieve an experimental correction spectrum for currently used cross-sections of liquid water effects in order to improve DOAS fits over water surfaces.

For performing these measurements, first, the existing IUP-Bremen MAX-DOAS instrument revealing some intrinsic problems had to be improved. The old instrument type used different viewing ports and a mirror for recording measurements towards the horizon and in the zenith. As a consequence, offsets were sometimes observed in the retrieved trace gas columns and artificial spectral structures were introduced, most likely by the mirror. Obviously, this instrument is not suited for the retrieval of so far unknown spectral structures of liquid water. The new instrument overcomes this problem by getting rid of the mirror. In addition, the improved instrument overcomes some general limitations of the old one, especially it provides the possibility of computer controlled pointing in any viewing direction (vertical as well as azimuthal) which was crucial for the water-pointing measurements during TransBrom. Also, it is smaller and lighter in weight and is mounted either on a tripod or on a mechanism attached to the ship's side which are important requirements aiming at the use as a (ship-borne) campaign instrument. Another advantage is that the new instrument can be easily used for TargetDOAS measurements. The first application of the improved MAX-DOAS instrument was an NO_2 intercomparison campaign, where it showed excellent performance and was chosen as one of the reference instruments.

To summarize, the objectives of this thesis are:

- The construction of an improved MAX-DOAS instrument, which participated at three campaigns in the context of this thesis (focusing on the TransBrom campaign) and is installed at several permanent sites within the BREDOM network (the IUP-Bremen network of permanently ground-based MAX-DOAS stations).

- The retrieval of trace gas profiles (not only IO, but also NO_2 and HCHO) in the marine boundary layer over the remote ocean from measurements during TransBrom and - if possible - to validate corresponding satellite measurements (Peters et al., 2012; Großmann et al., 2013).

- The investigation of spectral structures from liquid water effects and their impact on the DOAS analysis, especially the retrieval of a residual spectrum describing insufficiently compensated spectral structures of liquid water effects. For this purpose, MAX-DOAS measurements performed towards the water surface during TransBrom were used.

Outline of this thesis

The relevant aspects of atmospheric chemistry and physics are introduced in chapter 2. In chapter 3, the physical fundamentals of absorption and scattering processes are given, followed by a description of the applied methods of data analysis (DOAS and profile retrieval). The different instruments used in this thesis are explained in chapter 4. The focus of this chapter is on the improvement of the IUP-Bremen MAX-DOAS instrument.

In June-July 2009, the improved instrument participated in an NO_2 intercomparison campaign in Cabauw, The Netherlands. Results of this campaign where the new instrument showed excellent performance are given in chapter 5.

Atmospheric measurements during the TransBrom campaign are reported in chapter 6. Here, background concentrations and vertical columns of NO_2 and HCHO over the remote ocean were retrieved and used to validate corresponding satellite measurements. In addition, background concentrations of IO were retrieved. Furthermore, tropospheric IO measurements in the tropical marine boundary layer performed on/close to Borneo, Malaysia, during a third campaign (SHIVA) are briefly presented here.

The investigation of liquid water spectral effects and their impact on the DOAS analysis are described in chapter 7. From water-pointing measurements during TransBrom, residual spectra are retrieved describing liquid water structures that are unaccounted for by currently available cross-sections (of liquid water absorption and vibrational Raman scattering). The potential improvement provided by these correction spectra is then demonstrated in DOAS test fits on ground-based and satellite data.

Finally, the thesis closes with a brief summary about the main results, the conclusions that have been drawn and recommendations for future work.

2. Chemistry and physics of the Earth's atmosphere

This chapter provides an overview about physical and chemical processes and fundamentals of the atmosphere as far as it is related to the study presented in this thesis. The information given here is based on (Brasseur et al., 1999) and (Wayne, 2000). The figures are self-made, unless states otherwise. The interaction of light with matter, which is the basis of the remote sensing technique used in this thesis, is discussed in chapter 3.

2.1. Composition and structure of the atmosphere

The atmosphere is a thin gaseous layer that is attracted by the Earth's gravitation and separates its surface from space. The current state of the atmosphere is the result of a long evolutionary process starting ≈ 4.5 billion years ago right after the formation of planet Earth. Strong volcanic activity on the young Earth lead to outgasing of mainly water vapour and carbon dioxide. When the Earth cooled, the water vapour condensed forming seas and oceans. Photochemical reactions resulted in an enrichment of carbon dioxide as well as nitrogen. Large amounts of carbon dioxide were absorbed by the oceans where micro-organisms (and later also plants at land) converted it into oxygen through photosynthesis. The oxygen concentration in the atmosphere subsequently raised allowing the formation of the ozone layer as well as the evolution of lifeforms relying on oxygen for their metabolic cycle. The composition of today's atmosphere is given in Tab. 2.1.

Constituent	Volume mixing ratio	Remarks
Nitrogen (N_2)	78.08 %	
Oxygen (O_2)	20.95 %	
Argon (Ar)	0.93 %	
Carbon dioxide (CO_2)	0.035 %	increasing, anthropogenic impact
Water vapour H_2O	0-4 %	depending on location and situation
Helium (He)	5.5 ppm	
Neon (Ne)	18 ppm	
Methane (CH_4)	1.7 ppm	

Table 2.1.: Major constituents of the atmosphere (Wayne, 2000).

The major constituents of the atmosphere are nitrogen (N_2) and oxygen (O_2). Nitrogen is rather stable and an inert gas as a triple covalent bond develops between the nitrogen atoms (total binding energy 942 kJ/mol). Therefore, most chemical reactions between substances in air or exposed to air involve oxygen (e.g. corrosion) but are often not spontaneous as activation energy is required (e.g. combustion). Thus, chemical reactions in the atmosphere under standard conditions mostly involve radicals (e.g., OH, NO, NO_2) having an unpaired electron and therefore a high affinity to react with other molecules. As a result, the life-time of radicals is short (seconds to hours) and their abundance is small (mostly in the range of parts per billion) and highly variable as depending on conditions (sunlight, distance to source, availability of reactants).

The noble gases (e.g., He, Ar, Ne) are chemically inert and consequently their mixing ratio is stable. In contrast, the mixing ratio of water vapour is highly dependent on local conditions (humidity), showing a large variability. The abundance of carbon dioxide exhibits a seasonal variability from uptake and release from vegetation but also an increasing trend due to anthropogenic releases. Water vapour and carbon dioxide as well as methane (constant background concentration) are the major greenhouse gases.

Aerosols (solid or liquid particels suspended in the atmosphere) have a large impact on atmospheric properties and radiative transfer. E.g., the condensation of water vapour forming clouds starts at aerosols (so called cloud condensation nuclei (CCN)). Heterogeneous reactions can occur on the surface of particels. The influence on the radiative transfer can be observed sometimes even by eye, e.g. during dust events or at heavily polluted locations (Fig. 2.2). Aerosols originate from natural as well as anthropogenic sources, e.g. combustion processes (biomass burning, industry), volcanoes, meteoric debris, wind-blown dust, sea spray.

2.1.1. The greenhouse effect

The incoming solar radiation from the sun passing the atmosphere warms the Earth surface. The Earth re-emits black-body radiation (see Sect. 3.1) with a maximum at $\approx 10\ \mu$m (infrared) corresponding to a temperature of 255 K (-18° C), which is below the freezing point of water under normal conditions and $\approx$ 33 K below the average global temperature on the Earth's surface of 288 K (15° C). This difference between theoretical and actual temperature is a consequence of the trapping of energy (and therefore heat) in the Earth's atmosphere. The emitted infrared radiation from the Earth's surface excites infrared-absorbing greenhouse gases in the atmosphere. The excited states can decay by collision (passing energy to other particles) or by re-emission of photons. The probability for the direction of the re-emitted photon is spherically symmetric, i.e. some radiation is emitted into space (energy is lost) or back towards the Earth surface. Consequently, parts of the infrared radiation emitted by the Earth is reflected back to its surface resulting in the 33 K higher temperature compared to the temperature that the solar radiation would cause. This *greenhouse effect* is crucial for life on the Earth as the temperature would drop below the freezing point of water without.

The most important greenhouse gases are water vapour, carbon dioxide and methane (CH_4), but also ozone (O_3), nitrous oxide (N_2O), carbon monoxide (CO) and chlorofluorocarbons (CFCs) contribute to the greenhouse effect. The study presented in this thesis is not directly linked to the greenhouse effect, but the species that have been retrieved are ozone and background formaldehyde, which originates from methane oxidation. Also NO_2 and IO, which have been retrieved as part of this study, are linked to the greenhouse effect, predominently through their impact on ozone.

2.1.2. Vertical structure of the atmosphere

The vertical temperature profile divides the Earth's atmosphere into four different regimes with alternating positive and negative temperature gradients (Fig. 2.1). These regimes are (starting

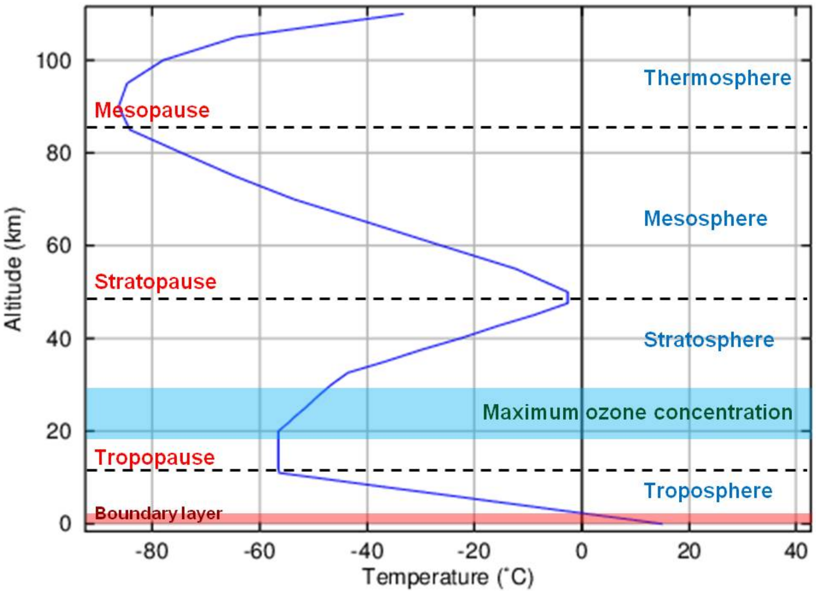

Figure 2.1: Vertical temperature profile in the atmosphere (U.S. standard atmosphere).

from the ground) the troposphere, the stratosphere, the mesosphere and the thermosphere.

The surface (heated by sunlight) warms the air above. In the troposphere, which contains about 80 % of the atmosphere's mass and almost all water vapour and aerosols, the temperature decreases according to the decreasing pressure with height (barometric formula) on average at an adiabatic lapse rate of ≈ 7 K/km. Due to the negative temperature gradient, hot air masses can rise and subsequently convection processes occur leading to a vertical mixing of the troposphere. When rising air masses cool down below the condensation point, the water vapour condenses forming clouds. Almost all weather phenomena take place in the troposphere.

In an altitude of ≈ 8 km (at the poles) and 18 km (at the equator) the linear temperature decrease stops (tropopause). In the following stratosphere, which extends up to an altitude of ≈ 50 km, the temperature increases again. The positive temperature gradient is a consequence of the ozone layer, which absorbs UV light from the solar radiation and subsequently warms up. About 90% of the total atmospheric ozone is located in the stratosphere. The maximum of the ozone volume mixing ratio is at an altitude of ≈ 25-30 km (the maximum concentration peaks at a lower altitude due to the decreasing pressure with height). Details of the stratospheric chemistry and especially ozone are given in Sect. 2.2.

As a consequence of the positive temperature gradient, no convection occurs in the stratosphere. For air parcels rising in the troposphere due to their temperature, the tropopause acts like a barrier and they cannot rise further as temperature raises again. Air masses from the troposphere can pass the tropopause and enter the stratosphere in the tropics due to overshooting of cumulonimbus clouds and radiative heating (or diffusion and horizontal mixing).

The temperature gradient, which is positive in the stratosphere, reverses again at the stratopause and the following mesosphere is characterized by a negative temperature gradient as the effect of heating due to UV-absorption of ozone molecules decreases.

The negative temperature gradient reverses at the mesopause in an altitude of ≈ 85 km. The following forth regime of the atmosphere is called thermosphere, which is strongly influenced by the solar wind (charged particles emitted from the sun). Moreover, the very short-waved solar radiation ionizes molecular and atomic oxygen and nitrogen and forms a plasma of very fast particles. The large kinetic energy of the particles correspond to extremely high temperatures (> 1000 K).

Figure 2.2: View across the Bosphorus (Istanbul, 23 March 2012). The boundary layer can be observed even by eye due to the large pollution. The brownish color of the boundary layer is caused by NO_2 absorption (in combination with aerosol extinction).

However, this temperature cannot be regarded in a classical (statistical) way as collisions are very rare due to the low density and the free path length is in the order of several kilometers.

A region of special interest for this thesis is the lowermost regime of the troposphere, which is called the planetary boundary layer (BL). The higher parts of the troposphere are called *free troposphere*. The BL is dominated by influences from the surface: Due to heating from the surface it is a very turbulent layer and subsequently well mixed. In contrast to the geostrophic winds in the free troposphere, the wind in the BL is dominated by friction at the ground and surface structures. Due to the strong mixing, aerosols and short-lived trace gases that are released at the surface are pretty much concentrated in the BL showing a block-like profile shape. In highly polluted regions (e.g. industrial regions, megacities), the boundary layer can be often observed even by eye (Fig. 2.2). The height of the boundary layer varies with surface temperature and ranges over land from a few hundred meters at night up to 2 kilometers and more at daytime (depending on location). Over the ocean, the marine boundary layer height (MBL) is much more constant according to the more constant surface temperature of the ocean and a few hundred meters high.

2.1.3. Circulation systems

On a global scale, three different wind patterns exist, which are referred to as the Polar cell, the Fresnel cell and the Hadley cell (Fig. 2.3). Across the equator, the sunlight intensity at the surface and therefore ground temperatures are highest, since the direction of the radiation is almost perpendicular to the ground and the air masses that have to be transmitted before reaching the surface are smallest. The region in that these conditions prevail is called the innertropical convergence zone (ITCZ). It's exact position shows a seasonal cycle as the Earth's rotational axis is not perpendicular to the ecliptic plane. Inside the ITCZ, air masses from the ground are elevated up to the tropopause as a consequence of the strong heating (and can sometimes even reach the stratosphere, especially above the western pacific warm pool, see chapter 6). At the ground, a low pressure regime developes and a high pressure regime right below the tropopause. Subsequently, the air masses below the tropopause escape polewards and start sinking as they cool. The pressure of the poleward moving air rises because a) the Earth's perimeter and therefore the available space decreases to the poles and b) the movement in the direction of the poles slows down because the air

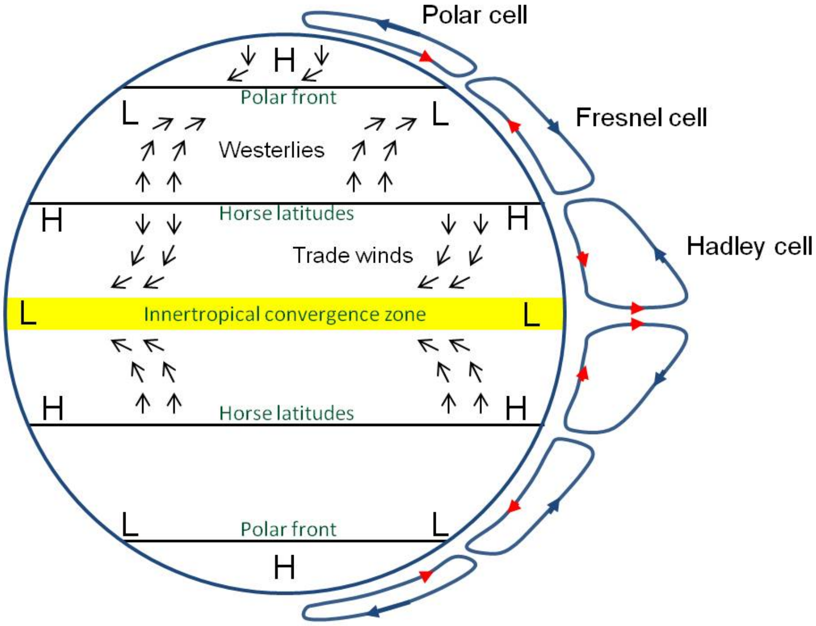

Figure 2.3: Global circulation and wind systems in the Earth's troposphere.

masses are deflected by the coriolis force. Therefore, the air sinks towards the surface at the *Horse latitudes* of about 30° where a high pressure area developes and causing a flow back on ground level to the low pressure regime in the ITCZ closing the so called *Hadley cell.* The ground winds towards the ITCZ are again deflected by the Coriolis force resulting in a component blowing from east to west. Due to their large impact on maritime navigation in times of sailing, these winds were called *Trade winds.* The Hadley cell is the most stable wind system.
On the poles, the surface heating due to solar radiation is smallest and subsequently air masses sink to the ground, forming a high pressure regime and move towards lower latitudes (again deflected by the coriolis force). At latitudes of about 60°, the air masses are warm enough to rise and flow back to the pole below the tropopause closing the *Polar cell.* Between Polar cell and Hadley cell that have the same direction of rotation developes a third, counter-rotating circulation, the so called *Fresnel cell.* The ground winds of the Fresnel cell move polewards and are deflected in easterly direction due to the Coriolis force. Consequently, the Fresnel cell is also referred to as the west wind zone, although it is the most unstable of the three wind systems.
The ship-borne TransBrom and SHIVA campaigns (chapter 6) took place in the Hadley cell. While the SHIVA campaign was perfomed entirely close to the ITCZ, the TransBrom campaign started in the West wind zone and crossed the Hadley cell from North to South.

2.2. Stratospheric chemistry

The stratospheric chemistry is not the focus of the work presented in this thesis. Nevertheless, stratospheric O_3 as well as NO_2 vertical columns were retrieved (Sect. 5 and 6) in order to validate complementary satellite measurements from the SCIAMACHY and GOME-2 instruments.

2.2.1. Stratospheric ozone and halogens

The most important trace gas in the stratosphere is ozone as it absorbs UV-light (λ < 320 nm) that can lead to DNA damage and skin cancer. The ozone layer prevents this UV radiation from reaching the surface. A first theory of the production and loss of stratospheric ozone was given by S. Chapman (Chapman, 1930). When ultraviolett radiation strikes the stratosphere, it can dissociate molecular oxygen. The atomic oxygen then reacts with further molecular oxygen giving ozone:

$$
\begin{aligned}
O_2 + h\nu\ (\lambda < 242nm) &\rightarrow 2O && (2.1)\\
O_2 + O + M &\rightarrow O_3 + M && (2.2)
\end{aligned}
$$

Loss of ozone occurs due to photolysis or reaction with atomic oxygen:

$$
\begin{aligned}
O_3 + h\nu\ (\lambda < 320nm) &\rightarrow O_2 + O && (2.3)\\
O_3 + O &\rightarrow 2O_2 && (2.4)
\end{aligned}
$$

The atomic oxygen that is produced from photolysis of O_3 (Eq. 2.3) can react again with molecular oxygen to form ozone according to Eq. 2.2. In principle, also two oxygen atoms could react to O_2, but this reaction is negligible due to the low concentrations of O. Consequently, Eq. 2.4 is the only real loss of ozone.

The system of reactions 2.1 - 2.4 is called the *Chapman cycle*. The concentration of O_2 that increases with pressure towards the surface and the UV intensity that decreases towards the surface (air becomes denser and UV parts of the spectrum diminish due to the reactions as described above) would result in an ozone layer having a maximum at a typical altitude of 35 km.

However, the production and loss reactions of the Chapman cycle would balance at an ozone concentration that is higher than observed values, i.e. additional loss terms are needed to explain the observations. Predominantly, these additional loss reactions are catalytic cycles

$$
\begin{aligned}
X + O_3 &\rightarrow XO + O_2 && (2.5)\\
XO + O &\rightarrow X + O_2 && (2.6)\\
\hline
net: O_3 + O &\rightarrow 2O_2 && (2.7)
\end{aligned}
$$

where X is either the hydroxil radical OH (Bates and Nicolet, 1950), nitrogen monoxide (NO) (Crutzen, 1970; Johnston, 1971) or a halogen radical, e.g. chlorine (Cl) (Molina and Rowland, 1974; Stolarski and Cicerone, 1974), bromine (Br) (Wofsy et al., 1975) or iodine (I) (Solomon et al., 1994, and references therein). In addition to these simple catalytic cycles, many other, combined cycles exist (e.g. the recovery of Br and Cl from the reaction of BrO with ClO). Some of these radicals have natural precursors, e.g. the TransBrom and the SHIVA campaign (chapter 5) were focussing on short-lived halogen compounds originating from the ocean and traveling into the stratosphere where the compounds are dissociated by solar radiation and the halogen released contribute to ozone depletion. A prominent example for anthropogenic sources is the emission of chlorofluorocarbons (CFCs), which lead to the Montreal Protocol in 1987 (becoming law in 1989) aiming to reduce these emissions. CFCs containing the halogens Cl and F were widely used as freezing agents because of many preferable characteristics (stable, fireproofed, odourless, colourless and not toxic). However, due to their stability they have almost unlimited lifetimes in the troposphere and thus finally reach the stratosphere, where they are dissociated by short-wave solar UV-light and the resulting halogens contribute to the catalytic ozone depleting reactions. Over the Antartic (and to a lesser extent also over the Arctic) a dramatic loss of stratospheric ozone is observed at antarctic (or arctic) springtime, known as the *ozone hole* (Farman et al., 1985). During the polar night, extreme cold temperatures ($T < -78°$ C) occur in the stratosphere resulting a) in a polar vortex separating the air masses inside from air masses outside at lower latitudes and b) in the formation of polar stratospheric clouds (PSCs). The PSCs consist either of particels made of HNO_3 (type I) or H_2O-ice and HNO_3-hydrates (type II). The catalytic ozone depleting cycles stop during the polar night, because no atomic oxygen is produced due to the lack of sunlight. In contrast, the halogens participate in reactions forming so called *reservoir species*, e.g. $ClONO_2$ and HCl. These reservoir species do not lead to ozone depletion, but *store* the halogens in an inactive form. In the presence of PSCs, heterogeneous reactions can occur on the particle surfaces leading to more active species, e.g.:

$$ClONO_2 + HCl \rightarrow Cl_2 + HNO_3 \tag{2.8}$$

$$Cl_2 + h\nu \rightarrow 2Cl \tag{2.9}$$

The Cl_2 does not engage ozone during the polar night, but it is quickly converted to atomic Cl (Eq. 2.9) at sunrise and depletes ozone according to Eq. 2.5. Because the concentration of atomic oxygen is too small at polar sunrise, a recovery of Cl according to Eq. 2.6 is not possible. Instead, the resulting ClO reacts with further ClO or BrO giving back Cl. Finally, when temperatures rise and the polar vortex becomes unstable and breaks, a mixing with air masses from lower latitudes and higher ozone levels occurs and the ozone hole disappears.[1]

2.2.2. Stratospheric nitrogen dioxide

The most important source of nitric oxides in the stratosphere is N_2O, which is emitted by microbial activity in soil (Bates and Hays, 1967). Nitrous oxide (N_2O) is stable enough to reach the stratosphere, where it reacts with atomic oxygen either forming N_2 and O_2 or nitrogen monoxide (NO):

$$N_2O + O(^1D) \rightarrow 2NO \tag{2.10}$$

The NO can then further react with ozone to NO_2 (reaction 2.6).

As already indicated in Sect. 2.2.1, NO_x species ($NO_x = NO + NO_2$) play an important role in the stratosphere. On the one hand, NO_2 reacts with ClO_x or HO_x forming reservoir species ($ClONO_2$, HNO_3), counteracting the ozone depletion. On the other hand, catalytic cycles according to Eq. 2.5 - 2.6 involving NO are most efficient in depleting ozone. In addition to Eq. 2.6, the recovery of NO from NO_2 occurs also in form of photolysis during daytime. The overall ozone depleting NO_x-cycle gives then

$$NO + O_3 \rightarrow NO_2 + O_2 \tag{2.11}$$

$$NO_2 + O \rightarrow NO + O_2 \tag{2.12}$$

$$NO_2 + h\nu \rightarrow NO + O \tag{2.13}$$

---

[1] While this is a general description of the formation of the ozone hole, the multiple pathways and reactions are still an issue of scientific investigation.

Also, NO_2 can directly react with ozone forming NO_3:

$$NO_2 + O_3 \rightarrow NO_3 + O_2 \tag{2.14}$$

$$NO_3 + h\nu \rightarrow NO + O_2 \tag{2.15}$$

During the day, the NO_3 is photolysed according to reaction 2.15 yielding again NO participating in the ozone depleting cycle. In the absence of sunlight during the night, the NO_3 reacts with NO_2 to N_2O_5:

$$NO_3 + NO_2 + M \rightarrow N_2O_5 + M \tag{2.16}$$

At sunset, also the photolysis of NO_2 (Eq. 2.13) as well as the reaction 2.12 (as atomic oxygen is produced by photolysis of ozone (Eq. 2.3) and therefore depending on sunlight as well) stop and subsequently the NO_2 concentration increases strongly. During the night, reactions 2.14 and 2.16 cause a slow decrease of the NO_2 concentration. At sunrise, NO_2 is rapidly photolysed towards an equilibrium of NO and NO_2 (Eq. 2.11 - 2.13). The diurnal cycle of stratospheric NO_2 shows therefore a minimum in the morning. The photolysis and thermal decomposition of N_2O_5, which is build up at night, is much slower and results in a slow linear increase during the course of the day. An example of the NO_2 diurnal cycle during daylight hours can be found in Fig. 6.6 in chapter 6.

2.3. Tropospheric chemistry

The retrieval of tropospheric trace gases is the focus of this thesis. Mostly, the measurements have been carried out in marine, tropical environments and background concentrations of nitrogen dioxide and formaldehyde as well as iodine monoxide were observed (chapter 6). Nevertheless, also measurements during an intercomparison campaign of nitrogen dioxide measuring instruments were perfomed in an anthropogenically polluted environment (chapter 5). In the following, the most important sources, sinks and chemical reactions of the related trace gases are introduced.

2.3.1. Tropospheric ozone

About 10% of total ozone is located in the troposphere. Whereas stratospheric ozone is it is essential for life as absorbing dangerous UV-light from solar radiation, tropospheric ozone is harmful for human health causing irritation of the respiratory tract and damaging the lung tissue when breathed in. Therefore, the ground-level concentration of ozone is routinely monitored in air quality networks (at levels $> 180\ \mu g/m^3 \approx 90\ ppb$ the public is informed). On the other hand, the photolysis of tropospheric ozone is the most important source for excited atomic oxygen ($O(^1D)$) and therefore the hydroxil radical OH:

$$O_3 + h\nu\ (\lambda < 320nm) \rightarrow O_2 + O(^1D) \tag{2.17}$$

$$O(^1D) + H_2O \rightarrow 2OH \tag{2.18}$$

(most of the excited $O(^1D)$ atoms decay by collisions und subsequently react with O_2 back to ozone; only 1-10% of the $O(^1D)$ atoms react with water vapour to form OH according to reaction 2.18). OH is the most important radical in the troposphere initializing the oxidation of almost all trace gases and pollutants. Therefore, OH is a key species in *cleaning* the atmosphere and is often referred to as the *detergent of the atmosphere*. The lifetime of OH is only ≈ 1 s due to its high reactivity.

Sources for tropospheric ozone are a) transport from the stratosphere (≈ 50 %) and b) reaction of atomic oxygen (ground state) with molecular oxygen in the troposphere. The atomic oxygen is produced by photolysis of tropospheric NO_2 (see also Sect. 2.3.2). In the presence of sufficient levels of NO and NO_2 (industrialized, urban areas), a major source of tropospheric ozone is the oxidation of carbon monoxide (CO):

$$CO + OH \rightarrow CO_2 + H \tag{2.19}$$

$$H + O_2 + M \rightarrow HO_2 + M \tag{2.20}$$

$$HO_2 + NO \rightarrow OH + NO_2 \tag{2.21}$$

$$NO_2 + h\nu\ (\lambda < 424nm) \rightarrow NO + O(^1D) \tag{2.22}$$

$$O(^1D) + O_2 + M \rightarrow O_3 + M \tag{2.23}$$

$$net: CO + 2O_2 + h\nu \rightarrow CO_2 + O_3 \tag{2.24}$$

The net reaction requires only carbon monoxide, O_2 and sunlight and yields ozone and CO_2, while the catalysts OH, HO_2, NO and NO_2 are reproduced within the cycle. However, the availability of NO_x-radicals is crucial. If no sufficient amount of NO_x is available (< 30-40 pptv), reaction 2.21 is substituted by

$$HO_2 + O_3 \rightarrow OH + 2O_2 \tag{2.25}$$

meaning that ozone can be even depleted in the CO-cycle. The importance of NO_x-radicals for the tropospheric ozone level is also discussed in Sect. 2.3.2.

Another production scheme of tropospheric ozone is the methane oxidation, which yields formaldehyde (HCHO) and is discussed in Sect. 2.3.3. The photolysis of HCHO also yields CO, which influences the tropospheric ozone level according reactions 2.19 - 2.25.

2.3.2. Tropospheric nitrogen dioxide

In the troposphere, the nitrogen oxides NO and NO_2 (= NO_x) are prominent pollutants. Major sources of NO_x-radicals are combustion processes, both anthropogenic (industry, traffic) and natural (e.g. bush fires, soil, lightning). Nitrogen dioxide (NO_2) is a reddish-brown, toxic gas and is routinely monitored by air quality networks in urban areas (information threshold for the public: $> 200\ \mu g/m^3 \approx 110\ ppb$). In heavily polluted environments, NO_2 can be observed even by eye (Fig. 2.2). As a consequence of its source regions, highest levels of tropospheric NO_2 are observed from space-borne platforms over urban and industrial regions, bush fires and shipping routes (Leue et al., 2001; Richter et al., 2004, 2005; Franke et al., 2009; Konovalov et al., 2010).

As mentioned in Sect. 2.3.1, tropospheric NO_x-radicals are key species determining the concentration of tropospheric ozone. Due to the high temperatures in combustion processes, energies are reached allowing reactions of N_2 with O_2 producing nitrogen monoxide (NO):

$$N_2 + O_2 \rightarrow 2NO \tag{2.26}$$

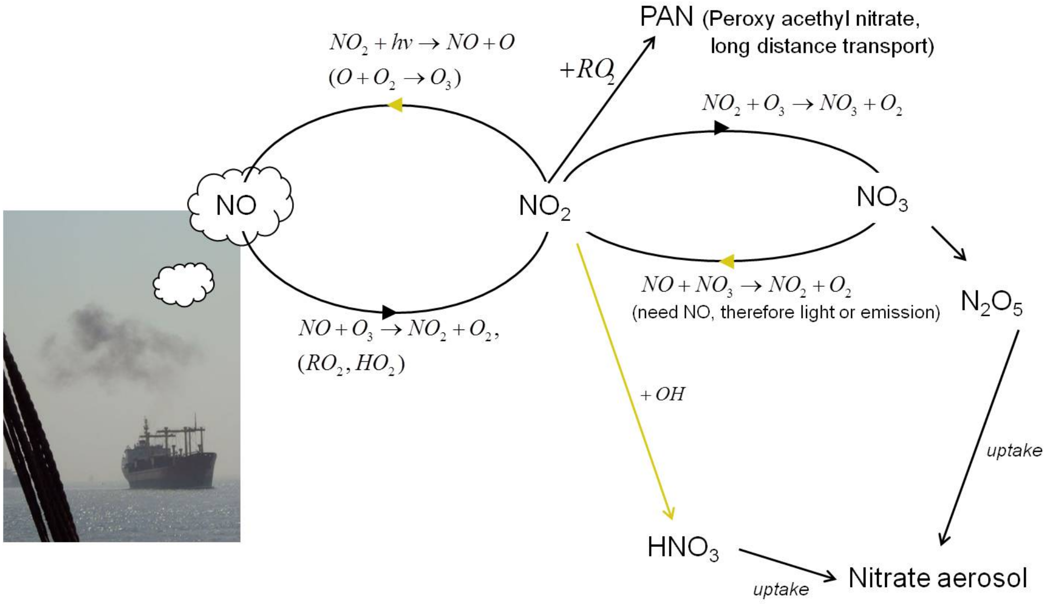

Figure 2.4.: NO_x-cycle in the troposphere. Combustion processes lead predominently to emissions of NO (and to a lesser extent also NO_2). Daytime reactions (depending directly or indirectly on sunlight) are indicated by a yellow arrow.

Nitrogen dioxide (NO_2) is subsequently produced from reactions of NO with ozone (reaction 2.27). During the day, the photolysis of NO_2 returns NO and an excited oxygen atom ($O(^1D)$) (reaction 2.28), which reacts with O_2 to ozone (reaction 2.29). Overall, this is an equilibrium cycle (see also Fig. 2.4):

$$NO + O_3 \rightarrow NO_2 + O_2 \tag{2.27}$$

$$NO_2 + h\nu\ (\lambda < 424nm) \rightarrow NO + O(^1D) \tag{2.28}$$

$$O(^1D) + O_2 + M \rightarrow O_3 + M \tag{2.29}$$

When neglecting all other species (very clean environment), a sunlight dependent equilibrium would develop between ozone, NO and NO_2 according to this NO_x-cycle during the day. Because in anthropogenic emissions predominently NO is released destroying ozone according to reaction 2.27, the ozone levels in polluted areas are usually lower than in rural areas. However, in the presence of HO_2 or RO_2 ($R = CH_3$ or larger hydrocarbons), reaction 2.27 can be replaced by

$$NO + HO_2 \rightarrow NO_2 + OH \tag{2.30}$$

$$NO + RO_2 \rightarrow NO_2 + RO \tag{2.31}$$

(i.e., this is reaction 2.21 in the oxidation of carbon monoxide in Sect. 2.3.1). Thus, NO is converted to NO_2 without destroying ozone. As photolysis of NO_2 yields in return NO and produces ozone (reaction 2.28 and 2.29), the result is an increasing ozone concentration (known as summer smog or photo-smog, because light is needed for the NO_2 photolysis).

The major sink for tropospheric NO_2 is the reaction with the hydroxil radical OH to nitric acid (HNO_3):

$$NO_2 + OH + M \rightarrow HNO_3 + M \tag{2.32}$$

Nitric acid has a low reactivity, can be uptaken by aerosols and is subsequently removed from the atmosphere. Reaction 2.32 is indirectly dependent on sunlight, because OH is formed from H_2O and $O(^1D)$ resulting from ozone photolysis (reactions 2.17 and 2.18). In the diurnal cycle (see Fig. 5.6 and the discussion in Sect. 5.2), the NO_2 level shows therefore a minimum at noon. In addition, NO_2 can react with organic compounds (RO_2) to peroxyacetyl nitrate (PAN), which is an organic nitric oxide. At surface conditions, the lifetime of PAN is in the order of days and increases when the temperature drops with altitude (in comparison, the lifetime of NO_2 is in the order of one day and less). Thus, long-range transports of NO_2 in form of PAN is possible (meaning a local removal).

During the night, the photolysis of NO_2 stops. In the absence of new emissions, the NO (and also O_3) level declines due to reaction 2.27. In addition, NO_2 reacts with ozone to form NO_3:

$$NO_2 + O_3 \quad \rightarrow \quad NO_3 + O_2 \tag{2.33}$$

During the day, NO_2 is recovered by the reaction

$$NO_3 + NO \quad \rightarrow \quad NO_2 + O_2 \tag{2.34}$$

which requires NO. As NO is removed after sunset, this reaction is not possible at night. Moreover, NO_3 reacts further with NO_2 to N_2O_5 (see reaction 2.16), which can be uptaken again by aerosols and removed from the atmosphere resulting in a loss of NO_x.

The above discussion is summarized in Fig. 2.4 illustrating the NO_x-cycle in the troposphere. An illustration of the NO and NO_2 diurnal cycles in a semi-rural area underlying anthropogenic impacts can be found in Fig. 5.6.

2.3.3. Formaldehyde

Formaldehyde (HCHO) is a highly reactive, flammable and colourless gas. It is soluble in water, which leads to removal (wash-out) of formaldehyde from the atmosphere during rain. In higher concentrations ($>$ 0.5 ppmv), HCHO is harmful for health, irritating the mucous membraces and causing skin and lung allergies.

In the atmosphere, HCHO is a natural trace gas, but anthropogenic emissions enhance its concentration locally. Formaldehyde is directly emitted by combustion of biomass and fossil fuel (e.g., Anderson et al., 1996). In addition, it is produced during photochemical degradation of methane (CH_4) and non-methane hydrocarbons (NMHC). An important precursor of formaldehyde is isoprene (C_5H_8), which is emitted by many plants into the atmosphere, where it is converted by radicals (e.g. OH) into other species. Sinks of formaldehyde (photolysis at wavelengths $<$ 400 nm, reaction with OH, wet deposition) result in a short life-time of a few hours (Arlander et al., 1995). Thus, elevated HCHO is found close to its sources, e.g. rain forests, industrial sites, shipping routes (De Smedt et al., 2008; Marbach et al., 2009; Stavrakou et al., 2009). Apart from these enhanced concentrations in the vicinity of sources, the oxidation of methane is considered to produce a global HCHO background. In remote marine environments, reported surface levels are in the range of

0.2 - 1 ppbv (e.g., Weller et al., 2000; Singh et al., 2001; Burkert et al., 2001).

Under the condition of high NO_x-levels, the oxidation of methane follows the reaction scheme

$$\begin{array}{lcll}
CH_4 + OH & \rightarrow & CH_3 + H_2O & (2.35) \\
CH_3 + O_2 + M & \rightarrow & CH_3O_2 + M & (2.36) \\
CH_3O_2 + NO & \rightarrow & CH_3O + NO_2 & (2.37) \\
CH_3O + O_2 & \rightarrow & HCHO + HO_2 & (2.38) \\
HO_2 + NO & \rightarrow & OH + NO_2 & (2.39) \\
2(NO_2 + h\nu) & \rightarrow & 2(NO + O(^1D)) & (2.40) \\
2(O(^1D) + O_2 + M) & \rightarrow & 2(O_3 + M) & (2.41) \\
\hline
net : CH_4 + 4O_2 & \rightarrow & HCHO + H_2O + 2O_3 & (2.42)
\end{array}$$

As a result, the oxidation of CH_4 produces formaldehyde and ozone. The HO_x and NO_x radicals are reproduced within the reaction scheme 2.35-2.42. Nevertheless, a sufficient amount of NO_x is necessary for catalysing this cycle.

In the absence of NO_x-radicals, the NO in reaction 2.37 can be substituted by HO_2 giving CH_3O_2H and subsequently photolysis (reactions 2.43 and 2.44). The overall cycle gives then (only new reactions are numbered):

$$\begin{array}{lcll}
CH_4 + OH & \rightarrow & CH_3 + H_2O & \\
CH_3 + O_2 + M & \rightarrow & CH_3O_2 + M & \\
CH_3O_2 + HO_2 & \rightarrow & CH_3O_2H + O_2 & (2.43) \\
CH_3O_2H + h\nu & \rightarrow & CH_3O + OH & (2.44) \\
CH_3O + O_2 & \rightarrow & HCHO + HO_2 & \\
\hline
net : CH_4 + O_2 & \rightarrow & HCHO + H_2O &
\end{array}$$

An alternative to the photolysis of CH_3O_2H (reaction 2.44 is the reaction with OH and subsequent conversion yielding HCHO.

Apart from deposition (washing out during rain), formaldehyde is destroyed by photolysis or reaction with OH:

$$\begin{array}{lcll}
HCHO + h\nu & \rightarrow & CO + H_2 & (2.45) \\
HCHO + h\nu & \rightarrow & CHO + H & (2.46) \\
HCHO + OH & \rightarrow & CHO + H_2O & (2.47)
\end{array}$$

The resulting CHO react rapidly with O_2:

$$CHO + O_2 \rightarrow CO + HO_2 \tag{2.48}$$

Altogether, the products of HCHO degradation are CO, H_2 and HO_2. In the presence of NO_x-radicals, the oxidation of CO produces tropospheric ozone (see Sect. 2.3.1).

2.3.4. The oxygen dimer O_4

The oxygen dimer O_4 is a collision complex of two oxygen molecules (O_2-O_2), which are attached to each other by Van der Waals forces, i.e. no covalent bonds are developing. As a consequence, the O_2-O_2 complex is in general chemically inert and instable due to the weak Van der Waals bonds. However, in the context of this work it is important for two aspects:

- O_4 has absorption bands in the UV and visible spectral region and therefore it has to be included in the DOAS fit (the DOAS analysis is described in Sect. 3.4).

- Because a) O_4 is a collision complex of two O_2 molecules and b) it is chemically inert, its vertical profile depends only on meteorological conditions and can be calculated from the (known) pressure and temperature profiles. This is used for estimating the aerosol load in the trace gas profile retrieval (see Sect. 3.6).

2.3.5. Halogens in the troposphere

In the stratosphere, halogens (Cl, Br, I) have a large impact on the ozone concentration, which was briefly discussed in Sect. 2.2.1. The respective reactions (2.5 and 2.6) are not restricted to the stratosphere (except that the ozone mixing ratio is much higher than in the troposphere). However, ozone is a key species in tropospheric chemistry as discussed in Sect. 2.3.1. By their impact on tropospheric ozone, halogens influence the oxidizing capacity and therefore the composition of the atmosphere. An overview about halogen chemistry (focussing on polar regions) is given in (Simpson et al., 2007b).

Iodine monoxide plays a special role as it reacts with itself forming higher complexes I_xO_y finally leading to the formation of marine particels and cloud condensation nuclei and therefore affecting global radiative forcing and climate (O'Dowd et al., 2002).

Prominent anthropogenic precursors of atomic halogens are chlorofluorocarbons (CFCs), which have been discussed earlier (Sect. 2.2.1). CFCs are rather stable and photolysed predominently only by harder UV-radiation in the stratosphere. Nevertheless, a wide range of industrially used halogen containing compounds are photolysed more easily and release halogens already in the troposphere.

A natural source for halogen precursors is the ocean, as sea salt contains chlorine ions (Cl^-) and to a lesser extent also Br^- and I^- (Wayne, 2000). Sea spray and sea salt particels are therefore an inorganic source for halogen compounds (e.g. I_2). Furthermore, various types of algae and microalgea were found to produce volatile organic halogen compounds, e.g. CH_3Br, CH_3I or CH_2I_2. The latter is considered to be the main form of organic iodine release from algea (Carpenter, 2003). The various organohalogen species differ in their life-times, e.g. CH_3Br (bromomethane) has a relative long life-time and predominently reaches the stratosphere before it is destroyed releasing atomic bromine. In contrast, the life-time of CH_3I is in the order of days and it is photolysed mostly in the troposphere.

In polar regions, strong depletion events of tropospheric ozone were found to coincide with the presence of bromine compounds (Barrie et al., 1988). High bromine abundances, so called *bromine explosions*, are occasionally observed in the first months after Polar sunrise. Most likely, this bromine release is caused by inorganic processes on frost flowers, aerosols or sea-ice surfaces (e.g., Simpson et al., 2007a). Similarly, marine biogen activity (e.g., a spring bloom of under-ice algae) producing organohalogens leads to high levels of observed IO (e.g., Schönhardt et al., 2012).

On a global scale, halogens and halogen oxides in the troposphere are found predominently in coastal regions (biogenic release from algea) and in the Arctic and Antartic (frost flowers, sea-ice, biogenic release) (e.g., Schönhardt et al., 2008; Theys et al., 2011) as these are the source regions. As discussed above, the ocean is considered to be a source for inorganic release of halogen species (focusing on iodine, this is explained in detail in Sect. 6.1.5). For example, close to the northwest African coastal upwelling system, IO mixing ratios of ≈ 1.4 pptv were observed in the subtropical marine boundary layer (Read et al., 2008). Nevertheless, measurements of halogens in remote marine air are sparse. Space-borne satellite observations of halogen oxides over the remote ocean have problems (compare Sect. 1 and Fig. 1.1) because of a) the small amount of respective trace gases of interest and b) interference with (partly unknown) spectral structures resulting from liquid water absorption. Therefore, this thesis comprises the detection of halogen oxides with an improved ground-based MAX-DOAS system above the remote ocean (chapter 6) as well as the investigation of the effects of liquid water absorption on the DOAS analysis (chapter 7).

3. Absorption Spectroscopy and Data analysis

This chapter describes the measurement technique used in this thesis from physical fundamentals to the data retrieval. After an introduction to solar radiation (Sect. 3.1), the molecular physics being responsible for the absorption behaviour of different species is discussed (Sect. 3.2). Scattering processes in the atmosphere and the DOAS measurement technique using scattered sunlight spectra to detect trace gases in the atmosphere are explained in Sect. 3.3 and Sect. 3.4. At the end of this chapter (Sect. 3.5 and 3.6), a description of the radiative transfer model and the IUP Bremen profiling algorithm is given, which are used in this work for the retrieval of trace gas profiles. The figures in this chapter are self-made unless stated otherwise.

3.1. The solar spectrum

Most of the matter in our solar system is concentrated in the sun, which is therefore its center of gravity. When the solar system was formed, the matter in its center condensed to a *protostar* (Weigert and Wendker, 1996). This protostar collapsed due to its own gravity and subsequently its core temperature and pressure raised until the ignition of thermonuclear fusion processes. Since that time, the energy released in the fusion reactions produces a counter force stopping the gravitational collaps and the sun will remain in its current state until its nuclear fuel is spent and it ends as a *white dwarf*.

The dominating fusion process in the sun's core is the pp-cycle (proton-proton chain reaction), where effectively four protons (hydrogen cores) unite to form a helium core. The energy released by it is transported upwards to the surface by means of electromagnetic radiation and convection. When it reaches and heats the *photosphere*, the energy can escape into space in form of light as following outer layers are at least partially transparent. The photosphere is an only 300 km thick layer that emits black-body radiation corresponding to its temperature of $\approx$ 5800 K. The spectral distribution is given by *Planck's law*

$$B(\lambda, T) = \frac{2\pi hc^2}{\lambda^5} \cdot \left(e^{\frac{hc}{\lambda kT}} - 1\right)^{-1} \tag{3.1}$$

where c is the speed of light, h the Planck constant and k the Boltzmann constant. B is the spectral irradiance, i.e. the emitted power per unit area and wavelength interval (unit $W/m^2/nm$). The corresponding spectrum is shown in Fig. 3.1.

The maximum's wavelength position of the black-body radiation is given by Wien's displacement law

$$\lambda_{max} \cdot T = 0.2879 \ cm \ K \tag{3.2}$$

For a temperature of $T \approx 5800K$, the maximum's wavelength is $\approx$ 500 nm (green).

The sun is not a perfect black body emitting light only as a result of its temperature. Substances in

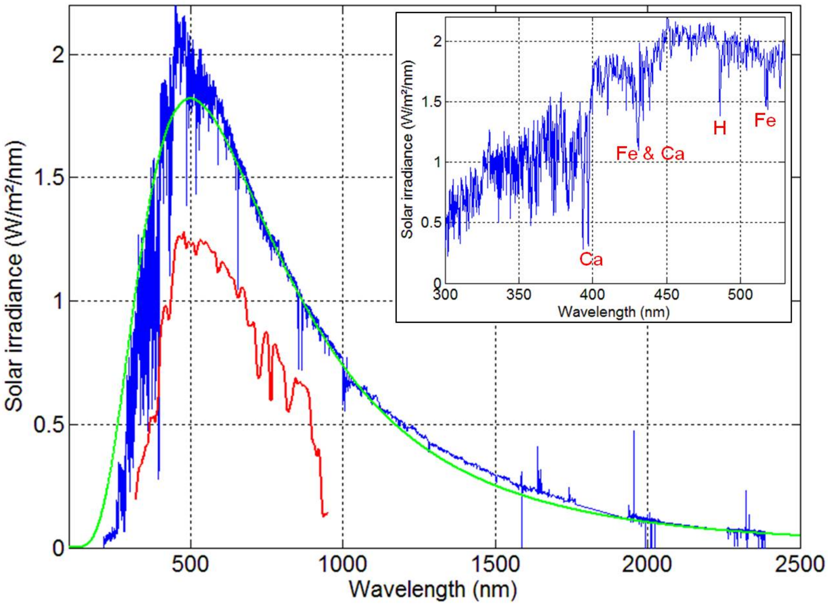

Figure 3.1.: Green line: Black-body radiation for T=5800 K. Blue line: Solar radiation outside the atmosphere as measured from SCIAMACHY satellite instrument. The spectrum has been assembled and calibrated by Jochen Skupin, IUP Bremen (Schönhardt, 2009). Red line: Measured radiation from 300 - 1000 nm at the Earth's surface during the TransBrom (see chapter 6) field campaign (the data was provided by T. Dinter, IUP Bremen). In the inset, covering the spectrum from 300 - 530 nm, dominant Fraunhofer lines are identified by corresponding absorbing species in the sun's atmosphere.

the sun's atmosphere emit and absorb light at characteristic wavelengths, which is a consequence of their emission or absorption cross-sections (see chapter 3.2). Thus, the continuous black-body radiation is interfered with these emission and absorption peaks. As a result, the incoming solar radiation at the Earth shows characteristic structures. For illustration, the blue line in Fig. 3.1 is an observed sunlight spectrum from the SCIAMACHY satellite instrument outside the atmosphere. The characteristic absorption lines in the solar spectrum are referred to as *Fraunhofer structures*. In the inset in Fig. 3.1, dominant Fraunhofer lines are identified in the wavelength region used for trace gas analysis in this thesis.

When passing the Earth's atmosphere, the sunlight is not homogeneously attenuated, but again absorbers (this time in the Earth's atmosphere) cause absorptions at characteristic wavelengths. Consequently, the sunlight observed at the ground (see Fig. 3.1) shows additional structures due to these absorbers. This is the initial point for remote sensing of the Earth's atmosphere. A prominent feature in Fig. 3.1 is the suppressed transmitted radiation at short wavelength, which is a result of absorption by ozone in the stratosphere.

3.2. Absorption spectra and band structures

In the following, the physics leading to characteristic absorption spectra of different trace gases is introduced. For a detailed description, the reader is referred to the common specialized textbooks (e.g., Hellwege, 1990; Mayer-Kuckuck, 1997; Demtröder, 2010).

The absorption and emission spectra of molecules show characteristic band structures, which are a consequence of inner-molecular energy levels $E_{k,n,L}$ (with the quantum numbers k, n, L denoting the energy levels). Similar to atoms, the states of a molecule (and therefore the position of the respective energy levels) can be described by the time-independent Schrödinger equation:

$$\hat{H}_0\psi(\boldsymbol{r}, \boldsymbol{R}) = E_{k,n,L}\psi(\boldsymbol{r}, \boldsymbol{R}) \tag{3.3}$$

where $\psi(\boldsymbol{r}, \boldsymbol{R})$ is the wavefunction of the molecule, $\boldsymbol{r}$ represents the position vectors of the electrons and $\boldsymbol{R}$ the nuclei position vectors.

Solving the Schrödinger equation for molecules is much more complex than for atoms and can be performed only in approximation (e.g. Born-Oppenheimer approximation or LCAO) as molecules consist of two or more nuclei and thus the electrical potential in the Hamiltonian $\hat{H}$ is polycentric. As a result of being not spherically symmetric, molecules have also degrees of freedom in rotation and vibration leading to further energy levels. In an approximation, the molecule's wave function solving the Schrödinger equation can be separated in a component for the electron shell's state, a component for rotations and a component for vibrations. The total energy is then the sum of all energies (eigen values of the Schrödinger equation):

$$E_{k,n,L} = E_k^{el} + E_n^{vib} + E_L^{rot} \tag{3.4}$$

where k comprises all quantum numbers for the state of the electron shell, n denotes the vibrational state and L the rotational state.

Interference with an external electromagnetic field (light) or quantum fluctuations can change the state of a molecule. As a result, energy is taken from or released to the external field in form of a photon whose wavelength corresponds to the difference in energies related to the initial and final state of the molecule (induced absorption and emission). Interference of an excited molecule with quantum fluctuations can only lead to the emission of a photon (spontaneous emission).

The transition from an initial to a final state cannot be described by a time-independent Schrödinger equation. Instead, the problem is described by means of pertubation theory. If $\hat{H}_0$ is the Hamiltonian of the time-independent Schrödinger equation, then the pertubation is described by a time-dependent term $\hat{H}'(t)$ so that $\hat{H} = \hat{H}_0 + \hat{H}'(t)$ and the time-dependent Schrödinger equation has the form

$$i\hbar\frac{\partial\varphi(\boldsymbol{r}, \boldsymbol{R}, t)}{\partial t} = [\hat{H}_0 + \hat{H}'(t)]\varphi(\boldsymbol{r}, \boldsymbol{R}, t) \tag{3.5}$$

If the pertubation is an electromagnetic field and the wavelength is much larger than the molecule's diameter (which is the case for visible light), the calculation leads to transition dipole moments, also called transition matrix elements (coupling between the electromagnetic field and higher multipole moments is possible, but in practice only coupling with the dipole moment is relevant)

$$\boldsymbol{M}_{if} = \int u_i^* \; \mathbf{p} \; u_f \; d\tau_{el} \cdot d\tau_N \tag{3.6}$$

where i and f denote all quantum numbers of the initial and final state, respectively, u_i, u_f are the position-depending parts of φ_i, φ_f and the integration is over all electron and nuclei coordinates (denoted by el and N).

The symbol $\mathbf{p}$ is the dipole moment operator. For example, in case of a 2-atomic molecule (with j

electrons and two nuclei of atomic numbers Z_1 and Z_2 at positions $\mathbf{R}_1$ and $\mathbf{R}_2$, respectively), the dipole moment operator is

$$\boldsymbol{p} = -e \cdot \sum_j \boldsymbol{r}_j + Z_1 e \boldsymbol{R}_1 + Z_2 e \boldsymbol{R}_2 = \boldsymbol{p}_{el} + \boldsymbol{p}_N \tag{3.7}$$

The probability of a transition from state i to f is proportional to the squared transition dipole moment ($|\boldsymbol{M}_{if}|^2$).

In the Born-Oppenheimer approximation, the wavefunction of a molecule is broken into its electronic and nuclear (vibrational, rotational) components:

$$u_{total} = u_{el} \cdot \chi_N \tag{3.8}$$

The transition matrix element is then

$$\boldsymbol{M}_{if} = \int u^*_{i,el} \cdot \chi^*_{i,N} \; (\boldsymbol{p}_{el} + \boldsymbol{p}_N) \; u_{f,el} \cdot \chi_{f,N} \; d\tau_{el} \cdot d\tau_N \tag{3.9}$$

Two cases can be distinguished:

1. The initial and final state belong to the same electron state ($u_{i,el} = u_{f,el}$). Then, only the nuclear wavefunction and the nuclear dipole moment $\boldsymbol{p}_N$ contribute to the transition matrix element. This is a pure rotational-vibrational transition of the molecule.

2. A mixed electron vibrational-rotational transition, i.e. the final state has another electron quantum number than the initial one.

The physical meaning of transitions is that the electromagnetic field (light) interacts with the charge density distribution and therefore the molecule's dipole moment. If the dipole moment does not change between states i and f, the transition is called *forbidden*. Otherwise, a photon of the wavelength corresponding to the transition (the energy difference between i and f) can be absorbed (or emitted) and therefore a peak occurs at the respective position in the absorption or emission spectrum. The strength of the respective line is propotional to the square of the dipole transition moment's magnitude.

3.2.1. Electron transitions

The potential of a covalent bonded molecule is a function of the nuclei distance: If the distance between the nuclei is large, the electronic energy levels will match those of single (isolated) atoms. If the distance is short, the Coulomb repulsion between the nuclei will dominate increasing the potential. Between these extrema is a local minimum in energy at the equilibrium distance R_0. The shape of the resulting potential can be approximated by the *Morse potential* (Fig. 3.2)

$$V(r) = C \left(1 - e^{-ar}\right)^2 \tag{3.10}$$

where C is a molecule specific constant.

The depth of the minimum depends on the electron density between the nuclei, which constitutes the strength of the binding. In excited states, the electron wave functions expand decreasing the electron density between the nuclei. As a consequence, the potential flattens and the equilibrium distance R_0 increases.

As discussed above, the incident light beam can change the state of a molecule leading to absorption (or emission) of a photon. If the configuration of the electron shell changes, this is called an electronic transition. The energies related to electronic transitions are in the order of 1 eV to 10 eV. The corresponding wavelengths are according to

$$\lambda = \frac{hc}{E} \tag{3.11}$$

in the range of $\approx$ 100 to 1000 nm, covering the UV, visible and near-infrared region.

3.2.2. Vibrational transitions

Atoms are often considered as ideal (point-like) particels. Consequently, they have no degrees of freedom in rotation as being rotationally symmetric. In contrast, molecules consists of two or more single atoms, thus having a three dimensional structure and therefore degrees of freedom in rotations as well as vibrations. In general, a molecule consisting of N atoms has in total $3N$ degrees of freedom for translations, vibrations and rotations:

$$3N = f_{trans} + f_{vib} + f_{rot} \tag{3.12}$$

A point mass with $N = 1$ has only 3 degrees of freedom for translations, a moldecule of $N = 2$ atoms has 3 degrees of freedom for translations, 1 for vibrations and 2 for rotations (the rotation around the molecule's axis is no degree of freedom as no physical property would change). A molecule with $N = 3$ has 3 degrees of freedom for each, translations, vibrations and rotations (for illustration, see Fig. 7.5). As a result, every molecule has degrees of freedom leading to both, rotational and vibrational energy levels.

Considering a molecule consisting of two atoms, an approximation for describing vibrational states is the harmonic oscillator: If the distance R between the nuclei changes from the stable distance in equilibrium R_0, the consequene is a restoring force. Close to the equlibrium R_0, the potential can be approximated by a parabola (see Fig. 3.2). The energy eigen values are then given by

$$E_n^{vib} = (n + \frac{1}{2})h\nu \ , \quad n = 0, 1, 2, ... \tag{3.13}$$

Thus, the vibrational energy levels are equally spaced. In general, wavelengths for vibrational transitions are in the infrared (e.g. ≈ 3 μm for H_2O).

3.2.3. Rotational transitions

Similar to Sect. 3.2.2, a two-atomic molecule is considered. This time, the approximation is that the molecule can rotate, but the distance between the nuclei cannot change (rigid rotator). According to eq. 3.12, this molecule has two degrees of freedom for rotations, meaning that it can rotate around two linear independent axes (as it is linear, rotation around the molecule's axis does not change its properties). The energy eigen values for rotations are then

$$E_L^{rot} = \frac{L(L+1)\hbar^2}{2I} \tag{3.14}$$

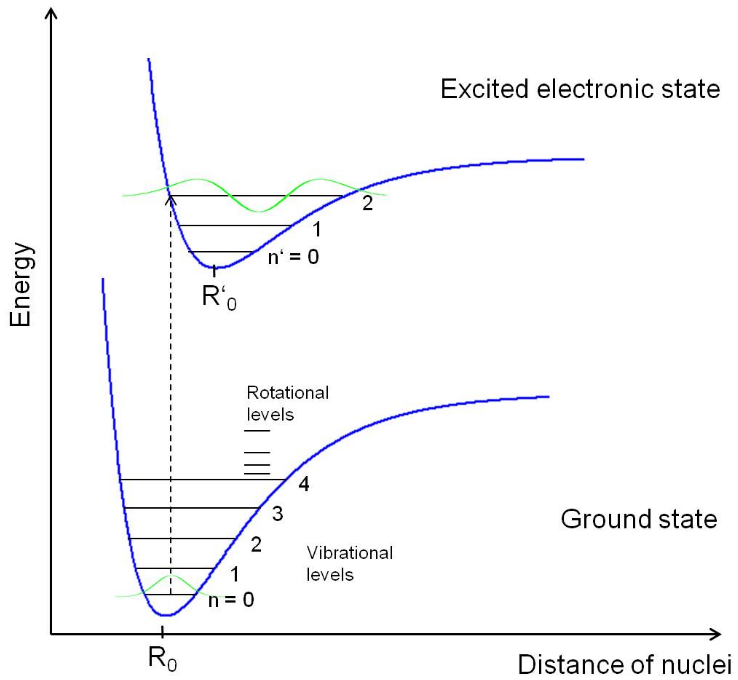

Figure 3.2: The Franck-Condon principle. The Morse potential for the ground state and an excited electronic state are displayed in blue. Vibrational and rotational energy levels are displayed in black. In green, vibrational wave functions (approximation of an harmonic oscillator) are displayed for the ground state and a 2nd excited vibrational state.

with the quantum number for rotations (L) and the moment of inertia (I). The rotational energy levels are not equally spaced, but proportional to L:

$$\Delta E^{rot} = E_L - E_{L-1} = \frac{L\hbar^2}{I} \tag{3.15}$$

For most molecules, the factor $\hbar^2/I$ is small (10^{-4} eV to 10^{-3} eV), which is smaller than the kinetic energy of gas molecules at room temperature ($2.5 \cdot 10^{-2}$ eV). Thus, collisions of gas molecules can easily lead to excitation of rotational levels. The corresponding wavelengths for pure rotational transitions are in the far infrared to microwave region (typically 1 mm to 1 cm).
The selection rule for pure rotational transitions is $\Delta L = \pm 1$ (photons carry an angular momentum of 1). In the absorption spectrum, peaks corresponding to transitions of $\Delta L = -1$ are referred to as *P-branch* and those of $\Delta L = +1$ are referred to as *R-branch*. P and R-branches are only possible for molecules with no unpaired electron, as an unpaired electron's spin could flip taking the photon's angular momentum (as a consequence, ΔL would be 0 and the rotational energy according to eq. 3.14 would not change). In pure rotational spectra, a gap occurs between P and R-branch, called *Q-branch* (corresponding to $\Delta L = 0$). However, in spectroscopy often combined electron and vibrational-rotational transitions are observed. In that case, the photon's angular momentum can change the electron angular momentum and a peak appears at the position of the Q-branch.

3.2.4. Band structures and Frank-Condon principle

As seen in Sect. 3.2 to 3.2.3, molecules can change their state under the influence of an external eletromagnetic field (light) and absorb a photon of the wavelength corresponding to the molecule's transition. As a result, sharp peaks occur in the absorption and emission spectra at the corresponding wavelengths (eq. 3.11). These peaks are broadened according to natural, doppler and pressure broadening. The probabilty of absorption and therefore the strength of the absorption lines is given by the dipole transition moments (eq. 3.6). Under the approximation of a harmonic

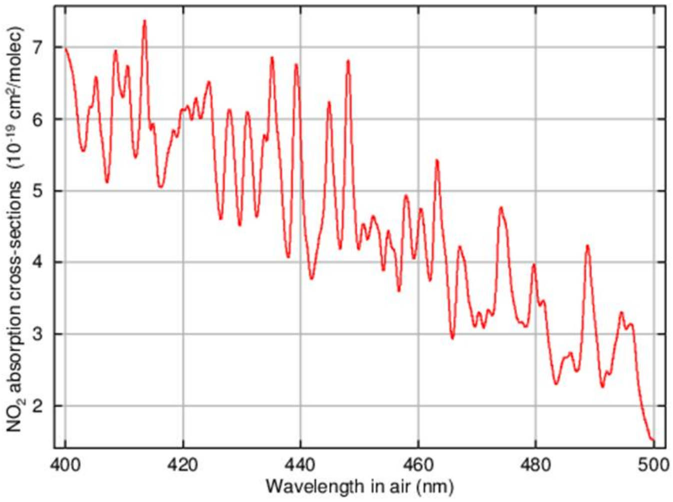

Figure 3.3: Absorption cross-section of NO$_2$ at 294 K between 400 and 500 nm as measured by Vandaele et al. (1998). The literature cross-section has been convolved with the MAX-DOAS instrument's slit function from 14 October 2009 (during the TransBrom campaign, see Sect. 6.1).

potential and a rigid rotator, the vibrational and rotational energies can be calculated according to eq. 3.13 and eq. 3.14. It is

$$E^{el} > E^{vib} > E^{rot} \tag{3.16}$$

Thus, the typical energy structure of a molecule consists of energy levels of the electron shell (summarized in the symbol k) and a system of vibrational levels that is build on each of these electron energy levels. Further, on each vibrational level a system of rotational levels is build on. The resulting structure of energy levels is indicated in Fig. 3.2. Mostly, the absorption of a photon is a combined excitation of electronic, vibrational and rotational states.

As discussed in Sect. 3.2.1, the equilibrium distance R_0 of the nuclei inceases for excited electronic states. Typical time spans for electronic transitions are in the order of 10^{-15} s whereas typical periods for vibrations of the nuclei are in the order of 10^{-13} s. As a consequence, the distance between the nuclei cannot adjust to the new equilibrium distance during an electronic transition. This leads to additional selection rules for combined electronic and vibrational (*vibronic*) transitions, which is illustrated in Fig. 3.2. The transition is indicated by a dashed arrow and the wave functions for a harmonic oscillator are displayed in green. The initial state is the ground state, both electronic and vibrational. Because the nuclei distance cannot change during the transition, the arrow starting at the point of highest wave function amplitude (largest probability density) is straight vertical. It hits the curve for the excited electronic state at a point where the wave function of the second vibrational mode has a large amplitude. Consequently, transitions between $n = 0$ in the electronic ground state and $n = 2$ in the electronic excited state are favoured. This effect is called the *Franck-Condon principle*. It is important that the wave functions of the initial and final state have large amplitudes (as in this example) since their overlap determines the dipole transition moment (eq. 3.6). Transitions between states with smaller overlap of wave functions can occur, but are less probable. The corresponding absorption lines would be less intense while absorption lines corresponding to states with higher overlap have more intensity.

The inner-molecular energy levels and transitions between them as well as mechanisms determining the probability of different transitions as explained in the previous sections result in characteristic absorption spectra (cross-sections) for each trace gas according to its physical properties. As an

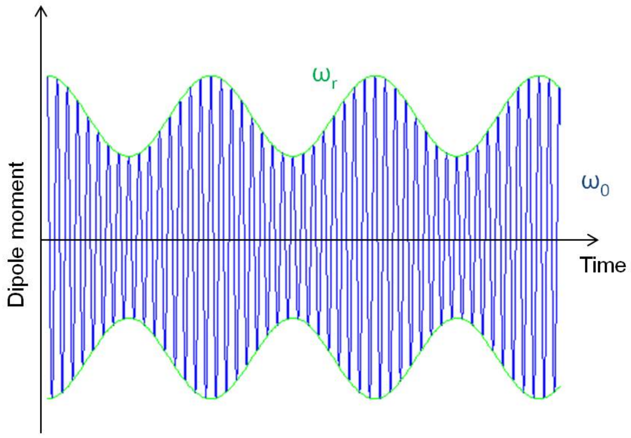

Figure 3.4: Blue curve: An induced dipole momentum oscillates with the frequency ω_0 of the incident light, which polarizes the molecule. If the polarizability is a function of natural oscillations ω_r (green), the induced dipole momentum's oscillation is modulated by this frequency.

example, Fig. 3.3 shows the cross section for nitrogen dioxide (NO_2). In remote sensing techniques, these absorption spectra are used like a *fingerprint* to identify the respective trace gases in recorded sunlight spectra, which are attenuated by absorption in the Earth's atmosphere.

3.3. Scattering processes

3.3.1. Rayleigh and Raman scattering

In remote sensing techniques, scattering of photons on molecules and aerosols can influence the observed spectra, which are used to retrieve trace gases. Scattering processes can be either elastic (photons are scattered, but not shifted in wavelength) or inelastic (wavelength shift).

The main reason for scattering processes on molecules is the induced dipole moment. The oscillating external electromagnetic field vector of light

$$\boldsymbol{E}_{ext} = \boldsymbol{E}_0 \cdot \cos(\omega_0 t) \tag{3.17}$$

changes the charge distribution of the molecule's electron shell, i.e. it induces a dipole moment

$$\boldsymbol{\mu}_{ind} = \hat{\alpha} \cdot \boldsymbol{E}_{ext} \tag{3.18}$$

where $\hat{\alpha}$ denotes the polarizability of the molecule, which is in general a matrix.

In the simplest case, the polarizability is isotropic, meaning that it is invariant under rotations or vibrations (or simply invariant as there are no rotations or vibrations). Then, $\hat{\alpha}$ is a scalar and the dipole moment is in the direction of the electromagnetic field oscillating with its frequency

$$\boldsymbol{\mu}_{ind} = \alpha \cdot \boldsymbol{E}_0 \cdot \cos(\omega_0 t) \tag{3.19}$$

This oscillating dipole moment can emit a photon of the original frequency ω_0. The result is elastic scattering (as the energy does not change), known as *Rayleigh scattering*. The probability of Rayleigh scattering is proportional to ω^4, i.e. preferred scattering of shorter wavelengths. A famous consequence is the blue color of the sky.

In general, molecules have natural oscillations (rotational or vibrational modes) changing periodically the charge distribution in the electron shell and therefore the polarizability. In the following, the vibration of a 2-atomic molecule is considered. According to Sect. 3.2.2 and Eq. 3.12, a 2-atomic molecule has only one degree of freedom on vibrations. If ω_r is the eigenfrequency of this vibrational mode, the movement can be described by the normal coordinate q (coordinate with respect to equilibrium conditions)

$$q = q_0 \cdot \cos(\omega_0 t) \tag{3.20}$$

and the polarizability is a function of q (i.e., $\hat{\alpha} = \alpha(q)$). If the oscillation is small, α can be expanded in a Taylor series:

$$\alpha(q) = \alpha_0 + \left(\frac{\partial \alpha}{\partial q_0}\right) q + \dots \tag{3.21}$$

Eq. 3.20 and 3.21 (until first order terms) in Eq. 3.19 yields:

$$\boldsymbol{\mu}_{ind} = \left[\alpha_0 + \left(\frac{\partial \alpha}{\partial q_0}\right) \cdot q_0 \cdot \cos(\omega_0 t)\right] \cdot \boldsymbol{E}_0 \cdot \cos(\omega_0 t) \tag{3.22}$$

And with help of trigonometric addition theorems[2] this gives

$$\begin{aligned} \boldsymbol{\mu}_{ind} &= \alpha_0 \cdot \boldsymbol{E}_0 \cdot \cos(\omega_0 t) && \text{Rayleigh scattering} \\ &+ \frac{1}{2} \cdot \boldsymbol{E}_0 \cdot q_0 \left(\frac{\partial \alpha}{\partial q_0}\right) \cdot \cos((\omega_0 - \omega_r) \cdot t) && \text{Stokes-Raman scattering} \\ &+ \frac{1}{2} \cdot \boldsymbol{E}_0 \cdot q_0 \left(\frac{\partial \alpha}{\partial q_0}\right) \cdot \cos((\omega_0 + \omega_r) \cdot t) && \text{Anti-Stokes-Raman scattering} \end{aligned} \tag{3.23}$$

The physical meaning is, that the induced dipole oscillates with the frequency ω_0 of the incident light, but the oscillation is modulated with the eigenfrequency ω_r of the vibrational mode. The resulting oscillation pattern (Eq. 3.23) is shown in Fig. 3.4. The three components of Eq. 3.23 correspond to elastic Rayleigh scattering (the induced dipole re-emits a photon of the original wavelength ω_0), Stokes-Raman scattering (the induced dipole re-emits a photon of lower frequency $(\omega_0 - \omega_r)$) and Anti-Stokes-Raman scattering (re-emission of a photon of larger frequency $(\omega_0 + \omega_r)$). Stokes-Raman and Anti-Stokes-Raman scattering are inelastic, as the re-emitted photon is of different wavelength.

In the energy diagram (Fig. 3.5), Stokes scattering is visualized by absorption of a photon with energy $\hbar\omega_0$, which excites a molecule from its ground state (i) to a virtual state (v). This virtual state decays under re-emission of a photon of lower energy $\hbar(\omega_0 - \omega_r)$ to a vibrationally excited state (f). Rayleigh scattering corresponds to the absorption of a photon into a virtual state, which decays back into the same state re-emitting a photon of the original energy $\hbar\omega_0$. Anti-Stokes-Raman scattering is the excitation from an excited state into a virtual state (v'), which decays into the ground state, thereby emitting a photon of higher energy $\hbar(\omega_0 + \omega_r)$ than the original one.

Fig. 3.6 shows the spectral distribtion of Rayleigh and Raman scattering. The inelastic Stokes and Anti-Stokes-Raman peaks are equally spaced around the Rayleigh scattering peak. The Anti-Stokes-Raman peak is lower than the Stokes-Raman peak, because the excited state (f) is normally less populated than the ground state (see Fig. 3.5(a) and Fig. 3.5(c)).

---

[2] $2\cos(x)\cos(y) = \cos(x+y) + \cos(x-y)$

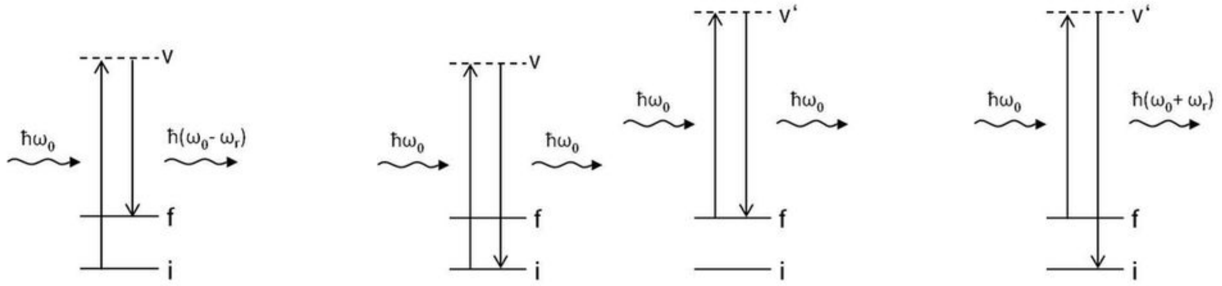

(a) Stokes (b) Rayleigh (c) Anti-Stokes

Figure 3.5.: Energy diagrams of Rayleigh and Raman scattering. For Rayleigh scattering, a photon of original energy is re-emitted, while Stokes scattering results in a red-shift ($\omega_0 - \omega_r$) and Anti-Stokes scattering in a blue shift ($\omega_0 + \omega_r$).

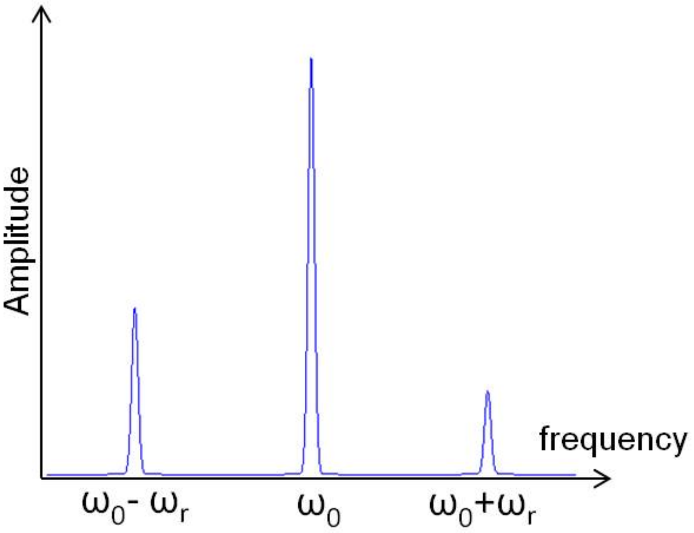

Figure 3.6.: Spectral distribution of Rayleigh (middle peak), Stokes (left peak) and Anti-Stokes (right peak) scattering. The Anti-Stokes peak is usually lower than the Stokes peak as the ground state (i) is more populated than excited states (f) (for denotation, compare Fig. 3.5).

As mentioned above, this is a qualitative eexplanation of scattering effects considering only the vibrational mode of a 2-atomic (linear) molecule. In general, molecules have $3N - f$ (N = number of nuclei) degrees of freedom for vibrations with $f = 5$ for linear and $f = 6$ for non-linear molecules (see Sect. 3.2.2). Accordingly, the degrees of freedom for rotations is 2 for linear molecules and 3 for non-linear molecules. In practice, the polarizability can depend on all eigenfrequencies of these vibrational modes, as well as rotational modes. The calculation is more complex then, but the underlying concept as explained above is not affected. As a system of rotational energy levels is build up on every vibrational level (see Sect. 3.2.4), each of the Rayleigh and (vibrational) Stokes and Anti-Stokes peaks in Fig. 3.6 would be accompanied by numerous peaks corresponding to combined vibrational-rotational transitions.

3.3.2. Mie scattering

In general, the Mie theory describes the solution of Maxwell's equations for the scattering of electromagnetic waves (light) on spherical objects. The size of these objects (radius r) in relation to the light's wavelength λ is parameterised by x:

$$x = \frac{2\pi r}{\lambda} \tag{3.24}$$

For $x << 1$, the scattered electromagnetic radiation is those of an oscillating dipole, and therefore the problem is approximated by Rayleigh scattering. An example is the scattering on gas molecules in air.
For $x >> 1$, the problem is reduced to classic geometrical optics. An example is the scattering on water droplets.
Between these two approximations, scattering processes are called Mie scattering (e.g., on aerosols). Like Rayleigh scattering, it is an elastic process but differing in terms of phase function and scattering probability. While the probability for the Rayleigh scattering (also called its cross-section σ_{Ray}) is

$$\sigma_{Ray} \propto \lambda^{-4} \tag{3.25}$$

with λ being the wavelength, the cross-section for Mie scattering is

$$\sigma_{Mie} \propto \lambda^{-\kappa} \ , \quad \kappa = 0..2 \tag{3.26}$$

Both, Rayleigh scattering on molecules and Mie scattering on aerosols are elastic and do not change the photon energy and therefore the wavelength of the incident light. Nevertheless, photons can be scattered off the original lightpath. As a result, the spectrum will change, but the changes are smooth ($\lambda^{-\alpha}$ dependance, see Eq. 3.25 and 3.26)

3.3.3. The Ring effect

In 1962, J. F. Grainger and J. Ring found, that in spectra of scattered sunlight the Fraunhofer lines are not as deep as expected, which is nowadays referred to as the *Ring effect*. They concluded that "‘in addition to scattered sunlight, there is some extra light reaching us from the sky"’ (Grainger and Ring, 1962). However, in contrast to these first speculations, there is no extra light in the atmosphere. Instead, the photons filling-up the Fraunhofer lines originate from different wavelengths in the sunlight spectrum. E.g., Brinkmann (1968) and Kattawar et al. (1981) pointed out that the wavelength shifts due to Rotational Raman Scattering (RRS) in the atmosphere are adequate to explain the observed filling-in of Fraunhofer lines (see also Sect. 3.3.1 for the physics of Raman scattering).
In Sect. 7.4.1, the Ring effect caused by Vibrational Raman Scattering (VRS) in liquid water is explained in more detail. For the Ring effect due to RRS (on N_2), which dominates in the atmosphere, the same equations (Eq. 7.3 - 7.5) can be used to calculate the Raman shift. According to (Kattawar et al., 1981), the RRS shifts are in the order of several cm^{-1} (up to 50 cm^{-1}). Using Eq. 7.3 - 7.5, some intensity from an initial wavelength of 400 nm would be Raman shifted to $\approx$ 400.8 nm, which is comparable to the width of strongest (broadest) Fraunhofer structures (see Fig. 7.8 and 7.15 in Chapter 7). Consequently, more intensity is shifted from the edge of a broad

Fraunhofer line into the line than from the line's minimum to the outside (simply because there is less intensity in the minimum than outside). For a more complex description of the filling in of Fraunhofer lines (focussing on VRS and Brillouin scattering in water), see Sect. 7.4.1 and 7.4.2.

In remote sensing techniques, the Ring effect is treated as a *pseudo absorber* as it affects the observed spectrum similar to an absorbing trace gas. Several attempts have been carried out to retrieve a pseudo absorption cross-section accounting for the Ring effect. E.g. Solomon et al. (1987) used the different polarization of Rayleigh and Raman scattered light, neglecting the Mie scattering. A summary about different group's approaches to the Ring effect within the DOAS community can be found in (Wagner et al., 2001). Extensive studies of the Ring effect using radiative transfer models were performed by Burrows et al. (1996) focusing on satellite measurements in the UV and visible range.

For the work presented in this thesis, a pseudo cross-section calculated with the radiative transfer model SCIATRAN was used to account for the Ring effect due to Rotational Raman scattering in the atmosphere (Vountas et al., 1998; Rozanov et al., 2005). The investigation of inelastic scattering effects in liquid water is one of the objectives of this thesis and can be found in chapter 7. For inelastic Vibrational Raman Scattering (VRS), Sect. 7.4.1 explains the filling up of Fraunhofer lines and the calculation of a Ring cross-section.

In addition to inelastic Raman scattering, also the inelastic Brillouin scattering causes a Ring effect (Sect. 7.4.2). However, this affects only the most narrow Fraunhofer structures (Kattawar et al., 1981), which are far below the resolution of MAX-DOAS instruments. Consequently, this effect is neglected in the DOAS analysis.

3.4. The DOAS method

The beginnings of Absorption spectroscopy in environmental physics go back to the detection of ozone by Dobson and Harrison (1926). Improvements of these first approaches resulted in the Differential Optical Absorption Spectroscopy (DOAS) method, that has been adopted to the detection of more and more trace gases during the last decades (e.g., Noxon, 1975; Platt and Perner, 1980; Solomon et al., 1987). At the institute of Environmental physics of the University of Bremen, DOAS measurements were established and conducted since the mid 1990s (Richter, 1997).

The measurements in this thesis were performed with a ground-based DOAS instrument consisting of a telescope unit collecting scattered sunlight in the atmosphere and one (or two) spectrometers which are connected to the telescope via an optical fibre and analyse the light. A description of the IUP Bremen instrument can be found in chapter 4. The viewing geometry is explained in Sect. 3.4.3 while Sect. 3.4.1 introduces the DOAS analysis in general. A detailed work on the method can be found for example in Platt and Stutz (2008).

3.4.1. The DOAS equation

The DOAS method consists of spectral measurements of scattered sunlight. The data analysis is based on Lambert-Beer's law describing the spectral attenuation of an initial spectrum I_0 due to absorption by an absorber of concentration $\rho(s)$ along the light path s:

$$I(\lambda) = I_0(\lambda) \cdot e^{-\int \sigma(\lambda,s)\cdot\rho(s)\ ds} \tag{3.27}$$

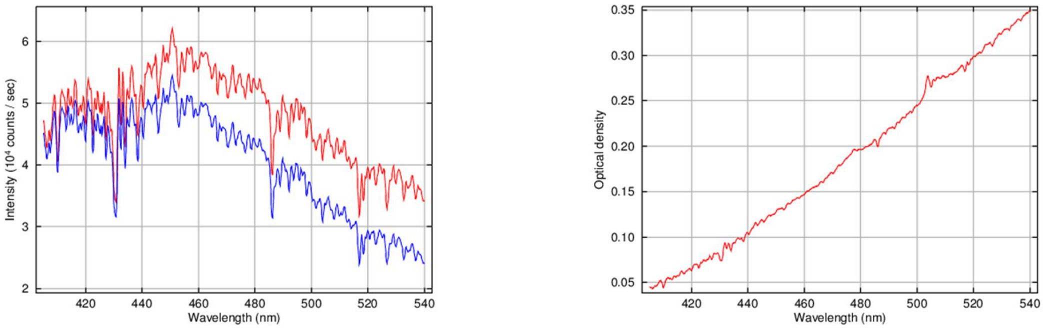

(a) Zenith (I_0) and 30° (I) spectra (b) Optical density $\ln(I_0/I)$

Figure 3.7.: 3.7(a): Spectra in zenith direction (red) and 30° off-axis direction (blue) taken over the western Pacific on 14 October 2009, during the TransBrom campaign (see Chapter 6). 3.7(b): Optical density of these spectra.

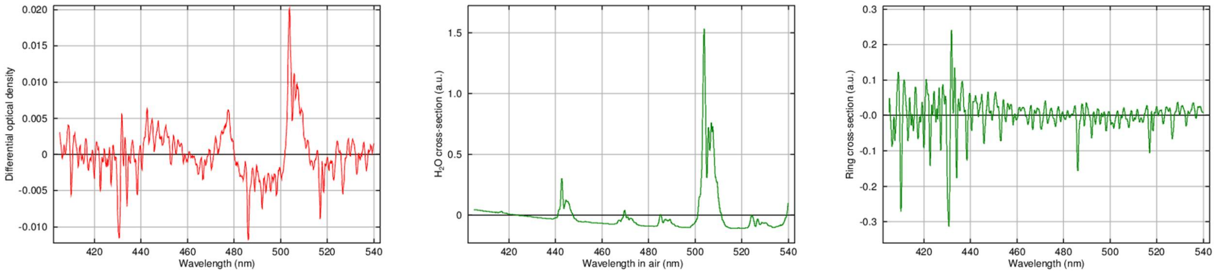

(a) Differential optical density (b) Water vapour cross-section (c) Ring cross-section

Figure 3.8.: 3.8(a): Differential optical density of the spectra shown in 3.7(a). 3.8(b): Differential absorption cross-section of water vapour. 3.8(c): Differential Ring cross-section.

Here, $\sigma(\lambda, s)$ is the absorption cross-section of the absorber and λ the wavelength.

In laboratory measurements, the cross-section is usually not varying along the light path and the concentration of the absorbing gas is constant (σ and ρ are independent of s). Then, the exponent simplifies to

$$\int \sigma(\lambda, s) \cdot \rho(s)\; ds = \sigma(\lambda) \cdot \rho \cdot s \tag{3.28}$$

and the factor $\sigma(\lambda) \cdot \rho$ is referred to as *absorption coefficient* (unit $1/m$).

In contrast, the conditions in field measurements are more complex. The trace gas concentration is a function of altitude and therefore it varies along the light path (see Figs. 3.9 and 3.10 in Sect. 3.4.3 in which the viewing geometry is explained). Further, the extinction of sunlight in the atmosphere is a result of many simultaneous trace gas absorptions. In addition, elastic Rayleigh and Mie scattering (on molecules and aerosols, respectively) as well as the inelastic Raman scattering (Ring effect) influence the attenuation of the spectrum (see Sect. 3.3.1 to 3.3.3). The modified Lambert-Beer law is then given by

$$\begin{aligned} I(\lambda) = \alpha \cdot I_0(\lambda) \cdot \exp\Big\{ - \int \Big[& \sum_{i=1}^{n} \sigma_i(\lambda, s) \cdot \rho_i(s) + \\ & + \sigma_{Ray}(\lambda, s) \cdot \rho_{Ray}(s) + \sigma_{Mie}(\lambda, s) \cdot \rho_{Mie}(s) + \end{aligned}$$

$$+ \sigma_{Ring}(\lambda, s) \cdot \rho_{Ring}(s)\Big]\Big\}ds \tag{3.29}$$

where n is the number of trace gases contributing to the light extinction and the elastic Rayleigh and Mie scattering as well as the Ring effect are considered as *pseudo absorptions* having a cross-section σ and a density ρ. When scattered sunlight is observed, the Intensity I is not only the attenuated solar radiation (from outside the atmosphere), but the attenuated radiation scattered in the atmosphere and depends therefore on viewing geometry. This is accounted for by the factor α depending on the density of scatterers and their phase function. The factor α is a smooth function of wavelength.

If the cross-sections are considered to be independent of the position along the light-path[3], the σ_i can be factored out. The remaining integrals

$$SC_i = \int \rho_i(s)ds \tag{3.30}$$

are referred to as *slant column densities*, in the following called *slant columns* (SC) for simplicity, as being the integrated concentration ρ_i along the light path s (unit molec/cm^2).

The basic idea of the DOAS method is to separate the different components in the extinction into contributions varying slowly with wavelength (broad-band structures) and contributions varying quickly with wavelength (narrow-band structures). The contributions varying slowly with wavelength are then accounted for by a polynomial. The polynomial comprises the influences of elastic Rayleigh and Mie scattering on the spectrum, which are smooth (sect: 3.3.2) as well as instrumental effects. Eq. 3.29 is then

$$I(\lambda) = \alpha \cdot I_0(\lambda) \cdot \exp\left\{-\sum_{i=1}^{n} \sigma_i'(\lambda) \cdot SC_i - \sum_p a_p \lambda^p\right\} \tag{3.31}$$

or by taking the logarithm

$$\ln I(\lambda) = \ln \alpha + \ln I_0(\lambda) - \sum_{i=1}^{n} \sigma_i'(\lambda) \cdot SC_i - \sum_p a_p \lambda^p \tag{3.32}$$

where the Ring effect is treated as an additional absorber i (with slant column SC_i), the low-order polynomial $\sum_p a_p \lambda^p$ accounts for the low frequency contributions as discussed above and

$$\sigma_i'(\lambda) = \sigma_i(\lambda) - \text{polynomial} \tag{3.33}$$

is the high frequency (narrow-band) component of the respective trace gas absorption cross-section $\sigma_i(\lambda)$ and is called the *differential* absorption cross-section (this is the origin of the D in DOAS). As a consequence of the separation into a low frequency and a high frequency contribution, only trace gases showing differential (narrow-band) absorption structures in the observed spectral window can be retrieved by the DOAS method (e.g. NO_2 in the visible, see Fig. 3.3). Absorbers having only broad-band structures (e.g. N_2O_5) affect the spectrum similar to elastic scattering

---

[3] This is an approximation since the cross-sections are normally slightly temperature-dependant and thus depending on altitude. Nevertheless, the retrieved trace gases are normally not spread across the whole atmosphere, but located at certain altitudes. Sometimes, cross-sections of a trace gas at different temperatures are fitted simultaneously to overcome the temperature-dependance (e.g. ozone in the UV).

effects and are compensated by the polynomial.
After taking the natural logarithm, Eq. 3.34 can be re-arranged yielding

$$\tau(\lambda) = \ln \frac{I_0(\lambda)}{I(\lambda)} = \sum_{i=1}^{n} \sigma_i'(\lambda) \cdot SC_i + \sum_p a_p^* \lambda^p \tag{3.34}$$

where $\ln(\alpha)$ has been included into the polynomial (as varying smoothly with wavelength). $\tau(\lambda)$ is called the *optical depth* and consists of measurements of $I(\lambda)$ and a reference spectrum $I_0(\lambda)$. Eq. 3.34 is called the **DOAS equation**.
As an example, Fig. 3.7(a) shows a spectrum I (blue) and a reference spectrum I_0 (red), both taken during the TransBrom campaign across the western Pacific on 14 October 2009 (see Chapter 6). Compared to the reference spectrum, the red part of the spectrum I is relatively lower than the blue, as a consequence of the preferred scattering of short wavelengths (3.3.2) making the clear sky to appear blue. Fig. 3.7(b) shows the resulting optical depth $\tau = \ln(I_0/I)$. In Fig. 3.8(a), the differential optical depth is shown, i.e. the optical depth after subtraction of a fitted polynomial accounting for elastic scattering effects. The differential optical depth is a result of absorption processes. The strong similarity of the differential optical depth and the differential absorption cross-sections of the two most important absorbers (in this case water vapour and the Ring effect, see Fig. 3.8(b) and 3.8(c)) is obvious even by eye.

3.4.2. Retrieval of trace gas slant columns

In order to retrieve trace gas slant columns in the DOAS analysis, a least squares fit is performed with the help of known differential cross-sections $\sigma_i'(\lambda)$ (from laboratory measurements) according to Eq. 3.34 yielding a fitted optical depth $\tau_{fit}(\lambda)$. The data analysis is perfomed with the IUP Bremen in-house software *NLIN_D* (Richter, 1997). The coefficients of the polynomial as well as the slant columns of interest are obtained as fit parameters. The spectra I and I_0 (and therefore τ) are measured at discrete spectral points (wavelengths) λ_j. Since the number of spectral points in the respective fitting window is always much larger than the number of fit parameters, this is a over-determined problem. If r_j is the difference between measured and fitted optical depth at the spectral point λ_j

$$r_j = \tau(\lambda_j) - \tau_{\text{fit}}(\lambda_j) \tag{3.35}$$

the best fit parameters (a_p and SC_i) are determined in the least squares sense

$$\sum_j r_j^2 \rightarrow minimize \tag{3.36}$$

The r_j at the respective wavelength positions λ_j form a *residual spectrum* $r(\lambda)$ (simply referred to as *residual*) and the fitted optical depth τ_{fit} matches the measured optical depth τ except for this residual spectrum:

$$\begin{aligned} \tau(\lambda) &= \tau_{\text{fit}}(\lambda) + r(\lambda) & (3.37) \\ \Leftrightarrow \tau(\lambda) &= \sum_{i=1}^{n} \sigma_i'(\lambda) \cdot SC_i + \sum_p a_p \lambda^p + r(\lambda) & (3.38) \end{aligned}$$

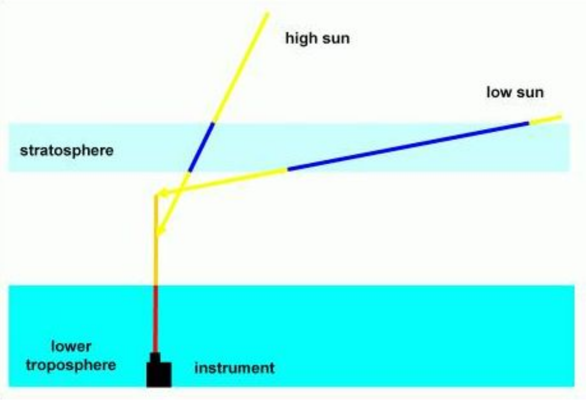

Figure 3.9.: Viewing geometry in zenith direction (http://www.doas-bremen.de/maxdoas_instrument.htm). During twilight, the light path in the stratosphere increases increases.

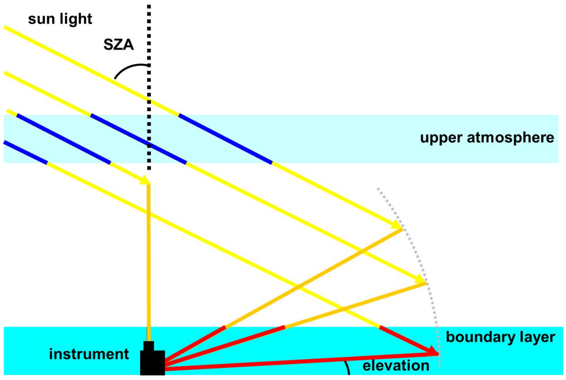

Figure 3.10.: Viewing geometry in off-axis direction leading to extended light paths in the boundary layer (A. Richter, personal communication, 2012).

A quality criterion for the performed fit is the quadratic mean or root mean square (RMS) of the residual:

$$RMS = \sqrt{\frac{1}{N}\sum_{j=1}^{N} r_j^2} \tag{3.39}$$

In addition, also the residual's shape is a quality criterion. An unstructured residual (looking like *noise*) is the result of a proper DOAS fit whereas a structured residual is a hint for a missing trace gas cross-section.

Care has to be taken when choosing a wavelength region (also called fitting window) for the trace gas of interest. The most important criteria are (Wittrock, 2006)

- Using the strongest differential absorption lines of the species of interest
- As less as possible other absorbing compounds in the wavelength region
- Little correlation between different cross-sections
- Avoiding strong Fraunhofer lines

In practice, the choice of an appropriate fitting window for a specific trace gas of interest is always a compromise between these criteria. The applied settings for the perfomed DOAS fits in this thesis are explained for the retrieved trace gases in Chapters 5 and 6 individually.

3.4.3. Measurement geometry and the reference spectrum I_0

In space-borne DOAS retrievals (e.g., Schönhardt, 2009), usually an extraterrestrial measured sun spectrum (without the atmosphere being between the instrument and the sun) is used as the reference spectrum I_0. This spectrum contains only Fraunhofer structures (see Fig. 3.1 in Sect. 3.1) without any changes of the solar spectrum due to absorptions of trace gases in the Earth's atmosphere. As a consequence, the retrieved slant columns from DOAS analysis are absolute, i.e. the absorbers' concentrations integrated along the whole light path in the atmosphere.

In contrast, the observation of pure solar spectra from the ground without the influence of absorbers in the Earth's atmosphere is not possible, which is illustrated by Figs. 3.9 and 3.10 showing the measurement geometry for ground-based instruments (see explanation below). In principle, an extraterrestrial solar spectrum measured by another instrument could be used (e.g. a satellite instrument like SCIAMACHY), which would contain no absorptions due to trace gases in the atmosphere. The disadvantage is, that this instrument has different characteristics than the ground-based instrument, e.g. a different slit function, meaning that the solar spectrum is measured with another resolution. By taking the ratio of I and I_0, artificial structures could arise in the optical depth due to the different instrumental characteristics and completely mask the small absorption signals from atmospheric trace gases. To overcome this, the reference spectrum I_0 is measured with the same ground-based instrument, because then instrumental effects compensate each other by taking the ratio of I and I_0.

The measurement of I_0 is mostly performed in zenith direction either shortly before or after the measurement of I or around noon, when the solar zenith angle (SZA, see below) is small. Taking the closest zenith spectrum has the advantage that the *auto-compensation* of instrumental effects works best, as they can change with time. Also the atmosphere's condition is most similar. The spectrum around noon at small SZA has the advantage that the light path through the atmosphere is shortest then (see Fig. 3.9), i.e. the absorptions due to trace gases are minimal. Nevertheless, I_0 will contain structures from these absorptions. As a result, the retrieved slant columns are not absolute, but the difference between the slant column of the spectrum I (SC) and the slant column of the reference spectrum I_0 (SC_{ref}) and called *differential slant columns* (DSC)[4]:

$$DSC = SC - SC_{\text{ref}} \tag{3.40}$$

The light path shown in Fig. 3.9 and 3.10 (which is a mean light path of photons travelling through the atmosphere before being detected by the instrument) is quantified by

- the solar zenith angle (SZA), which is the angle between zenith and position of the sun
- the elevation angle, which is the viewing angle above the horizon
- and the solar azimuth angle (SAA) being the angle between viewing direction and position of the sun, if both are projected to the plane of surface level (the SAA is neglected in Fig. 3.9 and 3.10)

High sensitivity for stratospheric absorbers is achieved during twilight in zenith pointing direction (Fig. 3.9). Photons entering the atmosphere are mostly scattered only once before being detecting by the instrument. The scattering probability is proportional to the light intensity times the density of scatterers, i.e. the air density, and therefore decreasing exponentially with altitude (barometric formula). On the other hand, the deeper the photons penetrate into the atmosphere, the more are scattered and consequently the light intensity increases with altitude. These opposing functions of altitude define a most probable scattering height, which is a function of the sun zenith angle (SZA). When the sun sets, the light intensity close to the ground decreases even further than in higher altitudes (and vice versa the light intensity in higher altitudes increases even earlier than close to the ground at sunrise). As a result, the most probable scattering height is shifted upwards

---

[4] For simplicity, the *differential slant column* resulting from ground-based DOAS measurements is often only called *slant column* (although this is in principle incorrect).

during twilight and therefore the light path through the stratosphere extends (see Fig. 3.9), while the light path through the troposphere stays almost unchanged. E.g. for light of 440 nm the most probable scattering height is ≈ 5 km for 30° SZA, but ≈ 15 km for 90° (Oetjen, 2002, and references therein). Consequently, stratospheric absorbers are measured with highest sensitivity (and largest slant columns as being the concentration integrated along the light path) during dawn and dusk. Therefore, values for stratospheric trace gases measured with the DOAS technique are given as am and pm values. At small SZA, the light path through the whole atmosphere is shortest and the reference spectrum I_0 is taken.

Measurement directions different from the zenith direction are called *off-axis* measurements. By applying small elevation angles relative to the horizon (Fig. 3.10), the light path trough the troposphere can be extended without (approximately) affecting the stratospheric light path. As a result, the sensitivity of trace gases in the surface layer is enhanced. This is the concept of Multi-AXis DOAS (MAX-DOAS). As the enhancement of the light path trough the surface layer depends rather on the applied elevation angle than on the position of the sun, high sensitivity for absorbers in the lowest part of the atmosphere can be achieved throughout the day. If the (last) scattering point lies above the surface layer (which is the case for the two larger elevation angles shown in Fig. 3.10), the path through this layer is given by geometry only. Nevertheless, viewing conditions (e.g. aerosol load) influence strongly the light path. Also Rayleigh scattering on molecules (λ^{-4} dependence) leads to shorter free path lengths of UV photons, meaning that the last scattering point is closer to the instrument and lies inside the surface layer, effectively reducing the light path. This is true for the smallest elevation angle shown in Fig. 3.10. As a result, the light path cannot be calculated by simple geometrical approaches and a radiative transfer model (Sect. 3.5) has to be used.

To conclude, the slant columns obtained from measurements in different elevation angles increase with the light path trough the absorbing layer and the absorber's concentration along it (Eq. 3.30), which is a function of altitude. As a consequence, a set of MAX-DOAS measurements taken at different elevation angles contains information about the trace gas vertical distribution. This profile can be retrieved using an optimal estimation approach and a radiative transfer model to account for the different light paths (Sect. 3.6).

3.4.4. The DOAS fitting routine

After the spectra I and I_0 are recorded as explained in chapter 4, the data analysis is performed. Therefore, IUP Bremen in-house software is used. The data analysis comprises the preparation of the raw data with help of the programs *nprepare* and *resolut* as well as the actual DOAS fit using the program *NLIN_D* (Richter, 1997).

In the automatic measurement mode, nightly spectra of the unexposed CCD as well as a HgCd line lamp spectrum are recorded. During the process of data preparation, first, for each day the dark spectra are subtracted from scattered sunlight spectra to account for the dark signal (which consists of an instrumental offset, dark current and noise). Then, the raw spectra, which are of unit counts (y-axis) and pixel position (x-axis), are converted into counts/sec (y-axis) and wavelength (x-axis). For the wavelength calibration, the pixel positions of the HgCd lines are identified by literature wavelength positions. In addition, the instrument's slit function is determined from the HgCd lines.

In the actual DOAS analysis using *NLIN-D*, the wavelength interval of the fitting window, the reference spectrum I_0 as well as the order of the DOAS polynomial and the trace gas cross-sections have to be chosen. The cross-sections are convolved with the instrument's slit function reaching for the same resolution. Before the main fitting routine, the reference spectrum I_0 is calibrated again (for better accuracy than the pre-calibration as described above) using the high-resolution Fraunhofer atlas (Kurucz et al., 1984), which is convolved with the instrument's slit function. For matching of the Fraunhofer lines, I_0 is allowed to shift and squeeze within selectable limits. In order to compensate for small differences in the calibration of I and I_0, e.g. caused by thermal drifts of the spectrometer, the spectra I are calibrated to I_0 during the main DOAS fitting routine. Again, a small shift and squeeze is allowed within the same selectable limits.

The DOAS fit itself consists of two alternating fitting routines. A non-linear fit is performed for the wavelength fitting, i.e. for matching of I and I_0 (see above). For the corresponding shift and squeeze parameters, the optical depth is calculated and a linear fit is perfomed according to Eq. 3.38 minimizing the sum of the squared differences of measured and calculated optical depths (Eq. 3.36). As a result, the trace gas slant columns and the polynomial coefficients are obtained simultaneously as being the fit parameters. Both fits are repeated iteravely until no further improvement is achieved.

The recorded spectra might be affected by straylight having two possible contributions: 1) *Real* straylight, i.e. illumination of the spectrometer interior due to incomplete sealing might contaminate the measurements. 2) Light that originates from the telescope (and that was conducted through the optical fibre) might be reflected on surfaces inside the spectrometer and finally reach the CCD at a *wrong* position not corresponding to its wavelength. *NLIN_D* allows compensating for straylight effects (as well as other effects which are additive in I, see Eq. 3.41): In first approximation, the amount of straylight may be a constant C (i.e. independent of the wavelength). This would influence the optical depth

$$\begin{aligned} \tau(\lambda) &= \ln\left(\frac{I(\lambda)+C}{I_0(\lambda)}\right) = \ln\left(\frac{I(\lambda)}{I_0(\lambda)} + \frac{C}{I_0(\lambda)}\right) \\ &= \ln\left(\frac{I(\lambda)}{I_0(\lambda)}\right) + \ln\left(1+\frac{C}{I(\lambda)}\right) \\ &\approx \ln\left(\frac{I(\lambda)}{I_0(\lambda)}\right) + \frac{C}{I(\lambda)} \end{aligned} \tag{3.41}$$

where the Taylor expansion $-\ln(1-x) = \sum_{k=1}^{\infty} \frac{x^k}{k}$ was stopped after the term of first order. When C is chosen as I_{max} (maximum intensity of I) multiplied by an arbitrary factor (for this analysis set to 0.03), the resulting factor

$$\sigma_{\text{offset}}(\lambda) = \frac{0.03 \cdot I_{max}}{I(\lambda)} \tag{3.42}$$

can be used as additional pseudo cross-section in the DOAS fit accounting for an offset on the CCD due to straylight in the spectrometer. The cross-section $\sigma_{\text{offset}}(\lambda)$ is scaled in the DOAS fitting routine with the scaling factor (slant column) being the fit parameter. As a consequence of the $1/I$-dependence, the spectral shape of the straylight correction is similar to the Ring cross-section.

In a second order approximation, the amount of straylight could be in addition linearly dependent on the wavelength, i.e.

$$\tau(\lambda) = \ln\left(\frac{I(\lambda) + C + D(\lambda)}{I_0(\lambda)}\right) \text{, with} \tag{3.43}$$

$$D(\lambda) = 0.03 \cdot I_{max} \cdot \frac{\lambda_2 - \lambda}{\lambda_2} \tag{3.44}$$

where λ_2 is the upper limit of the respective fitting window. Again, an arbitrary initial *amplitude* of $0.03 \cdot I_{max}$ was selected. According to the discussion given above for a constant straylight correction, a pseudo cross-section

$$\sigma_{\text{linear}}(\lambda) = \frac{0.03 \cdot I_{max}}{I(\lambda)} \cdot \frac{\lambda_2 - \lambda}{\lambda_2} \tag{3.45}$$

can be used in the DOAS fit to account for linear straylight effects in the spectrometer. In both cases, the choice of the arbitrary factor of 0.03 has no large influence, since the cross-sections are scaled anyway in the DOAS fit.

3.4.5. Limitations and enhancements

The I_0-effect

The I_0-effect adresses the problem that the limited instrument's resolution can cause an incomplete removal of Fraunhofer structures in the optical depth. For clearness, within this section the solar spectrum is referred to as I_0 ($I_{Solar} \equiv I_0$), while the reference spectrum in the DOAS equation is referred to as I_{ref}.

Under the simplified conditions of only one absorber of constant concentration and well-defined light paths, the Lambert-Beer law yields

$$I(\lambda) = I_0(\lambda) \cdot \exp\left\{-\sigma(\lambda) \cdot \rho \cdot L\right\} \tag{3.46}$$

$$I_{\text{ref}}(\lambda) = I_0(\lambda) \cdot \exp\left\{-\sigma(\lambda) \cdot \rho \cdot L_{\text{ref}}\right\} \tag{3.47}$$

By taking the ratio of I and I_{ref} at the position of the instrument, the solar spectrum I_0 and therefore its Fraunhofer structures cancel out:

$$\frac{I_{\text{ref}}(\lambda)}{I(\lambda)} = \exp\left\{-\sigma(\lambda) \cdot \rho \cdot L_{\text{ref}} + \sigma(\lambda) \cdot \rho \cdot L\right\} \tag{3.48}$$

$$\ln \frac{I_{\text{ref}}(\lambda)}{I(\lambda)} = \sigma(\lambda) \cdot \rho \cdot (L - L_{\text{ref}}) \tag{3.49}$$

However, the DOAS instrument does not detect these accurate spectra, but spectra $I^* = F * I$ and $I^*_{ref} = F * I_{ref}$ that are convolved with its slit function F. The optical depth as observed from the instrument is therefore

$$\ln \frac{I^*_{\text{ref}}(\lambda)}{I^*(\lambda)} = \ln \frac{\int F(\lambda') \cdot I_0(\lambda - \lambda') \cdot \exp\left\{-\sigma(\lambda - \lambda') \cdot \rho \cdot L_{\text{ref}}\right\} d\lambda'}{\int F(\lambda') \cdot I_0(\lambda - \lambda') \cdot \exp\left\{-\sigma(\lambda - \lambda') \cdot \rho \cdot L\right\} d\lambda'} \tag{3.50}$$

Here, two different functions are integrated in the numerator and denominator.

Only if the slit function is much smaller than the Fraunhofer structures in I_0 (the original solar spectrum is resolved), I_0 can be regarded as being not affected by the convolution. Then, I_0 can be excluded from the integrals and would cancel out (together with all Fraunhofer structures). On the other hand, if the absorption cross-section is broad-banded compared to I_0 and the slit function, the exponential terms can be excluded from the integrals, which are then only over I_0 and would cancel out. Mathematically, this leads to

$$\ln \frac{I^*_{\mathrm{ref}}(\lambda)}{I^*(\lambda)} = \sigma(\lambda) \cdot \rho \cdot (L - L_{\mathrm{ref}}) \tag{3.51}$$

demonstrating that under these conditions Eq. 3.49 is reproduced. However, in practise a separation as explained above is often not possible, because the slit function is broader than most Fraunhofer structures (i.e. I_0 cannot be separated from the integral) and consequently narrow-band absorption structures (e.g. O_3 in the UV) interfering with Fraunhofer structures at the same spectral position lead to artifacts in the optical depth. As a result, the assumption of the DOAS analysis (Eq. 3.51) is not true.

The introduced error in the DOAS analysis caused by the I_0-effect scales with strength of Fraunhofer line and absorption. This is especially problematic when absorption structures of weak absorbers overlap with structures of strong absorbers (e.g. ozone and BrO), because then fragments of incompletely removed Fraunhofer lines may destroy the retrieval of the weak absorber. E.g., for ground-based measurements of BrO the I_0-effect can cause differences up to 30% at 90° SZA (Aliwell et al., 2002).

In principle, the I_0-effect can be corrected for (Richter, 1997, and references therein). Nevertheless, these corrections require the knowledge or a guess of the slant column, introducing new uncertainties. On the other hand, the species of interest in this thesis are tropospheric, i.e. they were retrieved at smaller SZAs, and are usually less structured and/or not overlayed by strong absorbers. Therefore, the influence of the I_0-effect was neglected in this thesis.

Advanced DOAS

The underlying concept of the DOAS analysis is the separation of the actual DOAS fit yielding slant columns on the one hand and the radiative transfer modelling to calculate the light path and convert the slant columns into vertical columns or retrieve profiles on the other hand (see Sect. 3.5 and 3.6). A condition for this separation is, that the light path is independent on the trace gas absorption, which is true for an optically thin atmosphere and most measurement conditions. Nevertheless, for some situations this assumption is not fulfilled, especially for observations of ozone absorptions in the UV during twilight. In this situation, the ozone absorption becomes so large that the photons tend to prefer light paths of shorter passages through the ozone layer.

In this case, the ozone cross-section cannot be excluded from the integral in Eq. 3.29 and the slant column concept fails. Instead of fitting the ozone cross-section with the slant column being the fit factor, the differential *slant optical density* can be fitted directly to the observed optical depths (Richter, 1997). Eq. 3.31 then reads

$$I(\lambda) = \alpha \cdot I_0(\lambda) \cdot \exp\left\{ -SOD_{\mathrm{ozone}}(\lambda, \vartheta) - \sum_{i=1}^{n} \sigma'_i(\lambda) \cdot SC_i - \sum_p a_p \lambda^p \right\} \tag{3.52}$$

The slant optical densities have to be calculated with a radiative transfer model. The least squares fit then returns fit parameters, which are the scaling factor between the modelled slant optical

density and the retrieved one. If normalized slant optical densities are used, these scaling factors are the vertical columns.
In this thesis, the concept of advanced DOAS has not been used, since the focus is on tropospheric trace gases. Stratospheric trace gases (e.g. ozone) for the validation of satellite instruments have been retrieved in the visible where ozone absorption in comparatively small.

3.5. Radiative transfer

3.5.1. The air mass factor concept

The results of the DOAS fit are slant columns (differential slant columns for ground-based measurements), which are the trace gas concentration integrated along the light path. As a consequence of the light path dependence - which depends itself on viewing conditions, elevation angle and position of the sun - the slant columns cannot be easily interpreted. Therefore, the (differential) slant columns are converted into vertical columns (VC), which are the trace gas concentrations integrated over altitude z

$$VC = \int \rho(z)dz \tag{3.53}$$

Thus, vertical columns are independent of the light path and therefore measurement conditions. The ratio between slant column and vertical column is called the Air Mass Factor (AMF):

$$AMF(\vartheta, \alpha, \varphi, \lambda) = \frac{SC(\vartheta, \alpha, \varphi, \lambda)}{VC} = \frac{DSC + SC_{\text{ref}}}{VC} \tag{3.54}$$

which is (as well as the slant column) a function of sun zenith angle ϑ, elevation angle α, relative azimuth angle φ between the sun and the line of sight, and wavelength λ. DSC is the differential slant column and SC_{ref} is the slant column of the reference measurement (see Eq. 3.40).
Consequently, the differential slant column (DSC) as derived from ground-based DOAS measurements can be converted into a vertical column (considering that $SC_{\text{ref}} = AMF_{\text{ref}} \cdot VC$) according to

$$VC = \frac{DSC}{AMF - AMF_{\text{ref}}} \tag{3.55}$$

For trace gases in the boundary layer, a simple geometric approach can be made calculating the AMF as a function of the elevation angle α (e.g., Hönninger et al., 2004):

$$AMF_{\text{trop}} = \frac{1}{\sin\alpha} \tag{3.56}$$

This approach has some strong limitations. It is only true, if the respective trace gas is entirely below the scattering point (see Fig. 3.10). It neglects changes of the light pass due to multiple scattering (aerosol load) and to the sun's position (increasing at high SZA). Therefore, this approach gives only reasonable results for clear viewing conditions, SZA $< 80°$ and elevation angles $\geq 10°$.
For trace gases in the stratosphere, a similar approach can be made. With ϑ being the sun zenith angle, the stratospheric AMF is given by

$$AMF_{\text{strat}} = \frac{1}{\cos\vartheta} \tag{3.57}$$

this time assuming that the scattering point is below the trace gas layer (see Fig. 3.9) and again neglecting multiple scattering. This approximation gives reasonable results up to $\vartheta \approx 80$.
For more accurate results and observations in small elevation angles, resp. large SZA - i.e. when offaxis measurements are most sensitive to the boundary layer, resp. zenith measurements are most sensitive to the stratosphere - the AMF has to be calculated with help of radiative transfer models when using these measurements.

3.5.2. Radiative transfer calculation of air mass factors

In the atmosphere, the radiative transfer equation describes the change of the diffuse intensity I at the location $\boldsymbol{r}$ in the direction $\boldsymbol{e_s}$, which is given in its coordinate-independent form as

$$\frac{I(\boldsymbol{r}, \boldsymbol{e_s})}{ds} = -\alpha(\boldsymbol{r}) I(\boldsymbol{r}, \boldsymbol{e_s}) + \alpha(\boldsymbol{r}) B(\boldsymbol{r}, \boldsymbol{e_s}) \tag{3.58}$$

The change of intensity I over the length ds (left hand side) is a combination of loss and gain. Loss of radiation due to absorption and scattering out of the line of sight is described by the first term on the right hand side. Therefore, α represents the sum of scattering and absorption coefficients and is called extinction coefficient. Scattering into the line of sight can also lead to gain of radiation, which is described by the second term where B is the source function. In general, B is the sum of the single-scattering source function B_{SS} and multiple-scattering source function B_{MS}

$$B = B_{SS} + B_{MS} \tag{3.59}$$

The single-scattering source function B_{SS} describes the gain of radiation due to the photons that are scattered only once and into the line of sight. This contribution is given by

$$B_{SS}(\boldsymbol{r}, \gamma_R) = \frac{\omega(\boldsymbol{r})}{4} F_0 P(\boldsymbol{r}, \gamma_R) \exp\left\{ - \int_0^S \alpha(s)\ ds \right\} \tag{3.60}$$

where γ_R is the angle between the direct solar beam and the line of sight, P is the phase function giving the probability of scattering in the direction of γ_R and ω is the single-scattering albedo (describing the probability for scattering of a photon rather than absorption). The incident solar flux at the top of atmosphere is given by πF_0. In the exponent, α (sum of absorption and scattering coefficients) is integrated along the light path, i.e. along the direct solar beam until the scattering point and afterwards along the line of sight, giving the optical depth

$$\tau = \int \alpha(s)\ ds \tag{3.61}$$

The multiple-scattering source function

$$B_{MS}(\boldsymbol{r}, \boldsymbol{e_s}) = \frac{\omega(\boldsymbol{r})}{4\pi} \int d\Omega P(\boldsymbol{r}, \gamma) I_{dif}(\boldsymbol{r}, \boldsymbol{e_s}) \tag{3.62}$$

describes the gain in the line of sight due to diffuse radiation I_{dif} (multiple scattered photons). Here, γ is the scattering angle and the integral is over the solid angle $d\Omega = \sin\theta\ d\theta\ d\varphi$.

For all radiative transfer calculations within this thesis, the SCIATRAN software in its version

2.2 was used (e.g., Rozanov et al., 2001, 2005). Integration of Eq. 3.58 yields the diffuse intensity I_{dif}, which depends on the single and multiple-scattering function. As the multiple-scattering function again depends on the diffuse Intensity I_{dif}, an iterative approach is perfomed until convergence is achieved. An initial guess for I_{dif} is obtained from a model run calculating the radiation field in a pseudo-spherical atmosphere. The single-scattering radiation field as well as the attenuation of the direct solar beam are calculated in a truly sperical atmosphere.

In order to obtain the air mass factor for an absorber i, first, the slant optical density SOD_i of the absorber i as well as the vertical optical density VOD_i are calculated.
The slant optical density SOD_i depends on the wavelength λ and the light path s, which is parameterized by the the sun zenith angle ϑ, the sun azimuth angle φ and the elevation angle α. For given ϑ, α, φ and λ, the radiative transfer model SCIATRAN calculates the radiance at the end of the light path for two szenarios: First, under consideration of all scattering and absorption processes on the light path except for the absorber i of interest (yielding I_{-i}) and afterwards under consideration of all scattering and absorption processes including the absorber of interest (yielding I_{+i}). Because

$$\begin{aligned}
\ln\left(\frac{I_{-i}}{I_0}\right) &= -\sum_{j\neq i} SOD_j \\
\ln\left(\frac{I_{+i}}{I_0}\right) &= -\sum_{j=1}^{N} SOD_j \\
\Rightarrow \ln\left(\frac{I_{-i}/I_0}{I_{+i}/I_0}\right) &= -\sum_{j\neq i} SOD_j \ + \ \sum_{j=1}^{N} SOD_j = SOD_i \qquad (3.63)
\end{aligned}$$

the slant optical density of absorber i is with all angular and wavelength dependencies given by

$$SOD_i(\vartheta,\alpha,\varphi,\lambda) = \ln\left(\frac{I_{-i}(\vartheta,\alpha,\varphi,\lambda)}{I_{+i}(\vartheta,\alpha,\varphi,\lambda)}\right) \qquad (3.64)$$

The vertical optical density VOD_i is the product of the profile $\rho_i(z)$ and absorption cross-section $\sigma_i(\lambda,z)$ of the absorber i integrated over altitude z from the ground to the top of atmosphere (TOA):

$$VOD_i(\lambda) = \int_0^{TOA} \rho_i(z)\sigma_i(\lambda,z)\ dz \qquad (3.65)$$

With this, the air mass factor is obtained by

$$AMF_i(\vartheta,\alpha,\varphi,\lambda) = \frac{SOD_i(\vartheta,\alpha,\varphi,\lambda)}{VOD_i(\lambda)} \qquad (3.66)$$

Two limitations arise when calculating the air mass factor as explained above: a) the absorbers profile $\rho_i(z)$ has to be known and b) Eq. 3.64 is only true for an optically thin atmosphere, i.e. the light path has to be the same whether the calculations are performed with or without the absorber i. The latter condition is true for the analysis within this thesis (see Sect. 3.4.5). The first limitation is stronger as the profile is in general not known. In addition, the profile can change during the course of the the day, especially for tropospheric absorbers (e.g., change of the

mixing layer height). In this thesis, profiles from the US standard atmosphere have been used for calculating stratospheric vertical columns. For tropospheric vertical columns, the profile retrieval BREAM as explained in Sect. 3.6 has been applied.
A detailed discussion about the air mass factor concept focusing on the DOAS analysis can be found in (Rozanov and Rozanov, 2010).

3.5.3. Block air mass factors

The sensitivity of MAX-DOAS measurements performed under certain elevation angles is a function of altitude. To characterise the altitude-dependent sensitivity, the block air mass factor concept is used.
Block air mass factors (BAMF) are air mass factors, which are not total but altitude-dependent. They correspond to single layers j (of thickness Δz) in the atmosphere. In analogy to Eq. 3.54, the block air mass factor for layer j is

$$BAMF_j = \frac{SC_j}{VC_j} \tag{3.67}$$

where SC_j is the slant column in layer j and VC_j is the vertical column of this layer (and the dependence on the wavelength, the solar zenith angle, the solar azimuth angle and the elevation angle have been omitted). The total slant column is then

$$SC = \sum_{j=1}^{TOA} BAMF_j \cdot VC_j \tag{3.68}$$

In contrast to air mass factors, the advantage of block air mass factors is that they are independent of the trace gas profile (they are calculated with a constant profile). The air mass factors can be calculated from block air mass factors according to

$$AMF = \frac{\sum_{j=1}^{TOA} BAMF_j \cdot VC_j}{\sum_{j=1}^{TOA} VC_j} \tag{3.69}$$

where the information on the trace gas profile is in the VC_j. For more details on the block air mass factor concept see (e.g., Wagner et al., 2007).
In SCIATRAN, block air mass factors are calculated from so-called weighting functions (WF), which give the absolute change in intensity for a relative change of a particular parameter. Under the condition of an optically thin atmosphere, the block air mass factor $BAMF_j$ for the layer j can be calculated as

$$BAMF_j(\lambda) = -\frac{WF_j^I(\lambda, z)}{I^{TOA}(\lambda) \cdot \sigma(\lambda) \cdot \rho_j^{air}(z) \cdot \Delta z} \tag{3.70}$$

with the intensity weighting function WF_j^I (change of intensity when absorber of interest is switched on or off), the intensity at the top of the atmosphere I^{TOA}, the absorption cross-section σ of the absorber of interest and the air density ρ_j^{air} of layer j.

3.6. Profile retrieval

As discussed in Sect. 3.4.3, the (differential) slant column of a tropospheric absorber in the boundary layer depends on the applied elevation angle (see also Fig. 3.10). Consequently, a set of MAX-DOAS measurements taken at different elevation angles contains some information about the absorber's profile.

3.6.1. Theory

The retrieval of the absorber's profile from measured slant columns is based on the block air mass factor concept. The relationship between the slant column and the vertical column within a specific layer j at altitude z and thickness Δz is given by Eq. 3.68. If y_i is a single measured slant column and the vertical column in layer j is expressed by the corresponding volume mixing ratio x_j, Eq. 3.68 gives

$$y_i = \sum_j BAMF_j \cdot x_j \cdot \Delta z \cdot \frac{p_j}{k_B \cdot T_j} \tag{3.71}$$

where k_B is the Boltzmann constant and p_j and T_j are the temperature and pressure in layer j, respectively. The factor $(p_j \cdot \Delta z)/(k_B \cdot T_j)$ is the conversion factor between x_j (the volume mixing ratio in layer j) and the corresponding vertical column VC_j. The N elements x_j are the profile of interest (given at discrete altitude steps), that can be written as a vector $\boldsymbol{x} = (x_1, ...x_j, ...x_N)$. Considering a set of M measured (differential) slant columns $\boldsymbol{y} = (y_1, ...y_i, ...y_M)$, Eq. 3.71 can be expressed as

$$\boldsymbol{y} = \boldsymbol{K} \bullet \boldsymbol{x} \tag{3.72}$$

with the elements of the matrix $\boldsymbol{K}$ given by

$$K_{ij} = \frac{BAMF_{ij} \cdot p_j \cdot \Delta z}{k_B \cdot T_j} \tag{3.73}$$

This is a linear equation that has to be inverted to retrieve the profile $\boldsymbol{x}$ from the measurements $\boldsymbol{y}$. In general, the inverse problem is under-determined since a) the number of measurements M is smaller than the number of altitude steps N for the profile and b) the M measurements are not linearly independent. If two measurements are perfomed in almost the same direction, the result will be similar and no gain of information is achieved. On the other hand, if the difference in the applied viewing angle is too large, then information will be missed. (Wittrock, 2006) found, that a 1° spacing for the lower elevation angles (up to 5-6°) is the best compromise. In addition, the problem can be ill-posed, i.e. no unique solution exists as many solutions (profiles $\boldsymbol{x}$) could cause the same observations (measured set of slant columns $\boldsymbol{y}$).[5]

For solving this ill-posed inverse problem, the well-known optimal estimation method (Rodgers, 2000) is applied, which is widely used in remote sensing techniques to retrieve profile information (e.g., Löhnert et al., 2004, 2009; Wittrock, 2006; Frieß et al., 2011). Due to the lack of information,

---

[5] In principle, also the DOAS equation is an inverse problem, but here, the number of independent measurements (spectral points of the optical depth) is larger than the number of unknowns (slant columns plus polynomial coefficients). Such overdetermined problems are normally solved by the least squares method. If the fitting window is well choosed (no interference between different cross-sections), the problem is well-posed giving a unique solution.

an a priori profile $\boldsymbol{x}_a$ as well as its covariance matrix $\boldsymbol{S}_a$ are required. The profile of interest $\boldsymbol{x}$ is then retrieved according to (Rodgers, 2000) by

$$\boldsymbol{x} = \boldsymbol{x}_a + (\boldsymbol{K}^T \boldsymbol{S}_\epsilon^{-1} \boldsymbol{K} + \boldsymbol{S}_a^{-1})^{-1} \boldsymbol{K}^T \boldsymbol{S}_\epsilon (\boldsymbol{y} - \boldsymbol{K}\boldsymbol{x}_a) \tag{3.74}$$

where $\boldsymbol{S}_\epsilon$ is the measurement covariance matrix containing the measurement errors of $\boldsymbol{y}$ on the diagonal and the superscript -1 denotes the inverse of a matrix and T the transposed matrix.
A quality measure for the retrieval is the Averaging kernel matrix $\boldsymbol{A}$. Assuming that $\boldsymbol{x}$ is the retrieved profile and $\boldsymbol{x}_{true}$ is the true profile, the averaging kernel matrix gives the change of the retrieved profile with the true profile and is calculated according to (Rodgers, 2000)

$$\boldsymbol{A} = \frac{\partial \boldsymbol{x}}{\partial \boldsymbol{x}_{true}} = (\boldsymbol{K}^T \boldsymbol{S}_\epsilon^{-1} \boldsymbol{K} + \boldsymbol{S}_a^{-1})^{-1} \boldsymbol{K}^T \boldsymbol{S}_\epsilon \boldsymbol{K} \tag{3.75}$$

Consequently, the rows of $\boldsymbol{A}$, which are called averaging kernels, describe how the retrieved volume mixing ratio in one specific altitude layer changes when the true profile changes. E.g., the first row of $\boldsymbol{A}$ corresponds to the lowermost layer of the retrieved profile and the i-th position within the first row is the change of the retrieved lowermost layer when the i-th layer of the true profiles changes. Thus, the averaging kernel matrix describe how the layers at different altitudes are *smoothed*. In an ideal case when the retrieved profile is the true profile ($\boldsymbol{x} = \boldsymbol{x}_{true}$), the averaging kernel matrix is the identity matrix. The trace of $\boldsymbol{A}$ is the number of linearly independent layers of the retrieved profile (degrees of freedom). For typical scanning times ($\approx$ 20 min) and a moderate aerosol load, the degrees of freedom is about 1.5-3 (Wittrock, 2006). Examples of averaging kernels can be found in Figs. 6.11 and 6.17 for profile retrievals of NO_2 and HCHO during the TransBrom campaign (Sect. 6.1).
A limitation for this profile retrieval is that it can be applied only under the condition of an optically thin atmosphere. However, this is true for the study within this thesis (retrieval of NO_2, IO and HCHO).

3.6.2. BREAM

The profile software used in this thesis is the BRemian Advanced MAX-DOAS Retrieval Algorithm (BREAM) (Wittrock, 2006). As an input, the (differential) slant columns of the trace gas of interest resulting from ground-based measurements in different elevation angles are read in. Accordingly, the (differential) slant columns of the oxygen dimer O_4 from the same observations are read in. The retrieval grid consists of 50 m thick layers from ground to 4 km altitude (81 layers, if the instrument is at 0 m.a.s.l.). BREAM uses a three-step approach to retrieve trace gas profiles for distinct time-steps. In this thesis, time-steps of 0.5 h were used, comprising typically 2 complete *scans* (a series of ground-based observations in different elevation angles is referred to as a *scan*).
In the first step, an aerosol extinction profile is estimated for the actual time-step. The aerosol load has a large influence on the radiative transfer and therefore on the calculation of the trace gas amount (e.g. Oetjen, 2002; Heckel et al., 2005, and references therein). Thus, knowledge of the true aerosol extinction is essential for the profiling. As the profile of the oxygen collision complex O_4 (O_2 - O_2) depends only on the O_2 profile and meteorological conditions (e.g., temperature, pressure) and can be calculated, comparisons between modelled and measured O_4 slant columns can be used to derive aerosol information (e.g., Wagner et al., 2004; Wittrock et al., 2004). In

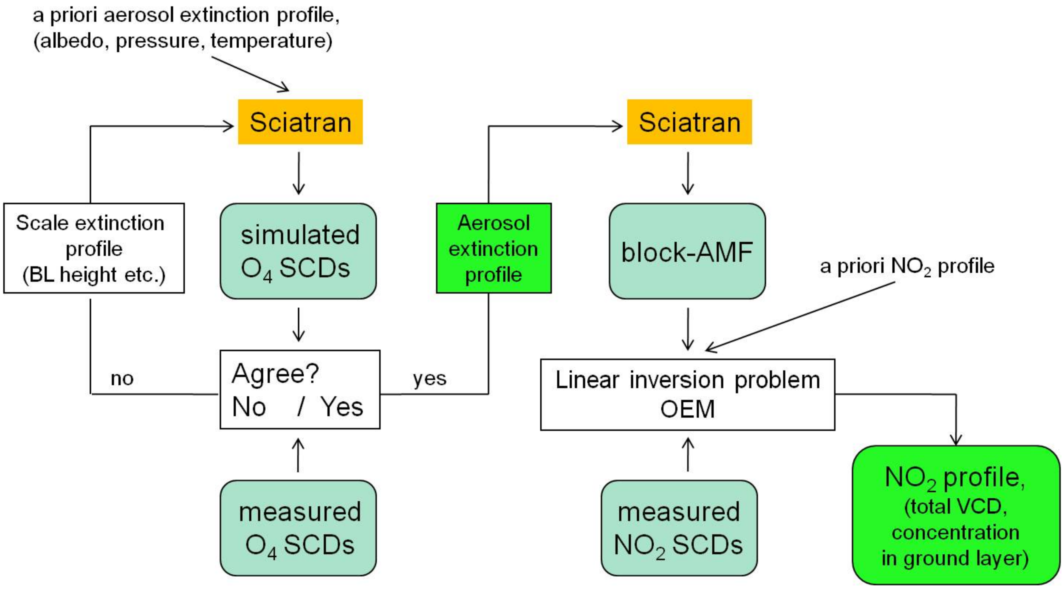

Figure 3.11.: Structure of BREAM

BREAM, an a priori aerosol extinction profile has to be set. With this, the radiative transfer model SCIATRAN (see Sect. 3.5.2) calculates O_4 slant columns for all viewing directions within the respective time-step, which are then compared to the measured O_4 slant columns. In an iterative process, the aerosol extinction profile is scaled until modelled and measured O_4 slant columns agree within selectable limits. Within this study, a correlation factor of 0.6 was demanded as a quality criterion. When all iterations failed this minimal correlation factor (because of clouds, fog, etc.), the retrieval was continued with the next time step.

In the second step, differential block air mass factors are calculated for the trace gas of interest (see Sect. 3.5.2) describing the relationship between the measured differential slant columns and the profile of interest according to Eq. 3.71 - 3.73. Again, these calculations are perfomed using the radiative transfer model SCIATRAN with the previously derived aersosol extinction profile.

In the third step, the linear inversion is performed by applying the optimal estimation method with a reasonable a priori profile that can be defined by the user. In an iteration, the a priori profile is scaled various times, each time yielding a trace gas profile according to Eq. 3.74. For each retrieved profile, a set of slant columns is computed according to Eq. 3.72 and compared to the measured trace gas slant columns. The retrieved profile yielding modelled slant columns that correlate best with the measured set of slant columns is selected and saved. Again, a minimal correlation factor of 0.6 is applied to judge whether the retrieval was successful or not and if necessary to skip the profile. After this, BREAM continues with the next time step.

The overall program structure of BREAM is shown as a sketch in Fig. 3.11. More information about the profiling and BREAM can be found in (Wittrock et al., in prep. for AMTD) and (Wittrock, 2006). In this thesis, BREAM was used to retrieve profiles of tropospheric NO_2, HCHO and IO. The results are presented and discussed in chapter 5 and chapter 6.

4. Instruments

In this chapter, the instrumentation used in this study is introduced. Sect. 4.1 describes in general the function and operation of a ground-based MAX-DOAS instrument. The improvement of the traditional Bremen MAX-DOAS instrument was one of the tasks of this work and is presented in Sect. 4.3. For intercomparison purposes during the CINDI campaign (chapter 5), a commercial NO_x in situ monitor was used (Sect. 4.5). The SCIAMACHY and GOME-2 satellite instruments, whose data were validated as an objective of this thesis, are introduced in Sect. 4.6.

4.1. General function of the MAX-DOAS instrument

In general, the Bremen MAX-DOAS instrument consists of a telescope unit collecting scattered sunlight, a Y-shaped optical quartz fibre bundle and two spectrometers for the visible and UV-range, respectively (for illustration, see Fig. 4.1). The telescope unit is the part of the instrument that has been improved during this work and is discussed in detail later. The Y-shaped optical quartz fibre bundle transmitting the light from the telescope to the spectrometers consists of 76 cylindrical mixed single fibres at the telescope side. After 20 m, the fibre bundle splits and ends after additional 2 m in two separate connectors, each consisting of 38 vertically aligned single fibres forming the entrance slit into the spectrometers. The use of the quartz fibre bundle has several advantages:

- It efficiently depolarises the light and therefore overcomes polarisation effects in the spectrometer. The sky-light is polarised due to Rayleigh scattering and the trough-put of the spectrometers depends on the polarisation of the incoming light.
- By separating the light collecting telescope from the spectrometers, some flexibility in terms of installation is gained, i.e. the telescope unit can be set-up outside and the spectrometers inside a building (protected from environmental influences).

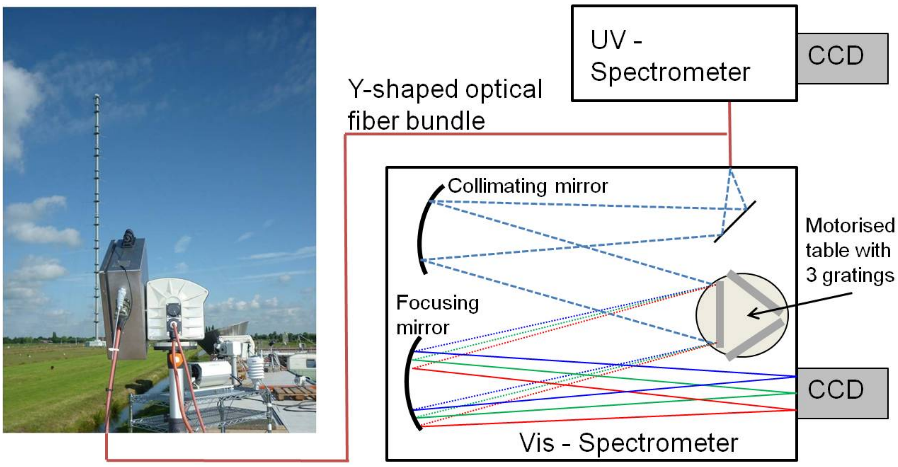

Figure 4.1: Illustration of the MAX-DOAS instrument (already equipped with the new telescope housing mounted on a pan-and-tilt-head, which allows any viewing direction).

Spectrometer	Grating	Spectral range (nm)	Resolution (nm) (FWHM slit function)	CCD
Andor Shamrock 303i	1200 l/mm, 300 nm blaze	315 - 384	0.4	Andor Newton DU940N (512x2048 pixels)
Acton500	300 l/mm, 300 nm blaze	401 - 573	0.8	Roper Scientific Princeton NTE/CCD -1340/100-EMB (100x1340 pixels)

Table 4.1.: Spectrometer-CCD-system characteristics of the MAX-DOAS instrument used in the CINDI (chapter 5) and TransBrom (chapter 6) campaigns as well as for ship-borne measurements contributing to the SHIVA campaign (chapter 6). Both spectrometers are equipped with three different selectable gratings. The gratings and values given here apply to the instrument characteristics that were realized in the campaigns mentioned above.

- Due to the Y-shape, two spectrometers for different wavelength regions (e.g. Visible and UV) can be connected to the same telescope unit. This allows the simultaneous retrieval of multiple (in the visible or the UV absorbing) trace gases in the same viewing directions.

To avoid any thermal drifts of the spectrometers (and therefore drifts in the wavelength axis), they are placed inside an insulation box. In addition, the spectrometers are actively temperature stabilised to +35° C by heat foils and an electronic control loop.

The light path inside the spectrometers, which are of type *Czerny-Turner* using a (reflective) diffraction grating, is indicated in Fig. 4.1. The theory of reflective diffraction gratings can be found in standard textbooks, e.g. (Demtröder, 2006). A motorized table allows to adjust the inclination of the grating and therefore to select the spectral region. In addition, it can be selected between three gratings of different line widths and therefore different resolution that are mounted on the table. The gratings are designed (*blazed*) for a certain wavelength (see Tab. 4.1). After diffraction on the grating, the entrance slit is re-focussed on a two-dimensional CCD (charge- coupled device) detector (different colors/wavelengths are laterally shifted, see. Fig. 4.1). The spectral resolution depends on the characteristics (line width) of the grating, the spectrometer's focal length, and on the width of the entrance slit and is measured in terms of the full width of half maximum (FWHM) of the so called slit function, which is the image of the monochromatically illuminated entrance slit on the CCD. The spectrum, which is measured and recorded by the spectrometer-CCD-system, is the original scattered sunlight spectrum (of infinite spectral resolution), convolved with the instruments slit function (see also Sect. 3.4.5). The slit function is measured by illuminating the entrance slit with a HgCd line lamp that is installed inside the telescope unit (see description of telescope unit below). The CCD chips are cooled to decrease dark currents. Under strong illumination normally spillover effects on single pixels leading to *blooming effects* on the CCD occur earlier than the CCD's readout register is saturated. Therefore, several pixels are binned (until the readout register becomes the limiting criterion for saturation). Afterwards, all rows that were read out are co-added by the measurement software to increase the signal-to-noise ratio and to avoid problems with pixel-to-pixel variation on the chip.

Table 4.1 summarizes the characteristics of the different spectrometer-CCD-systems used in the campaigns that are issue of this thesis. The whole instrument operation is performed by an IUP Bremen in-house software called AMAX_OMA (Richter, 1997).

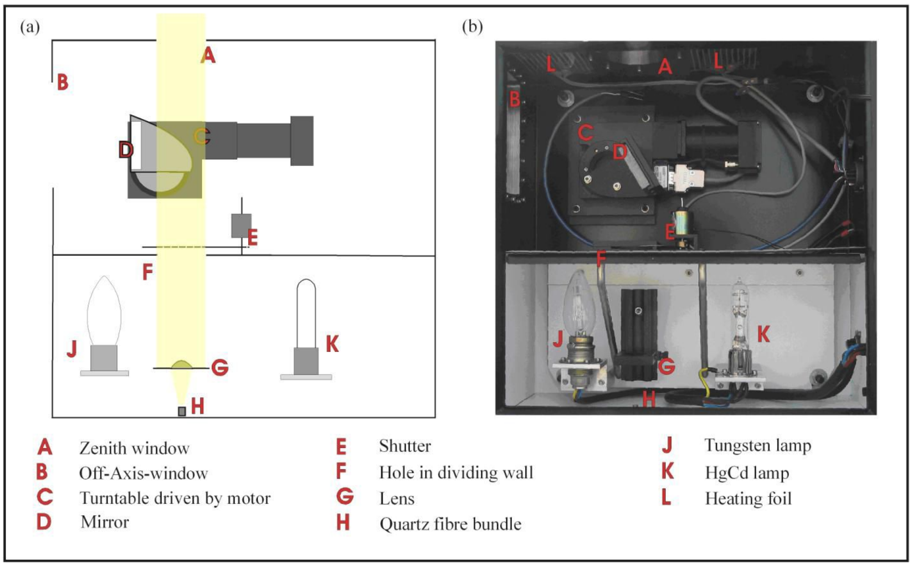

Figure 4.2: Schematic view and photo of the old Bremen MAX-DOAS telescope unit using a mirror to apply off-axis viewing directions.

The elevation angle as well as the sun azimuth angle (SAA) of the measurement geometry (see Sect. 3.4.3) can be selected by the line of sight of the the telescope unit. In the following section (4.2, the traditional Bremen telescope unit will be briefly introduced as well as the problems connected to it. Section 4.3 describes the improved telescope.

4.2. The old telescope unit and its limitations

In Fig. 4.2, the traditional telescope unit of the Bremen MAX-DOAS instrument is illustrated, which was derived from zenith-sky-only instruments (e.g., Richter, 1997; Oetjen, 2002; Wittrock, 2006). When measuring in off-axis directions, light is entering the telescope through a fused silica window (B) and reflected by a movable mirror (C and D) towards the optical fibre bundle (H). A lens (G) in front of the optical fibre is used to reduce (and define) the field of view. Measurements in different elevation angles (different lines of sight) are achieved by positioning of the motorized mirror. For measurements in zenith direction, the mirror can be moved out of the optical path and the scattered sunlight is entering the telescope through a second window (A). A shutter (E) can be closed for dark measurements. For calibration measurements, a line lamp (K) is used illuminating the interior telescope. All system operations and measurements are controlled by the IUP Bremen in-house software AMAX-OMA (Richter, 1997), which allows an automatic measurement mode.

This telescope is very robust, stable and appropriate for use in extreme environments (e.g., the Arctic), as all moving parts are integrated in the telescope housing and not exposed to environmental influences. It is constructed for long-term installations on various measurement sites. However, due to its weight and size, it is unflexible and not appropriate for measurement campaigns.

One of the major disadvantages of this telescope is that it does not allow to change the azimuthal viewing direction. Once installed, the azimuthal viewing direction is fixed and cannot be changed unless the telescope is re-aligned by hand. Therefore, automatic measurement sequences in different azimuthal directions or pointing at targets (*TargetDOAS*, see Sect. 4.3) is impossible.

Another problem affecting the DOAS analysis of off-axis measurements arise due to the mirror: Whereas the reference spectrum I_0 is measured in zenith direction, i.e. without the mirror, the off-axis measurement I is performed using the mirror. As a result, optical effects of the mirror do

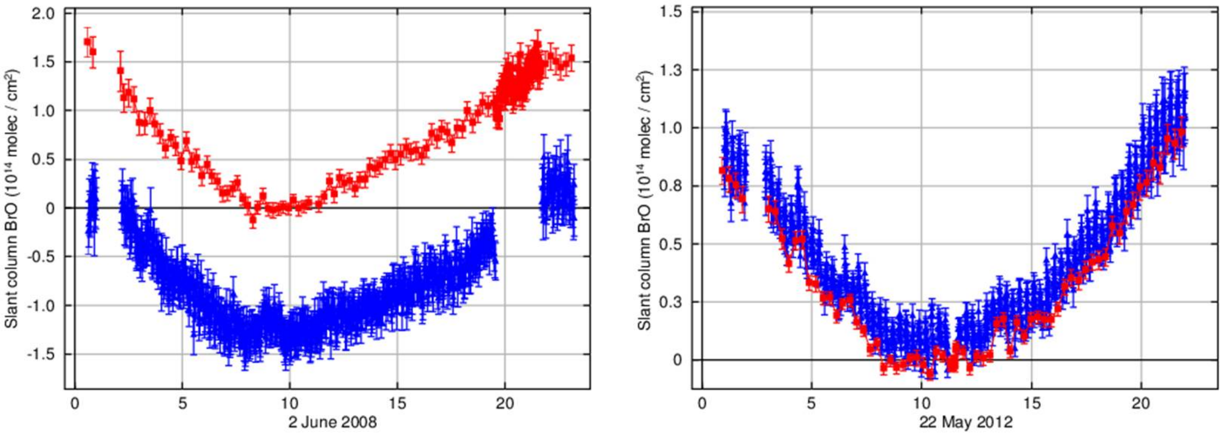

(a) Strat. BrO, old telescope

(b) Strat BrO, new telescope

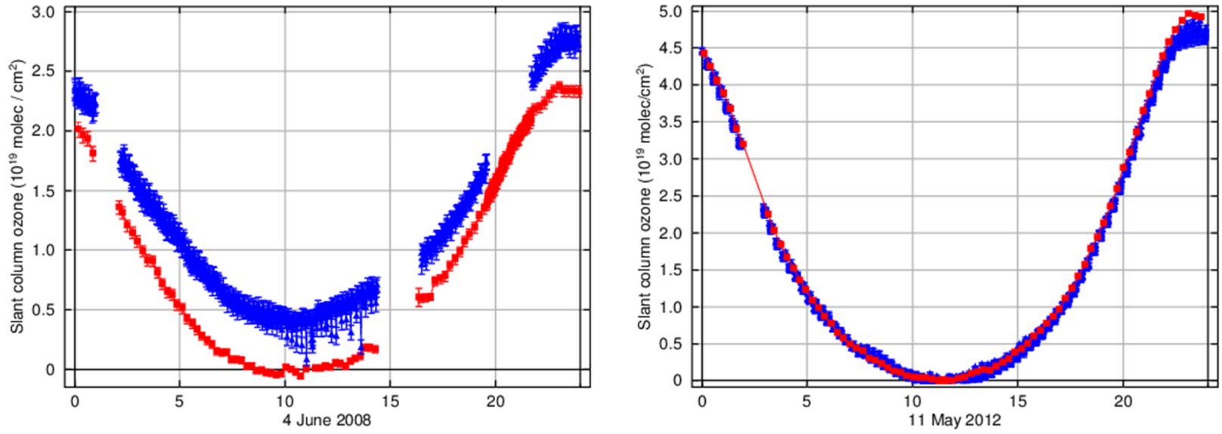

(c) Strat. ozone, old telescope

(d) Strat ozone, new telescope

Figure 4.3.: Example comparisons of stratospheric BrO (top) and ozone (bottom) timeseries as observed by the old and new instrument. Zenith observations are displayed in red, off-axis measurements in blue, time is UT. For the old telescope, the negative offset between BrO off-axis measurements compared to zenith measurements is obvious in Fig. 4.3(a). For measurements taken with the new telescope, this offset vanishes (Fig. 4.3(b)). Fig. 4.3(c) shows a positive offset of ozone off-axis measurements compared to zenith observations taken with the old telescope. For the new telescope, the off-axis measurements are closer to the zenith measurements. All data is taken from the BREDOM station in Ny-Ålesund.

not cancel out by taking the ratio of I and I_0 when calculating the optical depths (see Sect. 3.4 and 3.4.3). The observed influence on the DOAS analysis is an offset between the zenith measurements and the off-axis measurements. Fig. 4.3 showing stratospheric BrO and ozone slant columns from the BREDOM station in Ny-Ålesund illustrates the problem for some exemplarily selected days. The telescope unit in Ny-Ålesund was updated to the new system in winter 2010, i.e. Fig. 4.3(a) and 4.3(c) show slant columns derived from measurements with the old telescope while Fig. 4.3(b) and 4.3(d) are results taken with the new telescope. The offset between the slant columns in zenith directions (red) and off-axis directions (blue) is obvious in the old telescope observations. For BrO, this offset is even negativ (Fig. 4.3(a)). This is in contrast to the expectation: Under the condition that the respective trace gas is present in the BL, the off-axis slant columns measured at low elevation angles are higher than in the zenith direction and decrease towards the zenith slant columns for increasing elevation angles. If a neglectable amount of the respective trace gas is

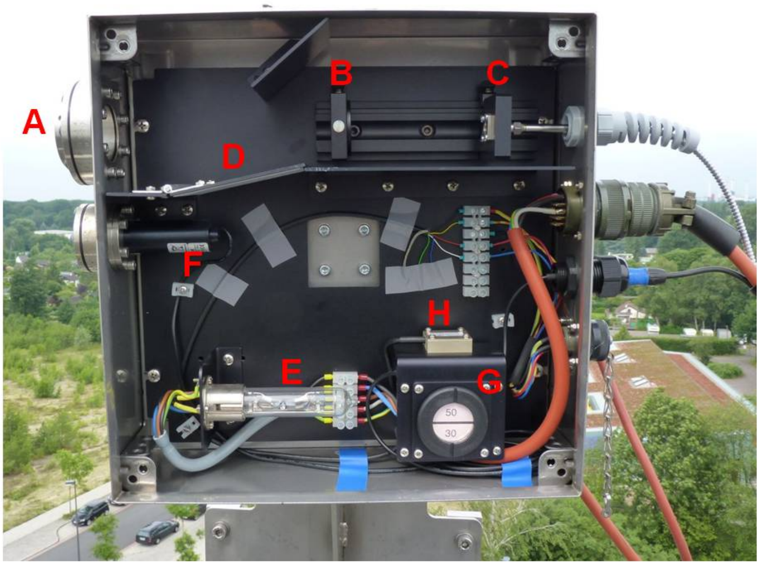

Figure 4.4: The improved Bremen MAX-DOAS telescope unit. Components: (A) Fused silica entrance window, Optical bank with lens (B) and fibre mount (C), gravity-driven shutter (D), HgCd line lamp (E), video camera (F), drying agent (G) and inclinometer (H). A schematic view of the normal measurement mode as well as the calibration mode is given in Fig. 4.5. For blueprints, see Fig. A.1-A.3 in the Appendix.

present in the BL (e.g. ozone), the off-axis slant columns should at least scatter around the zenith measurements. As Fig. 4.3(b) and 4.3(d) show, measurements performed with the new telescope unit fulfill these expectations and the disagreement between zenith and off-axis measurements vanished, meaning that a) the new telescope overcomes this problem and b) the disagreement between zenith and off-axis observations with the old telescope is most likely an effect of the mirror that is used for off-axis but not for zenith observations as explained above. Further, a degradation effect of the mirror can be speculated because this behaviour was not observed when using new mirrors and seems to increase with time. For example, this degradation could consist of some oxidation on the surface and evaluation of a thin layer in that incoming radiation interfers through multiple reflections introducing spectral structures that influence the DOAS fit yielding the above described behaviour. However, the new telescope successfully overcomes this problem by pointing directly in any viewing direction. This newly designed telescope unit is described in the next section.

4.3. The improved Instrument

The first objective of this thesis was the developement of a new telescope unit. In addition to overcome the limitations and problems mentioned above, several further requests were imposed on the instrument.
In summary, the requirements for the new telescope unit were:

- Allow all viewing directions, including azimuthal changes - potential use for TargetDOAS or direct-sun measurements
- Get rid of the mirror and associated problems (see Sect. 4.2)
- Include a video camera in the telescope unit for viewing condition surveillance and identification of events during the observations
- Flexible, light-weighted construction for campaign purposes
- Set-up on tripod (land campaign)

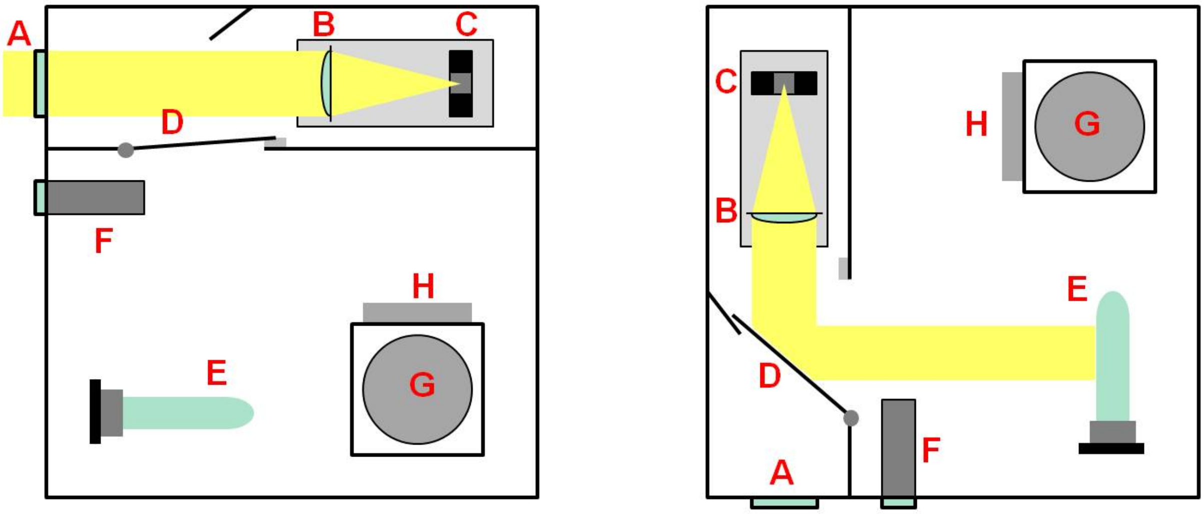

(a) Meaurement mode (b) Calibration mode

Figure 4.5.: Schematic view of the new telescope unit in its normal measurement mode (gravity-driven shutter is not blocking the sunlight) and calibration mode (gravity-driven shutter is blocking the sunlight) when the instrument is pointing straight downwards to the ground. The legend is the same as in Fig. 4.4, blueprints are in the Appendix.

- Construction for set-up on a ship (ship-borne campaign)
- Include line-lamp for calibration measurements in telescope housing
- Possibility for dark measurements (shutter)
- As simple construction as possible (operation without maintenance)
- Include operation control in existing measurement program AMAX-OMA

In order to meet these requirements, a new telescope unit was designed. The construction work for the telescope housing was perfomed by Stachl Elektronik GmbH[6], near Bremen. The wiring and electronic works were self-made.

The largest difference in comparison to the old telescope is that the pointing is no longer achieved by an internal mirror, but the whole telescope housing is mounted on a Pan-and-Tilt head. This is possible because of its reduced dimensions (30 x 30 x 12 cm) and weight (5-6 kg). For the Pan-and-Tilt head, a commercial product (ENEO VPT-501) for carrying security cameras was chosen. This head has a maximum payload of 12 kg and a maximum speed of up to 100°/sec (depending on payload). The range for the vertical angle (elevation angle) is ± 90°, the horizontal range ± 185°. Therefore, pointing into virtually any direction is possible. The ENEO VPT-501 is controlled via a RS-422 or RS-485 interface port. For communication and operation of the Pan-and-Tilt head, computer code in terms of a Delphi-unit was written and implemented in the Bremen in-house measurement software AMAX-OMA. This code enables to set the vertical as well as the horizontal angle and to read-out parameters from the head (actual angles, motor temperature). A control loop ensures that the adjusted angles are reached before the measurement starts and subsequently overcomes communication errors to allow safe automatic measurement operation.

---

[6] Stachl Elektronik GmbH, Dibberser Dorfstr. 5, 27321 Thedinghausen (www.stachlelektronik.de)

The new telescope mounted on the Pan-and-Tilt head is shown in Fig. 4.1, which is a photo taken during the Cabauw intercomparison campaign (chapter 5). The telescope/Pan-tilt-head system itself is mounted on a tripod, which allows a flexible set-up and application as a campaign instrument and was one of the requirements for the new instrument. In addition, a mounting device was build to fix the system on a ship's side, enabling ship-borne measurements.

Fig. 4.4 is a photo from the (opened) new telescope unit and Fig. 4.5 shows schematic drawings (see also blueprints in the Appendix, Fig. A.1-A.3). The light is entering the telescope through an entrance window (A) that is made of quartz glass to prevent cut-off of UV radiation. A lens (B) limiting the field of view focusses the light on the optical fibre mount (C). When the Pan-tilt-head points the telescope towards the ground, a *gravity-driven* shutter (D) fixed on a hinge closes the optical path and allows dark measurements. In addition, the shutter is covered with a white PTFE plane. If the instrument is pointing down and subsequently the shutter is closed, this white area can be illuminated by a HgCd line lamp[7] (E) allowing calibration measurements. This design using only gravitation and the possibility of moving the new telescope box in any direction is very simple and avoids unnecessary electronics, which reduces the failure-proneness. The different measurement types (normal measurements as well as calibration mode) are illustrated in Fig. 4.5. Another newly added component is a video camera[8] (F) that is installed in the telescope unit. The video camera is used for scene documentation. Again a Delphi-unit was written to implement the camera into the measurement software AMAX-OMA. In automatic measurement mode, a picture is captured and saved for every adjusted viewing direction. These pictures help interpreting the data in terms of viewing condition surveillance or identification of events. In addition, the video

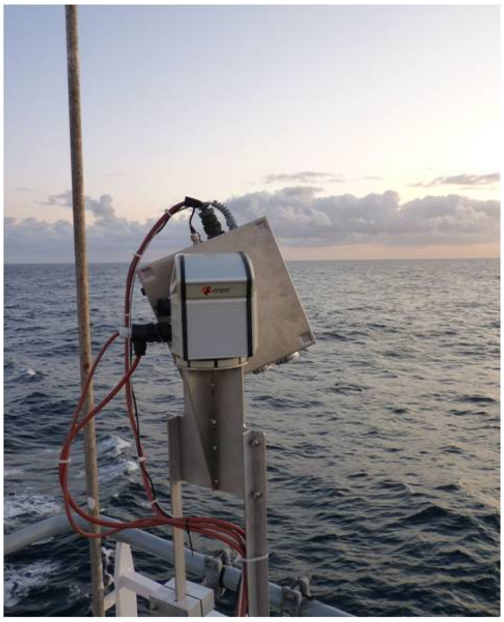

Figure 4.6.: The new telescope unit performing measurements towards the water surface (photo taken during the TransBrom campaign).

Figure 4.7.: The new telescope unit as installed on Pulau Boheydulang (off the coast of Borneo, Malaysia) performing measurements during SHIVA. In the foreground is a weather station.

---

[7] OSRAM HgCd/10 on PICO9 socket, 25W, 1A, datasheet available at `http://www.osram.de/osram_de/produkte/lampen/speziallampen/spektroskopie-lampen/index.jsp?productId=ZMP_56381` (accessed at 12 December 2012).

[8] 2M-CAM finger camera with 1/3" Sony HQ1 Ex-View CCD 752x582 pixels

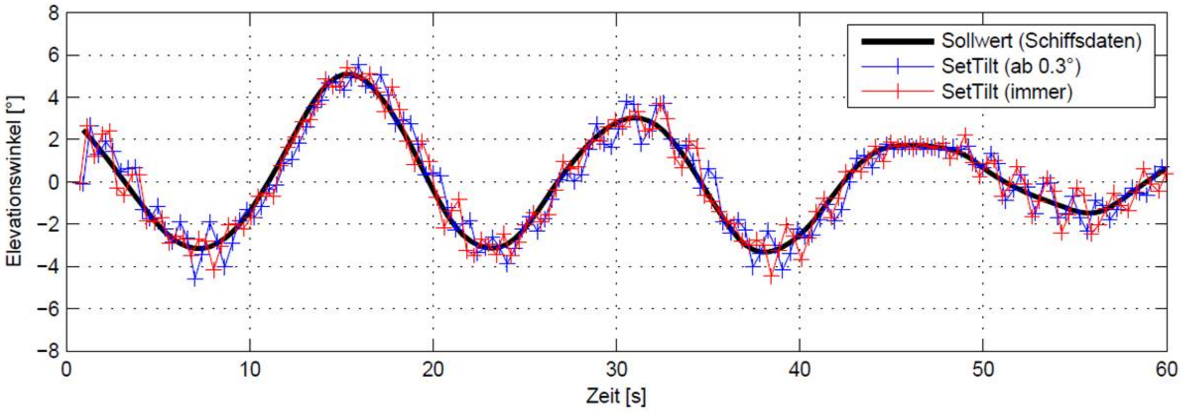

Figure 4.8.: Tracking mode of the new telescope: In black is the recorded ship's roll angle for an arbitralely selected period during TransBrom. Two different approaches (red and blue data points) were tested for the instrument to reproduce (follow) the variation. The difference between the set angles (black) and the actual angles (blue, resp. red) is in both cases ≈ 0.5°. The image has been taken from Seyler (2011).

camera is used for pointing at targets as the center of the video picture is identical to the center of the telescope's field of view. For removing air moisture, a drying agent (G) is added in the telescope housing. The telescope's position can be monitored with help of a biaxial inclinometer[9] (H). For ship-borne measurements, the inclinometer can be used for recording the ship's pitch and roll angles. Read-out of the inclinometer was implemented in the measurement software AMAX-OMA in terms of a Delphi-unit again. For measurements in the tropics and subsequently small SZA during noon, an anti-dazzle device (visual cover) was designed to prevent direct sunlight in the telescope (during the TransBrom campaign, this turned out to cause problems in the DOAS analysis). Fig. 4.1 and 4.6-4.7 give an impression of the running telescope during the different campaigns. While 4.1 shows the instrument during the Cabauw campaign, Fig. 4.6 is a photo taken during TansBrom illustrating the ship-borne application of the instrument. Fig. 4.7 shows the instrument with mounted visual cover during the SHIVA campaign on Borneo, Malaysia.

To summarize, the work for the developement of the new telescope unit meeting the requirements given above comprised

- The design of the new telescope box in collaboration with an external workshop (manufactured by external workshop, see footnote 6 on page 52).

- Self-made electrics and wiring of the telescope box.

- Writing code (Delphi-units) for the Pan-Tilt-head, capturing pictures from the video camera, and read-out of the inclinometer in order to implement the new telescope and its features to the measurement software AMAX-OMA.

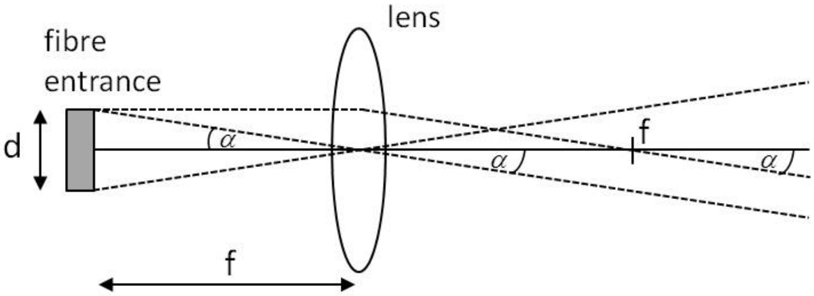

Figure 4.9: The instrument's field of view (total FOV $= 2 \cdot \alpha$) is determined by the diameter d of the optical fibre bundle and the focal length f of the lens.

4.3.1. Characterisation of the improved telescope unit

The pointing accuracy of the instrument is determined by the Pan-and-Tilt-head and is 0.2°. As mentioned before, the correct pointing can be monitored by an inclinometer installed in the telescope housing (however, as the pointing of the Pan-and-Tilt head turned out be reliable, this is usually not necessary).

Within the scope of a bachelor thesis (Seyler, 2011), it was tested to use the inclinometer signal in combination with the Pan-and-Tilt head to actively compensate for movements of the ground and therefore of the whole instrument during ship-borne measurements, i.e. to correct for the ship's roll angle in order to point in a fixed direction. Therefore, a tracking routine for the Pan-and-tilt head was created and implemented in the measurement program. A 1-minute-sequence of recorded ship's roll angles from 12 October 2009 during the TransBrom cruise (Sect. 6.1) were arbirtraley selected and used as nominal angle. The tracking routine then read out the inclinometer in fixed intervals, compared the telescope's current inclination with the actual nominal angle and corrected for the difference. The result is shown in Fig. 4.8 which has been taken from Seyler (2011) who performed this test (see also there for more detailed information). In general, the instrument's inclination (blue and red data points) follows successfully the sequence of nominal angles (black points), the difference is on average ≈ 0.5°. As a consequence, the tracking method is able to compensate for sea swell similar to the simulated one with an average pointing uncertainty of ≈ 0.5°. However, it was decided not to use this active tracking method because of two resons: 1) Concerns were arising about overstraining the Pan-Tilt-head, which had to re-adjust the whole telescope box (5-6 kg) several times per second. 2) Shocks (which occur frequently during operation on a ship) turned out to be a problem as leading to mismeasurements of the inclinometer and subsequently the tracking method would set the telescope in a wrong direction. The pointing problem during ship-borne measurements were finally solved following another approach, which is explained in Sect. 6.1.

An important parameter of the instrument is its field of view (FOV), which is the full telescope's opening angle. The FOV is predominently a result of the finite size of the optical fibre bundle entrance (C in Fig. 4.5). In geometrical optics, the lens inside the telescope (B in Fig. 4.5) would focus a parallel beam of incoming light on a single spot at the focal distance f. However, the optical fibre entrance is not a single spot but has some (small) diameter d. Figure 4.9 illustrates the optical path of the lens-optical fibre system. Obviously, the half opening angle α is given by:

$$\tan\alpha \quad = \quad \frac{1/2d}{f}$$

---

[9] ALTHEN AIT720-001-30 Dual Axis Inclinometer in MEMS Technology, analog output, ±30°, non-linearity $< 0.5\%$, datasheet available at `http://www.althensensors.com/public/media/PDF_Datenblatt/3a_Neigungsmesstechnik/en/AIT700-inclinometer-en.pdf` (accessed at 12 December 2012).

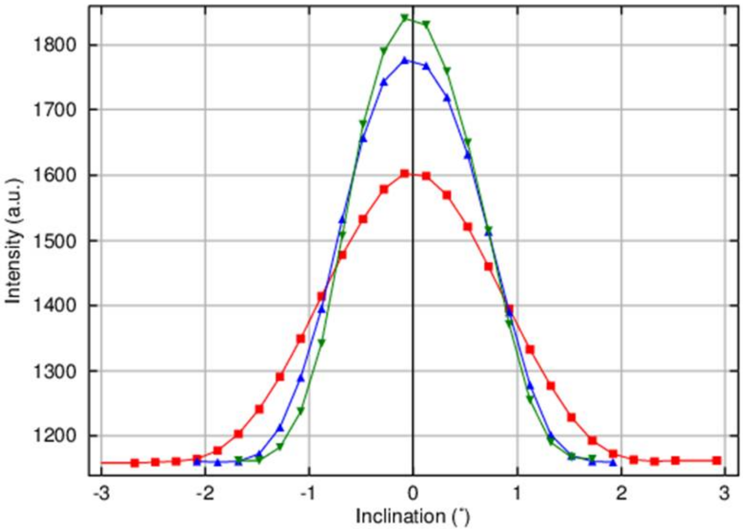

Figure 4.10: Laboratory measurements of the instrument's field of view: The telescope was scanning across an illuminated slit. Note, that the uncertainty of the inclination is ≈ 2° due to the Pan-and-tilt head's precision.

$$\alpha = \arctan\left(\frac{d}{2f}\right) \tag{4.1}$$

The full field of view is then twice the half opening angle: FOV $= 2 \cdot \alpha$.

The diameter of the optical fibre bundle is ≈ 2 mm. For instruments measuring on permanent sites and the instrument used during the CINDI (Chapter 5) and TransBrom (Sect. 6.1) campaigns, as well as the instrument performing land-based measurements during SHIVA (Sect. 6.2), the focal distance f of the lens is 50 mm. This results in $\alpha \approx 1.14°$ and a full field of view of FOV $= 2 \cdot \alpha \approx 2.3°$. In the instrument performing ship-based measurements during SHIVA, a 100 mm - lens was used, resulting in a FOV of ≈ 1.14°.

For the instruments equipped with a 50 mm lens, the FOV was also experimentally determined in laboratory measurements. Therefore, a HgCd calibration lamp was illuminating a slit (≈ 0.5 cm broad). This slit was installed in front of the instrument (≈ 2 m away). Then the telescope unit scanned stepwise (in 0.2°-steps) across the illuminated slit and the intensity of a prominent calibration line was recorded. In Fig. 4.10, the recorded intensity is displayed as a function of the telescope's inclination for different distances between the lens and the optical fibre mount. The green line corresponds to a distance close to the focal distance $f = 50$ mm, while the red and the blue line correspond to shorter distances (≈ 41 and 37 mm, respectively). This demonstrates the importance of an accurate alignment, since the FOV increases when the optical fibre is not at the focal distance of the lens. The total width of the green line in Fig. 4.9 agrees with the theoretical value of 2.3°. In practise, sometimes also the Full Width at Half Maximum (FWHM) range is used to define the FOV. This yields a nominal FOV of $1.6 - 1.7°$.

4.3.2. Advantages of the improved instrument

One advantage of the new instrument is its potential to perform TargetDOAS measurements (also called ToTaL-DOAS). This has been demonstrated by Seyler (2011) as part of a bachelor thesis (the same mentioned in Sect. 4.3.1).

During these measurements, the telescope was pointing from the roof-top terrace of the IUP-Bremen building on a target (another building in some distance) which then effectively acts as well-defined last scattering point for photons reaching the telescope. To achieve pointing on a target, the video

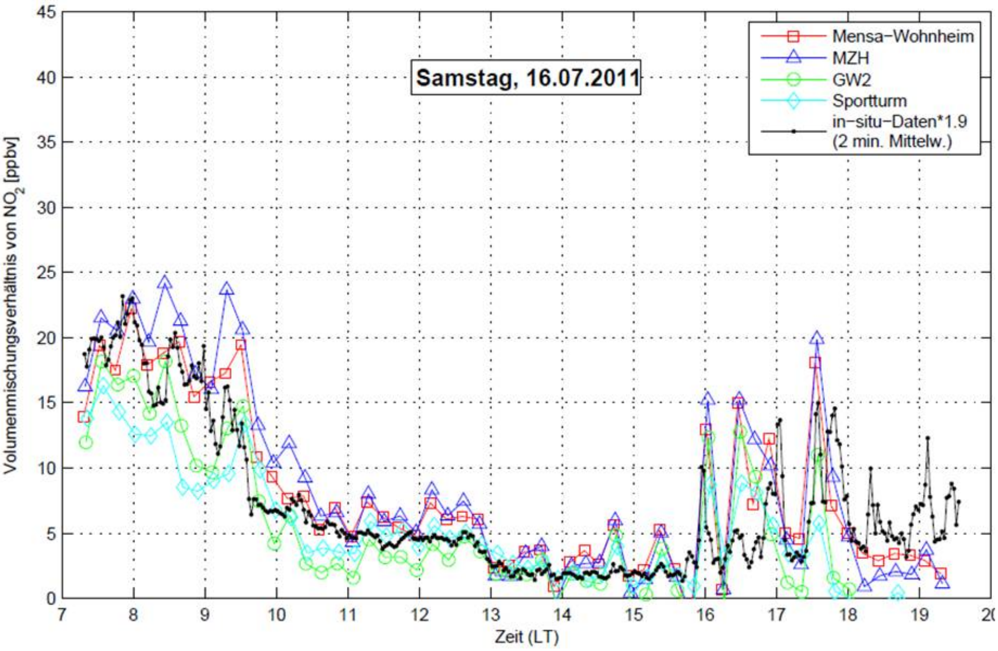

Figure 4.11.: Results from TargetDOAS tests performed with the new instrument mounted on the IUP roof-top terrace at 16 July 2011 pointing on different buildings of the University of Bremen (color-coded). In black is the NO_2 volume mixing ratio measured by an in-situ monitor nearby (see Sect. 4.5, note that the in-situ monitor produced a known offset due to instrumental problems which has been corrected for in this figure). The image has been taken from Seyler (2011).

picture from the camera inside the telescope turned out to be helpful. The reference measurement was taken by pointing on another target very close to the instrument. The corresponding light path of the reference measurement is more or less the same as in the first case with the exception of the light path between target and instrument. Thus, when taking the ratio $ln(I_0/I)$ and performing the DOAS fit, the resulting differential slant column corresponds only to this light path between target and instrument. If the distance to the target is known, the obtained differential slant columns, which are of unit molec/cm^2, can be easily converted into the average concentration between the target and the instrument. A more detailed explanation is given in (Seyler, 2011) where NO_2 volume mixing ratios are calculated using the TargetDOAS method on the Campus of the University of Bremen and compared to NO_2 values from an in-situ monitor next to the instrument (the in-situ instrument is explained in Sect. 4.5).

Figure 4.11 shows the results exemplarily for one specific day. The NO_2 volume mixing ratios derived with the TargetDOAS method pointing on different buildings are displayed color-coded. In black is the measured NO_2 volume mixing ratio from the in situ monitor. A good agreement is found between the two instruments, the general NO_2 variation throughout the day is detected by both instruments as well as single maxima. The higher values in the morning and in the evening are most likely caused by traffic (rush hour) and the minimum around noon is the result of removal of NO_2 by OH radicals (the tropospheric NO_2 chemistry is explained in Sect. 2.3.2; in addition, extensive studies of tropospheric NO_2 measured with in situ as well as using the DOAS technique were performed during the CINDI campaign and can be found in Chapter 5).

Apart from the TargetDOAS application which is now possible, the most important advancement of the new telescope is, that the problems of the old telescope with respect to the DOAS analysis as explained in Sect. 4.2 (see Fig. 4.3(a) and 4.3(c)) disappeared when using the new system

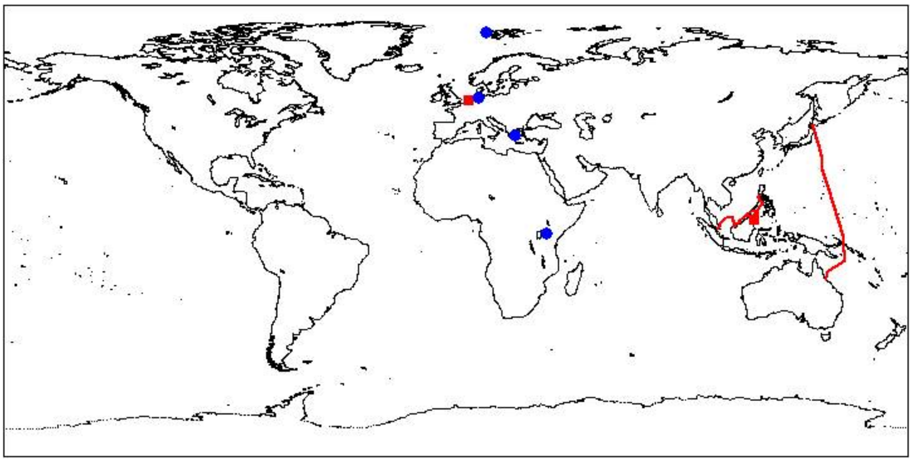

Figure 4.12: Measurement sites. Permanent BREDOM stations operational at the end of this thesis in blue, campaigns (2009-2011) in red.

(Fig. 4.3(b) and 4.3(d)). As a consequence, it was not only used on several campaigns, but the MAX-DOAS instruments of the BREDOM sites are step-by-step updated to the new system. Until the end of this work, four telescope units have been built in total. Sect. 4.4 gives an overview about the operating sites of the new instrument.

4.4. Measurement sites - Campaigns and the BREDOM network

As mentioned above, the improved instrument consisting of the new telescope unit and the spectrometers as described in Tab. 4.1 was designed for land and ship-borne field campaigns, which are subject of this thesis.

The first campaign in which the new instrument and the IUP Bremen research team participated was the Cabauw Intercomparison Campaign of Nitrogen Dioxide measuring Instruments (CINDI) in Cabauw, Netherlands, in summer 2009. Here, the instrument prooved excellent performance in comparison to other MAX-DOAS systems and was selected as one of the reference instruments. Chapter 5 reports on this as well as on comparison results to in situ and satellite instruments.

The main focus of this thesis is on the ship-borne TransBrom campaign from Tomakomai, Japan across the Western Pacific towards Townsville, Australia. Measurement results are presented in Sect. 6.1 as well as in (Peters et al., 2012).

The last campaign on which is reported here is the SHIVA campaign (Sect. 6.2). The Bremen research team participated in this campaign with MAX-DOAS land measurements in a tropical, marine environment (on the island of Borneo) as well as ship-borne measurements perfomed on a cruise from Singapore to Manila, Philippines.

The locations of these three campaigns, resp. the cruise tracks are indicated by red marks and lines in Fig. 4.12.

As a consequence of the excellent instrument's performance, the new telescope unit was additionally implemented to the MAX-DOAS stations composed in the BREDOM network (for the BREDOM network, see e.g. Wittrock, 2006). In Fig. 4.12, the BREDOM stations that were operational at the end of this thesis are indicated by blue points. The first station that has been updated to the new system was Ny-Ålesund. The improved telescope unit was installed during a maintenance visit in March 2010. In Bremen, a MAX-DOAS instrument that is equipped with the new telescope unit is running since Spring 2012. The BREDOM station in Nairobi was visited for maintenance reasons after a long system breakdown in February 2011. During this stay, it was decided not to update the system because a) the architectural situation and vegetation (trees and buildings near by) allow only one azimuthal viewing direction and b) the system is installed in a very professional way, i.e. an update of the telescope unit (subsequently new cables are needed) would require rebuilds on the close-by office building hosting the spectrometers and computers operating the instrument. In addition, c) the instrument is set up on an outdoor staircase, meaning that people are walking by close to the telescope. Consequently, a moving telescope unit is not an option and the old telescope unit was maintained. In September 2012, a new MAX-DOAS system was installed on a measurement site in Athens, Greece. This instrument was previously operating on Crete and maintained and updated with the new telescope unit in Bremen.

4.5. NO_x in-situ monitor

During the CINDI intercomparison campaign (chapter 5), a commercial in-situ monitor for measuring NO and NO_2 in sampled air was used. This instrument was from ECO PHYSICS and consisted of a CLD88p chemiluminescence detector and a PLC860 photolytic converter. Fig. 4.13 shows a sketch of the instrument.

A constant air flow of 0.6 l/min is pumped through an outdoor-installed inlet and a tube to the instrument. In general, the chemiluminescence detector (CLD) measures NO while in the photolytic converter (PLC), that is activated periodically, NO_2 in the sampled air is partially converted to NO. As a result, the CLD is alternatingly measuring the NO in the sampled air (PLC off) and the NO plus the fraction of converted NO_2 to NO (PLC on). After calibration of the PLC and knowledge of its conversion factor, the content of NO_2 can be calculated from the difference of the alternating measurement modes. This type of instrument using a photolytic converter has the advantage of adressing the NO_2 selectively. In contrast, the frequently used Molybdenum catalysers convert all NO_y species to NO and measure subsequently not (only) NO_2.

The measurement of NO in the CLD follows the reactions:

$$NO + O_3 \rightarrow NO_2 + O_2 \tag{4.2}$$

$$NO + O_3 \rightarrow {NO_2}^{\bullet} + O_2 \tag{4.3}$$

$${NO_2}^{\bullet} \rightarrow NO_2 + h\nu \tag{4.4}$$

$${NO_2}^{\bullet} + M \rightarrow NO_2 + M \tag{4.5}$$

The ozone for reactions 4.2 and 4.3 is produced by an ozone generator that is integrated in the CLD housing (see Fig. 4.13). The NO in the air sample reacts with this ozone to NO_2 (see also Sect. 2.3.2). The resulting NO_2 may be either in the ground state (reaction 4.2) or excited (reaction 4.3). Most of the excited ${NO_2}^{\bullet}$ decays by collision with other molecules in the air sample (reaction 4.4), but a small fraction also decays by emission of a photon. This luminescence is detected by a photomultiplier. As the intensity is proportional to the number of decays, the original NO level can be obtained after calibration.

For removing the contribution of light resulting from other sources (e.g., NO_2 can be excited also by collisions or reaction with the atmospheric ozone that is present in the air sample), two alternating measurement modes are applied. In the first measurement, additional ozone is injected in the air sample and the photo-signal is recorded as described above. In the second measurement, no addi-

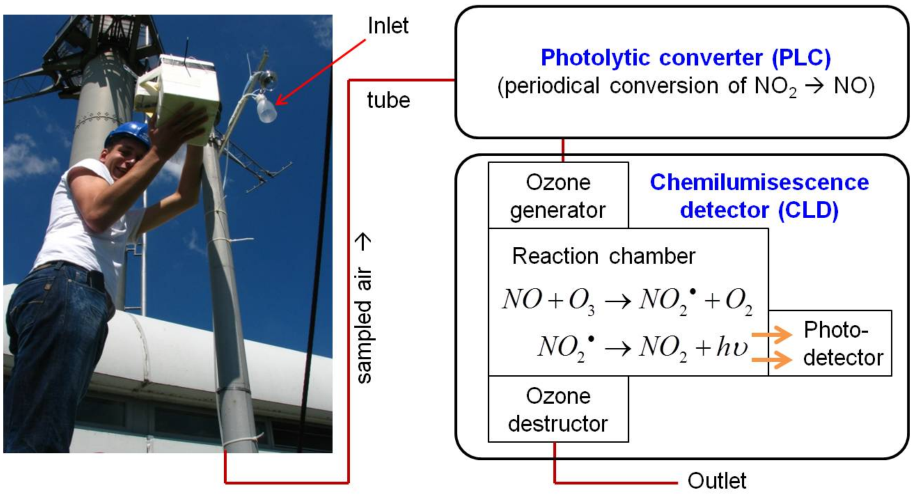

Figure 4.13: Sketch of the NO_x in-situ monitor (photo: Installation of the inlet). The chemiluminescence detector (CLD) measures NO. In the photolytic converter (PLC) that is activated periodically, NO_2 in the sampled air is partially converted to NO.

tional ozone is injected and the corresponding photo-signal (baseline measurement) is subtracted from the first one to account for photons resulting from other processes. To prevent contamination of following measurements and/or the laboratory (health effect), left-over ozone is destroyed before the sampled air is released from the instrument (Fig. 4.13).

As mentioned above, NO_2 is measured indirectly from NO measurements with the PLC prior to the CLD alternating switched on and off. If the PLC is switched on, the air sample inside the PLC is exposed to radiation provided by a metal-halide lamp. An optical filter limits the light spectrum to the range of 320-400 nm, which selectively photolyses NO_2 according to

$$NO_2 + h\nu \quad \rightarrow \quad NO + O$$

This is the reaction 2.28 in Sect. 2.3.2. The efficiency of the PLC has to be determined during calibration. In the CLD, the produced NO is detected together with the *true* NO that is initially present in the air sample. If the PLC is switched off, no NO_2 is converted and the true NO content of the air sample is measured. Subtraction of this NO level from the one with running PLC and knowledge of the PLC's conversion efficiency yields the NO_2 content of the air sample.

Consequently, the measured NO_2 level is only correct under the condition that the NO level does not change during the measurement modes. Due to this error source (and other mismeasurements), spikes can occur in the timeseries of measured NO_2 and NO levels. Before the analysis of the data (chapter 5), these spikes have been removed and the data has been averaged to 1-10 min time steps.

4.6. Satellite instruments

As mentioned before, one focus of this thesis is the validation of trace gas observations retrieved from the satellite instruments SCIAMACHY and GOME-2. The validation results can be found in chapter 5 and 6 as well as in (Peters et al., 2012). In addition, in chapter 7, residual spectra of liquid water retrieved with the MAX-DOAS instrument during TransBrom (chapter 6.1) are tested in OMI satellite data.

The SCIAMACHY (Scanning Imaging Absorption spectroMeter for Atmospheric CHartography) instrument is a UV/Vis-NIR spectrometer on board the environmental satellite ENVISAT of the

European Space Agency (ESA). The satellite (26 x 10 x 5 m diameters) hosts 10 different remote sensing instruments and was launched on an Ariane-5-rocket into space on 1 March 2002. ENVISAT's mean altitude is $\approx$ 800 km, the orbital period 100.6 min. Due to its polar, sun-synchronous orbit, a fixed equator crossing time of 10:00 a.m. (± 5 min) local time is achieved.
SCIAMACHY consists of 8 simultaneously measuring channels, six continuous channels from 214-1750 nm and two further channels for near-infrared light. The relevant channels for the retrieval of species presented in this thesis are channel 2 (300-412 nm, 0.26 nm resolution) and channel 3 (383-628 nm, 0.44 nm resolution). Measurements are perfomed in different viewing geometries (limb, nadir, solar and lunar occultation). In this thesis, only results from nadir measurements are used, i.e. the instrument points straight downwards and measures spectra of sunlight backscattered in the atmosphere or reflected from the surface. The typical ground-pixel size is 60x30 km^2, the scan width (swath) 960 km. Due to the swath and the alternating limb-nadir-measurements, global coverage at the equator is achieved within six days while ENVISAT's repeat cycle is 35 days.
Further information, details of the instrument and mission objectives can be found in (Burrows et al., 1995; Bovensmann et al., 1999; Gottwald et al., 2006). After contact to ENVISAT was lost on 8 April 2012 and attempts to resume communication failed, the end of the mission was announced on 9 May 2012 (5 years beyond the planned mission lifetime).

The GOME-2 (Global Ozone Monitoring Experiment-2) instrument is derived from SCIAMACHY and its precursor, the GOME instrument, which flew on ERS-2 from 1995 to 2011 (Burrows et al., 1999, and references therein). GOME-2 is a nadir viewing UV/Vis spectrometer system mounted to the flight direction side of the MetOp-A satellite, which was launched into a sun-synchronous orbit on 19 October 2006. The satellite's altitude is $\approx$ 820 km, the equator crossing time 9:30 a.m. LT. The spectrometer covers a wavelength range of 240-790 nm with a spectral resolution of 0.2-0.4 nm. The nominal ground-pixel size is 80x40 km. Global coverage can be achieved within one day due to a scan-width of 1920 km. More detailed information about the GOME-2 instrument can be found in (Callies et al., 2000).

The Ozone Monitoring Instrument (OMI) is a nadir-viewing imaging spectrometer on NASA's EOS Aura satellite launched on 15 July 2004 into a Sun-synchronous, polar orbit at approximately 705 km altitude. The local equator crossing time is between 13:40 and 13:50. OMI measures direct and atmosphere-backscattered sunlight in the UV-VIS range from 270 nm to 500 nm. Atmospheric observations are performed perpendicular to the flight direction in a 114° field of view corresponding to a 2600 km wide spatial swath on the Earth's surface. Due to the large field of view, the ground-pixel size varies across-track from 24 km (nadir) to 128 km (edge of the swath). Global coverage is achieved in one day. Further information about the OMI satellite instrument can be found in (Levelt et al., 2006a,b).

5. Intercomparison measurements in an anthropogenically polluted environment

The first application of the improved MAX-DOAS instrument (chapter 4) was the Cabauw Intercomparison Campaign of Nitrogen Dioxide measuring Instruments (CINDI), which took place in Cabauw, Netherlands, in June/July 2009 (immediately after construction of the first improved instrument). During the campaign, the instrument showed excellent performance and was chosen as one of the reference instruments.

An introduction to the CINDI campaign is given in Sect. 5.1. Results from the NO_x-in situ instrument, which participated as part of the IUP-Bremen contribution to the campaign, are presented in Sect. 5.2. The formal MAX-DOAS slant column intercomparison, which was on focus of the campaign, is presented in Sect. 5.3. In Sect. 5.4, profiling results that have been retrieved from the Bremen MAX-DOAS measurements are discussed and compared to in situ measurements (ground concentration) as well as to satellite measurements (vertical columns). Early results as well as background information of the campaign can also be found in (Piters et al., 2012). The slant column intercomparison results between the different participating MAX-DOAS instruments have been published in (Roscoe et al., 2010; Pinardi et al., 2013).

5.1. Introduction to the CINDI campaign

The objective of the Cabauw Intercomparison campaign for Nitrogen Dioxide Measuring Instruments (CINDI) was the intercomparison and intercalibration of ground-based instruments measuring NO_2, which are commonly used for validating tropospheric NO_2 retrievals from satellite observations (Piters et al., 2012). CINDI was mainly organized and hosted by the Royal Netherlands Meteorological Institute (KNMI). In total, 22 DOAS-like instruments (MAX-DOAS, mini-MAX-DOAS, zenith-only-DOAS, mobile DOAS systems mounted on cars), 4 NO_x in situ instruments, aerosol and NO_2 LIDAR systems, prototypes of NO_2 sondes and measurement systems for complimentary areosol and weather condition surveillance from different instituts participated in the campaign. Tab. 5.1 gives an overview about the participating instruments and institutes.

The measurements were perfomed at the Cabauw Experimental Site for Atmospheric Research (CESAR), which is located near the village of Lopik (see Fig. 5.1, top picture) between the cities of Utrecht (≈ 18 km distance) and Rotterdam. An aerial view of the CESAR site is given in Fig. 5.1 (bottom). In situ measurements of NO_2 (see Sect. 5.2) were perfomed on platforms in different altitudes at a meteorological tower (≈ 200 m total height). A photo of this tower can be seen in Fig. 4.1 and Fig. 5.3 while its location is indicated in Fig. 5.1 (bottom). LIDAR measurements were perfomed from the Remote Sensing Site (RSS), in a few hundred meters distance from the tower. DOAS-measurements were performed predominently from the RSS as well, but also from the wind profiler (WP, see Fig. 5.1) and from elevated platforms of the tower. As Fig. 5.1 (bottom)

DOAS-like instruments participating in the intercomparison				
Institute	Country	Instruments	Range (nm)	Location
BIRA-IASB	Belgium	2-channel MAX-DOAS	300-388 400-700	RSS
		Mini-MAX-DOAS	290-433	Tower
		mobile DOAS	270-500	mobile
IUP-Bremen	Germany	2-channel MAX-DOAS	315-384 401-573	RSS
CNRS	France	SAOZ	270-630	WP
		Mini-SAOZ	270-800	Tower
		mobile SAOZ	270-630	mobile
GIST	Korea	Mini-MAX-DOAS	290-430	RSS
IUP-Heidelberg	Germany	3-channel MAX-DOAS	290-790	WP
INTA	Spain	NEVA-II	387-514	RSS
		RASAS-II	393-510	RSS
JAMSTEC	Japan	MAX-DOAS	223-558	RSS
KNMI	Netherlands	Mini-MAX-DOAS UV	290-433	Tower
		Mini-MAX-DOAS Vis	400-600	RSS
U Leicester/Leeds	UK	MAX-DOAS	425-490	RSS
MPIC-Mainz	Germany	Mini-MAX-DOAS	310-461	Tower
		mobile DOAS	320-466	mobile
NASA	USA	PANDORA	280-530	RSS
NIWA	New Zealand	DOAS system	389-510	RSS
U Toronto	Canada	DOAS system	341-545	RSS
Washington State U	USA	MF-DOAS	282-498	RSS

Non-DOAS instruments				
IUP-Bremen	Germany	NO_x in situ monitor^a	-	Tower (3m)
EMPA	Switzerland	NO_x in situ monitor^a	-	Tower (3m)
KNMI	Netherlands	NO_2 sondes weather surveillance	-	Tower, WP
RIVM	Netherlands	NO_x in situ monitor^b	-	Tower (3m)
		2 NO_x in situ monitors^a		Tower (200m, 3m/100m)^c
		NO_2 and aerosol - LIDAR systems		RSS
PSI	Switzerland	Nephelometer	-	Tower
TNO	Netherlands	MAAP, SMPS/APS, Nephelometer	-	Tower

Table 5.1.: Overview about participating institutes, instruments and location of deployment during the CINDI campaign (RSS = Remote Sensing Site, WP = Wind profiler, mobile = installation on cars). Notes: ^{a} Chemilumienscence detector with photolytic converter, ^{b} molybdenum converter instead of photolytic converter, ^{c} instrument from 3 m moved to platform in 100 m for campaign extension.

Figure 5.1: CINDI overview maps. Top: The measurement site is located between Utrecht and Rotterdam. The MAX-DOAS viewing direction (287° from North) is indicated by a red arrow. The length of the arrow is 43 km, which is the horizontal distance inside a boundary layer of 1.5 km height under the condition of 2° elevation angle. Bottom: Aerial picture of the measurement site. The instruments were installed predominently at the remote sensing site (RSS), but also at the tower and the wind profiler (WP). The in situ instruments were installed in different altitudes at the tower. Source: Google maps (http://maps.google.de).

shows, the terrain was flat and provided almost undisturbed viewing conditions in a wide range of azimuth angles. However, all DOAS instruments agreed on a fixed viewing direction of 287° from North, for comparison reasons. This viewing direction is indicated by a red arrow. Under the condition that clear-sky MAX-DOAS measurements in a 2° elevation angle are performed and that the NO_2 is well mixed within a boundary layer of 1500 m height, the horizontal averaging of the light path within this boundary layer is $\approx$ 43 km. This is the length of the arrow in Fig. 5.1 (top) illustrating the horizontal distance on which the MAX-DOAS measurement is averaged under these conditions (and which extends until the city of Den Haag, close to the North Sea). As the next vicinity is dominated by grassland, local influences of NO_2 pollution are restricted to the village of Lopik in the back of the MAX-DOAS observations and to a local road connecting Utrecht with Rotterdam and the villages in between (5.1, top picture) about 20-30 m away from the RSS and $\approx$ 400 m away from the in situ instruments at the tower (see Fig. 5.1, bottom picture). During morning and evening rush hours, a considerably increased number of cars on this road was observed by eye. As a consequence, the NO_2 pollution from local sources is strongly dependent on a) wind direction and b) traffic situation. Nevertheless, the absolut level of pollution from local sources is low due to the limited anthropogenic activity. On a larger scale, the Cabauw site is located between sources of strong anthropogenic NO_2 releases, which are predominantly the harbours of Rotterdam, Netherlands (40 km distance) and Antwerp, Belgium (90 km) as well as the German

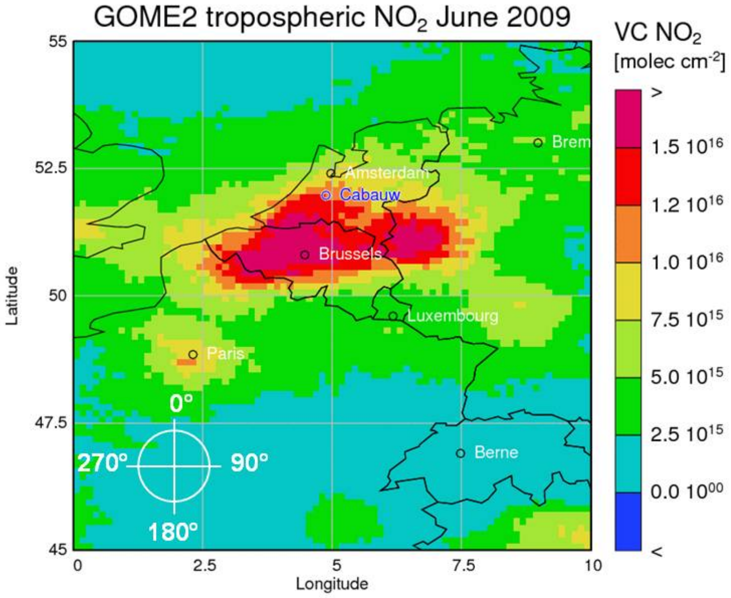

Figure 5.2: June 2009 average of tropospheric NO_2 as derived from GOME-2 measurements. The Cabauw measurement site is affected by regions of high pollution.

Rhein-Ruhr-area ($\approx$ 150 km distance) (Piters et al., 2012). Fig. 5.2 shows the tropospheric NO_2 column as derived from GOME-2 measurements for June 2009 illustrating the location of Cabauw at the edge of these source regions. The small local emissions on the one hand and the location within regions of high emissions on the other hand make the Cabauw measurement site a *semi-rural* area. The resulting large variability of NO_2 was one of the reasons for selecting the site as it allows intercomparison between NO_2 measuring instruments under varying conditions.

A photo from the Remote Sensing Site is shown in Fig. 5.3. The site was equipped with air-conditioned portable cabins serving as laboratories. The MAX-DOAS instruments, resp. telescope units were installed in front or on top of the containers, while the spectrometers (of those instruments using an optical fibre similar to the Bremen instrument) were installed inside the containers. The incerpts in Fig. 5.3 show photos of different MAX-DOAS instruments/telescopes, which participated at the campaign. Not all instruments were similar to the Bremen instrument and not all DOAS instruments were installed at the RSS. E.g., some groups used commercial Mini-MAX-DOAS instruments mounted at the tower and some instruments (Mini-MAX-DOAS, SAOZ) were installed on cars (Mainz, CNRS) driving around during the satellite overpass to evaluate the spatial homeogenity within a satellite pixel. The type of instrument used by the different groups and the location of its installation is listed in Tab. 5.1.

The DOAS observations were accompanied by several complimentary measurements. E.g., meteorological data (wind direction, wind speed etc.) was collected in different altitudes on platforms of the tower. Mounted on the truck in Fig. 5.3 is a movable NO_2 LIDAR from the dutch National Institute for Public Health and the Environment (RIVM). Also an aerosol LIDAR was operated during CINDI. From IUP-Bremen, a commercial NO_x in situ monitor was contributed, which was a chemiluminescence detector (CLD) with photolytic converter (PLC). This instrument measures continuously the local volume mixing ratio (VMR) of NO and NO_2 and is described in detail in Sect. 4.5. From the Swiss Federal Laboratories for Materials Science and Technology (EMPA), a similar NO_x in situ monitor was contributed. The EMPA research team provided the infrastructure for calibration of the Bremen in situ instrument[10]. Both in situ instruments were installed in the

---

[10] At this point, many thanks to the EMPA team for their support.

Figure 5.3: Picture from the Remote Sensing Site (RSS). The meteorological tower can be seen in the background. MAX-DOAS telescope units (incerpts) were deployed on top or in front of the portable cabins, while the spectrometers were installed inside the air-conditioned containers (for those systems using a quartz fibre). The truck on the left site is the mobile RIVM NO_2 LIDAR.

basement of the tower and collected air samples through tubes from outside the tower in an altitude of ≈ 3 m. In addition, the RIVM was running NO_x in situ monitors in different altitutes at the tower: Two monitors using a PLC (like the Bremen and EMPA systems), one in 200 m altitude and one in 3 m altitude (which was moved to a platform in 100 m for the campaign extension) and one in situ instrument using a molybdenum converter instead of a PLC[11]. Again, all non-DOAS instruments participating in CINDI are listed in Tab. 5.1.

The timeline of CINDI is shown in Fig. 5.4 together with the weather condition (precipitation). The IUP-Bremen research team arrived in Cabauw on 12 June 2009 to set up the instruments. The campaign's focus was a 16 days period from June 15 - 30. During that time, a formal semi-blind intercomparison for NO_2 and O_4 slant columns as measured from the different MAX-DOAS instruments was carried out (Sect. 5.3). In a following campaign extension, extra measurements were performed in different viewing angles in order to investigate the spatial variability on the scale of satellite pixels. For this purpose, some instrument were also moved to different locations. The spatial homeogeneity is not on focus of the work presented here although MAX-DOAS vertical columns are compared to satellite observations in Sect. 5.4. For early results of the CINDI campaign extending beyond the slant column intercomparison (Roscoe et al., 2010, and Sect. 5.3), the reader is referred to Piters et al. (2012). Results from the profile retrieval and comparison to in situ measurements are given in Sect. 5.4. On 20 July 2009, the Bremen MAX-DOAS and in situ instruments were packed and moved back to the IUP-Bremen.

As Fig. 5.4 shows, several rainy periods occured during the campaign having a) direct effects on the atmospheric chemistry and the trace gas abundances (e.g. wet deposition, washing out) and b) influences on the viewing condition (clouds). These bad weather periods occured predominently during the campaign extension and in the beginning of the semi-blind intercomparison, when heavy thunderstorms were observed especially during night and in the evening and early morning hours. Besides this, the semi-blind intercomparison was mostly dominated by dry and sunny weather conditions. Nevertheless, most of the days had some hazy or cloudy periods that effect the viewing condition and impede the profile retrieval. As a consequence, the retrieval of profiles and compari-

---

[11] This instrument is measuring NO_y instead of NO_x due to the chemical conversion replacing the selective photolytic conversion of a PLC.

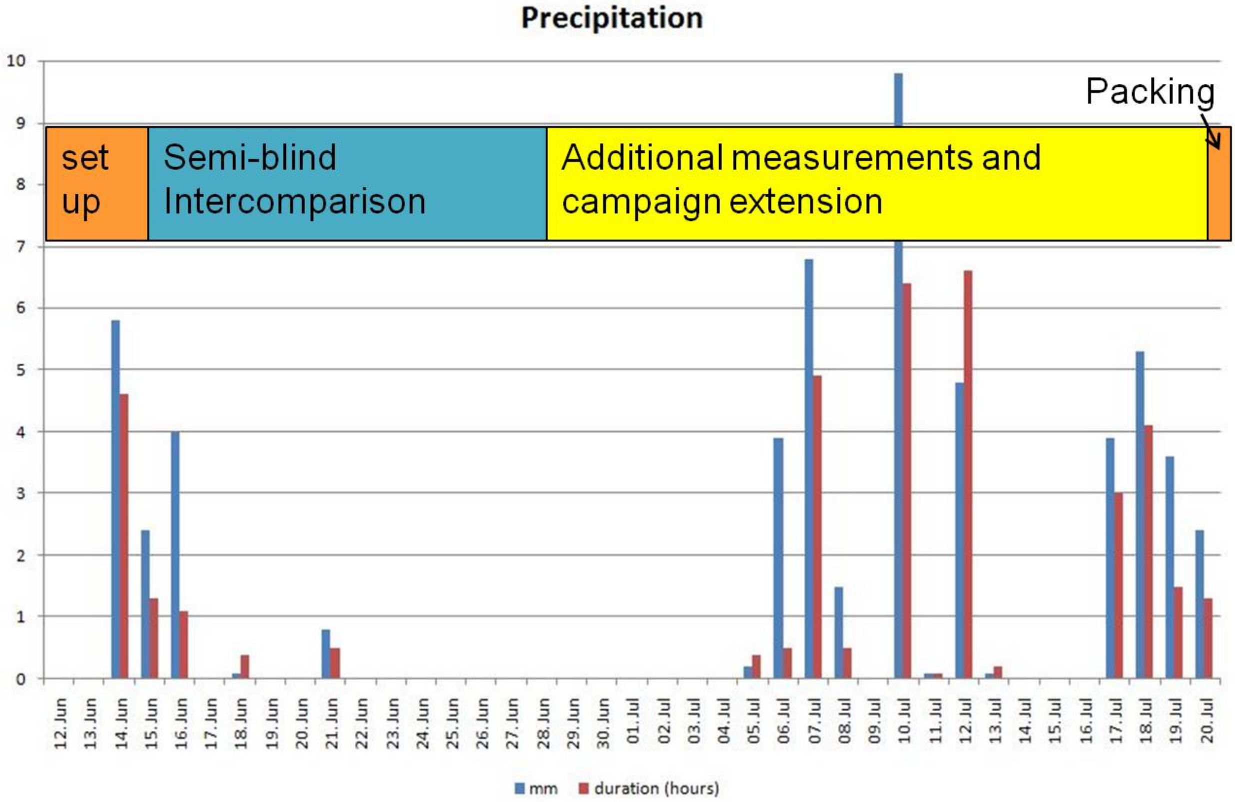

Figure 5.4.: Timeline of CINDI and precipitation (mm and duration) during the campaign.

son to in situ measurements were focussed on *golden days*, which were almost completely haze- and cloud-free and dominated by excellent viewing conditions. These golden days were June 12-13, 18, 23-25, 30 and July 2, 4, 16 and 25 (for the extension, only July 2 and 4 are covered by measurements of the IUP-Bremen instrument).

5.2. In situ measurements

In addition to the MAX-DOAS instrument, the IUP-Bremen contributed to the CINDI campaign with a commercial NO_x in situ monitor. This instrument and its measurement principle is explained in detail in Sect. 4.5. The in situ instrument was installed at the meteorological tower (see map in Fig. 5.1). The instrument's analyzing components (CLD and PLC) were located in the tower's basement while the sampled air was pumped through a tube that was fixed outside the tower in an altitude of $\approx$ 3 m. The in situ monitor was operating continuously (day and night) from 12 June - 20 July 2009.

As mentioned above, further in situ instruments were contributed by the Swiss Federal Laboratories for Materials Science and Technology EMPA (Eidgenössische Materialprüfungs- und Forschungsanstalt) and the Dutch National Institute for Public Health and the Environment RIVM. The Bremen and EMPA instruments both use a photolytic converter (see Sect. 4.5) and were installed side-by-side at the tower (surface). The RIVM was running in situ instruments with photolytic converter on top of the meteorologic tower ($\approx$ 200 m) and at the surface, next to the Bremen and EMPA instruments. For the campaign extension, the instrument from the surface was moved to an elevated tower platform in $\approx$ 100 m to gain additional profile information. In addition, an in

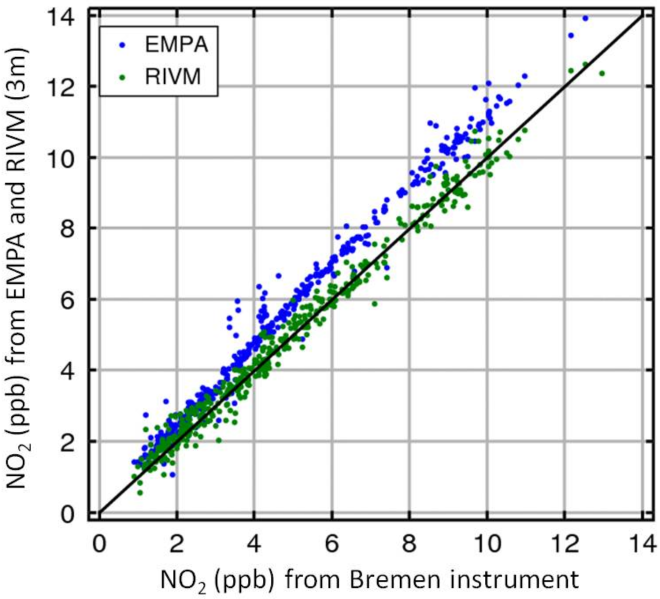

Figure 5.5: Correlation between the IUP-Bremen in situ instrument and EMPA (blue data points), resp. the RIVM instrument at the surface (green data points) for 23-25 June 2009 (golden days). Bremen-EMPA: Correlation 0.993, Slope 1.11, Correlation Bremen-RIVM 0.992, Slope 0.985.

situ monitor from RIVM using a molybdenum converter was running at the tower's basement (all in situ instruments are listed also in Tab. 5.1). As the molybdenum converter does not selectively convert NO_2 into NO, its data was not used in the further analysis. A correlation plot between the Bremen, EMPA and RIVM instruments using a photolytic converter at ground-level is shown in Fig. 5.5 for the golden days 23-25 June 2009 when all instruments were running side-by-side. The correlation between the Bremen and RIVM instrument is 0.992, between Bremen and EMPA 0.993, which is a reasonable result. Nevertheless, the correlation plot in Fig. 5.5 exhibits a factor of 1.11 between the Bremen and EMPA results, while Bremen and RIVM measurements agree with each other upon a factor of 0.985, i.e. the EMPA observations are $\approx$ 10% higher than Bremen and RIVM results. Possible calibration problems do not explain this behaviour, because the EMPA calibration source was also used for calibrating the Bremen instrument while the RIVM used another, independent source. Unfortunately, the reason stayed unexplained until the end of the campaign. However, all instruments measured the same variability of NO_2 as the good correlation coefficients demonstrate.

In Fig. 5.6, all data from the Bremen in situ instrument has been binned to 30 min resolution and plotted as a function of time. The resulting curves exhibit the diurnal cycle of NO (red) and NO_2 (blue) at the Cabauw measurement site. The NO cycle is dominated by a strong morning peak of 3-4 ppb (on average), which decreases during the course of the day. The NO_2 level shows morning and evening peaks of $\approx$9 ppb and 7-8 ppb, respectively, decreasing values during the night and a strong minimum of $\approx$ 3 ppb in the afternoon. The error bars in Fig. 5.6 are not caused by instrumental errors, but are standard deviations of the corresponding volume mixing ratios within the single time steps. Therefore they give an impression about the strong day-to-day variation of the NO and NO_2 levels.

The shape of the diurnal variation follows meteorological conditions, dominating reactions at different points of time during the course of the day as well as anthropogenic impacts. E.g. for NO (red line), the morning rush hour on the close-by street causing the dominant peak is obvious. In the NO_2 diurnal cycle (blue line), this peak appears even earlier. The reason is, that predominantly NO is produced in combustion processes, but in the early morning, this NO reacts with left-over

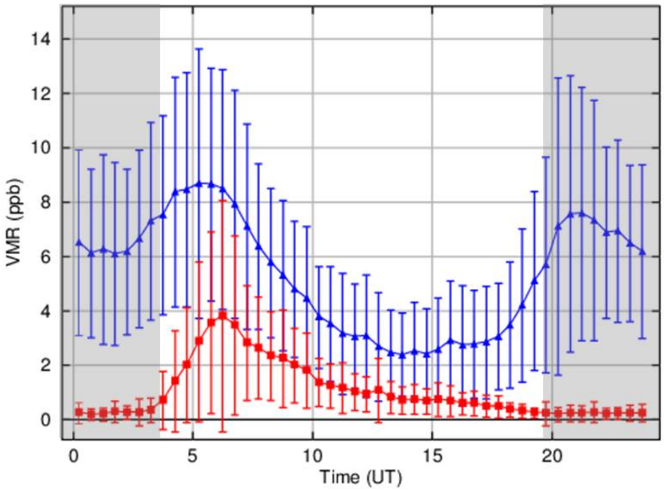

Figure 5.6: Averaged diurnal cycle of the NO (red) and NO_2 (blue) volume mixing ratio (VMR) as measured by the IUP-Bremen in situ instrument during CINDI (all data binned to 30 min time steps). The error bar is not the instrumental error but the standard deviation of the single values illustrating the day-to-day variabililty. The shaded area corresponds to periods without sunlight (night).

ozone[12] yielding NO_2 according reaction 2.27. Due to the lack of sunlight, this NO_2 is not photolysed back to NO and ozone (according to reaction 2.28). As a result, the emission peak appears in the NO_2 earlier than in the NO level. As soon as sufficient sunlight is available, photolysis of NO_2 starts and the morning rush hour peak appears in NO as well. When the surface heats up during the day, the boundary layer (BL) height rises and convection causes NO_2 (and NO) to dilute vertically. Consequently, the volume mixing ratios decrease. In addition, the hydroxyl radical OH is formed during the day and reacts with NO_2 to HNO_3 (reaction 2.32). This is the most dominant chemical loss of NO_2 and therefore NO_x from the atmosphere. NO_2 increases again when the sun sets and subsequently the photolysis (as well as reaction with OH) stops. Due to the high level of ozone that developed during the day (for ozone production, see Sect. 2.3.1, 2.3.2 and 2.3.3), the second afternoon rush hour peak is invisible in the NO level because all NO molecules are converted to NO_2 by reaction with ozone (causing the NO_2 level to increase again). During the night, NO_2 reacts with ozone to NO_3 (reaction 2.33) and further to N_2O_5 (reaction 2.16), which can be uptaken by aerosols and subsequently removes NO_x from the atmosphere. As a result, NO_2 and ozone levels fall during the night. The next morning, left-over ozone may again react with NO released from the morning rush hour causing the corresponding peak to appear earlier in NO_2 than in NO and the loop is repeating. Details of the tropospheric ozone and NO_x chemistry are also given in Sect. 2.3.1 and 2.3.2.

The strong day-to-day variations as illustrated by the standard deviations in Fig. 5.6 are caused by variabilities in emission rates and meteorological conditions (wind direction, temperature etc.). E.g. the emission rates are higher on working days than on sundays (therefore see Fig. 5.19) and on days with more extended BL height the trace gases would be more vertically diluted.

An example illustrating the influence of the surface temperature and corresponding convection processes pushing the BL height upwards is given in Fig. 5.7. The top picture shows the NO_2 volume mixing ratio as measured at the ground by the RIVM (green line) and the IUP-Bremen (red line) in situ instruments on 25 June 2009, which was one of the *golden days*. The blue line is the in situ measured NO_2 VMR measured by the RIVM instrument in 200 m altitude on top of the meteorological tower. While the Bremen and the RIVM instruments on the ground are in good agreement, discrepancies exists between the NO_2 level in 200 m and at the surface. As expected,

---

[12] During the night, no ozone is produced from NO_2 photolysis; instead, ozone is depleted by reaction with NO_2, see Sect. 2.3.2

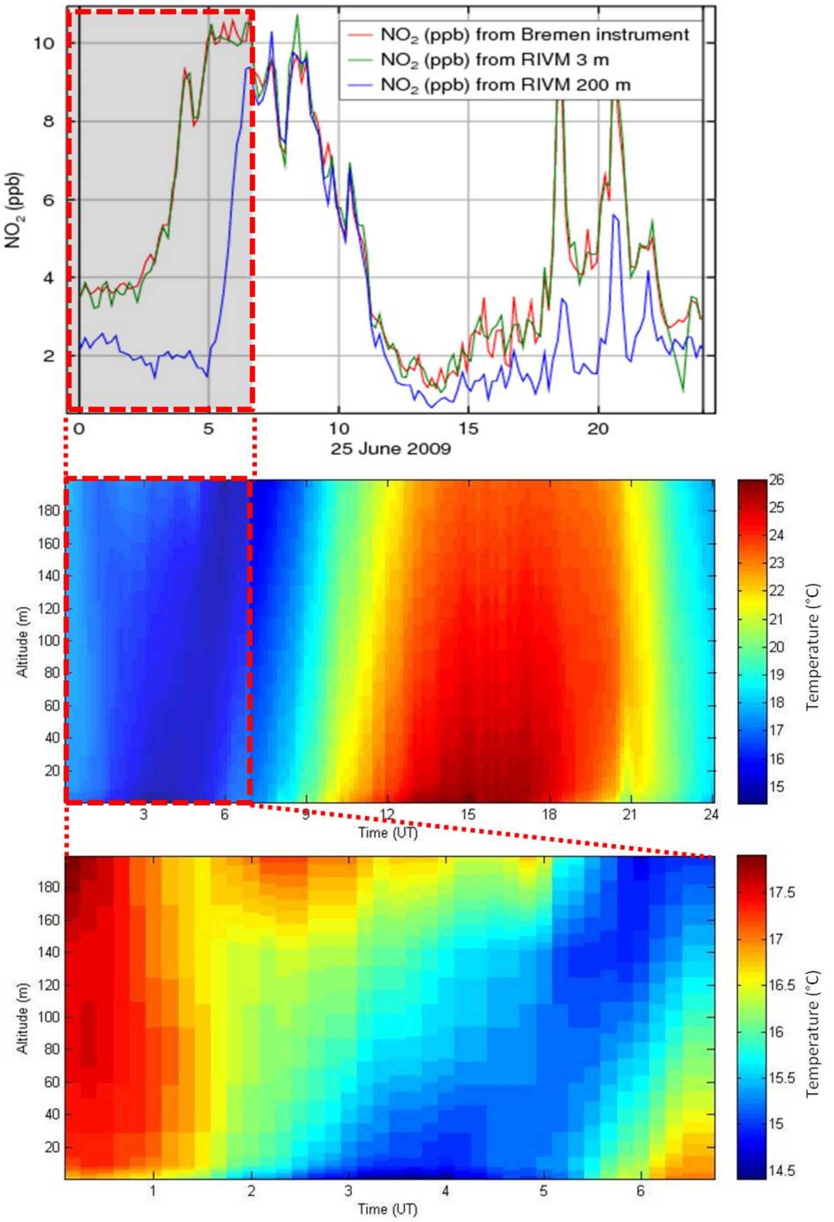

Figure 5.7: Top: In situ NO$_2$ measured from RIVM instrument in 200 m (blue line) and from RIVM and Bremen instruments in 3 m (green and red line, respectively) on 25 June 2009. In 200 m, the morning rush hour peak is delayed by a few hours. Middle: Temperature profile derived from measurements at the tower (platforms in different altitudes) for the same day. Bottom: Zoom-in to the temperature profile showing an inversion layer (surface colder than air above) that breaks up around 5 am. Afterwards, the NO$_2$ rises due to convection towards the same level as on the ground.

the NO$_2$ VMR in 200 m is lower than or equal to the ground VMR, because the emission sources are at the surface. Beyond that, the morning rush hour peak is clearly visible in all three data sets, but in 200 m it starts with a delay of several hours. The reason for this behaviour is shown in the middle and bottom pictures, which are vertical temperature profiles derived from measurements on platforms in different altitudes of the meteorological tower. In the early morning hours, the surface temperature is lower than the temperature of elevated air masses (Fig. 5.7, bottom picture). Consequently, the air close to the surface cannot rise, i.e. no convection processes take place and an inversion layer develops. When the morning traffic sets in, the NO$_2$ VMR increases in the surface air, but not above the inversion layer. Around 5 a.m., the surface warms up and the inversion layer breaks up. From then on, NO$_2$ enriched air is transported upwards by convection and the morning rush hour peak is now visible as well in the NO$_2$ in situ measurements performed on top of the tower.

In Fig. 5.8, the influence of the wind direction on the measured in situ NO$_2$ volume mixing ratio is illustrated. The red line is the NO$_2$ volume mixing ratio as measured by the IUP-Bremen in

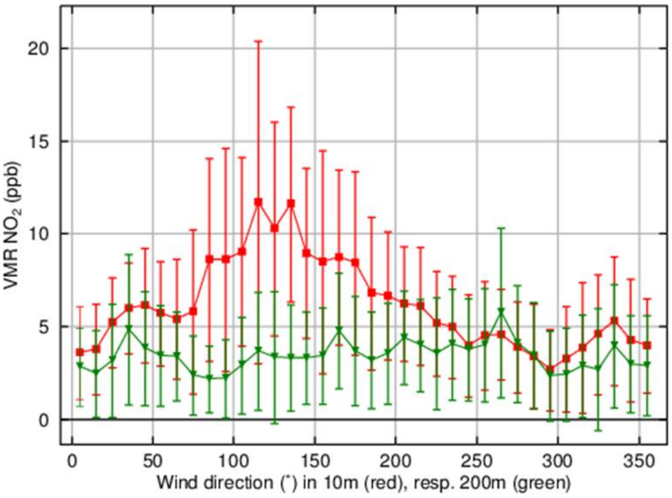

Figure 5.8: Red curve: NO_2 VMR measured by the IUP-Bremen in situ instrument at the surface as a function of wind direction in 10 m. Green: NO_2 VMR measured in 200 m by the RIVM instrument as a function of wind direction in 200 m. NO_2 values have been binned to 10°-steps, the error bars are corresponding standard deviations of the binning procedure.

situ instrument at ground level as a function of the wind direction measured at the meteorological tower in an altitude of 10 m. Enhanced levels occur predominently for wind directions between $70° - 200°$ with a strong maximum at $120° - 130°$. This is roughly the direction of the village of Lopik and the local street in the South of the instrument (see locations and directions in Fig. 5.1, bottom picture). The strong maximum at $120° - 130°$ can be clearly assigned to traffic on the street. If the enhanced values of NO_2 were caused by long-range transports from polluted regions, Fig. 5.2 showing the NO_2 vertical column measured by GOME-2 would suggest highest levels for a wind direction of $\approx 220°$, which is not observed. Consequently, the in situ measured VMR at the ground results from local pollution. This hypothesis is supported by the green line showing the measured NO_2 VMR from the RIVM instrument on top of the tower ($\approx$ 200 m) as a function of the wind direction measured in 200 m. In contrast to the ground level (red line), the NO_2 VMR in 200 m is a) lower, because the emission sources are at the ground, and b) smoother, without any clear maximum at a particular wind direction. If the NO_2 concentration was dominated by non-local pollution, the dependance on wind direction would be the same (at least there would be some for 200 m). To conclude, the Cabauw site shows a background pollution because of its location (compare Fig. 5.2), but the ground concentration variability of NO_2 is dominated by local pollution.

5.3. MAX-DOAS slant column intercomparison

The central part of the CINDI campaign was the semi-blind intercomparison from 15-30 June 2009. For this formal intercomparison period, all groups performed intensive MAX-DOAS measurements in common viewing directions and used common settings for the DOAS analysis that were agreed on in advance. The retrieved slant columns using the standardized settings had to be submitted to a referee[13] before 10:00 a.m. on the following day. The basic idea of the semi-blind intercomparison was that the different groups were not allowed to share their observations with each other except for the referee, who performed comparisons of the measurements and presented anonymized results during every day's afternoon meetings. This prevented that different groups tried to harmonize with each other's results and guaranteed an unbiased intercomparison.

All instruments that were able to perform off-axis measurements pointed in an azimuthal direction

---

[13] Howard K. Roscoe, British Antarctic Survey, Cambridge, UK

Parameter	Settings	Remarks
Spectral range	425-490 nm	Some instruments had to use smaller or UV fit window
O_3	(Bogumil et al., 2003)	223 K
NO_2	(Vandaele et al., 1996)	295 K
O_4	Hermans et al.	http://spectrolab.aeronomie.be/o2.htm
H_2O	(Vandaele et al., 2005), (Rothman et al., 2003)	Using HITRAN 2004
Ring	following (Chance and Spurr, 1997)	
Polynomial	Degree 3-5	IUP-Bremen used 5
Reference (I_0)	Zenith spectrum at noon	Daily
Elevations	2°, 4°, 8°, 15°, 30°, Zenith	Additional angles by Bremen
Azimuth	287° (from North)	Additional angles by Bremen

Table 5.2.: Standardized settings for the DOAS analysis of tropospheric NO_2 and O_4 during the CINDI intercomparison in the visible spectral range.

of 287° (from North, see Fig. 5.1). Measurements were then taken in elevation angles of 2°, 4°, 8°, 15°, 30° and in zenith direction. For the DOAS analysis of NO_2 and O_4 in the visible, which was on focus of the campaign, a fitting window of 425-490 nm was selected, because almost all instruments covered this range (see Tab. 5.1). Considered trace gas absorption cross-sections within this fit were ozone, NO_2, O_4, water vapour and a pseudo cross-section accounting for the Ring effect. To ensure common settings, data files for these cross-sections were provided and had to be used for the intercomparison fit. For the reference (I_0 spectrum in the DOAS analysis), a daily noon spectrum in zenith direction was used. A summary of these standard settings is given in Tab. 5.2.

In spite of the attempt to use settings that could be achieved by every instrument, some instruments were not able to use the standard settings as listed in Tab. 5.2. These instruments had to perform the DOAS analysis in the UV (e.g. GIST) or in a smaller fit window in the visible (e.g. MPI-Mainz). Also not all instruments were able to perform off-axis measurements and instead measured continuously in zenith direction (e.g. SAOZ).

The IUP-Bremen two-channel MAX-DOAS instrument was able to perform the standard DOAS fit in the visible as explained in Tab. 5.2. In addition, its UV-channel participated in the intercomparison of instruments performing the alternative NO_2 fit in the UV. Also HCHO was retrieved in the UV. The new instrument's speed of changing between different viewing angles also allowed measurements in additional elevation angles (to gain profile information, see Sect. 5.4) and azimuthal angles while at the same time a reasonable amount of observations into the standard viewing directions was ensured.

Fig. 5.9 shows exemplarily the NO_2 slant columns retrieved from several participating instruments in 2° elevation angle on July 2 (during the campaign extension, almost all instruments shared their observations with other groups). Although this day was slightly after the official intercomparison, it was one of the best days having excellent viewing conditions. The top picture in Fig. 5.9 is the

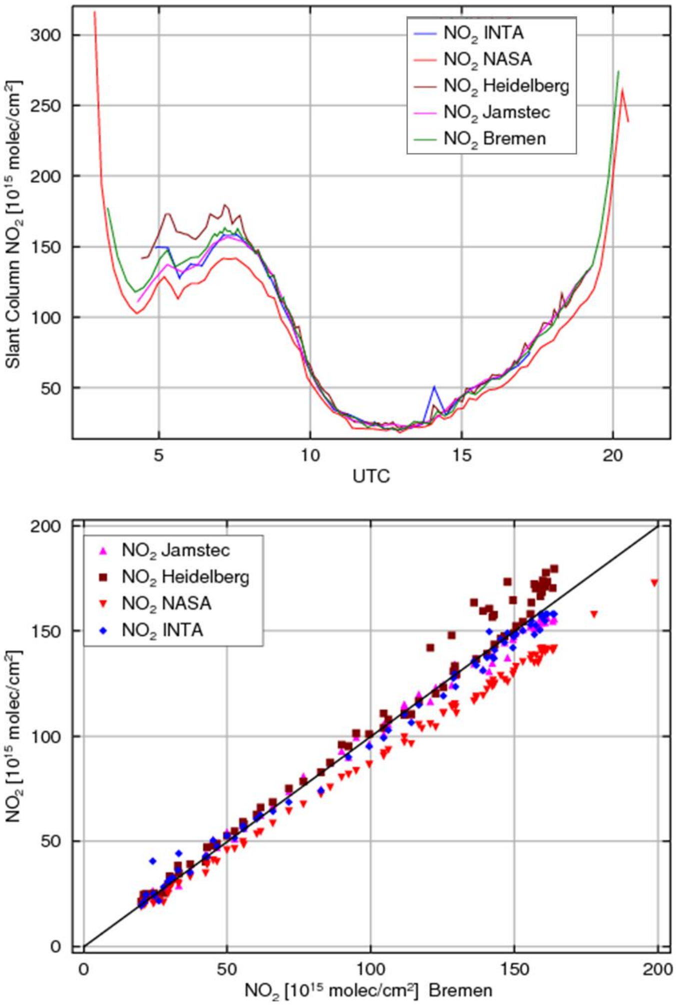

Figure 5.9: NO_2 intercomparison case study. Top: NO_2 slant columns as measured by different groups in an elevation angle of 2° on 2 July 2009 (good viewing conditions). Measurement errors are not shown for better visibility. The large slant columns in the morning and evening are caused by a long light path through stratospheric NO_2 at twilight. The local maximum around 5-10 a.m. is caused by anthropogenic pollution (rush hour, see. Fig. 5.6 and top picture in 5.7). Bottom: Correlation plot of the top picture. Correlation (Slope) between Bremen and JAMSTEC: 0.998 (0.96), Heidelberg: 0.993 (1.06), NASA: 0.999 (0.86), INTA: 0.997 (0.96).

timeseries of the measured slant column. The results of the IUP-Bremen instrument are shown in green, JAMSTEC in pink, Heidelberg in brown, NASA in red and INTA in blue. In general, the shape of the NO_2 slant column timeseries is well reproduced by all instruments. The large values in the morning and evening are a result of the enhanced lightpath in the stratosphere during twilight, i.e. these large values correspond to absorption caused by stratospheric NO_2. The local maximum between 5-10 a.m. results from anthropogenic emissions, i.e. due to tropospheric NO_2. This rush hour peak is also visible in the in situ data (compare Fig. 5.6). In contrast to the MAX-DOAS slant columns, the peak in the in situ data appears earlier with a maximum between 5-6 a.m. instead of 7-8 a.m. as it is seen from the MAX-DOAS instruments. The reason is that the in situ instrument measures the concentration at the surface, whereas the MAX-DOAS measurement is an average along the light path, i.e. an horizontal and vertical average. As the NO_2 is diluted vertically with some time delay (e.g. this was shown by Fig. 5.7), consequently, the maximum (weighted) vertical average appears later as well.

Apart from this good general agreement, differences between the instruments occur most clearly for high values (splitting of the curves during the morning rush hour peak). Nevertheless, even during a disagreement of the absolut value, all instruments observe the same structures, e.g. the small peak at 5.a.m. suggesting a factor between the instruments. In Fig. 5.9, a correlation plot of the top picture is shown (same color-coding). The correlation of the observations with respect to the Bremen slant columns are: 0.998 (JAMSTEC), 0.993 (Heidelberg), 0.999 (NASA) and 0.997

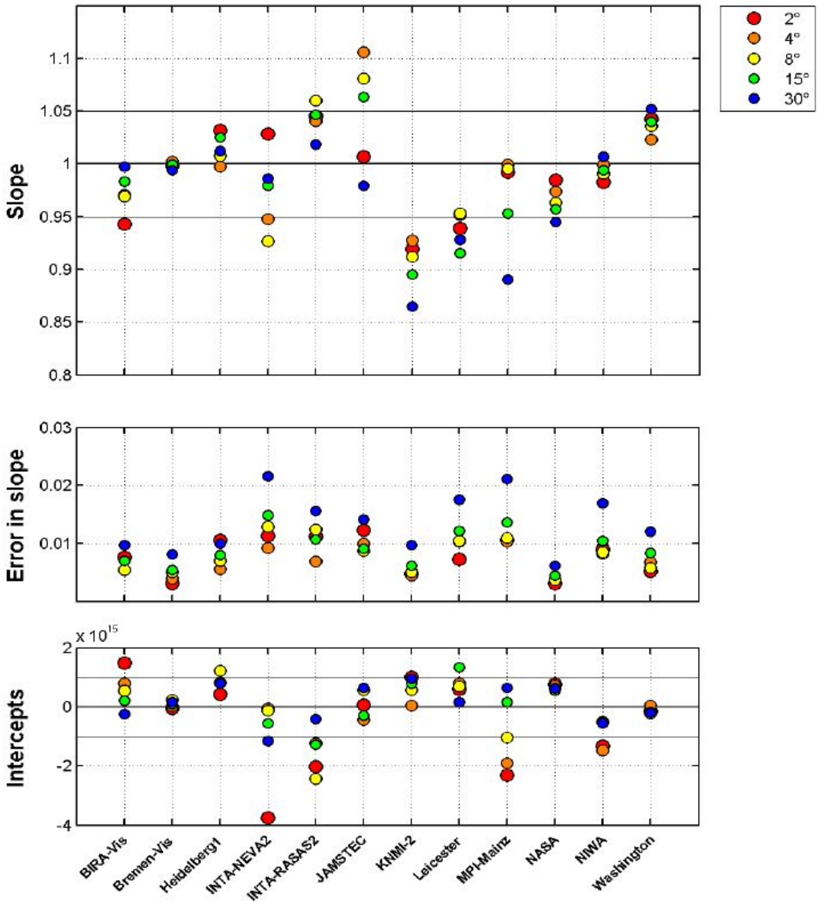

Figure 5.10: Formal intercomparison result for NO_2 retrieved in the visible (425-490 nm, see Tab. 5.2). Image taken from (Roscoe et al., 2010).

(INTA), which is reasonable good. The worst correlation was found for the Bremen-Heidelberg observations, resulting from the outliers around $150 \cdot 10^{15}$ molec/cm^2. These outliers were found later to be caused by a misalignment of the elevation angle of the Heidelberg instrument, i.e. the real correlation is supposedly better. The slopes were found to be (with respect to Bremen): 0.96 (JAMSTEC), 1.06 (Heidelberg), 0.86 (NASA) and 0.96 (INTA). Therefore, the maximum difference is 14%, but most instruments agree within 10% even for this single example day.

A more comprehensive study was done by (Roscoe et al., 2010), where the results of the formal semi-blind NO_2 and O_4 intercomparison are published. For the study presented there, all slant columns from the different instruments throughout the semi-blind period were used and for each instrument a linear regression against a reference data set was performed. This reference data set is composed of the slant columns as measured by the IUP-Bremen, BIRA, INTA-RASA2, NASA, NIWA and Washington, as these were the most consistent instruments.

Fig. 5.10 and 5.11 are taken from (Roscoe et al., 2010). Fig. 5.10 shows the result of the NO_2 intercomparison in the visible range (for fit parameters see Tab. 5.2), Fig. 5.11 is the same for O_4. The top subfigure in both pictures is the slope of the regression line for each instrument with respect to the reference data set and should be close to 1. The subfigure in the middle is the slope's error. The bottom subfigure is the intercept of the regression line, which should be close to 0.

For the NO_2 intercomparison in the visible, the slope in all viewing directions (color-coded data points) of the IUP-Bremen instrument is close to the unity line with corresponding errors < 0.01. The intercept for all viewing angles is close to 0. In comparison to the other instruments in Fig. 5.10, IUP-Bremen shows best performance for this retrieval. Also for the O_4 intercomparison in

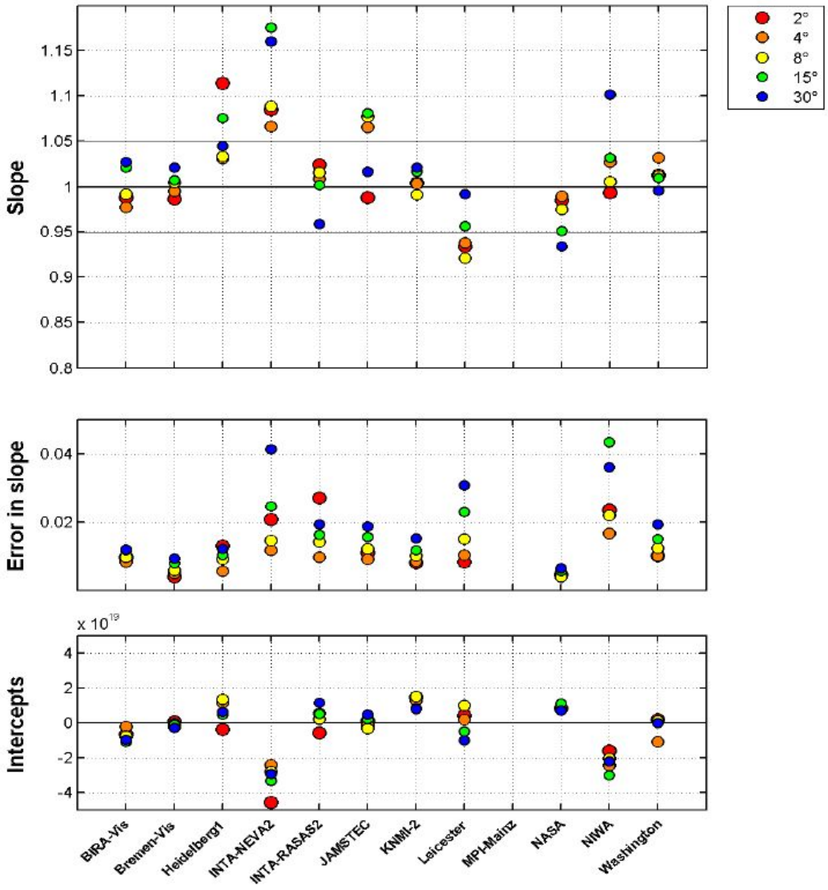

Figure 5.11: Formal intercomparison result for O_4 retrieved in the visible (425-490 nm, see Tab. 5.2). Image taken from (Roscoe et al., 2010).

the visible (Fig. 5.11), the IUP-Bremen instrument prooved excellent performance.

In general, all instruments in Fig. 5.10 agree within 15% on the measured NO_2 slant column, most within 5%. This is close to what has been found already for the case study presented in Fig. 5.9. For the O_4 fit, all instruments agree within 20% (Fig. 5.11), most measurements are within 10%. Further results and details of the alternative UV-fit for NO_2 that have been performed by some instruments can be found in (Roscoe et al., 2010).

In addition to the NO_2 and O_4 intercomparison that was presented above, nine groups participated in an intercomparison of HCHO slant columns that were retrieved in the UV (336.5-359 nm). Details about the fit, sensitivity tests and the slant column intercomparison that was performed similar to the analysis in (Roscoe et al., 2010) can be found in (Pinardi et al., 2013). Again, a reference dataset was created, this time consisting of the slant columns from Bremen, BIRA and INTA instruments. Fig. 5.12 is an image taken from (Pinardi et al., 2013) showing the intercomparison's result. Most instruments agree within an uncertainty of 15% with each other. The excellent performance of the IUP-Bremen instrument is again obvious for the HCHO intercomparison: Its slope is close to 1 and the intercept close to 0 for all viewing angles resulting from a good agreement to the other reference instruments.

5.4. Further results and interpretation

Besides the participation in the intercomparison of slant columns, the IUP-Bremen MAX-DOAS observations during CINDI were used to retrieve tropospheric NO_2 profiles and vertical columns that have been compared to in situ data and satellite observations.

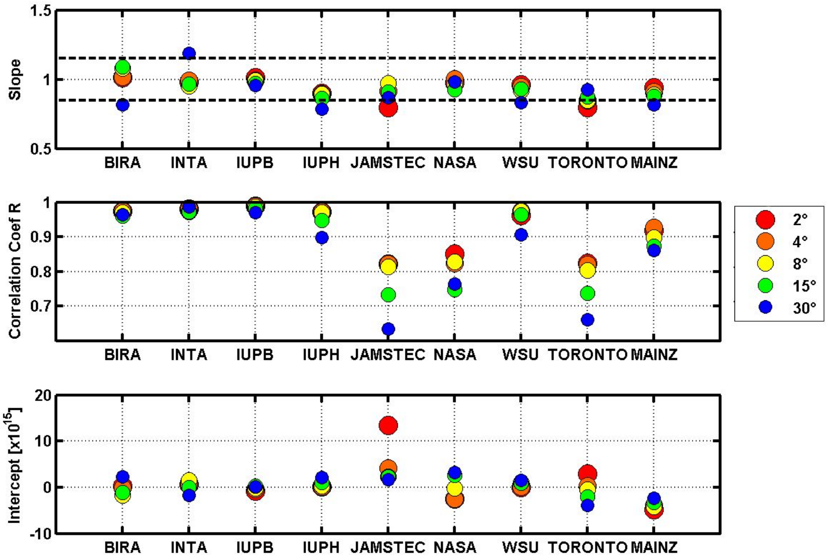

Figure 5.12: Intercomparison results for HCHO in that nine groups participated during CINDI. Image taken from (Pinardi et al., 2013).

5.4.1. Vertical columns: Geometrical approach and profile retrieval

As mentioned before (Sect. 3.5), the resulting slant columns depend on the light path and are not well suited for comparison to other observations (with the exception of MAX-DOAS observations taken under the same viewing condition, e.g. during the intercomparison as presented in Sect. 5.3). Therefore, the slant columns are usually converted into vertical columns, which are no longer the trace gas concentration integrated over the light path, but integrated over altitude, i.e. the vertically integrated profile.

In a first approximation, the slant columns (SC) can be converted into vertical columns (VC) with help of geometrical air mass factors (AMF) according to Eq. 3.56 in Sect. 3.5.1:

$$AMF_{\text{trop}} = \frac{1}{\sin(\alpha)} \tag{5.1}$$

with the elevation angle α. This approximation assumes all NO_2 to be within below the scattering point (for illustration, see Fig. 3.10). To ensure this, only slant columns in an elevation angle of 30° have been used for calculating so-called geometrical vertical columns. In addition, also geometrical vertical columns from measurements in 15° elevation angles have been calculated in order to perform a quality check. For differences $> 20\%$, the corresponding VCs in 30° have been rejected. For 23-25 June 2009, which were *golden days* (see Sect. 5.1), the geometrical vertical columns are plotted (red curve) together with the in situ volume mixing ratio (blue curve) for the same period. The NO_2 diurnal cycle with high values due to anthropogenic emission in the morning and a minimum mostly caused by chemical reaction with OH during the day is obvious in both data sets. Nevertheless, the geometrical vertical columns look *compressed* compared to the in situ data. As already mentioned in Sect. 5.3, this is a consequence of comparing surface values to vertical averages. Whereas the in situ volume mixing ratio at the surface will decrease if a) NO_2 is chemically destroyed or b) vertically diluted by an elevating boundary layer (see also example in Fig. 5.7), the vertical column measured by MAX-DOAS is only sensitive on the true removal of NO_2 from the atmosphere as it is already a vertical average. For illustration, Fig. 5.14 shows the Boundary Layer Height (or Mixing Layer Height, MLH) derived from LIDAR measurements during CINDI. The diurnal cycle in Fig. 5.14 is the average of June 2009. The time of MAX-DOAS measurements,

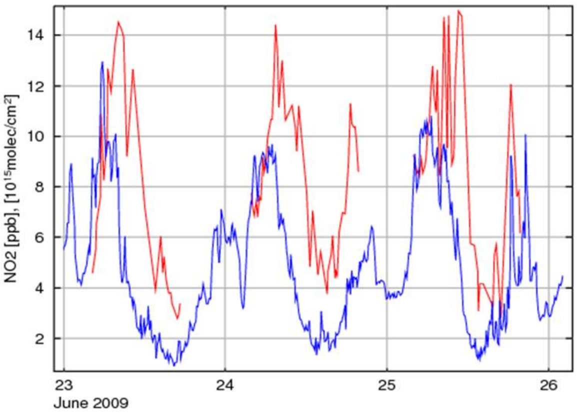

Figure 5.13.: NO_2 in situ volume mixing ratio in ppb (blue) and geometrical vertical columns in 10^{15} molec/cm^2 (red) for 23-25 June 2009 (golden days).

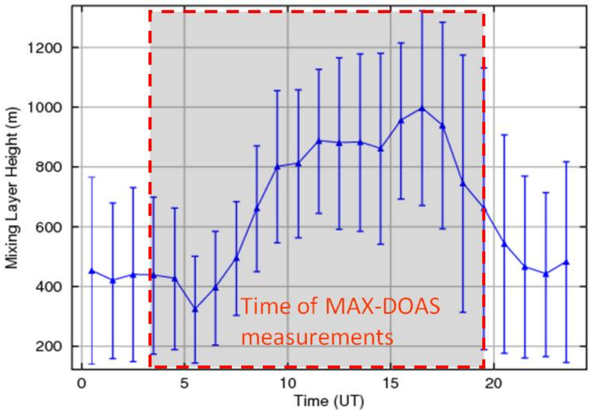

Figure 5.14.: June 2009 average of the mixing layer height as measured by a LIDAR system at the Cabauw measurement site. The red box indicates daytime, i.e. the time of MAX-DOAS observations.

which require daylight, is indicated. While the average MLH in the early hours of MAX-DOAS observations in the morning is ≈ 400 m (with a standard deviation ± 200 m), the MLH increases to 800-1000 m during the day and drops again in the evening. Especially the elevation of the MLH in the morning causes the NO_2 VMR (which is high due to the anthropogenic emission during the rush hour) to dilute vertically and therefore to decrease. This is not seen by the vertical columns, which only decrease due to chemical destruction of NO_2 during the day.

Another limitation of the geometrical vertical columns arises because the NO_2 is not restricted to reside below the scattering point (the geometrical approach forces all NO_2 to be there). In practice, the NO_2 concentration will not drop to zero sharply at the top of the mixing layer height (as it is indicated in Fig. 3.10) and with increasing aerosol load the amount of photons scattered inside the mixing layer increases (destroying the assumption of the geometrical approach).

For a better comparison with in situ data as well as better vertical columns taking into account the whole viewing geometry and aerosol load, the profiling algorithm BREAM has been used. BREAM is explained in detail in Sect. 3.6. The result of BREAM is the trace gas profile of interest on a vertical resolution of 50 m, although the degrees of freedom is usually 2-3, i.e. the profile retrieval is capable to retrieve 2-3 linear independent layers. Therefore, the input parameters (especially the a priori profile) have to be selected with care and as much complimentary data as possible has to be used aiming at an accurate result. For the profile retrieval performed here, the actual[14] mixing layer heights derived from a KNMI Ceilometer that was installed at the Cabauw site have been used to design the apriori profile. Above the MLH, the profile was assumed to decrease exponentially. Below the mixing layer height, a linear trend was assumed. The absolute values of the volume mixing ratios at the surface and at the MLH (fix points of the profile) are scaled multiple times yielding different retrieved profiles. From each retrieved profile, slant columns are calculated in return and the profile whose slant columns fit best to the measured ones is selected. The time steps for the profile retrieval were 0.5 hours.

A comparison between vertical columns calculated with the simple geometrical approach as ex-

---

[14] When the actual value was not available due to frequent data gaps, the average mixing layer height was used instead.

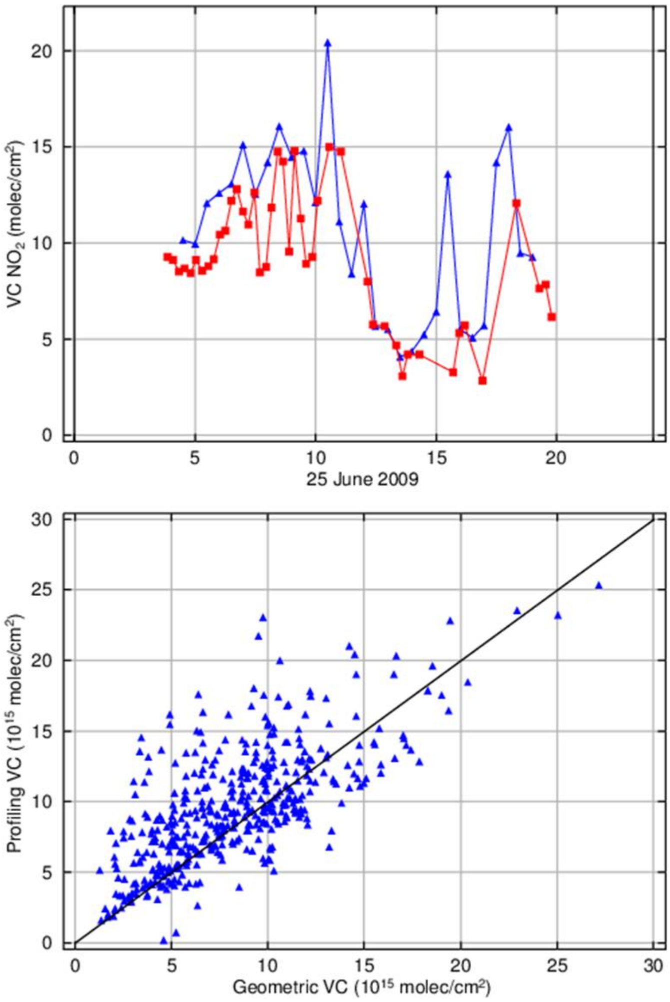

Figure 5.15: Top: Comparison between vertical columns resulting from profile retrieval (blue) and geometrical approach (red) for 25 June 2009. Bottom: Correlation plot between vertical columns from geometrical approach (x-axis) and profile retrieval (y-axis) for the whole campaign. The correlation is ≈ 68%. In black, the 1:1-line is displayed.

plained above and those resulting from profile retrieval is shown in Fig. 5.15. The top picture in Fig. 5.15 shows a case study for 25 June 2009. This was a golden day having excellent viewing conditions, which is essential for a successful profiling (both, geometrical as well as BREAM). The red curve is the geometrical vertical column while the blue curve is the vertical column calculated with BREAM. Both data sets exhibit the same shape and agree even for smaller structures, although some structures are more distinct in one of the data sets. In general, the vertical columns calculated with help of geometrical air mass factors seem lower than those from BREAM. This is supported by the bottom picture of Fig. 5.15 showing a correlation plot between the geometrical vertical columns (x-axis) and the BREAM vertical columns (y-axis) for the whole campaign. For this analysis, the correlation is ≈ 0.68. Most of the data points are located above the 1:1-line meaning that the BREAM vertical columns tend to be larger than the geometrical vertical columns. This is an artifact of the simplified light path that is calculated with more accuracy by BREAM considering the aerosol load, the position of the sun as well as the wavelength. Also the measurement sensitivity in a given viewing direction varies with altitude, which is neglected by the geometrical approach. While BREAM uses measurements in all viewing directions, which are increasingly sensitive towards the surface for small elevation angles, the geometrical approach takes into account only measurements in 30° elevation angle (and 15° for the quality check). As a result, only the vertical column is approximized by the geometrical approach whereas BREAM returns whole trace gas profiles.

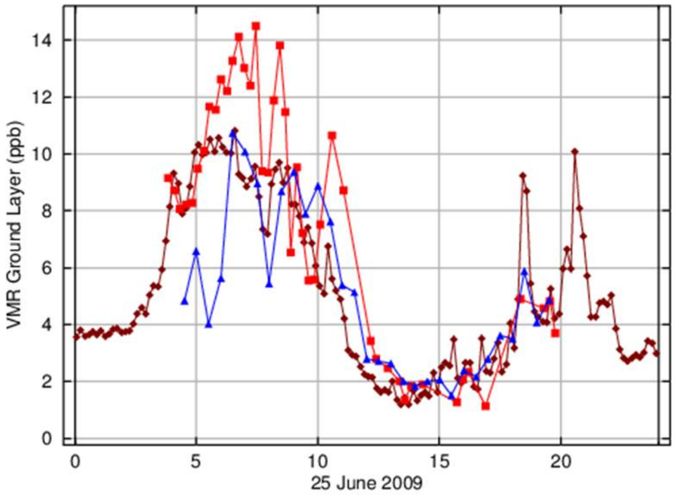

Figure 5.16: Comparison between the IUP-Bremen in situ measurements (10-min averages, brown) and the ground volume mixing ratio retrieved by BREAM (blue) on 25 June 2009. In red is the average VMR calculated according to Eq. 5.2 from geometric VCs.

5.4.2. Comparison to in situ data

For comparison with in situ data, the lowest 200 m of the retrieved profiles from BREAM were averaged. In the following, these values are called the BREAM ground volume mixing ratio. In Fig. 5.16, the BREAM ground VMR for 25 June 2009 is displayed in blue and the IUP-Bremen in situ measurements taken at the meteorological tower in brown (note, that the in situ instrument was measuring day and night, while the MAX-DOAS measurements start at sunrise and stop at sunset as they require daylight). 25 June 2009 was a golden day with good viewing conditions, which is essential for a successful profiling. In addition, a successful profiling needs at least one complete set of measurements taken in different elevation angles. To ensure enough measurements, BREAM calculates one profile each 30 min (the duration of one complete scan is 15-20 min). In contrast, the in situ measurements in Fig 5.16 are given at a finer resolution of 10 min.

The in situ values and the retrieved ground VMR in Fig. 5.16 agree nicely on both, the absolut scale of VMR as well as the shape of the diurnal cycle. Even smaller structures, e.g. the local minimum at 7-8 a.m. and the peak at ≈ 18 p.m. are reproduced by both data sets. The only disagreement is found in the early morning, when in situ values rise while BREAM ground VMR stay low. However, the MAX-DOAS values start to rise after 5-6 a.m. to the same level as the in situ observations. This behaviour is a known issue that has been observed already when comparing in situ observations from the surface to those in 200 m altitude at the meteorological tower on 25 June 2009 (see Fig. 5.7). While the in situ NO_2 level at the surface started to rise in the early morning, the in situ measured NO_2 in 200 m altitude was rising with a delay of a few hours (Fig. 5.7 top picture). The reason for this was an inversion layer in the morning hours that prevents (polluted) air from the surface to rise (Fig. 5.7 middle and bottom pictures). As the BREAM ground volume mixing ratio is the averaged profile in the lowest 200 m, the same behaviour is found.

In addition, also volume mixing ratios for 25 June 2009 have been calculated from vertical columns derived from the simple geometric approach according to

$$VMR = \frac{VC_{\mathrm{geom}}}{\mathrm{MLH}} \cdot \frac{R \cdot T}{p \cdot N_A} \tag{5.2}$$

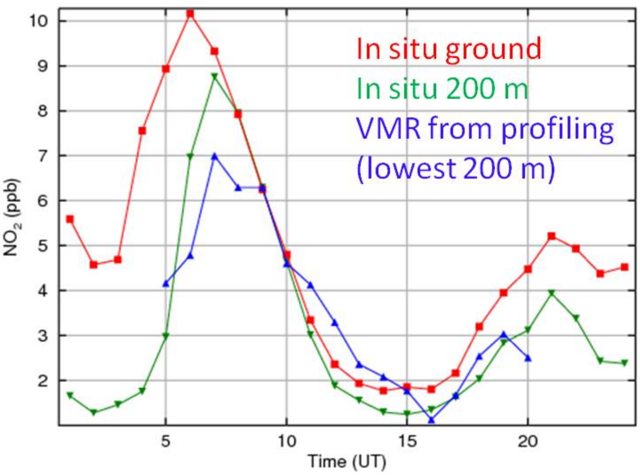

Figure 5.17: 23-25 June 2009 (golden days having good viewing conditions) averages of the IUP-Bremen in situ measurements at the surface (red), the RIVM in situ measurements in 200 m (green) and the ground volume mixing ratio retrieved by BREAM (blue). For better visualisation, all data is binned to 60 min resolution.

where p denotes the pressure at surface level ($1 \cdot 10^5 Pa$), $T = 300K$ is the temperature, R the gas constant and N_A the Avogadro constant. The resulting VMRs are shown as red data in Fig. 5.16. After noon, the calculated VMR values match both, the BREAM ground VMR as well as the in situ values. In contrast, differences up to $\approx$ 40% are observed before noon. This can have two reasons: First, it should be noted that only a few measurements of the MLH exist for 25 June 2009 (most likely due to instrumental problems of the Ceilometer). To fill the data gaps, whole campaign averages have been used, as explained above. This leads potentially to wrong volume mixing ratios. However, for the profiling algorithm, the same mixing layer heights have been used. Second, a physical explanation is, that for the geometric approach only the MAX-DOAS measurements in 30° elevation angle are used and according to Eq. 5.2 only an average volume mixing ratio below the mixing layer height is calculated (no NO$_2$ above the MLH). Consequently, this method yields reasonable results when the vertical extent is large and the trace gas is well mixed within the boundary layer. In the morning, when the NO$_2$ is close to the ground where the measurements in 30° direction have low sensitivity, this approach fails.

For the period of several following golden days, 23-25 June 2009, Fig. 5.17 shows in situ data from the IUP-Bremen instrument at the surface (red), from the RIVM instrument in 200 m altitude (green) and the BREAM ground volume mixing ratio (blue). For better visualisation, all data has been binned to 1 hour time steps and displayed without errors. Three general observations can be derived from Fig. 5.17: a) The in situ values at the surface are higher, which can be expected as the emissions are at the surface and the NO$_2$ is diluted when ascending; b) the general shape agrees for all curves, except for the morning inversion layer (this event was not unique for 25 June, but appears on multiple days) and c) the BREAM ground VMR is much closer to the in situ observation in 200 m than to the surface level. This can be expected, as the the BREAM ground VMR is a vertical average. Apart from these general agreements, the first two and the last data points of the BREAM ground VMR seem too low even in comparison with the 200 m in situ observations. The reason for this is unclear, but it is a hint that the profile retrieval is problematic at large sun zenith angles. Also it can be speculated, that prevailing aerosol conditions in the morning and evening (very thin ground layer) might be not well taken into account in the profiling retrieval (for a description of how the aerosol content is considered in the profile retrieval, see Sect. 3.6.2). As a consequence, only retrieved ground volume mixing ratios for $<$ 80° SZA should be regarded as reliable results. In addition, the profiling is only successful on days with clear viewing conditions

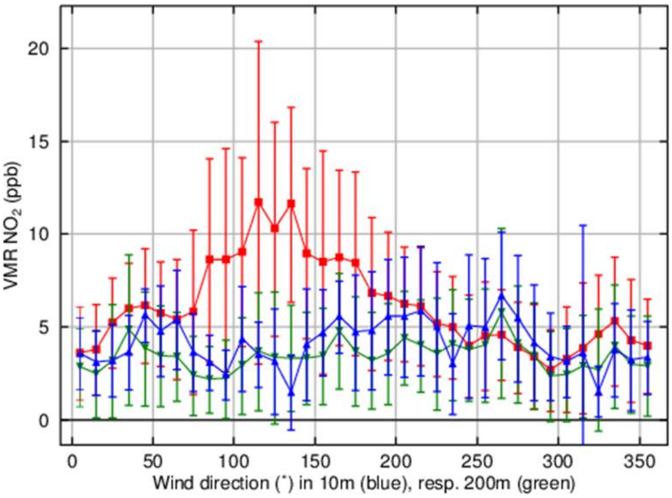

Figure 5.18: Red and green curve: Wind direction dependance of NO_2 VMR measured at the surface, resp. on top of the meteorological tower (see. Fig. 5.8). Blue: Ground volume mixing ratio as retrieved from BREAM as a function of the wind direction in 200 m.

as light path extensions due to clouds or fog cannot be taken into account by the aerosol treatment and the radiative transfer calculations implemented in the profile retrieval.

The influence of the wind direction on the retrieved BREAM ground VMR is shown in Fig. 5.18. Apart from the blue curve, Fig. 5.18 is identical to Fig. 5.8: The red curve is the measured in situ volume mixing ratio at the surface as a function of wind direction in 10 m. Green is the same for 200 m. In addition, the BREAM ground volume mixing ratio is displayed as a function of wind direction (in 200 m) in blue. The similarity between the in situ observations from the top of the tower and the BREAM ground VMR is obvious. As a result, the ground VMR retrieved with BREAM should be regarded as a measure for the trace gas mixing ratio in elevated altitudes ($\approx$ 200 m) rather than the VMR at the surface.

When comparing in situ to MAX-DOAS observations on the time scale of single days, Fig. 5.13 demonstrated that the diurnal cycle of vertical columns does not fit to in situ surface measurements, but the ground VMR derived from the profile retrieval reproduces successfully the in situ measurements, especially in elevated altitudes (Fig. 5.16 and 5.17). As already pointed out, the reason is that in situ observations are sensitive to vertical dilution of NO_2, in contrast to MAX-DOAS vertical columns. However, on the scale of weeks, the variability of NO_2 as observed by in situ measurements coincide even with the variability of MAX-DOAS vertical columns. This is demonstrated by Fig. 5.19 showing the weekly cycle of the NO_2 volume mixing ratio measured by the IUP-Bremen in situ instrument at the surface in black and MAX-DOAS vertical columns (retrieved with BREAM) in red. The data set presented here is composed from all in situ and MAX-DOAS observations taken during the CINDI campaign between 4-19 UT as MAX-DOAS measurements require daylight. At the weekend (Saturday and Sunday, indicated by shaded area), the NO_2 observations reach only 60-70% of their absolute value during working days. This is observed in both, MAX-DOAS as well as in situ measurements. The only disagreement occurs for the Monday value[15]. This could be simply a consequence of bad statistics, as the measurement duration comprised only $\approx$ 6 weeks, which also results in the large standard deviations plotted as error bars in Fig. 5.19. The difference of NO_2 values between the weekend and working days is caused by lower emissions at the weekend. Especially the emission from traffic is lower then because

---

[15] Monday values lower than the working days averages have been observed on some locations already by Beirle et al. (2003) based on GOME measurements. However, here only the in situ results indicate a lower Monday value giving rise to the assumption of simply bad statistics due to the short timeseries.

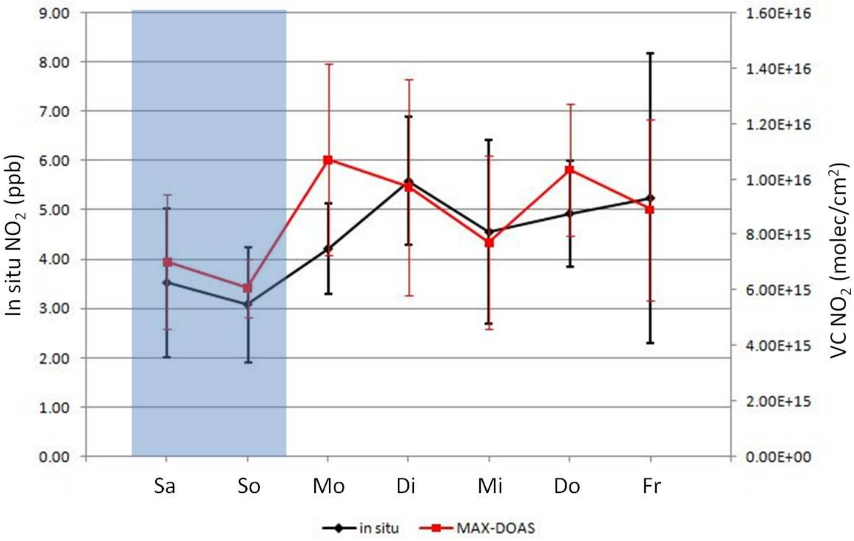

Figure 5.19: Weekly cycle of NO$_2$. In situ observations from IUP-Bremen in black, retrieved vertical columns (BREAM) in red. In order to compare both instruments, only values between 4-19 UT are used as MAX-DOAS requires daylight. During the weekend, lower emissions (no rush hour) cause smaller NO$_2$ values.

of the lack of a rush hour. For the pollution at the Cabauw site this is important as dominating the emission on a regional scale (Sect. 5.2).

5.4.3. Satellite validation of tropospheric NO$_2$ columns

The retrieved tropospheric NO$_2$ vertical columns from MAX-DOAS measurements were used to validate corresponding satellite measurements. An example of satellite observations around Cabauw (on a larger scale) is given in Fig. 5.2, which is a GOME-2 average of the month June 2009. For the location of the measurement site, Fig. 5.2 suggests a vertical column of $1 - 1.5 \cdot 10^{16}$ molec/cm^2 for tropospheric NO$_2$. In general, this is in good agreement to tropospheric NO$_2$ columns derived from MAX-DOAS observations during CINDI (see values in Fig. 5.13, 5.15 and 5.19). However, these figures exhibit a variation of the tropospheric NO$_2$ vertical column of ≈ 200 % during the day (Fig. 5.13, 5.15) and between different days (weekend - working day difference, see Fig. 5.19). Thus, taking into account the exact satellite's overflight time is crucial.

Fig. 5.20 shows the timeseries of tropospheric NO$_2$ vertical columns (blue) as derived from MAX-DOAS measurements using BREAM for the whole CINDI campaign (top picture). Tropospheric NO$_2$ vertical columns from the SCIAMACHY instrument are displayed in red and observations from GOME-2 in green. A description of these satellite instruments was given in Sect. 4.6. For both instruments, pixels were regarded to coincide with the location of the measurement site, if the distance between the center of the pixel and the Cabauw site was < 50 km. If this criterion was fulfilled by more than one pixel, the corresponding pixels were averaged and plotted in Fig. 5.20. The error bars are the standard deviations of the averaging, i.e. pixels without error bar are unique pixels within 50 km around the measurement site.

In general, most satellite columns agree within the range of MAX-DOAS tropospheric columns at the corresponding day. For a better visualisation of the position of satellite values in the diurnal variation of tropospheric NO$_2$, the bottom picture of Fig. 5.20 shows the period of 24 June - 2 July 2009 in more detail. The satellite's overflight time is in the morning at 9:30 - 10:00 local time. On days with excellent viewing conditions, e.g. 25 June and 2 July 2009 (golden days), the satellite values reproduce well MAX-DOAS observations taken at the same time. However, even on days with good viewing conditions, differences of up to 50% are observed (e.g., 24 June 2009).

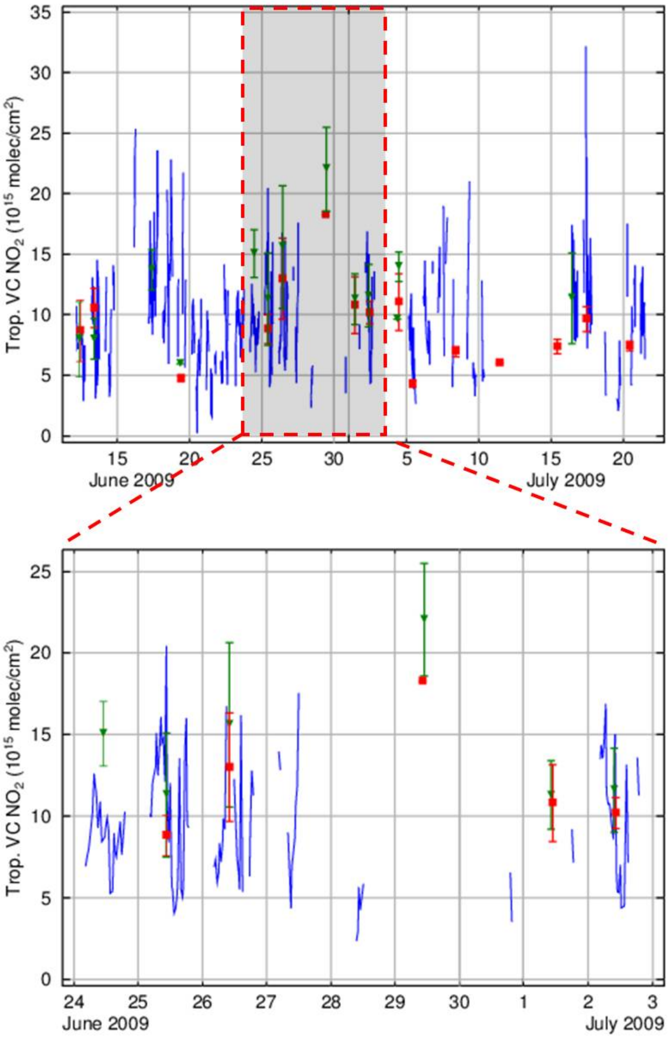

Figure 5.20: Satellite validation of tropospheric NO_2 columns during CINDI. Top: Timeline of retrieved NO_2 tropospheric columns using BREAM in blue. Vertical columns from SCIAMACHY in red, GOME-2 in green. All satellite pixels within 50 km around the Cabauw site (distance between site and center of pixel) were averaged. Bottom: Excerpt from the top picture.

The reason could be strong local pollution that is within the satellite pixel but not in the line of sight of the MAX-DOAS instrument and therefore not detected by it.

As the time period of the CINDI campaign was rather short, only a few direct comparisons between satellite and ground-based MAX-DOAS observations exist (see Fig. 5.20). Using satellite observations within a larger radius around the Cabauw measurement site would increase the number of potential comparisons. But due to the large spatial variability (location at the edge of a highly polluted region, see Fig. 5.2) the agreement between satellite and MAX-DOAS would decrease. Due to the limited number of data points, no reliable statistics could be performed. Nevertheless, some qualitative conclusions can be drawn for the location of Cabauw and the duration of the CINDI campaign:

On days having good viewing conditions, MAX-DOAS and satellite tropospheric NO_2 columns agreed mostly within 50%, often the agreement was much better (25 June, 2 July 2009). Differences (e.g., 24 June 2009) could be caused by local pollution that is within the satellite pixel but not in the MAX-DOAS instrument's line of sight. While in situ instruments measuring NO_2 are sensitive towards local emissions (Sect. 5.2) and contain no vertical profile information, satellite vertical columns are large spatial (and vertical) averages. MAX-DOAS observations contain profile information, which are horizontally averaged along the line of sight (see arrow in Fig. 5.1). As a consequence, MAX-DOAS observations are a link between in situ and satellite observations. For the golden day of 25 June 2009, it was shown that the MAX-DOAS vertical column of tropospheric NO_2 agree with the satellite values at the overflight time (Fig. 5.20, bottom picture) while simultaneously the ground volume mixing ratio derived from MAX-DOAS coincides in shape and absolute value with in situ observations performed close-by (Fig. 5.16).

5.5. Summary

During the Cabauw Intercomparison Campaign of Nitrogen Dioxide measuring Instruments (CINDI), the IUP-Bremen MAX-DOAS instrument with the newly designed telescope unit as well as a commercial NO_2 in situ monitor (chapter 4) participated successfully from 12 June - 20 July 2009. The results of the campaign were published in (Roscoe et al., 2010; Piters et al., 2012; Pinardi et al., 2013). The campaign's focus was a 15 days period of formal semi-blind intercomparison of NO_2 and O_4 slant columns from DOAS instruments (Roscoe et al., 2010). For the standardized DOAS analysis (in the visible spectral range) that was used from all groups during the semi-blind intercomparison, all instruments agreed within 15%, most within 5%. The IUP-Bremen instrument was selected as one of the reference instruments because of it's complete time coverage of observations during the formal intercomparison (reliability) and consistent results in comparison to other reference instruments. In addition, an intercomparison of HCHO slant columns has been performed between nine instruments measuring in the UV. Again, the IUP-Bremen instrument was chosen as one of the reference instruments for the same reasons. Differences of $< 15\%$ were found between most of the instruments (Pinardi et al., 2013).

Apart from the intercomparison, the MAX-DOAS measurements were used for retrieving NO_2 profiles in the troposphere and comparisons to in situ observations and satellite measurements were performed. For days with very good viewing conditions (case study of 25 June 2009), MAX-DOAS is capable to close the gap between satellite measurements averaging over a large area on the one hand and continuous in situ observations at a specific location on the other hand, i.e. the retrieved vertical column is consistent to the satellite observation while at the same time the retrieved ground VMR coincides in shape and absolute value with in situ observations. Nevertheless, it has to be pointed out that very thin layers, e.g. morning inversion layers, are problematic for the profile retrieval and can cause large differences between in situ and ground VMR retrieved from MAX-DOAS. In general, the MAX-DOAS ground VMR is closer to the in situ measurements performed in an altitude of 200 m than to in situ measurements at the surface.

For the satellite comparison, monthly averages of GOME-2 suggest an NO_2 vertical column of $1 - 1.5 \cdot 10^{16}$ molec/cm^2 for the location of the measurement site, which is in general reproduced by MAX-DOAS observations. For a more detailed comparison, the exact satellite's overflight time is crucial as vertical columns from MAX-DOAS exhibit a strong variation during the day and also between different days. On days with good viewing conditions (golden days), the agreement between satellite values and coinciding MAX-DOAS values is often almost perfect (e.g., at 25 June 2009). Nevertheless, occasionally differences of up to $\approx 50\%$ are observed even on days with good weather and clear viewing conditions (24 June 2009), most likely due to pollution that is within the satellite pixel but not in the MAX-DOAS instrument's line of sight. Due to the limited number of coinciding measurements, no quantitative analysis of MAX-DOAS and satellite vertical columns could be performed.

6. Measurements in the Tropics and Subtropics

This chapter describes measurements in the Tropics and Subtropics, that have been performed with the newly designed MAX-DOAS campaign instrument (chapter 4) during two campaigns.

The focus of this thesis is on the *TransBrom* campaign (Sect. 6.1), which was a ship-borne field campaign carried out onboard the german research vessel *Sonne* across the western Pacific from Tomakomai (Japan) to Townsville (Australia) in October 2009. During this cruise, profiles and background concentrations of NO_2 and HCHO have been retrieved and used to validate corresponding SCIAMACHY and GOME-2 satellite measurements. These results have been published in Peters et al. (2012). In addition, IO background concentrations have been retrieved. Part of the TransBrom analysis is also the investigation of spectral effects of liquid water, which is described in chapter 7.

The *SHIVA* campaign (Sect. 6.2) was carried out in November 2011. It was focussed on halogen species and consisted of ground-based, ship-borne as well as air-borne measurements. The IUP-Bremen participated with two MAX-DOAS systems: One instrument was installed again on board the research vessel Sonne going from Singapore to Manila (Philippines), and one instrument was installed in the Tun Sakaran marine park close to Semporna (Malaysian part of Borneo).

6.1. The TransBrom campaign

The TransBrom campaign was organized by the GEOMAR[16] Kiel and carried out onboard the German Research vessel *Sonne*[17] (Fig. 6.1). The ship departed from Tomakomai, Japan (42° 38' N, 141° 37' E) on 9 October 2009 and arrived in Townsville, Australia (19° 15' S, 146°49' E) on 24 October 2009. In Fig. 6.2, the cruise track across the western Pacific is indicated.

Figure 6.1: Photo of the RV Sonne (portside). The instrument's position at the monkey deck during TransBrom is indicated by a red cross. Source: `http://de.wikipedia.org/wiki/Sonne_(Schiff)`.

---

[16] GEOMAR | Helmholtz-Zentrum für Ozeanforschung Kiel, Wischhofstr. 1-3, 24148 Kiel, Germany, web: `http://www.geomar.de/`. Many thanks especially to Birgit Quack and Kirstin Krüger for organizing.

[17] `http://www.bgr.de/fs_sonne/`

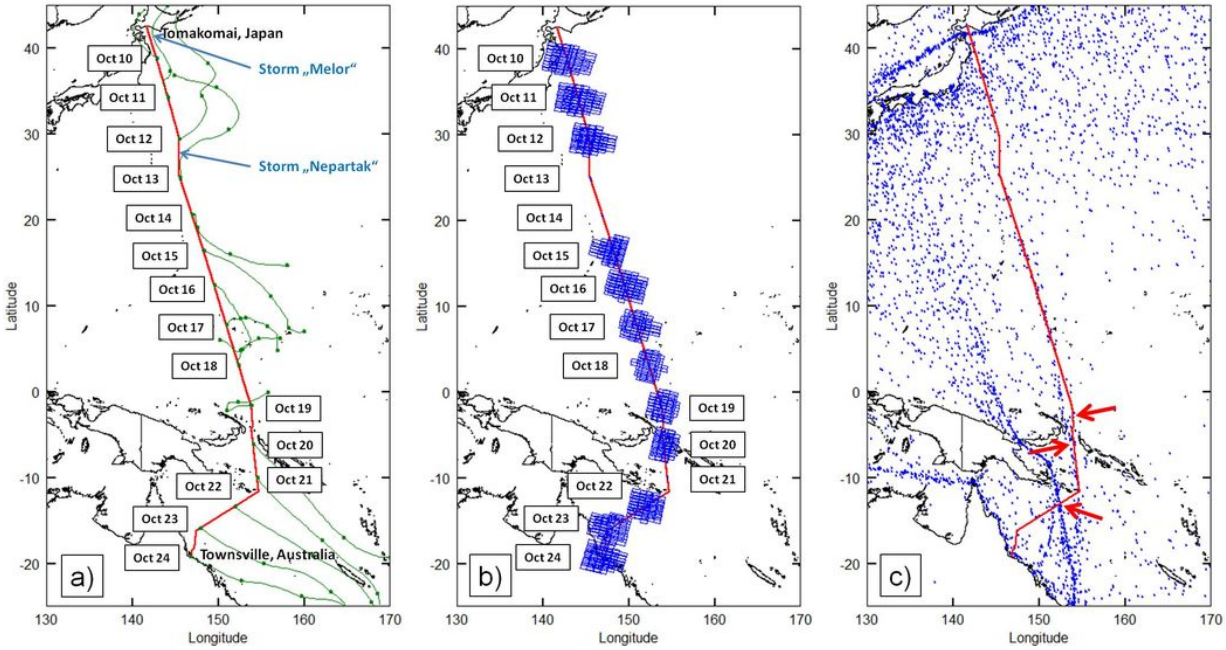

Figure 6.2.: a) TransBrom Cruise Track (red) and 72 h backward trajectories calculated by the NOAA HYSPLIT model (green marks indicate starting point, -1 day, -2 days, -3 days). b) GOME-2 satellite pixels within a radius of 200 km around the ship's positions at the time of the overflight. c) Ship density for October 10-24, 2009 (ship positions reported to the U.S. Coast Guard AMVER System). Source: Peters et al. (2012).

The campaign's main objective were measurements of short-lived bromine compounds in sea water and their transport pathways into the stratosphere. The western Pacific region is considered to be the main entrance gate for trace gases into the stratosphere, i.e. short-lived bromine compounds from oceanic sources possibly reach the stratosphere within their livetimes, where the bromine is released and contributes to stratospheric ozone depletion in catalytic cycles (see Sect. 2.2). An overview about the TransBrom campaign can be found in (Krüger and Quack, 2012).
The IUP Bremen MAX-DOAS instrument participated due to its potential of detecting atmospheric BrO. These measurements indicate that BrO was not present in the troposphere at levels above the estimated detection limit (≈ 1 ppt). However, further objectives of the participation of the Bremen MAX-DOAS instruments were:

- To study stratospheric NO_2 and its latitudinal dependance, as influences from tropospheric NO_2 contributions are small due to its small abundance (see below). Furthermore, corresponding satellite observations are validated.

- To study background concentrations of tropospheric NO_2 and HCHO over the remote ocean and to validate corresponding satellite observations. Both trace gases are emitted predominently over land as explained in Sect. 6.1.3 and 6.1.4 (see also Chapter 2) and extremely low concentrations are expected over the remote ocean. As a ground-based MAX-DOAS instrument provides substantially more sensitivity for tropospheric absorbers (as a light path extension inside the boundary layer can be achieved by applying small elevation angles, see Sect. 3.4.3), it is appropriate to retrieve background concentrations with higher accuracy and to validate satellite measurements.

Table 6.1: Prevailing weather and viewing conditions during the TransBrom cruise from 9–24 October 2009 (Peters et al., 2012).

Period	Conditions
< 10 Oct.	Storm Melor, delayed departure
10 Oct.	Good viewing condition, almost clear sky
11–12 Oct.	Increasingly cloudy
Night after 12 Oct.	Storm Nepartak, course correction
13 Oct.	Heavy rain before noon, clear up in the afternoon
14 Oct.	Best viewing conditions, almost clear sky
15–19 Oct.	partly cloudy and occasionally raining
19 Oct.	Backward trajectories reach to the island of *New Ireland* (closest distance ≈ 150 km in the evening)
20–22 Oct.	Almost full cloud cover, occasional rain
23 Oct. – end	improving weather and viewing conditions, sunny

- Especially to verify possible background concentrations of IO, for which negative columns are retrieved from satellite measurements over clear water surfaces (see Chapter 1).
- To investigate spectral effects of liquid water with respect to the DOAS analysis as these are thought to possible interfere with spectral structures of small absorbers (IO) leading to the observed negative columns. For this study, which is presented in Chapter 7, measurements towards the water surface have been performed as described in Sect. 6.1.1.

In Fig. 6.2a), 72 h backward trajectories are displayed in green, indicating easterly wind directions (i.e. from open ocean) for almost the entire campaign. Even in the Coral sea (21-24 October), air masses from the open ocean were measured. Thus, the results from measurements during TransBrom represent background concentrations for the remote ocean. These backward trajectories, which were calculated with the online model HYSPLIT[18] (Draxler and Rolph, 2011; Rolph, 2011) from the National Oceanic and Atmospheric Administration (NOAA), start 10 km off the ship in the viewing direction of our instrument and at an altitude of 350 m.a.s.l., as this was considered to be a reasonable approximation for the MAX-DOAS probed air at small elevation angles (given an elevation angle of 2° and a horizontal distance of 10 km, the altitude is $\tan(2°) \times 10\text{km} = 350\text{m}$). To illustrate the position of corresponding satellite measurements, Fig. 6.2b) shows GOME-2 pixels taken within a 200 km radius around the ship's position at the time of the overflight (≈ 09:30 LT). Figure 6.2c) shows the position (at 12 UT) of various ships that report continuously their location to the US Coast Guard's Automated Mutual-Assistance Vessel Rescue System (AMVER) (D. Horton, US Coast Guard Operations Systems Center, personal communication, 2010). After leaving the area of enhanced shipping around Japan, the cruise encountered a clean oceanic environment with very limited anthropogenic activities. Red arrows in Fig. 6.2c) indicate locations where tropospheric NO_2 events were observed in the MAX-DOAS data (Fig. 6.7).

The weather condition during TransBrom is summarized in Tab. 6.1. The extratropical storm *Melor* hitting Japan immediately before the campaign delayed the departure and allowed to set up the MAX-DOAS instrument only at sea when wind gusts ceased on 10 October. This day had good viewing conditions and almost clear sky, while 11 and 12 October were increasingly cloudy. A second storm *Nepartak* with wind speeds of 20 m/s forced a course correction in the night from 12 to 13 October. A heavy rain event dominated the morning of 13 October, followed by improving

---

[18] `http://ready.arl.noaa.gov/HYSPLIT.php`

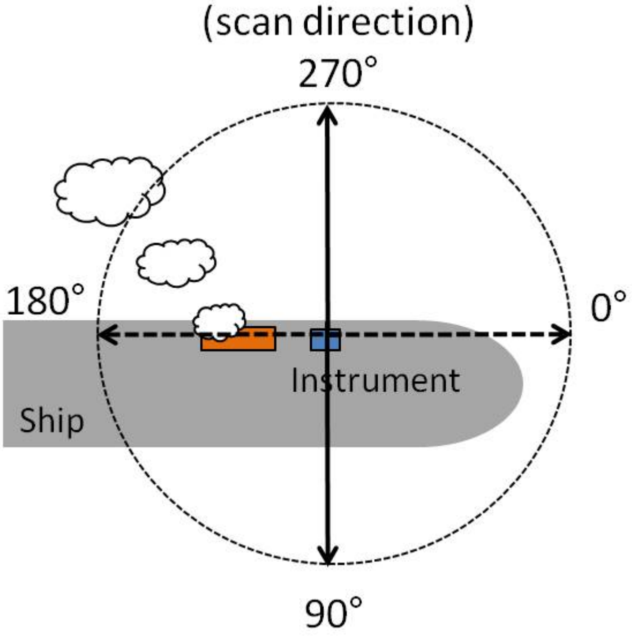

Figure 6.3: Schematic bird's eye view of the vessel (0° is the direction of movement). The grey-shaded area is the ship (seen from above), the orange rectangle the funnel emitting a plume and the blue box the MAX-DOAS instrument. Source: (Peters et al., 2012).

	Azimuth (°)	Elevation (°)
Scan	270	-3 to 6 in 1° steps 8, 10, 15, 30, 90
Water viewing	270, 315	-45, -60
Azimuthal	0, 185, 225, 270, 315	30

Table 6.2: Overview about the instrument's pointing for measurements during TransBrom.

viewing conditions in the afternoon. On 14 October, the ship encountered best viewing conditions and almost clear sky. 15-19 October were partly cloudy with some rain events. Apart from the beginning of the cruise, 19 October was the only event when 72 h backward trajectories reached to mainland (here: the island of New Ireland). An almost full cloud coverage was dominating 20-22 October, again with occasional rain events. Towards the end of the cruise (approaching Australia), the viewing conditions improved again.

6.1.1. Measurements and data analysis

The IUP-Bremen MAX-DOAS instrument was identical to the one participating at CINDI a few months before (see Chapter 5 and Chapter 4 for a description of the instrument), i.e. consisting of a telescope unit, a y-shaped optical fibre bundle and two spectrometers covering the UV and the visible wavelength range (see specifications in Tab. 4.1).

The MAX-DOAS telescope unit was mounted on the monkey deck above the bridge of the RV Sonne (red cross in Fig. 6.1, an image of the telescope can be also found in Fig. 4.6) looking portside. For most of the cruise, this was an easterly direction as the ship moved straight from north to south (see Fig. 6.2a). The spectrometers were installed at the scientific bridge of the RV Sonne (the deck below the telescope) and connected to the telescope unit via an optical fiber-bundle (the MAX-DOAS system is described in detail in chapter 4).

A schematic top view of the ship and the azimuthal measurement direction is provided in Fig. 6.3. Orthogonally to the ship's movement, i.e. in the 270° azimuthal direction (see Fig. 6.3), vertical

Parameter	Settings	Remarks
NO_2 (tropospheric and stratospheric)		
Reference	Zenith (trop: closest) Zenith (strat: fixed)	11 October: 30° elevation
Spectral range	450 - 497 nm	
Polynomial	3rd order	
Straylight corr.	Offset	
O_3	(Bogumil et al., 2003)	at 223 K
NO_2	(Vandaele et al., 1996)	294 K for tropospheric fit and 220 K stratospheric NO_2 fit
O_4	Hermans et al.	`http://spectrolab.aeronomie.be/o2.htm`
water vapour	HITRAN2009	`http://www.cfa.harvard.edu/hitran/`
Ring	SCIATRAN simul.	(e.g., Vountas et al., 1998)
HCHO		
Reference	Zenith	Daily spectrum at 45° SZA
Spectral range	335 - 357 nm	
Polynomial	4th order	
Straylight corr.	Offset	
O_3	(Bogumil et al., 2003)	223 K and 273 K
NO_2	(Vandaele et al., 1996)	220 K
O_4	Hermans et al.	`http://spectrolab.aeronomie.be/o2.htm`
HCHO	(Meller and Moortgat, 2000)	297 K
BrO	(Fleischmann et al., 2004)	223 K
Ring	SCIATRAN simul.	(e.g., Vountas et al., 1998)

Table 6.3.: DOAS fit parameters for the NO_2 and HCHO fit during TransBrom.

scanning sequences were performed. These vertical scans consist of measurements from -3° to 6° elevation angle in 1° steps and additionally in 8°, 10°, 15° and 30°. At the end of each scanning sequence, a zenith measurement was recorded. In addition to the scanning sequence, measurements in 30° elevation and different azimuthal directions were performed as well as measurements in different angles towards the water surface (these measurements are discussed in chapter 7). An overview about the performed pointing directions is given in Tab. 6.2.

The exposure time for all measurements was 100 ms, which is short enough to neglect movements (rolling) of the ship during this time. In off-axis directions the integration time (period in that measurements are taken before the telescope moves to the next viewing angle) was 40 s. In zenith direction, an integration time of 120 s was applied.

The adjusted pointing direction of the telescope was relative to the ship. As the ship moves (rolls) in the sea, these adjusted directions were not the actual ones, but overlayed by the ship's changing roll angle. Therefore, the ship's heading, pitch and roll angles were recorded every 50 ms and

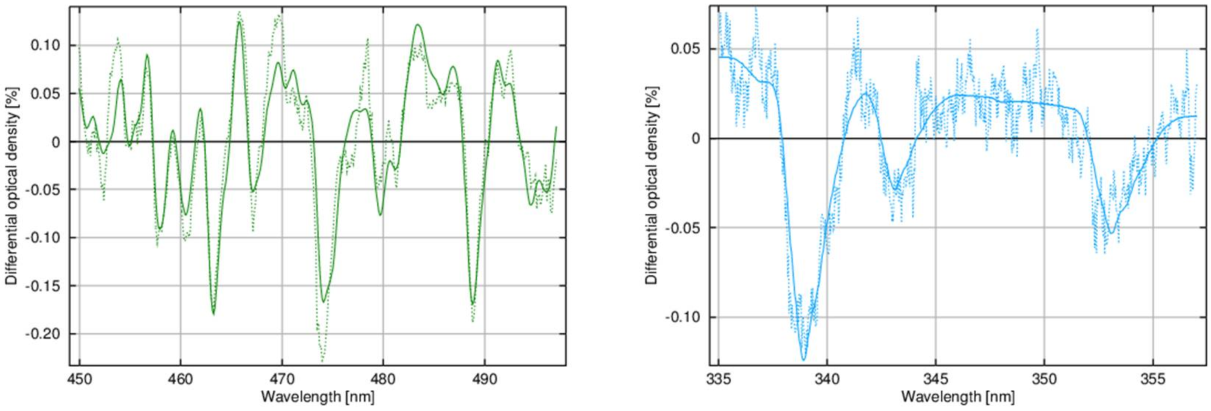

(a) Tropospheric NO_2

(b) HCHO

Figure 6.4.: Example fits for tropospheric NO_2 in green (slant column 1.38×10^{16} molec/cm^2 RMS 2.8×10^{-4}) and HCHO in blue (slant column 2.82×10^{16} molec/cm^2 RMS 1.6×10^{-4}) from 10 October 2009 (03:24 UT, 47.6° SZA, 2° viewing angle). The solid line is the scaled cross-section (with the scaling factor being the slant column) and the dashed line is the fit (scaled cross-section plus fit residual). Source: (Peters et al., 2012).

downloaded from the ship's data base at the end of the cruise. Then, for each single 100 ms measurement the real viewing direction, i.e. adjusted angle plus ship's roll, was calculated (during the exposure time of 100 ms, the movement can be neglected). Using these corrected angles, in each scanning sequence the single 100 ms measurements were grouped to real viewing directions with a tolerance of ±0.5°. Finally, all measurements assigned to a specific viewing angle (i.e., all single measurements ±0.5° around this viewing angle) were averaged. As a result, the pointing precision is ±0.5°, but the time resolution is reduced to the duration of one scanning sequence, which was typically 10-15 min.

As indicated in Fig. 6.3, the telescope unit was installed close to the ship's funnel and the exhaust plume potentially contaminates the measurements for *bad* wind directions, which are relative wind directions between ≈80° and 270° (with respect to the ship's bow). Therefore, the relative wind direction was recorded from the ship's weather surveillance systems and those single (100 ms) measurements taken at *bad* wind directions were rejected before being averaged.

The parameters for the DOAS fit of NO_2 - according to Richter (1997) - and HCHO - following Heckel et al. (2005) and Pinardi et al. (2013) - are summarized in Tab. 6.3, corresponding fit examples are displayed in Fig. 6.4. These trace gases could be clearly identified and corresponding measurements of SIAMACHY and GOME-2 were performed. In contrast, the retrieval of IO over the remote ocean was much more challenging and is subject of Sect. 6.1.5.

To obtain stratospheric vertical columns of NO_2, slant columns between 88° and 92° SZA were divided individually by air mass factors (calculated with SCIATRAN 2.2) and subsequently averaged. As input parameters for SCIATRAN, pressure, temperature and trace gas profiles from the US standard atmosphere were used. The retrieval of stratospheric NO_2 columns is explained in detail in Sect. 6.1.2.

Tropospheric vertical columns and profiles of NO_2 and HCHO were obtained from slant columns in different off-axis directions using the profile retrieval BREAM. The profile retrieval was explained in Sect. 3.6. BREAM has been already used for the analysis of the CINDI campaign (see Chapter 5).

During TransBrom, the background levels of tropospheric NO_2 and HCHO over the remote ocean are assumed to originate mainly from lightning events and methane oxidation, respectively, and therefore both trace gases are not strictly linked to the boundary layer (BL). Thus, no block-profiles (as in CINDI) but volume mixing ratios decreasing linearly with altitude were used as a priori profiles in the optimal estimation. Retrieved profiles and corresponding a priori profiles are shown exemplarily for NO_2 and HCHO in Figs. 6.11 and 6.17, respectively, together with corresponding averaging kernels.

The MAX-DOAS measurements during TransBrom have been used to validate corresponding satellite measurements of the SCIAMACHY and GOME-2 instruments (Sect. 4.6). Therefore, the following scientific data products as explained in Peters et al. (2012) from IUP-Bremen have been used:
For the SCIAMACHY satellite retrieval of NO_2, a fitting window from 425–450 nm was applied. For the stratosphere, only the stratospheric AMF was used and no correction for clouds or the troposphere has been taken into account. For the troposphere, only pixels with < 0.2 cloud coverage were considered (FRESCO+) (Wang et al., 2008) and a tropospheric AMF based on a MOZART NO_2 profile climatology was used. A reference sector (longitude 180°–210°) was subtracted to correct for the stratospheric NO_2 content. The applied DOAS fit settings are explained in detail elsewhere (Richter et al., 2005).
For the GOME-2 retrieval of NO_2 similar settings were used, but an extended fitting window from 425–497 nm was applied (Richter et al., 2011).
For the HCHO retrieval from GOME-2 a fitting window from 337–353 nm was applied (Vrekoussis et al., 2010).

6.1.2. Stratospheric NO_2

The following analysis of stratospheric NO_2 was performed as part of this thesis and has been successfully published in Peters et al. (2012):
"In the stratosphere, NO_2 undergoes a diurnal cycle due to photolysis of N_2O_5 causing NO_2 to increase during the course of the day, e.g. a recent study found an increase of 6×10^{13} molec/cm^2/h for the subtropics (Gil et al., 2008). The N_2O_5 is build up at night from the reaction of NO_2 with O_3 and subsequent reactions (Brasseur et al., 1999). As a result of this diurnal cycle, the content of NO_2 in the reference measurement cannot be obtained using a simple Langley plot, as it requires constant conditions during the day. Therefore, a fixed reference measurement was used for the whole campaign taken on 14 October a.m. (latitude 20.5° N), as this was the period with best weather and viewing conditions and the region is representative for open ocean conditions with negligible tropospheric NO_2 content (see Sect. 6.1.3 and Fig. 6.7). The SCIAMACHY and GOME-2 (interpolated) data imply a vertical column of about 1.9×10^{15} molec/cm^2 for this day at their overflight times (10:00 LT and 09:30 LT, respectively) when the MAX-DOAS performed measurements at 40° SZA. Consequently, the slant column of this reference measurement was estimated to be

$$SC_{\mathrm{ref}} = \mathrm{AMF} \cdot VC_{\mathrm{ref}} \approx \frac{1.9 \times 10^{15}}{\cos(40)} \approx 2.5 \times 10^{15}\ \frac{\mathrm{molec}}{\mathrm{cm}^2} \tag{6.1}$$

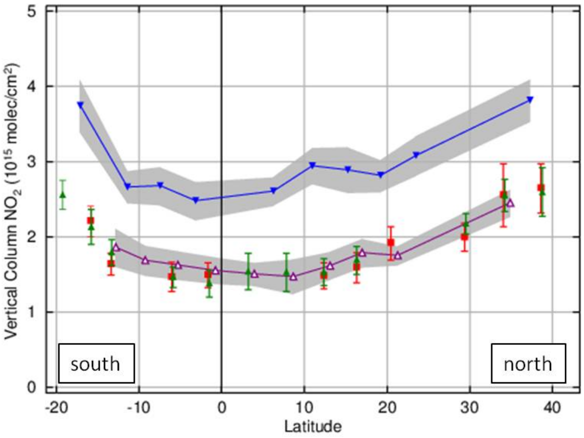

Figure 6.5.: Stratospheric NO_2 vertical columns as a function of latitude, MAX-DOAS morning values in magenta, evening values in blue (grey-shaded area indicates error margin), GOME-2 satellite values are displayed in green, SCIAMACHY satellite values in red (see text). Source: (Peters et al., 2012).

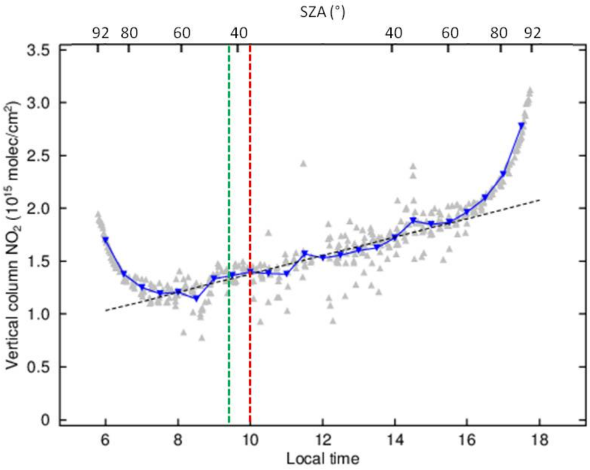

Figure 6.6.: Diurnal cycle of stratospheric NO_2 vertical columns on 15 October 2009 (grey: single measurements, blue: data binned to 0.5 h resolution). The black dashed line is the derived daytime linear increase, the green dashed line gives the approximate GOME-2 overpass time and the red line the SCIAMACHY overpass. Source: (Peters et al., 2012).

This reference SC was added to daily twilight measurements taken between 88° and 92° SZA and calculated airmass factors (see Sect. 6.1.1 and Sect. 3.5.1) were used to obtain vertical columns that were averaged for a.m. and p.m., respectively, and plotted in Fig. 6.5. An uncertainty of 30% of the reference vertical column would correspond to $\approx 0.7 \times 10^{15}$ molec/cm^2 in the reference slant column, which is added to the twilight measurements. With an airmass factor of ≈ 18 for measurements taken at 90° SZA this would lead to an uncertainty of 0.04×10^{15} molec/cm^2, which is negligible (compared to values in Fig. 6.5). The tropospheric NO_2 column across the ocean is even lower than 0.7×10^{15} molec/cm^2 (see Sect. 6.1.3) and has therefore been neglected.

As described in Sect. 6.1.1, for practical reasons the US standard atmosphere was used to calculate airmass factors. This is an approximation, because the true stratospheric NO_2 profile is unknown. Furthermore, the NO_2 changes rapidly during twilight due to photochemistry, i.e. its profile is a function of SZA. As a consequence of the curvature of the earth and the drastically extended light path during twilight, the photons experience different NO_2 profiles coupled to the local SZA on their way through the stratosphere. This can be considered by applying the actual NO_2 concentrations for each point of the light path, which are derived from a photochemical model (e.g., Hendrick et al., 2006, and references therein). Nevertheless, for a tropical scenario and SZAs between 89° and 91°, Gil et al. (2008) showed that the difference between airmass factors calculated with the standard atmosphere and more accurate airmass factors using profiles from a climatology is in the order of 5%. This is in the range of errors in Fig. 6.5. To account for the effect of unknown NO_2 profiles and other potential error sources related to the radiative transfer modelling, the airmass factors used for converting slant columns into vertical columns as described above were changed (arbitralely) by 1. Then, vertical columns were calculated again and the differences to the original results are used as error margin.

In Fig. 6.5 the stratospheric NO_2 vertical columns (a.m. and p.m. values) from MAX-DOAS are

Day	Latitude	MD a.m.	MD p.m.	SCIA	GOME-2	$\Delta_{\text{MD-SCIA}}$	$\Delta_{\text{MD-GOME-2}}$	Δ_{Sat}
10 Oct.	38.29	-	3.82	2.65	2.60	-	-	0.05
11 Oct.	33.70	2.45	-	2.56	2.55	-0.11	-0.1	0.01
12 Oct.	28.98	-	-	2.00	2.18	-	-	-0.18
13 Oct.	24.47	-	3.08	-	-	-	-	-
14 Oct.	20.26	1.75	2.81	1.92	-	-0.17	-	-
15 Oct.	16.05	1.79	2.89	1.59	1.69	0.2	0.1	-0.1
16 Oct.	12.01	1.62	2.94	1.49	1.54	0.13	0.08	-0.05
17 Oct.	7.41	1.47	2.61	-	1.54	-	-0.07	-
18 Oct.	2.73	1.50	-	-	1.54	-	-0.04	-
19 Oct.	-1.98	1.55	2.48	1.49	1.38	0.06	0.17	0.11
20 Oct.	-6.46	1.62	2.68	1.47	1.47	0.15	0.15	0
21 Oct.	-10.34	1.68	2.66	-	-	-	-	-
22 Oct.	-13.53	1.86	-	1.64	1.79	0.22	0.07	-0.15
23 Oct.	-16.06	-	3.75	2.21	2.13	-	-	0.08
24 Oct.	-19.25	-	-	-	2.56	-	-	-
mean all						0.068	0.045	-0.026
stdv						± 0.152	± 0.102	± 0.102

Table 6.4.: Stratospheric NO_2 vertical columns as observed from MAX-DOAS (MD), SCIAMACHY and GOME-2 (see also Fig. 6.5). All values are given in 10^{15} molec/cm^2. $\Delta_{\text{MD-SCIA}}$ is the difference between the MAX-DOAS a.m. and the SCIAMACHY value of the corresponding day ($\Delta_{\text{MD-GOME-2}}$ accordingly) and Δ_{Sat} is the difference between the satellite instruments. The last two rows give the mean and the standard deviation of the differences. As all observations differ in time and location from each other, the latitude (2nd column) is only an approximate value corresponding to the ship's location at noon (12 h) local time. Source: (Peters et al., 2012).

displayed as a function of latitude (see also Fig. 6.2 for the cruise track) in comparison to GOME-2 and SCIAMACHY satellite values. GOME-2 satellite pixels were averaged within a 200 km radius around the ship's position at the overflight time (for the location of GOME-2 satellite pixels being averaged, see Fig. 6.2b). For the SCIAMACHY instrument, averages within a 400 km radius were calculated to account for its sparser spatial coverage. All vertical columns shown in Fig. 6.5 are summarized in Tab. 6.4.

Both, the MAX-DOAS a.m. and p.m. values as well as the satellite values show a characteristic U-shape with latitude. MAX-DOAS a.m. values range from 2.3×10^{15} molec/cm^2 at 35°N to 1.3×10^{15} molec/cm^2 across the Equator and increase to 1.8×10^{15} molec/cm^2 at 13°S (note that especially at the beginning of the cruise values are missing due to instrumental problems and data with *bad* wind directions that were removed). MAX-DOAS p.m. values slowly decrease from 3.8×10^{15} molec/cm^2 at 38°N to 2.5×10^{15} molec/cm^2 at the equator and increase again to 3.8×10^{15} molec/cm^2 at 19°S. This general shape is in good agreement with results from a previous campaign performed in the Atlantic ocean (Kreher et al., 1995) while absolute values seem to be slightly smaller.

Figure 6.6 shows exemplarily the diurnal cycle derived from MAX-DOAS measurements on 15 October 2009 (latitude 16.4°N). For this figure, AMFs have been calculated not only for measurements between 88° and 92° SZA, being most sensitive to stratospheric absorbers due to the long light path in the stratosphere, but for all measurements. The sensitivity decreases rapidly for small

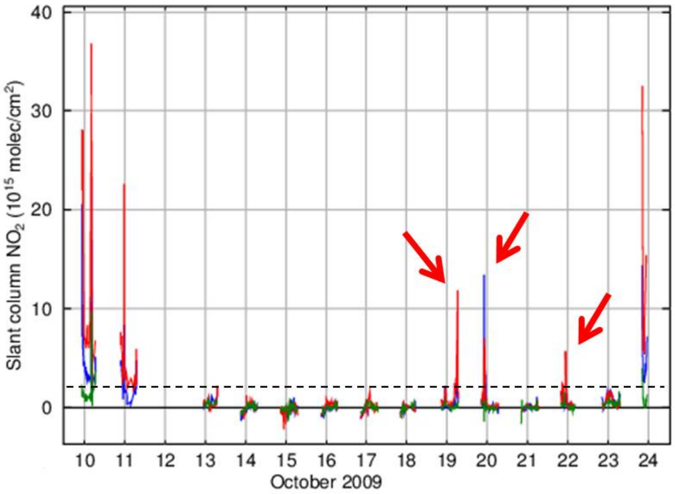

Figure 6.7: Color-coded tropospheric NO_2 slant columns (red = 2°, blue = 8°, green = 30° viewing direction). The dashed line indicates the estimated detection limit. The red arrows marking three NO_2 events over the remote ocean correspond to the red arrows in Fig. 6.2c indicating the ship's position during these events. Source: (Peters et al., 2012).

SZAs since the light path through the stratosphere diminishes. Consequently, the variance in retrieved NO_2 columns (grey data points in Fig. 6.6) increases. In order to increase the number of measurements yielding better statistics, all viewing directions $> 5°$ elevation angle were considered to contain only stratospheric NO_2 signals. This is a reasonable assumption as 15 October 2009 had open ocean conditions with negligible tropospheric NO_2 content (see Sect. 6.1.3 and Fig. 6.7). The resulting vertical columns (grey data points in Fig. 6.6) have been binned to 0.5 h steps (blue data points). After the a.m. value (88°-92° SZA average), the stratospheric NO_2 columns decrease towards a minimum and increase afterwards, reproducing the a.m. value around noon. A linear regression between 07:00 LT and 16:00 LT yields a slope of about $(8.7 \pm 0.5) \times 10^{13}$ molec/cm^2/h (indicated by the black dashed line). Consequently, the satellite values in Fig. 6.5 should be $\approx 1.7 \times 10^{14}$ molec/cm^2 lower than MAX-DOAS a.m. values due to their overflight time, which is slightly more than observed but in agreement with most of the observations considering the error bars (see Fig. 6.5). At the beginning of the campaign, on 10 and 11 October 2009 (latitudes 38.7° and 34.1°N), the satellite pixels considered for the comparison include areas over or close to Japan (Fig. 6.2b), a region of high anthropogenic pollution, meaning that polluted pixels may affect the satellite averages.

For the whole dataset shown in Fig. 6.5 (see values in Tab. 6.4), SCIAMACHY and GOME-2 agree with each other within their standard deviations resulting from spatial averaging (error bars of satellite data). The mean difference between the satellite instruments for this analysis is $(0.26 \pm 1.02) \times 10^{14}$ molec/cm^2 (corresponding to $\approx$ 1–1.7% of the vertical column). While reproducing the same latitudinal shape as the MAX-DOAS data, SCIAMACHY is on average $(0.68 \pm 1.52) \times 10^{14}$ molec/cm^2 and GOME-2 $(0.45 \pm 1.02) \times 10^{14}$ molec/cm^2 lower than the MAX-DOAS a.m. values, as a consequence of the stratospheric NO_2 diurnal cycle as discussed above."

6.1.3. Tropospheric NO_2

The following analysis of tropospheric NO_2 was performed as part of this thesis and has been successfully published in Peters et al. (2012):

"At low latitudes, the large concentration of water vapor in the humid air above the warm ocean's surface potentially limits the accuracy of the MAX-DOAS measurements as small misfits of H_2O would dominate the DOAS fit residual. This has been seen under similar conditions by Takashima et al. (2011)

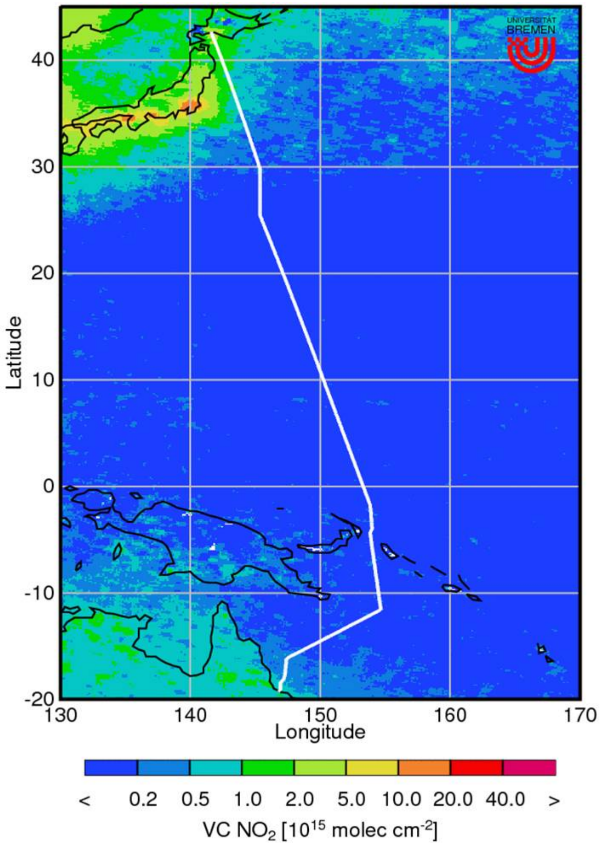

Figure 6.8: October 2009 monthly average of tropospheric NO_2 from GOME-2 (scientific product from Institute of Environmental Physics, University of Bremen). The Cruise Track is indicated by the white line. After the first days, having influences from Japan, a region of pure NO_2 background concentration is encountered.Source: (Peters et al., 2012).

where it is discussed in detail. Here we could avoid this problem by using the Hitran 2009 update for the water vapor cross section (HITRAN database, `http://www.cfa.harvard.edu/hitran/`) and the fitting window between 450 and 497 nm.

Figure 6.7 shows all retrieved NO_2 slant columns throughout the whole cruise that were taken under wind directions preventing the ship's exhaust plume to contaminate the measurements (see Sect. 6.1.1). As a result, no data is displayed for 12 October 2009. In addition, suspicious high and short-in-time peaks, especially when showing larger slant columns in high elevation angles, were removed as being most probably due to wind gusts blowing the plume into the instrument's line of sight (the distance between the instrument and the exhaust plume was only a few meters). As the MAX-DOAS measurements from the southward moving ship will contain a contribution from stratospheric NO_2 which shows a latitudinal variation (see Sect. 6.1.2), for each measurement the closest zenith[19] measurement was chosen as reference to minimize the stratospheric NO_2 signal. For comparison, Fig. 6.8 shows the monthly mean tropospheric NO_2 vertical columns as observed from the space-borne GOME-2 instrument.

The elevation angle in Fig. 6.7 is color coded. In the beginning and in the end of the cruise, smaller elevations yield higher slant columns as the light path through the trace gas layer is longer (this information is used for the profiling retrieval). After the first days of the cruise, having influences from Japan (Figs. 6.2 and 6.8), no split-up of different viewing directions is observed and NO_2 values decrease towards an estimated detection limit (the estimation is performed below). Elevated tropospheric NO_2 columns in the clean air over the open ocean were detected only for three events

---

[19] Note that for 11 October almost no zenith measurements exist due to instrumental problems and the 30° elevation was chosen as reference which will strongly reduce the sensitivity towards NO_2 in the free troposphere; nevertheless, it turned out that the NO_2 is close to the surface (Fig. 6.10) giving the possibility to achieve reasonable results even using the 30° reference for NO_2 measurements.

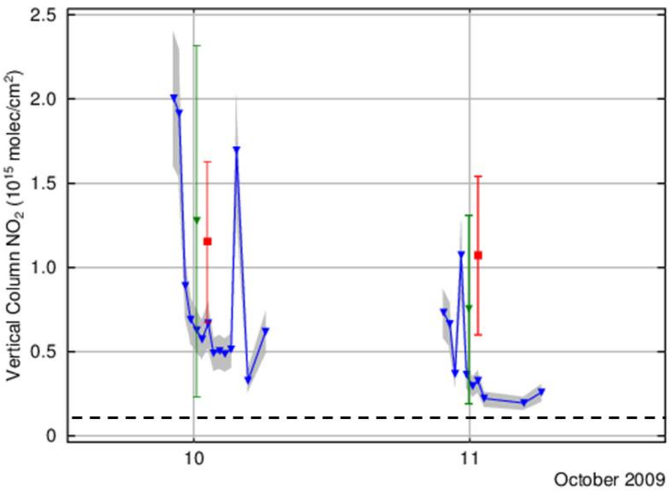

Figure 6.9: Retrieved vertical NO_2 columns from MAX-DOAS measurements for 10 and 11 October 2009 in blue (error margin plotted as grey-shaded area), GOME-2 values in green (satellite pixels averaged within 150 km around ship's position at time of overflight) and SCIAMACHY values in red (200 km radius). The dashed line indicates the MAX-DOAS detection limit. Source: (Peters et al., 2012).

(arrows in Fig. 6.7) corresponding to the position of the ship indicated by red arrows in Fig. 6.2c. Also on 10 and 11 October, being in the polluted marine environment close to Japan, peaks were found in the dataset. For all events, lower elevation angles show enhanced NO_2 slant columns while the NO_2 at 30° elevation angle is not affected. This behaviour indicates that the observed NO_2 is close to the ground and not originating from our ship's plume as this would increase the 30° elevation angle more than elevation angles close to the horizon. The spikes on 11 and 20 October are short-in-time and affect only measurements within single scans. These events could be assigned to other ship plumes as the video camera in our telescope housing detected other ships passing exactly at the time of these peaks. In comparison to these high and short-term events, elevated levels of NO_2 on 22 October are lower but persist for a time span of ≈ 3 h. The video camera did not detect any other vessels for this event, but Fig. 6.2c indicates the crossing of a clearly preferred shipping route. Higher concentrations of NO_2 along frequently used shipping routes is a known issue having been observed from space-borne platforms (e.g. Beirle et al., 2004; Richter et al., 2004). The origin of the events on 10 October remaining for ≈ 1 h is unclear. Backward trajectories calculated with the online tool HYSPLIT reach back to the Japanese mainland on 10 October, so that influences from the close Japanese coast (i.e. passing of towns, industrial regions) can be an explanation. The event in the evening of 19 October consists of multiple scans with increasing NO_2 slant columns, a clear maximum of 12×10^{15} molec/cm^2 and a rapid decrease afterwards. Emissions from other vessels missed by our telescope camera are a possible explanation. In addition, this event coincides with elevated levels of formaldehyde in the evening of 19 October when a minimum distance of ≈ 150 km is reached to the Island of New Ireland and calculated backward trajectories reach back to the island suggesting also transport events (see discussion in Sect. 6.1.4).

For the first days of the cruise (10–11 October 2009) the profiling software *BREAM* (see Sect. 6.1.1 and 3.6.2) was used to calculate tropospheric NO_2 vertical columns (Fig. 6.9) and profiles (Fig. 6.10). As Fig. 6.10 shows, maximum NO_2 concentrations are observed close to the ground. Apart from the peaks as discussed above (yielding up to 0.8 ppbv peak concentrations), the background concentrations do not exceed 0.2 ppbv even in the polluted marine environment close to Japan. Figure 6.11 (left picture) shows exemplarily some retrieved profiles from 11 October 2009 together with the a priori profile used in the retrieval. In Fig. 6.11 (right picture), typical averaging kernels are shown (from 11 October 2009, 10.25 LT; for this day, the 30°-measurements were used as reference). The averaging kernels associated with different points of the retrieved profile are color-coded. Especially

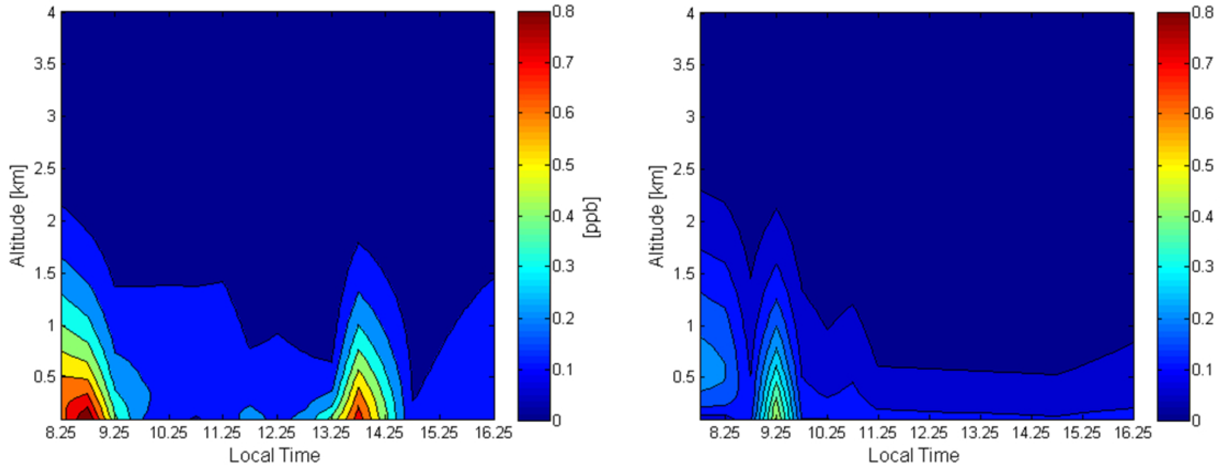

Figure 6.10.: Retrieved tropospheric NO_2 profiles for 10 October (left) and 11 October (right). Highest NO_2 concentrations are found close to the ground.

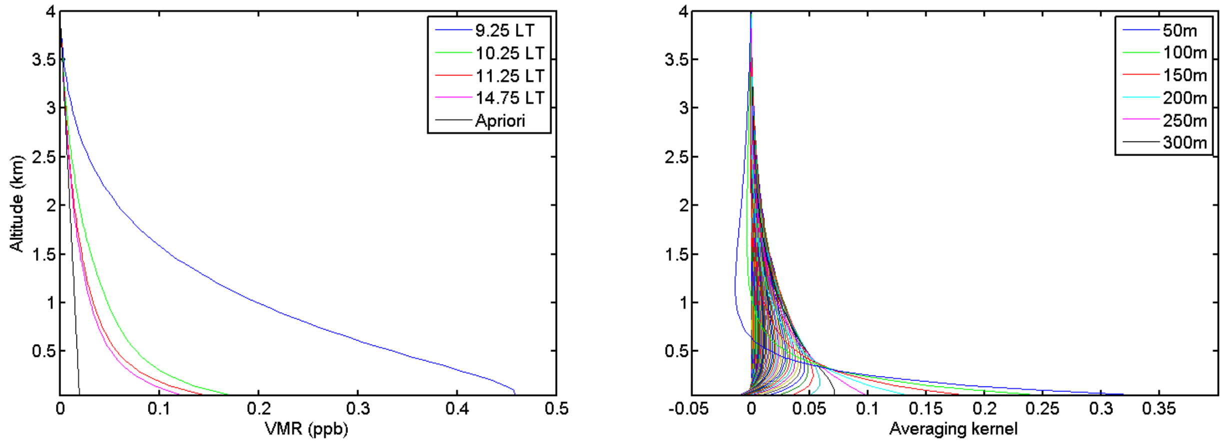

Figure 6.11.: Left: Example profiles of NO_2 from 11 October 2009 (corresponding to Fig. 6.10, right). The 9.25 LT profile is the distinct peak that was verified as another ship's plume. Right: Exemplarily averaging kernels of the retrieved profile on 11 October 2009, 10.25 LT (green profile on the left).

the lowest points of the retrieved profile exhibit an increasing sensitivity to the true profile close to the ground. For this example, the degrees of freedom are ≈ 1.6.

For the tropospheric NO_2 column and concentration above the open ocean, where NO_2 slant columns were close to the detection limit (Fig. 6.7), an upper limit has been estimated. Best RMS of the tropospheric NO_2-Fits are $\approx 1 \times 10^{-4}$ and the differential NO_2 absorption cross-section is in the order of 1×10^{-19} cm^2/molec. Assuming intuitively that an optical density of twice the RMS can be detected, a detection limit (DL) of 2×10^{15} molec/cm^2 for the slant column can be estimated. (Note that an even smaller DL of $\approx 3 \times 10^{-14}$ molec/cm^2 is obtained from the formula given by Platt and Stutz (2008), i.e. the DL following the intuitive approach can be regarded as an upper estimate.) This corresponds to a vertical column of $\approx 1.3 \times 10^{14}$ molec/cm^2 with a typical airmass factor of 15 for low elevation angles. Under the assumption of a block-profile of 1 km mixing layer height (MLH), this vertical column (VC) yields a volume mixing ratio (VMR) of

$$\mathrm{VMR} = \frac{\mathrm{VC}}{\mathrm{MLH}} \cdot \frac{k_\mathrm{B} \cdot T}{p} \approx 50\ \mathrm{pptv} \tag{6.2}$$

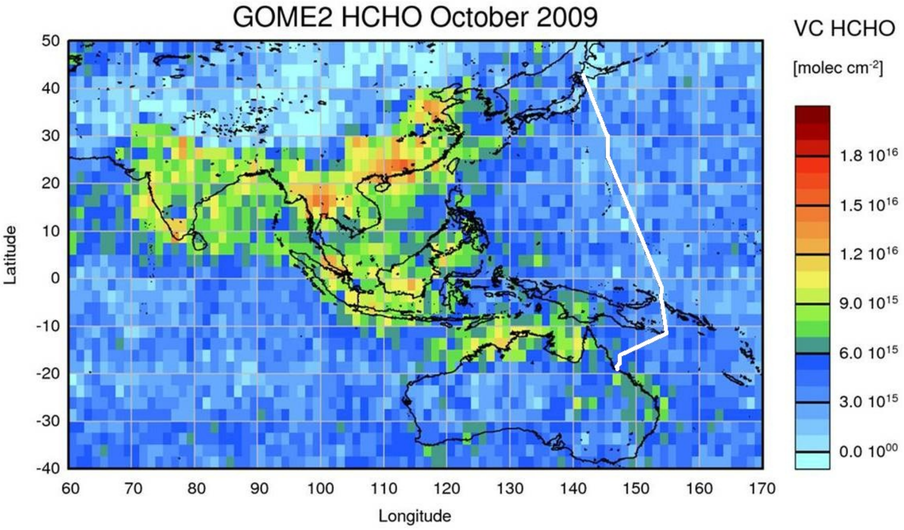

Figure 6.12.: October 2009 monthly average of tropospheric formaldehyde from the GOME-2 instrument (scientific product from Institute of Environmental Physics, University of Bremen). Measured HCHO columns during TransBrom (the cruise track is indicated) are background concentrations from methane oxidation (possible anthropogenic contributions at the beginning and end of the cruise). Source: (Peters et al., 2012).

with the Boltzmann constant k_B, $T = 300$ K and $p = 1 \times 10^5$ Pa. This detection limit can be regarded as an upper limit for the tropospheric NO_2 column under clean open ocean conditions, which is less than reported by Takashima et al. (2011) who found 0.2 ppbv as an upper limit for the marine background concentration of NO_2 in the lowest 1000 m.

Tropospheric vertical columns derived from GOME-2 and SCIAMACHY satellite measurements are shown in Fig. 6.9 as color coded data points in comparison to the MAX-DOAS values (blue points). The MAX-DOAS error margin (grey-shaded area) corresponds to a worst case error of 20% of the vertical columns resulting from sensitivity tests (Wittrock et al., in prep. for AMTD). For the comparison presented here, all satellite pixels within a 150 km radius around the ship's position at the time of the overflight were averaged for GOME-2 (for SCIAMACHY, 200 km averages have been calculated to account for the poorer spatial coverage). As a consequence of the spatial averaging, pixels over or close to Japan may increase the satellite averages, as there is a strong gradient in NO_2 pollution from land to ocean (see Fig. 6.8). This results also in the large standard deviations displayed as satellite error bars in Fig. 6.9. As a result, the satellite averages are 2–3 times higher than corresponding MAX-DOAS measurements, but agree within their standard deviations.

For the open ocean, satellite vertical columns from GOME-2 monthly average are $< 2 \times 10^{14}$ molec/cm^2 (Fig. 6.8), which is below the estimated uncertainty of the satellite (Boersma et al., 2004), but in good agreement with the background vertical column of 1.3×10^{14} molec/cm^2 derived from MAX-DOAS data."

6.1.4. Formaldehyde

The following analysis of Formaldehyde was performed as part of this thesis and has been successfully published in Peters et al. (2012):

"Source regions of formaldehyde (rain forests emitting precursors and direct anthropogenic emissions from industry) can be identified from space as Fig. 6.12 illustrates. The cruise track indicated

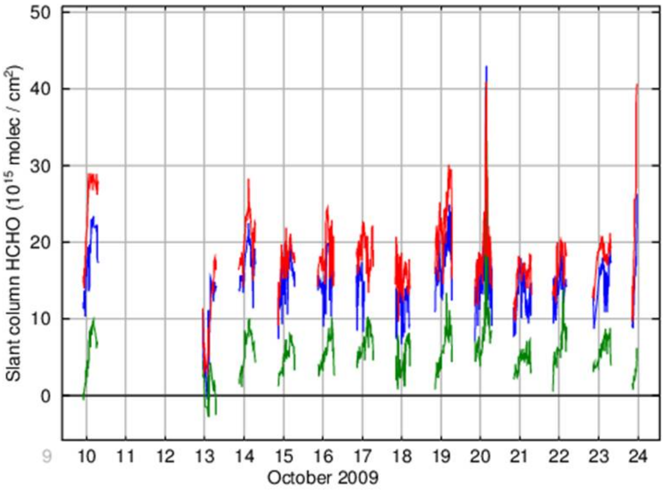

Figure 6.13: Color-coded formaldehyde slant columns (red: 2°, blue: 8°, green: 30° elevation angle). Different viewing directions clearly split-up for the whole campaign indicating a background level of HCHO in the marine boundary layer. No data is shown for 11 and 12 October due to a lack of zenith measurements (used as reference, see text) on 11 October and *bad* wind directions on 12 October. Source: (Peters et al., 2012).

in Fig. 6.12 implies that the MAX-DOAS formaldehyde measurements performed during TransBrom are far away from these source regions giving therefore the opportunity to investigate the formaldehyde background concentration (methane oxidation) and evaluating the accuracy of satellite measurements of small formaldehyde columns over the ocean.

In contrast to NO_2, no formaldehyde is expected to be in the stratosphere and therefore no stratospheric contribution has to be accounted for (i.e. by using the closest zenith spectrum as a reference). For the formaldehyde DOAS-fit, a daily reference spectrum at 45° SZA was used as the fit quality turned out to decrease using zenith measurements at small SZAs especially in the tropics.

In Fig. 6.13, the formaldehyde slant columns for the whole cruise are shown. Different viewing angles (color coded) are separated clearly from each other except for periods with bad weather. For example, the low HCHO slant columns on 13 October are a consequence of heavy rain (wash out) in the morning (the formaldehyde slant columns recover after the strong rain but do not reach the level of other days' slant columns). The dominant peak on 20 October is the consequence of a light path extension in sea fog (the oxygen dimer O_4 shows a peak at the same time and the camera in our telescope housing shows a nebulous scene).

Apart from this event, highest formaldehyde columns were obtained on 10 October (being in the polluted marine environment near Japan, compare Fig. 6.2c) and 24 October (approaching Australia's coast). Although the measurements were already stopped in the morning hours of 24 October when arriving in Townsville, Australia, a remarkable increase of formaldehyde slant columns was observed during the few hours of operation when approaching the coast, most likely connected to bush fires, as it was dry season and a lot of fires were observed in the next vicinity even by eye.

14 October (being on the open ocean, see Fig. 6.2) was the sunniest day of the cruise with best viewing conditions and lowest cloud coverage (around noon was the only completely cloud-free period throughout the cruise) going along with a local maximum in the HCHO timeseries. Thus, this maximum indicates that the observed formaldehyde results in a large part from methane oxidation and subsequent HCHO production which depends on sunlight. However, elevated levels of dimethyl sulfide (DMS) were measured when air masses were reaching the ship from the open ocean (see Fig. 6.2a for backward trajectories) in the afternoon of 14 October (Birgit Quack, personal communication, 2012). It can be speculated that other compounds having oceanic sources and being precursors for HCHO (e.g., aldehydes, methanol) are increased in these air masses as well. Former studies showed that methane is the major source for formaldehyde in very remote

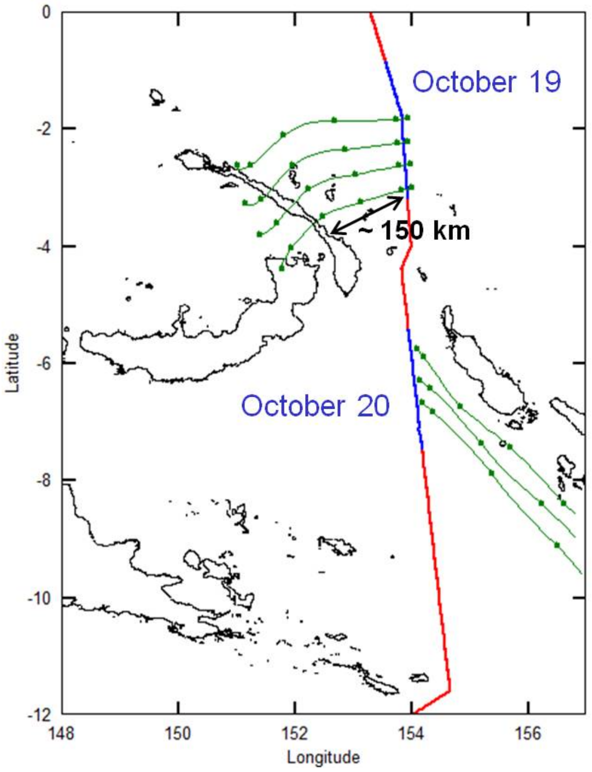

Figure 6.14: Detail map of the TransBrom cruise. Blue parts indicate 19 and 20 October daytime, when MAX-DOAS measurements were performed. Backward trajectories are displayed in green, marks meaning: starting point, −1, −6, −12, −18 and −24 h, respectively. Source: (Peters et al., 2012).

regions, but chemical models including only methane tend to underestimate observed formaldehyde concentrations (e.g., Still et al., 2006, and references therein). Thus, the observed formaldehyde during TransBrom is considered to originate mostly (but not entirely) from methane oxidation. Due to the elevated DMS levels, especially the peak at 14 October could be in addition influenced by other precursor species (from oceanic sources) giving rise to the observed HCHO concentration. A second local maximum in the formaldehyde timeseries was found in the evening of 19 October, dominated by almost complete cloud coverage making enhanced methane oxidation (depending on sunlight) an implausible source. However, these measurements of enhanced formaldehyde were not performed on the open ocean, but close (≈ 150 km) to *New Ireland*[20] as shown in Fig. 6.14 (being a zoom-in of Fig. 6.2). In addition, 24-h-backward trajectories (displayed in green) were calculated with the NOAA HYSPLIT model using the same settings as in Fig. 6.2a (starting point in a distance of 10 km off the ship in the viewing direction of our instrument and in an altitude of 350 m a.s.l.). The trajectories starting in the afternoon of 19 October reach back to the island groups of *Tabar* and *Lihir* after 12 h and to the island of *New Ireland* after less than 18 h. Backward trajectories starting in the evening of 19 October reach back to the island of *New Ireland* after ≈ 12 h (closest distance to the island ≈ 150 km in the evening of 19 October, which coincides with this day's HCHO maximum). Thus, the enhanced formaldehyde on 19 October, especially in the evening, is most probably a result of formaldehyde precursor transport from rainforest. On the next day, 20 October, Fig. 6.14 shows that the wind direction changed transporting clean air masses from the open sea to our position, resulting in lower formaldehyde slant columns.

Profiles and vertical columns of formaldehyde have been calculated using the profiling software

---

[20] New Ireland Province is part of the Bismarck Archipelago and the most northeastern province of Papua New Guinea encompassing the largest island of the province called *New Ireland* and numerous smaller islands including the *Tabar* and *Lihir group* at the Pacific side (the latter is famous for housing a gold mine holding one of the world's largest gold resources). The island of *New Ireland* has a length of ≈ 400 km but a width of mostly less than 10 km. The terrain is dominated by a central mountainous spine, the vegetation is tropical rainforest.

Figure 6.15: Time series of the retrieved tropospheric HCHO vertical columns. The dashed line indicates the MAX-DOAS detection limit.

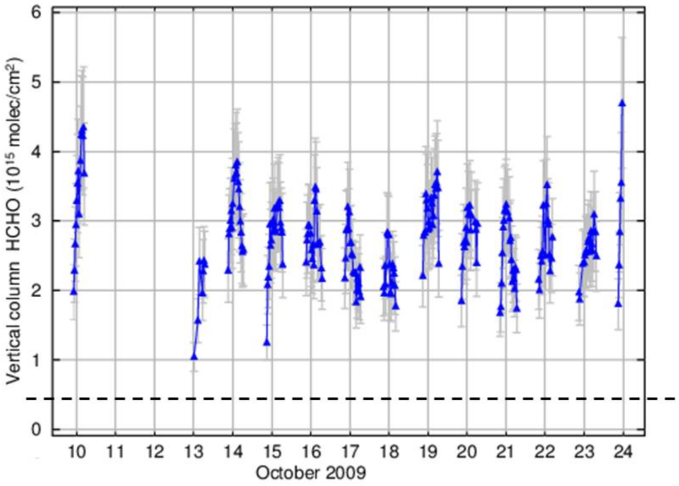

BREAM (Sect. 6.1.1 and 3.6.2) consistent to the retrieval of tropospheric NO_2 (Sect. 6.1.3). Tropospheric HCHO columns were retrieved successfully during the whole cruise above an estimated detection limit of 0.5×10^{15} molec/cm^2 (Fig. 6.15). The detection limit has been estimated using the same method applied for tropospheric NO_2. Again, this can be regarded as upper limit as the detection limit according to Platt and Stutz (2008) yields a value of $\approx 0.1 \times 10^{15}$ molec/cm^2 for the vertical column. The timeseries shown in Fig. 6.15 reproduce the local maxima as discussed above, plotted error bars correspond again to a worst case error of 20%. In addition, the vertical columns exhibit a diurnal cycle with low values in the morning and evening and maxima around noon, most clearly on days with good weather and viewing conditions, especially on 14 October.

As an example, Fig. 6.16 shows all retrieved profiles for 14 and 15 October, both having reasonable viewing conditions, although not being completely cloud-free. Exemplarily profiles together with the a priori profile used for the retrieval can be found also in Fig. 6.17 (left picture). Figure 6.17 (right picture) shows averaging kernels for the retrieval at 14 October 2009, 9.25 LT (DOF $\approx$ 1.8, the corresponding profile is displayed in the left picture). As already seen for tropospheric NO_2, the retrieved HCHO profile is most sensitive in low altitudes to the true profile close to the ground.

14 October (Fig. 6.16, left picture) had the lowest cloud coverage throughout the whole cruise with a completely cloud-free period around noon when highest concentrations of 1.1 ppbv occured. In contrast, 15 October (Fig. 6.16, right picture) had its best viewing conditions (rarely cloudy) in the afternoon to evening, partial to full cloud coverage in the morning and a short rain event at noon, most likely supressing a midday's maximum as seen on 14 October. The better viewing conditions on 14 October also result in a smoother shape of concentration isolines compared to 15 October. Both days show a diurnal cycle with enhanced levels of formaldehyde during noon/afternoon when the sunlight intensity driving the formaldehyde production is highest. Corresponding peak concentrations of 1.1 ppbv were found on 14 October at noon-time. In comparison to NO_2 showing highest concentrations close to the ground (see Fig. 6.10) formaldehyde's highest concentrations occur in elevated altitudes (in the 400 m regime) during the day. Apart from the midday's maximum, HCHO levels in the afternoon appear higher than before noon.

Judging from these results, cloud coverage seems to have a large influence on the formaldehyde production (mainly methane oxidation) making 14 and 15 October the best examples for the (almost) cloud-free behaviour and development of HCHO background concentration in the clean and remote marine environment. Precursor compounds from oceanic sources (DMS, methanol etc.)

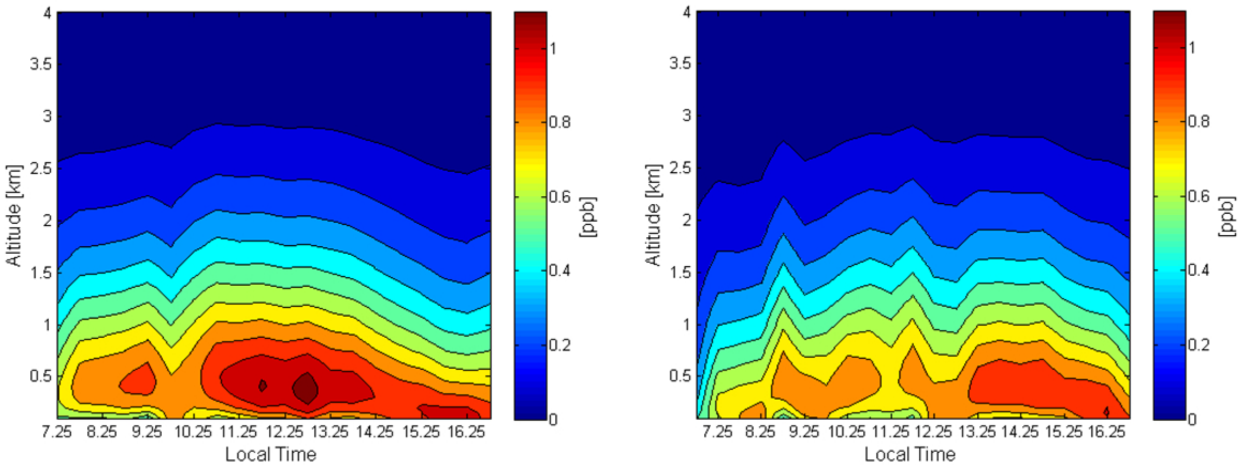

Figure 6.16.: Retrieved formaldehyde profiles for 14 October (left) and 15 October (right) having reasonable viewing conditions. The only completely cloud-free period of the cruise was on 14 October around noon coinciding with maximum formaldehyde concentrations of 1.1 ppbv in an altitude of ≈ 400 m.

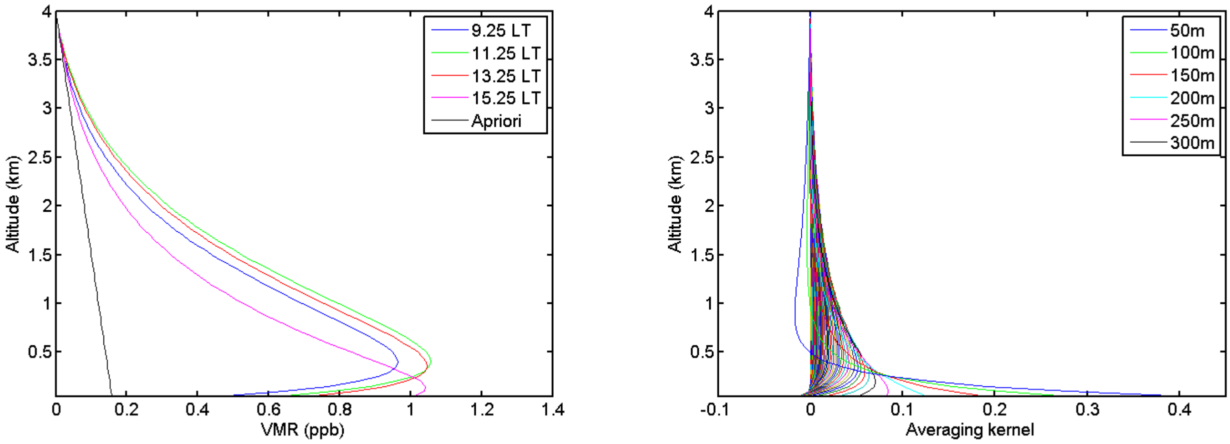

Figure 6.17.: Left: Example profiles of HCHO from 14 October 2009 (corresponding to Fig. 6.16, left). Right: Exemplarily averaging kernels of the retrieved profile on 14 October 2009, 9.25 LT (blue profile on left hand side).

possibly contribute especially to the HCHO maximum on 14 October, as mentioned above. Reported background concentrations from other studies ranging from 0.2–1.0 ppbv in remote marine environments (Singh et al., 2001; Weller et al., 2000) therefore agree with our results although we found a maximum concentration of > 1 ppbv in elevated altitudes under cloud-free conditions in the subtropical remote ocean (latitude ≈ 20° N) at noontime on 14 October. Still et al. (2006) reported a similar diurnal cycle with enhanced levels of HCHO during the day, which are comparable to our results, in the remote marine boundary layer measured by gas chromatography at Mace Head, Ireland. In comparison, reported formaldehyde levels as derived from DOAS measurements in the same tropical region as TransBrom, but close to local sources of precursor species in an rain forest environment on Borneo, Malaysia (compare Fig. 6.12), reach up to 4.5 ppbv (MacDonald et al., 2012). These observations show maximum concentrations also around noon and in the afternoon, but the diurnal cycle and absolut values here are dominated by the emission and chemistry of precursor substances.

Due to the diurnal cycle found in formaldehyde vertical columns, care must be taken with re-

Figure 6.18: Comparison between MAX-DOAS (blue) and GOME-2 (green) HCHO vertical columns as a function of latitude. MAX-DOAS data was averaged between 09:00–11:00 LT (approx. time of GOME-2 overflight). The GOME-2 values are calculated from monthly average for October 2009 and binned to a 2° grid for better visualisation of the results.

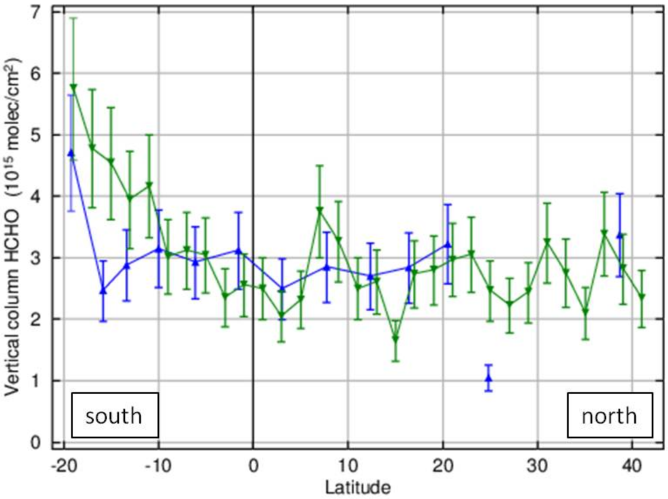

spect to the comparison between MAX-DOAS and satellite measurements. Therefore, the vertical columns have been averaged between 9 and 11 local time as this corresponds roughly to the satellite overflight time. In addition, as mentioned above, satellite instruments have a much shorter light path through the troposphere than MAX-DOAS instruments, resulting in a poorer sensitivity for tropospheric absorbers. Thus, as a result of the small amount of HCHO (pure background signal, see Fig. 6.12), the MAX-DOAS vertical columns had to be compared with monthly averages seen from satellite (Fig. 6.18). Due to the poor coverage of SCIAMACHY in comparison with GOME-2, this comparison could be performed only for GOME-2 data.

Two examples of the influence of bad weather can be found in the data (Fig. 6.18): the minimum of 1×10^{15} molec/cm^2 at $\approx 24°$ N in MAX-DOAS data results from the low formaldehyde columns on 13 October (compare Fig. 6.15 and Fig. 6.13) which are a consequence of washing out. A second example is the delay of MAX-DOAS data in comparison to GOME-2 when increasing at $\approx 10°$ S which is most likely an effect of comparing point-in-time measurements with monthly averages: as rainy and cloudy conditions predominated during the cruise in the coral sea (21–24 October, see Fig. 6.2), consequently, the MAX-DOAS measurements remain small, while GOME-2 values average also over periods with better weather and less clouds yielding higher formaldehyde concentrations.

As a consequence of the comparison of MAX-DOAS with monthly averages, the agreement of single maxima and minima cannot be expected. Apart from the effect of cloudy weather as discussed above, MAX-DOAS and GOME-2 data agree at a vertical column of about 3×10^{15} molec/cm^2, which can be considered as a typical value for the formaldehyde vertical column above the remote ocean for the time of the GOME-2 overflight."

6.1.5. Iodine monoxide

In general, iodine is present in ocean water predominantly in form of iodate (IO_3^-) and iodide (I^-) (e.g., Möller et al., 1996; Carpenter, 2003). Consequently, the ocean is a potential source for iodine release and therefore IO in the marine troposphere. However, the abundance of iodine in water is small and up to now higher amounts of IO in the atmosphere were found only over upwelling regions, coastal areas or in the Arctic/Antarctic (e.g., Read et al., 2008; Schönhardt et al., 2008, 2012) where iodine is assimilated in biogenic organisms and finally released to the atmosphere. For

Parameter	Settings	Remarks
Reference	Zenith	Daily spectrum at 45° SZA
Spectral range	417.5 - 438.2 nm	
Polynomial	2nd order	
Straylight corr.	Offset	
O_3	(Bogumil et al., 2003)	223 K
NO_2	(Vandaele et al., 1996)	220 K
IO	(Spietz et al., 2005)	
water vapour	HITRAN2009	
VRS	simulated	(Dinter, 2005)
Ring	simulated	(e.g., Vountas et al., 1998)

Table 6.5: DOAS fit parameters for the IO fit during TransBrom.

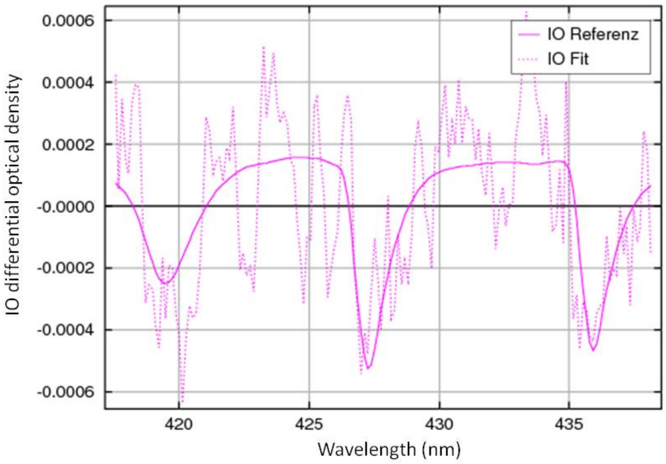

Figure 6.19: IO example fit from a measurement during TransBrom in 3° elevation angle (14 October 2009). The corresponding slant column is $2.6 \cdot 10^{13}$ molec/cm^2.

example, under-ice algea are considered to cause IO events in Antarctic springtime, which can be observed from space (see Fig. 1.1 in Sect. 1 or (Schönhardt et al., 2012)).

The same figure (1.1) also illustrates, that the DOAS retrieval yields negative IO slant columns over the open ocean. This may have two different reasons (as mentioned in chapter 1): 1. The amount of IO over the open ocean is considered to be low. This is because biogenic activity is needed to enrich the iodine. Inorganic sources (e.g., direct release from water) may exist, but so far, organic iodine compounds have been assumed to be the main source of oceanic iodine emissions (however, the results of the following study support the possibility of inorganic release from the ocean). 2. A second reason might be spectral interference with liquid water absorption effects. This assumption arises from the pattern of negative retrieved IO slant columns that coincide with locations where liquid water absorption ist large (comparison between Figs. 1.1 and 1.2). Over water surfaces, the satellites nadir measurements necessarily contain contributions from liquid water as a part of the light path is under water (the penetration depth of the light into the water scales with geometry and cleanliness of the water).

The optical properties and spectral effects of liquid water are not sufficiently known for consideration in the satellite DOAS fit. However, this is necessary as Figs. 1.1 and 1.2 demonstrate. The improvement of the consideration of liquid water spectral effects in the DOAS analysis is the topic of Chapter 7. The following analysis in this section aims at the retrieval of IO over the remote

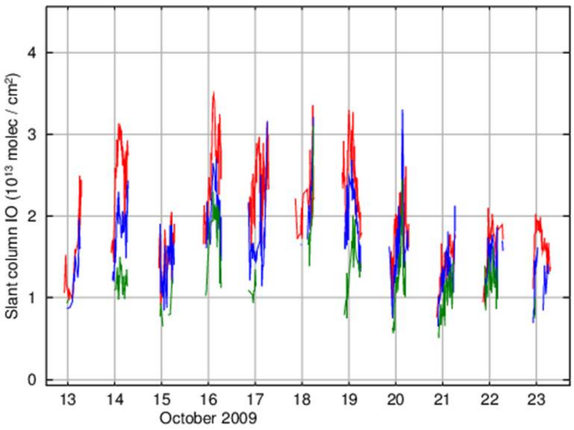

Figure 6.20.: IO slant columns during TransBrom. Only results with less than 30% error are plotted. The elevation angle is color-coded (red = 1°, blue = 6°, green = 15°).

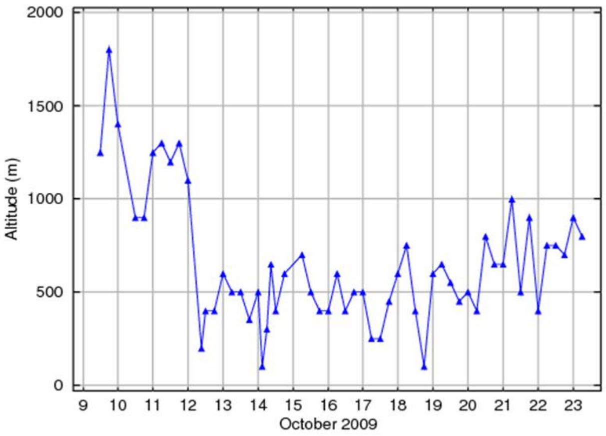

Figure 6.21.: Mixing layer height as retrieved from radio sondes data during TransBrom (K. Krüger, GEOMAR Kiel, personal communication 2011).

ocean using MAX-DOAS measurements and therefore the estimation of the true IO background concentration (for that the satellite instruments often yield negative values). As explained earlier, a MAX-DOAS is well-suited for this as the achieved light path in the marine boundary layer is much larger compared to the satellite resulting in a higher sensitivity for tropospheric trace gases. In addition, MAX-DOAS measurements normally do not point towards the water surface and thus the spectral interferences with liquid water can be assumed to be smaller.

During the TransBrom campaign it turned out that the IO DOAS retrieval is challenging even using ground-based MAX-DOAS measurements indicating that the amount of IO in the marine environment over the remote ocean is small. However, extensive studies were performed yielding optimal settings for the DOAS retrieval. Finally, a fit window from 417.5–438.2 nm and a 2nd order DOAS polynomial were selected. The advantage of this fit window is that it covers 3 absorption bands[21] of IO (an example fit is given in Fig. 6.19). In contrast, the SCIAMACHY standard fit (see Tab. 7.7 in Sect. 7.7.4) covers only 2 absorption bands[22]. Both fits were tested, but the larger fit window was selected as using more information (3 bands instead of 2) and therefore the results are considered to be more reliable. In addition to IO, cross-sections of ozone, NO_2, an offset straylight correction as well as a simulated pseudo-cross section accounting for the Ring effect were used.
One of the most limiting factors of the DOAS fit were artifacts from incomplete removed Fraunhofer structures. This leads to the application of a VRS spectrum describing the filling-in of Fraunhofer structures similar to the Ring effect caused by inelastic Vibrational Raman Scattering (VRS) in liquid water: A photon excites a H_2O molecule that decays (under re-emission) in a vibrational state different from the initial one resulting in a wavelength shift of the inelastically scattered photon. A theoretical explanation of Raman scattering in general is given in Sect. 3.3.1 and Sect. 7.4.1 describes in detail the effect of Vibrational Raman Scattering in liquid water and the resulting filling-in of Fraunhofer structures. Sect. 7.5 demonstrates the presence of the VRS effect in off-axis

---

[21] The fit uses three vibrational peaks on the transition from the ground state $X^2_{3/2}$ of the IO molecule to its first electronically excited state $A^2_{3/2}$, namely the transitions (ν'=3←ν''=0), (ν'=4←ν''=0) and (ν'=5←ν''=0).

[22] The IO standard fit used only the (ν'=4←ν''=0) and (ν'=5←ν''=0) absorption peaks on the ($A^2_{3/2} \leftarrow X^2_{3/2}$) transition.

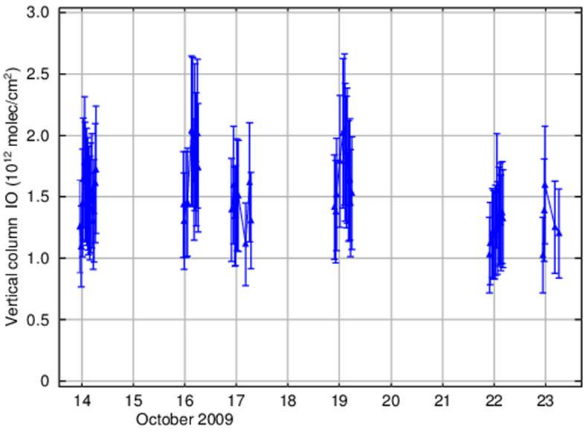

Figure 6.22.: IO vertical columns during TransBrom. The data is sparse because the profiling was possible only when having reasonable viewing conditions and reliable IO fits.

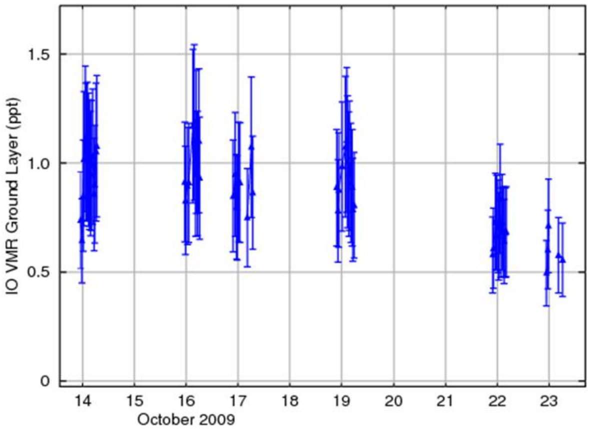

Figure 6.23.: Average IO VMR in the lowest 500 m during TransBrom.

MAX-DOAS measurements during TransBrom (Fig. 7.19) and therefore supports the use of a VRS spectrum in the DOAS analysis performed here.

As mentioned in previous sections, problems occured when using the zenith pointing measurements as reference predominantly in the tropics at small SZA. Most likely, this is due to intense sunlight leading to saturation effects on the CCD. Thus, daily zenith measurements at 45° SZA have been used to avoid this problem. The parameters of the ground-based TransBrom IO fit are summarized in Tab. 6.5.

Figure 6.19 shows exemplarily the fitted optical density of IO for a measurement in 3° elevation angle during TransBrom. Obviously, the IO optical density is very small and only marginally larger than the residual structures. Therefore, the resulting slant columns are highly uncertain and have to be interpreted carefully.

The obtained IO slant columns for the whole campaign are shown color-coded for different elevation angles in Fig. 6.20 (the IO timeseries starts only at 13 October because of too uncertain IO values and instrumental problems with the zenith pointing direction before). On days having very clear viewing conditions (most obviously on 14 October), the different viewing directions split-up indicating the presence of IO in the boundary layer. In contrast, on 13 and 20 October both having rain and bad viewing conditions, the different viewing directions are not separated. In general, largest slant columns occur between 16–20 October corresponding to locations close to the Equator (compare Fig. 6.2).

Consistent to the analysis of tropospheric NO_2 and HCHO in the previous sections, the profiling retrieval BREAM (Sect. 3.6.2) has been used to retrieve vertical columns and profiles. Both, tropospheric NO_2 and HCHO were considered not to be linked strictly to the boundary layer as being produced in the atmosphere, e.g. by lightning events and methane oxidation, respectively. Therefore, a linear decrease with altitude was assumed as apriori profile for both trace gases (Sect. 6.1.1 and Figs. 6.11 and 6.17). In contrast, IO is assumed to be emitted from the ocean and therefore it is linked to the boundary layer more strictly. As mentioned above, the IO signal is very weak and its slant columns have large uncertainty. Thus, the complimentary apriori profile information needed for the profile retrieval has to be as realistic as possible because the results will be highly

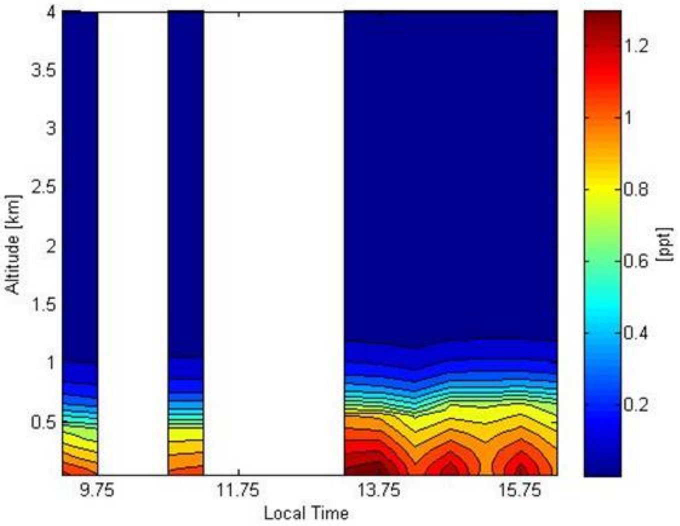

Figure 6.24: Exemplarily IO profiles for 16 October (clear split-up of viewing directions) using the MLH from radio sondes during TransBrom. Data gaps result from too large error bars (only slant columns of <30% error were used for the profile retrieval).

sensitive to the input parameters.

During TransBrom, radio and ozone sondes were launched every ≈6 hours recording the wind speed as well as the temperature profile. From these measurements, the mixing layer height was estimated (K. Krüger, GEOMAR Kiel, personal communication 2011) which is shown in Fig. 6.21 for the whole campaign. On the first days of the cruise when the ship was close to Japan, the vertical extent of the boundary layer is very large (these values might be also influenced by a storm in the beginning of the campaign). Over the remote ocean, the mixing layer height is mostly in the range of ≈500 m.

For the shape of the IO apriori profile, the actual values from Fig. 6.21 were used. As the ocean is considered to be the source of iodine release, a linear decrease from surface to the mixing layer height was assumed followed by an exponential decrease above. This apriori shape is scaled by various factors and the profile retrieval is repeated for each factor until the best match between simulation and measurements is found (see the introduction of BREAM in Sect. 3.6.2). The (best) retrieved profile is integrated over altitude (considering the altitude-depending pressure and temperature) yielding the IO vertical column.

The resulting IO vertical columns for the whole campaign are plotted in Fig. 6.22. Some data gaps exist because a) the profile retrieval was possible only on days when viewing directions split-up (compare Fig. 6.20) and b) only slant columns of <30% error were considered to be reliable enough to be used in the retrieval. In general, IO vertical columns were found in a range of 1–2.5·10^{12} molec/cm^2 with a tendency to higher values in the tropics (14–19 October). In Fig. 6.23, the profiles were avegaed in the lowest 500 m giving a mean volume mixing ratio (VMR) in the boundary layer (≈500 m, compare Fig. 6.21). The same tendency of higher VMR values in the tropics (on average ≈1 ppt) is found. The complete profiles retrieved during the day are shown exemplarily for 16 October (having the largest VCs) in Fig. 6.24. In fact, highest concentrations (≈1.3 ppt for this example) are found close to the surface.

The interpretation of the observed IO columns and volume mixing ratios and especially its potential source is not obvious. Previous studies suggest predominantly biogenic release mechanisms (e.g., Carpenter, 2003, and references therein) (see also Sect. 2.3.5), i.e. the assimilation of iodine from the ocean in organisms (macro- and microalgae).

To verify organic pathways into the atmosphere, Fig. 6.25 shows the Chlorophyll-a concentration

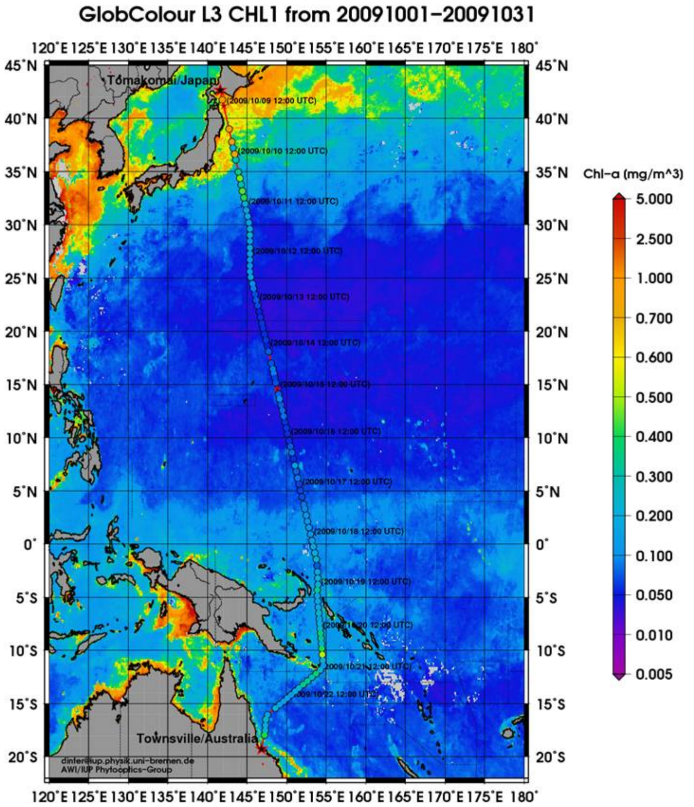

Figure 6.25: October 2009 average Chlorophyll-a concentration in the western Pacific ocean as observed from space (T. Dinter, IUP Bremen, personal communication 2011).

as measured from space for October 2009 in the western Pacific region (T. Dinter, IUP-Bremen, personal communication 2011). In addition, in situ measurements of Chl-a during TransBrom are shown as circles (same color-coding) along the cruise track. Obviously, apart from two sharp events of moderate Chl-a enhancement in the in situ data, the enhanced IO values over the remote ocean between 14–19 October anti-correlate with the Chlorophyll content. Although biogenic activity is not exclusively linked to Chl-a , this result makes a biogenic pathway implausible and suggests an inorganic release mechanism. This is further supported by the fact that organic iodine species (e.g. CH3I) measured in situ during TransBrom do not correlate with the enhanced IO columns over the open ocean either (see discussion below and (Großmann et al., 2013)).

A possible inorganic source of atmospheric iodine is the oceanic release of molecular iodine (I_2) which is in the atmosphere quickly photolysed (during the day) producing atomic iodine:

$$I_2 + h\nu \quad \rightarrow \quad 2 \cdot I \tag{6.3}$$

The I atoms can react with ozone forming IO and participate in a number of tropospheric ozone-depleting catalytic cycles, e.g.:

$$\begin{array}{lcl} I + O_3 & \rightarrow & IO + O2 \qquad (6.4) \\ IO + HO_2 & \rightarrow & HOI + O2 \qquad (6.5) \\ HOI + h\nu & \rightarrow & I + OH \qquad (6.6) \\ \hline net : HO_2 + O_3 & \rightarrow & OH + 2O_2 \end{array}$$

This cycle is important at low halogen oxide levels (e.g., Saiz-Lopez et al., 2012), which is true for the open ocean.

Measurements of aqueous I_2 are sparse. For example, in Adriatic coastal surface water, Möller et al. (1996) found occasionally molecular iodine in the range of 10^{-9} mol/l (= 10^{-6} mol/m^3). Möller et al. (1996) state also that these occasional I_2 measurements correlate with strong sun irradiation and proposed the reaction of photochemical formed ozone with iodide (I^-) to be the most probable source of I_2 in surface water. Reactions of atmospheric ozone deposited at the sea surface with iodide yielding I_2 had been already suggested by Garland and Curtis (1981). The reactions are proposed to take place in a thin film on the water surface (Thompson and Zafiriou, 1983), also called interfacial layer. It can be speculated that a quiet sea is an important factor for the developement of such a surface layer and therefore the formation and release of I_2. This is consistent to a) the measurements of Möller et al. (1996) who found positive I_2 in water samples predominantly under the conditions of strong sun and a quiet sea and b) the measurements during TransBrom indicating largest IO columns over the open ocean also under strong sun irradiation and a relatively quiet sea.

A very recent study by Carpenter et al. (2013) demonstrated that I_2 - as well as HOI - is indeed produced within the interfacial layer by inorganic reactions of gaseous ozone with iodide:

$$H^+ + I^- + O_3 \rightarrow HOI + O_2 \tag{6.7}$$

$$H^+ + HOI + I^- \rightleftharpoons I_2 + H_2O \tag{6.8}$$

Carpenter et al. (2013, and references therein) believe reaction 6.7 to be the major contributor to the chemical loss of atmospheric O_3 in open ocean waters and thus to its dry deposition. This is important for the interpretation of the TransBrom IO measurements. As mentioned above, ozone sondes were launched during the campaign. Ozone retrieved from the sondes data in low altitudes dropped below the detection limit (≈15 ppb) at the same time when maximum IO levels were observed from MAX-DOAS, i.e. an anti-correlation was found between [IO] and [O_3] (with $R = -0.47$, see Großmann et al. (2013)). The above mechanism suggests that a large ozone loss is linked to enhanced [HOI] and [I_2] in the water which could evaporate yielding enhanced levels of IO. On the other hand, the I_2 production was found to be almost linear in the O_3 concentration (Carpenter et al., 2013). Thus, decreasing levels of ozone in the atmosphere would cause decreasing levels of I_2 in the water and subsequently smaller atmospheric IO levels. Furthermore, the iodine in the atmosphere participates in a number of ozone-depleting catalytic cycles as mentioned above. To calculate concentrations of O_3, IO etc. influencing each other, a chemical model is required that includes the iodine release mechanism in the interfacial layer due to ozone deposition as explained above.

Reaction 6.8 describes an equilibrium between HOI and I_2 in the interfacial layer with a ratio HOI/I_2 ≈ 500 in sea water. Furthermore, Carpenter et al. (2013) found that the major iodine species evolved in their laboratory measurements was HOI (followed by I_2) suggesting also HOI as an inorganic precursor for IO from oceanic release, although the HOI flux was found to be suppressed during the day because of the built up of HOI in the atmosphere through gas-phase chemistry of iodine and HO_x (I_2 shows the opposite behaviour: a larger flux was found during the day because of the rapid photolysis of I_2). However, these findings were obtained from laboratory measurements of aqueous iodide solutions. In real sea water, ozone can also react with dissolved organic matter (DOM) at the surface. Although this is obviously more important in coastal waters (more DOM) the effect is in general present in the ocean as well. As being an additional loss of O_3, the effect of DOM will potentially decrease the emission of gaseous iodine.

The MAX-DOAS results of IO presented here are in agreement with observations of a second MAX-DOAS instrument from IUP-Heidelberg which participated at TransBrom (K. Großmann, personal communication 2009–2013). The resulting IO concentrations retrieved from Bremen and Heidelberg agree within ≈50%, which is reasonable considering the weak absorption of IO and the large corresponding errors in the TransBrom observations. Even more relevant is that the same behaviour of IO was found.

The IO analysis of TransBrom data was published (in cooperation between IUP-Heidelberg and Bremen) by Großmann et al. (2013) who performed in addition photochemical model simulations using the MISTRA model (e.g., von Glasow et al., 2002) and comparisons to organic iodine species (e.g., CH_3I, CH_2I_2) that were measured in situ during TransBrom. In detail, the published findings are:

Largest values of in situ observed iodocarbons occured in the southern tropical hemisphere, especially when passing New Guinea and when approaching Australia (organic iodine from algea in coastal regions). In general, the in situ measurements of organic iodine species show only weak correlation with the IO observed from MAX-DOAS. In contrast, the IO correlates with humidity and sea surface temperature supporting the idea of an inorganic source. The MISTRA model (where inorganic iodine release from the ocean is included as an additional emission that has to be selected) underpredicted the observed IO levels unless an I_2 flux of $\approx 1 - 1.8 \cdot 10^8$ molec/cm^2/s was assumed. Between latitudes 15°N and 8°S, i.e. when highest IO levels were observed, ozone mixing ratios measured by in-situ ozone sondes dropped to values at or below the detection limit of ≈15 ppb near the surface (anti-correlation of -0.47).

To conclude, from both data sets (IUP-Bremen and IUP-Heidelberg) the same IO behaviour was found and the same conclusions were drawn. Most important is the proposed inorganic source of oceanic iodine release, which is most likely caused by the reaction of atmospheric ozone and iodide in the interfacial layer. The finding of the model calculations that an I_2 flux of $\approx 1.8 \cdot 10^8$ molec/cm^2/s is needed to reproduce the observations is consistent to reported I_2 emissions from iodine solutions in laboratory measurements (see red line in Fig. 1a (upper panel) in (Carpenter et al., 2013) and extrapolate to 10-20 ppb [O_3]). However, as mentioned above, the reaction of ozone with DOM in real sea water introduces further uncertainty (probably reducing the I_2 flux) while at the same time also the emission of HOI will contribute to the effective iodine release. For an accurate understanding of the inorganic pathways of iodine from the ocean into the atmosphere (reproducing the measured values), this has to be implemented in chemical models.

In summary, MAX-DOAS measurements over the remote ocean during TransBrom yield IO background concentrations in the range of 0.5–2 ppt close to the surface or $1 - 3 \cdot 10^{12}$ molec/cm^2 for the vertical column, respectively (depending on the actual conditions, e.g. O_3 concentration). These values are proposed to be realistic background levels of IO in the oceanic regions for which the satellite retrieves (unrealistic) negative values. Furthermore, inorganic pathways for the iodine to reach the atmosphere are most probable, for example the reaction of gaseous ozone with iodide in the interfacial layer.

6.2. The SHIVA campaign

The SHIVA campaign is not on focus of this thesis. However, measurements using the improved MAX-DOAS instrument have been performed as part of the campaign in the tropical marine boundary layer (although not over the remote ocean but - mostly - in a coastal environment).

After Sect. 6.2.1 giving a short overview about the SHIVA campaign, the IO results in this tropical coastal environment are presented in Sect. 6.2.2.

6.2.1. Introduction to SHIVA and campaign overview

The SHIVA (**S**tratospheric Ozone: **H**alogen **I**mpacts in a **V**arying **A**tmosphere) campaign was a comprehensive German-Malaysian research campaign with core field activities in the South China Sea and on Borneo in November/December 2011 focusing on the emission of halogen-containing ozone depleting substances (ODSs). These substances are broken down by solar radiation in the stratosphere releasing halogens (chlorine, bromine, iodine) which participate in catalytic ozone depleting cycles (see Sect. 2.2.1). The ODSs enter the stratosphere predominantly in the tropics because of the warm, ascending air (powerful deep convective systems). Thus, in these regions even short-lived ODSs of natural origin (e.g. emitted by the oceans and by marine organisms) can enter the stratosphere.

The main objective of SHIVA was to reduce uncertainties in the amount of halogen-containing ODSs reaching the stratosphere and the resulting ozone depletion, especially to better predict the rate, timing and climate-sensitivity of ozone-layer recovery and to identify potential risks from the recovery. Therefore, sophisticated numerical models were combined with a number of different measurement types (Pfeilsticker et al., 2012). The SHIVA campaign was organized by the University of Heidelberg (Germany) in cooperation with the University of Malaya (Malaysia). Several institutes, e.g. University of Bremen, Deutsches Zentrum für Luft- und Raumfahrt (DLR), IFM-GEOMAR Kiel, University of East Anglia etc., participated at SHIVA. The core field activities carried out in November-December 2011 comprised

- A ship cruise (RV Sonne) in the South China Sea from Singapore to Manila (15–29 November 2011)
- Multiple flights of the DLR Falcon aircraft from Miri/Borneo in November and December 2011
- Local boat trips (in situ measurements), e.g. from Kuching and Semporna
- Land-based measurements, e.g. MAX-DOAS in Semporna
- In addition, space-borne observations from ENVISAT and MERIS satellites

Detailed information about SHIVA, especially the various trace gases and quantities observed by the different measurement types (air-borne, ship-borne etc.) can be found at the SHIVA webpage[23] or the SHIVA activity report (Pfeilsticker et al., 2012).

The IUP-Bremen contributions reported here are MAX-DOAS observations of IO. These have been performed using instruments at two locations:

---

[23] `http://shiva.iup.uni-heidelberg.de/index.html`

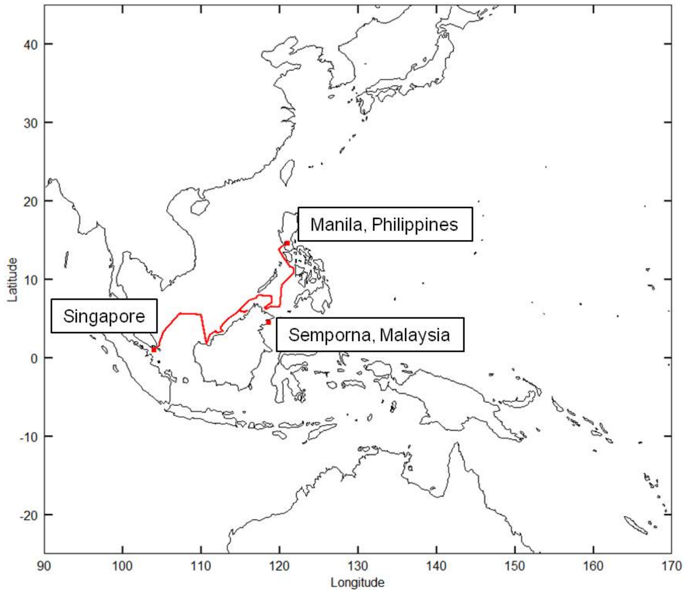

Figure 6.26: Locations of the two IUP-Bremen MAX-DOAS instruments during SHIVA. The cruise track of the RV Sonne (ship-borne measurements) is indicated as well as the location of the land-based instrument in the Tun Sakaran marine park close to Borneo, Malaysia.

- One MAX-DOAS instrument was deployed on the RV Sonne and participated on the cruise from Singapore to Manila.
- A second IUP-Bremen MAX-DOAS instrument was operated at the island of Bohey Dulang (≈20 km offshore) in the Tun Sakaran Marine Park close to Semporna, Borneo (Malaysian part of Borneo) for the period of the RV Sonne cruise.

The first IUP-Bremen MAX-DOAS instrument was installed on the RV Sonne in Singapore at 13–15 November 2011, i.e. before the campaign, and operated automatically during the cruise. The cruise track is indicated in Fig. 6.26. The set-up of the instrument was in large parts identical to the set-up during the TransBrom campaign: The telescope head was again installed at the monkey deck above the bridge, but this time pointing starboard (instead of portside during TransBrom). This means, measurements were performed pointing towards the land for most of the time in the South China Sea, especially around Borneo (compare to the cruise track in Fig. 6.26). The telescope unit was slightly modified since TransBrom. For example, a cylindric metal tube was attached shading the entrance window and preventing direct sunlight to enter the telescope. Via a Y-shaped optical fiber bundle, the telescope was connected with two spectrometers for the Visible and UV, respectively. The optical fiber-bundle and the spectrometer system were identical to the system used during TransBrom. Again, the spectrometers were installed at the scientific bridge of the RV Sonne (at the deck below the telescope unit). The spectrometer characteristics are summarized in Tab. 4.1 in chapter 4.

In the azimuthal direction perpendicular to the ship, vertical scans were performed. Starting from -3° elevation angle, off-axis measurements were taken in 1° steps until 10°. In addition, measurements were performed in 15° and 30° elevation angles. At the end of each scanning sequence, a zenith spectrum was recorded. Consistent to TransBrom, the exposure time for off-axis measurements was only 0.1 s and the ship's roll angle was recorded. After the campaign, the elevation angle of each individual 0.1 s measurement was corrected in terms of the roll angle. Then, in each scan the single 0.1 s measurements were re-sorted and averaged according to their effective (corrected) elevation angle with a tolerance of ±0.5°. Individual measurements taken at *bad* relative wind directions (i.e. blowing the ship's exhaust plume into the line of sight) were rejected

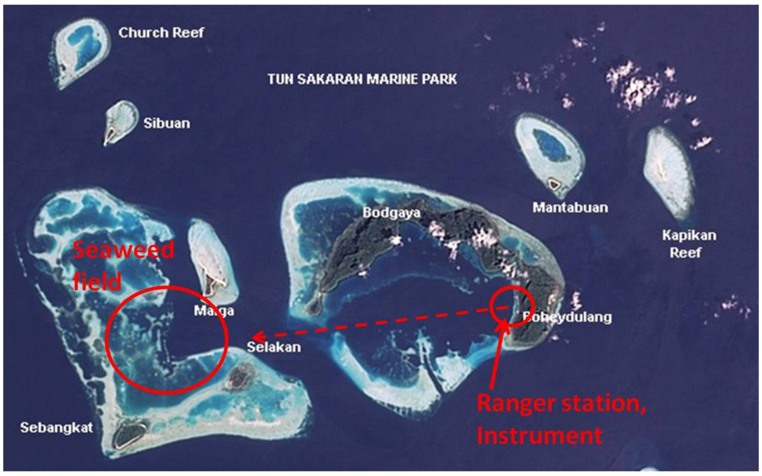

Figure 6.27: Map of the Tun Sakaran Marine Park (close to Semporna on Borneo, Malaysia). The MAX-DOAS instrument was installed at the island of Bohey Dulang. The viewing direction towards a commercial seaweed field (≈ 12 km) is indicated by a dashed arrow. Source: `http://www.sempornaislandsproject.com/pages/map.htm`

before this averaging procedure, consistent to the pre-processing of TransBrom data. The wind direction was measured by the ship's weather surveillance system and it was downloaded from the RV Sonne database after the campaign. The result is a MAX-DOAS measurement timeseries that can be considered to be free of influences from the ship's plume. The (vertical) pointing accuracy is $\pm 0.5°$, but the temporal resolution is in the order of the duration of one scan (typically 15 min) as a consequence of the averaging. Apart from minor problems, the ship-borne MAX-DOAS instrument operated automatically and reliably during the campaign and produced an almost complete timeseries of measurements[24].

After the ship-borne MAX-DOAS instrument was successfully installed at the RV Sonne in Singapore, the IUP-Bremen research team moved to Semporna in the northeast of Borneo (indicated by a red point in Fig. 6.26). Here, a second MAX-DOAS instrument was installed at the island of Bohey Dulang, which is located in the Tun Sakaran Marine Park in a distance of ≈20 km off the coast. A satellite image of the Marine Park and the island of Bohey Dulang is shown in Fig. 6.27. Bohey Dulang is an old volcanic crater, which is water-filled today (only half of the crater rim is still existing). A park Ranger station is located on the eastern side of the rim (oriented to the inside of the crater). The station provided electricity and an air-conditioned room for the spectrometers of the second MAX-DOAS instrument. A photo of the telescope unit installed outside the station is shown in Fig. 4.7 in chapter 4.

This measurement site was chosen because of its proximity to a commercial seaweed field, which is located close to the island of Selakan in a distance of ≈ 12 km from the Ranger station on Bohey Dulang. Underwater macro-algae are cultivated here in a large area indicated in Fig. 6.27. The algae grow immediately beneath the water surface and are a potential source of biogenic IO precursor species. Therefore, the MAX-DOAS main azimuthal pointing direction was towards the seaweed field as indicated by a red arrow in Fig. 6.27. In this direction, vertical scans were performed: Off-axis measurements from 1° to 6° elevation angle in 1° steps and additionally measurements in 8°, 10°, 15° and 30°.[25] At the end of each scanning sequence, a zenith spectrum was recorded.

The land-based instrument was installed at 17-18 November and operated until 27 November. Originally, the instrument was a 2-channel system like the ship-borne instrument, i.e. equipped

---

[24] At this point, many thanks to Johannes Lampel from IUP-Heidelberg who had a look after the IUP-Bremen MAX-DOAS instrument during the cruise and restarted the system if necessary.

[25] For the land-based measurements, no negative elevations were performed in the scanning sequence. These viewing directions were only necessary for ship-borne installations because of the roll angle correction.

Parameter	Settings	Remarks
Reference	Zenith	closest in time
Spectral range	417.5 - 438.2 nm	
Polynomial	2nd order	
Straylight corr.	Offset	
O_3	(Bogumil et al., 2003)	223 K
NO_2	(Vandaele et al., 1996)	298 K
VRS	retrieved	Approach 2, chap. 7 (Fig. 7.23)
IO	(Spietz et al., 2005)	
water vapour	HITRAN2009	
Ring	simulated	(e.g., Vountas et al., 1998)

Table 6.6: DOAS fit parameters for the IO fit during SHIVA.

with two spectrometers for the visible and the UV range, respectively. Unfortunately, the visible spectrometer turned out to be damaged which happened either on the transport from Germany to Borneo or later by transportation of the instrument from mainland to Bohey Dulang inside a small motorboat. However, extensive attempts to repair the system failed and consequently measurements could be performed in the UV only. As important trace gases, especially IO, are retrieved in the visible, the grating of the remaining (UV) spectrometer was re-adjusted at 23 November, i.e. after a few days (to ensure that some measurements have been performed successfully at least in the UV). Thus, only 4 days of IO measurements could be performed by the land-based instrument. After the re-adjustment, the (originally UV) spectrometer covered a range from $\approx$ 413–497 nm in the visible with a resolution of $\approx$ 0.5 nm.

6.2.2. SHIVA IO results

For the retrieval of IO from both, ship-borne as well as land-based measurements, settings similar to the IO fit during TransBrom were selected. The applied fit parameters are summarized in Tab. 6.6. In contrast to the IO fit during TransBrom, no fixed reference spectrum but the closest zenith spectrum was used as reference measurement I_0. This was possible because the MAX-DOAS instruments designed and built after the TransBrom cruise were equipped with cylindric plates shading the telescope's entrance window (e.g., see Fig. 4.7 in chapter 4) and therefore preventing direct sunlight to enter the telescope. This overcomes the problem of saturation effects on the CCD as observed during TransBrom (see above). A second difference to the TransBrom IO fit is that instead of a simulated VRS cross-section, this time the measured VRS spectrum retrieved in chapter 7 (see Fig. 7.23) was included as a cross-section in the fit. The measured VRS spectrum was chosen because it was found to increase the DOAS fit quality in comparison with a simulated VRS spectrum (see Fig. 7.24 in Sect. 7.6.3 and Fig. 7.33 in Sect. 7.7.1).[26]

The retrieved IO slant columns from ship-borne and land-based MAX-DOAS measurements during

---

[26] In chapter 7 it is recommended to use the experimental VRS spectrum only in combination with the specific liquid water absorption spectrum used in the retrieval fit. However, in the small IO fit window, all broad-band structures are considered to be compensated efficiently by the DOAS polynomial, especially the broad-band structure of liquid water absorption. For this reason, no liquid water cross-section is included at all and the experimental VRS spectrum can be used here.

Figure 6.28: IO example fit during SHIVA from ship measurements at 25 November 2011, 5:32 UT (37.3° SZA, 3° elevation angle).

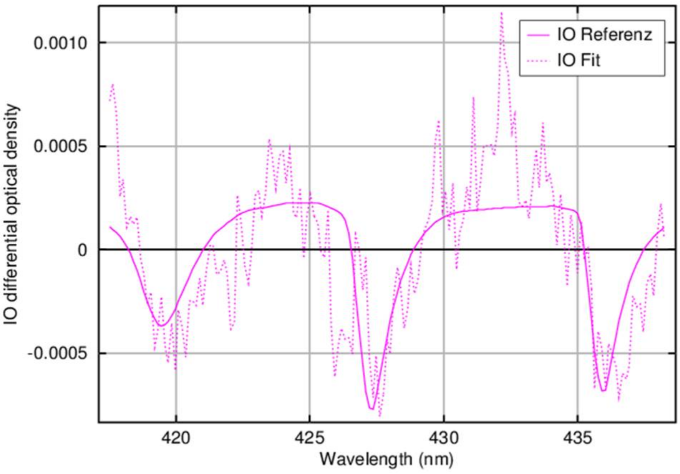

SHIVA are plotted in Fig. 6.29 color-coded for different elevation angles (as mentioned above, only 4 days of land-based IO measurements exist due to instrumental problems). In comparison to the ship-borne observations, larger slant columns were obtained from the land-based measurements on Bohey Dulang especially on 26 and 27 November 2011, most likely because of its proximity to the near-by seaweed field (Fig. 6.27).

For both, ship- as well as land-based measurements, the viewing directions in low elevation angles do not split-up very well. In the performed MAX-DOAS scanning sequences, largest slant columns are often observed in 4–5° elevation angle only. A possible explanation for this behaviour is an elevated layer of IO, which could be a result of slow photolysis of organic precursors emitted by algae. The lifetimes of organoiodines range from several days (e.g., CH_3I) over several hours (e.g., CH_2ICl) to about 5 min at midday (e.g., CH_2I_2) (Carpenter, 2003, and references therein). Thus, especially for the land-based measurements performed across a seaweed field, an elevated layer of IO might be realistic.

However, the same behaviour was found for the O_4 slant columns (which were retrieved in a larger fit window). The O_4 profile is a function of pressure only, i.e. under clear viewing conditions largest slant columns should be observed in lowest elevation angles. In contrast, O_4 slant columns in low elevation angles were found to be systematically smaller than maximum O_4 slant columns which occurred only at ≈ 5°. This is most pronounced in the ship-based measurements where often the O_4 slant column in 1° elevation angle is only half of the maximum value at ≈ 5°. In the land-based measurements this behaviour is present as well, although to a lesser extent (for illustration, see the red line in Fig. 6.30). As the O_4 slant column is a measure of the length of the light path, such behaviour suggests either a deep cloud cover or a strong (and strange/unclear) aerosol scenario (at least for the land-based measurements, a permanent, deep cloud cover was not observed by eye during the campaign). This limits the possibility for a profile retrieval, especially for the ship-borne data, as a realistic aerosol extinction profile is crucial.

As explained in Sect. 3.6.2, the first step of BREAM is to retrieve an aerosol extinction profile by comparing measured O_4 slant columns with O_4 slant columns that are simulated for different aerosol profiles using SCIATRAN. This method was tested for land-based measurements (because here the effect appeared to be less). In Fig. 6.30, measured and simulated O_4 slant columns are plotted as red and blue lines, respectively, for some scans at 26 November 2011 having very good weather and viewing conditions. Obviously, the simulations are not able to reproduce the men-

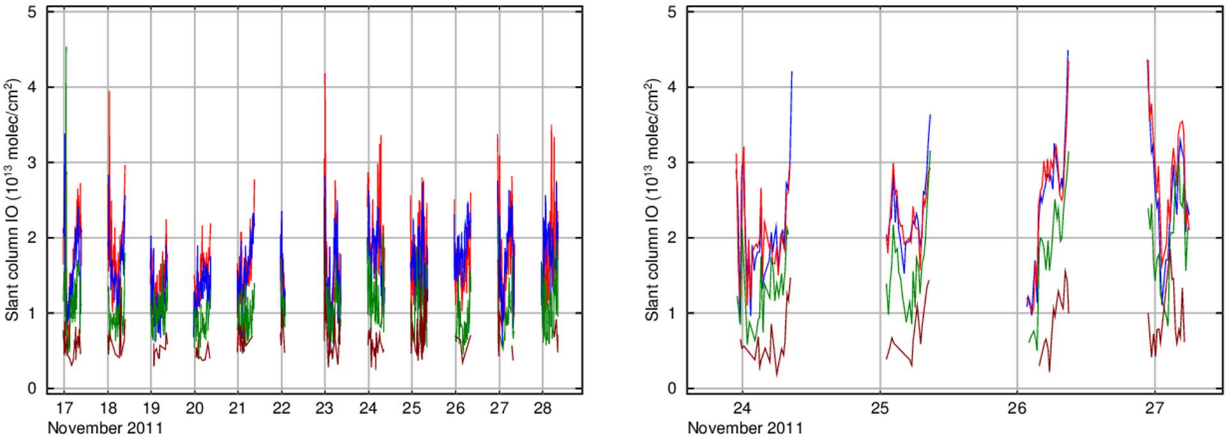

(a) Ship-borne measurements

(b) Land-based measurements

Figure 6.29.: IO slant columns retrieved from ship-based (Fig. 6.29(a)) and land-based (Fig. 6.29(b)) measurements during SHIVA. The elevation angle is color-coded (blue = 2°, red = 4°, green = 10°, brown = 30°).

tioned behaviour of small O_4 slant columns in low elevation angles. Although large efforts have been made changing the shape of the aerosol profile as well as the aerosol composition, unfortunately, all attempts failed. As a consequence, the results of the profile retrieval cannot be considered to be realistic. As mentioned before, this problem is even larger in the ship-based measurements.

Instead of using a profile retrieval, a more simple approach was performed in order to retrieve vertical columns and volume mixing ratios of IO. Therefore, only the slant columns in 5° elevation angle have been used. These are the observations of largest O_4 slant columns, i.e. longest light paths in the troposphere. In addition, the strange behaviour of small slant columns in low elevation angles stop around 5° as Fig. 6.30 demonstrates. For larger elevation angles, the O_4 slant columns decrease, as it is normally expected right from the beginning (i.e. from 1° on). Thus, the strange aerosol scenario is most uncertain close to the ground and affect the 5° elevation angle (as well as the following, larger elevation angles) to a much lesser extent as small elevation angles because the light path in the uncertain layer is comparably small. On the other hand, IO is expected to be relatively close to the ground as well (even if it can be speculated about an uplifted layer), i.e. a relative long light path in the boundary layer is needed. Thus, the 5° elevation angle appeared to be the best compromise to retrieve IO vertical columns and volume mixing ratios from.

In a first step, all IO slant columns (in 5° elevation angle) having fit errors $> 30\%$ were sorted out as they are considered to be unreliable. In addition, only slant columns taken at SZAs $\leq 80°$ were used to avoid light path extensions at low sun positions during twilight. An intensity limit was applied to remove (as far as possible) cloudy data. Finally, all slant columns below an estimated detection limt (DL) have been removed. The DL was calculated following the intuitive approach as explained in Sect. 6.1.3: For the IO fit described above, best RMS values are $\approx 1.5 \cdot 10^{-4}$. The differential optical structures of the IO cross-section in the applied fit window are $\approx 3 \cdot 10^{17}$ cm^2/molec. Assuming that IO can be detected if its optical density is twice as large as the typical RMS, a detection limit of DL $\approx 1 \cdot 10^{13}$ molec/cm^2 can be estimated for the slant columns.

After applying these restrictions, the left-over slant columns in 5° elevation angle have been converted into vertical columns using an AMF of 10. This AMF has been retrieved from SCIATRAN

Figure 6.30: Measured (red) and simulated (blue) O_4 slant columns from land-based measurements for a time period comprising 6 scanning sequences at 26 November 2011. The scans consist of the following elevation angles: 1°, 2°, 3°, 4°, 5°, 6°, 8°, 10°, 15°, and 30°. Obviously, the O_4 slant columns in 1° are systematically smaller than maximum slant columns at 5° and this behaviour cannot be reproduced by the simulations (blue line).

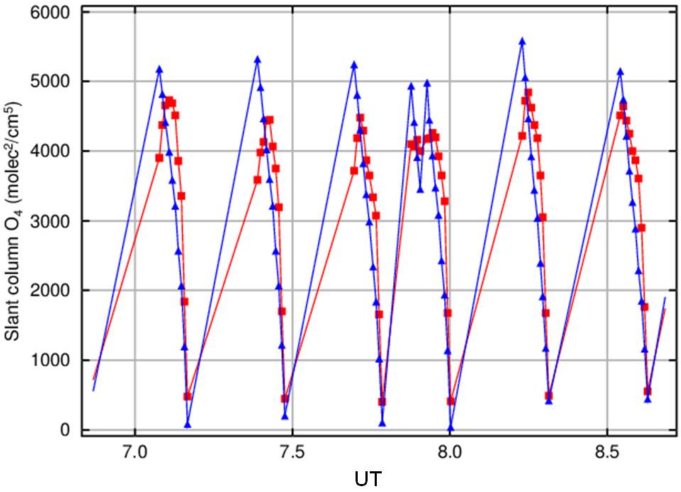

simulations for a maritime environment. Note, that this is only slightly smaller than the AMF derived from the simple geometrical approach $AMF_{\text{geo}} = 1/\sin(5°) \approx 11.5$. The detection limit estimated above corresponds to a vertical column of $\approx 1.1 \cdot 10^{12}$ molec/cm^2.

The resulting vertical columns from ship-based data are shown in Fig. 6.31(a), those from land-based data in Fig. 6.31(b). As all slant columns having $\leq 30\%$ error were used to calculate vertical columns, the data in Figs. 6.31(a)–6.31(b) are again plotted with an uncertainty of 30%. The ship-based vertical columns are in a range of $1 - 4 \cdot 10^{12}$ molec/cm^2. For the land-based measurements, vertical columns at 24 and 25 November are comparable with the ship-based vertical columns, while they are slightly higher (between $\approx 2 - 5 \cdot 10^{12}$ molec/cm^2) at 26 and 27 November. The afternoon of 26 November and the whole 27 November were extremely sunny and had excellent viewing conditions. A clear sight towards the seaweed field in $\approx$ 12 km distance could explain the slightly higher values. Also, some cloudy periods occured especially on 24 November. As the IO is considered to originate from iodine precursor species emitted by the seaweed, less light could cause a lower photolysis rate of these precursors and therefore smaller IO amount compared to the sunny periods at 26 and 27 November. In general, larger IO columns from land measurements compared to the ship measurements can be expected because of the proximity to the near-by commercial seaweed field.

In comparison to the vertical columns observed during TransBrom (ranging from $\approx 1 - 2.5 \cdot 10^{12}$ molec/cm^2) the IO columns measured during SHIVA are higher. This is expected because for the IO during TransBrom only an inorganic source - release from the ocean surface by inorganic reactions - is suggested (see Sect. 6.1.5). In contrast, the SHIVA campaign was carried out (most of the time) in a coastal environment where much more biogenic activity can be found than over the open ocean; this is even true for the ship-based measurements over the Sulu sea (between Borneo and the Phillippines, see cruise track in Fig. 6.26), which is very deep but has more biologic activity than the open ocean (this can be seen from the chlorophyll map in Fig. 6.25). Thus, larger IO amounts (from biogenic precursor emissions) compared to TransBrom are reasonable.

In a further step, volume mixing ratios were derived from the vertical columns by a simple approach: A block profile was assumed, i.e. a constant IO volume mixing ratio from ground to the mixing layer height (and no IO above). As an input parameter, the mixing layer height was selected to be 500 m. This is the average mixing layer height retrieved from radio sondes during the TransBrom campaign over the remote ocean (see Fig. 6.21 in Sect. 6.1.5). Although the measurements during

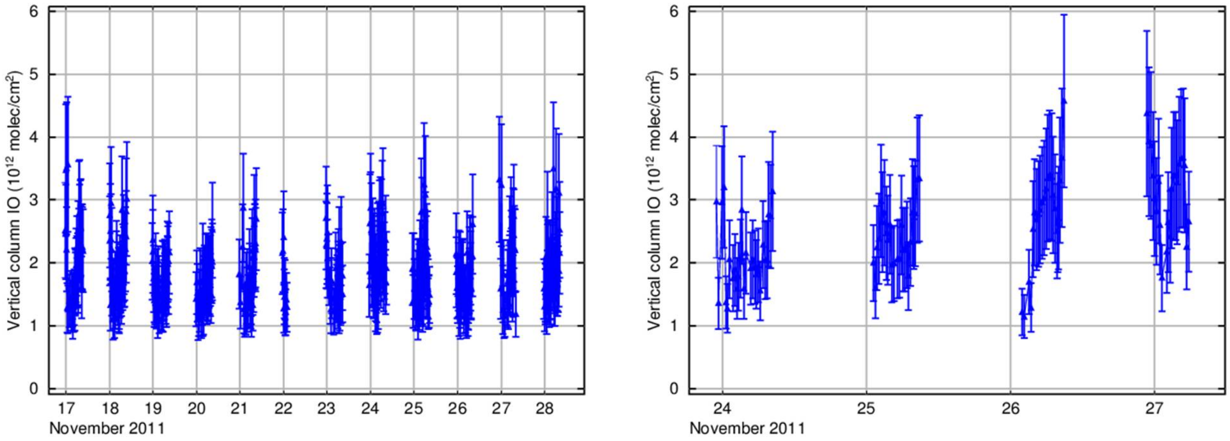

(a) Vertical columns from ship measurements (b) Vertical columns from land measurements

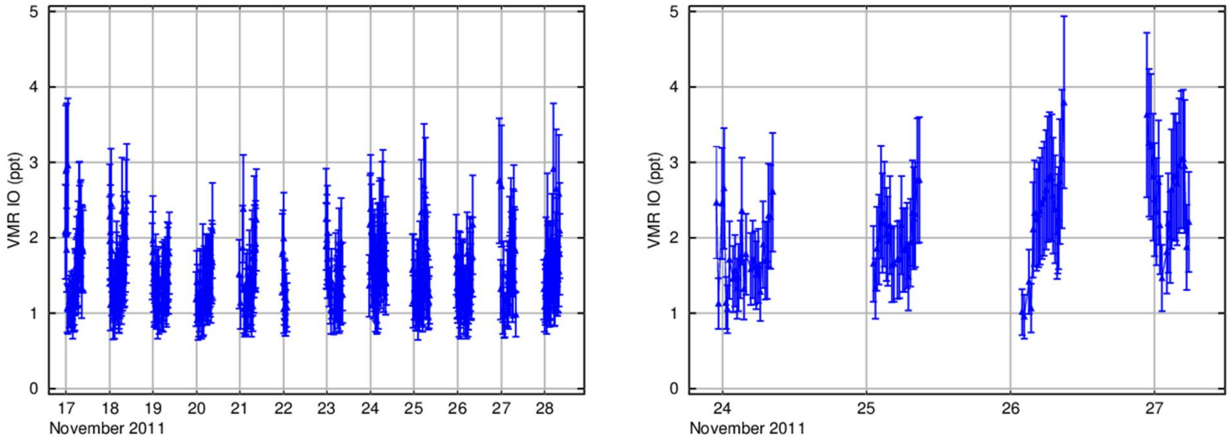

(c) VMR from ship measurements (d) VMR from land measurements

Figure 6.31.: IO vertical columns and volume mixing ratios retrieved from ship-based and land-based measurements during SHIVA.

SHIVA have been performed not above the remote ocean but in a marine environment close to the coast, this value was chosen as the mixing layer height over land is quite variable (e.g., see Fig. 5.14 in Sect. 5.4). It should be clearly pointed out that due to the missing possibility of running a standard BREAM profile retrieval on the SHIVA data, the vertical columns and volume mixing ratios retrieved here are only estimates.

Under the assumptions described above, the IO volume mixing ratios have been calculated according to

$$VMR = \frac{VC}{MLH} \cdot \frac{k_B \cdot T}{p} \tag{6.9}$$

with the Boltzmann constant k_B, the temperature $T = 300$ K and the pressure $p = 1 \cdot 10^5$ Pa.

The calculated IO volume mixing ratios are shown in Fig. 6.31(c) for the ship-based measurements and in Fig. 6.31(d) for the land-based measurements, respectively. Note that due to Eq. 6.9, the vertical columns and obtained volume mixing ratios are proportional. For this reason, the volume mixing ratios have been plotted again with an error of 30%. Also the shape of the volume mixing ratio timeseries is identical to the vertical column timeseries. Thus, no new information can be obtained from this timeseries and the comments and characterisation of the vertical columns given

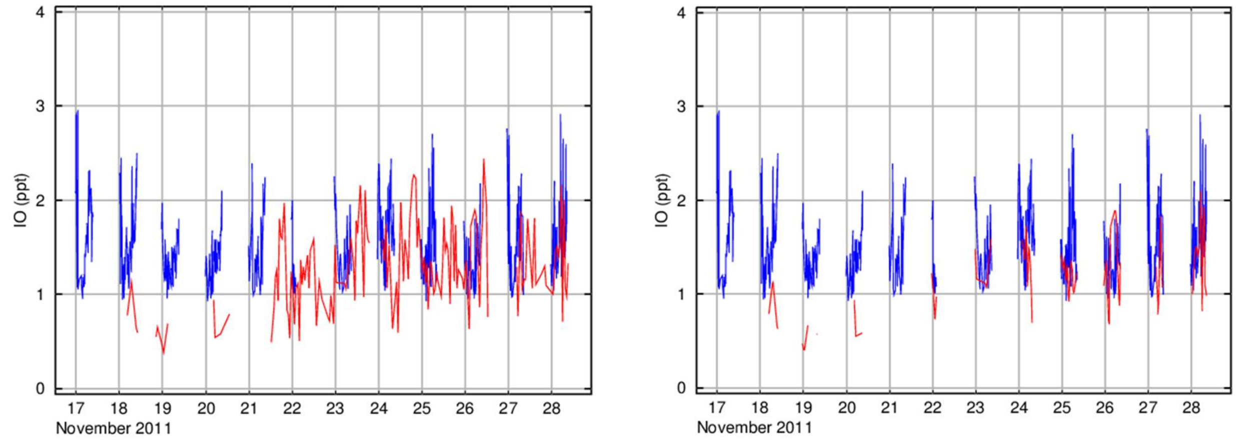

(a) MAX-DOAS (blue) and LIF (red) IO VMR

(b) LIF values interpolated to MAX-DOAS time

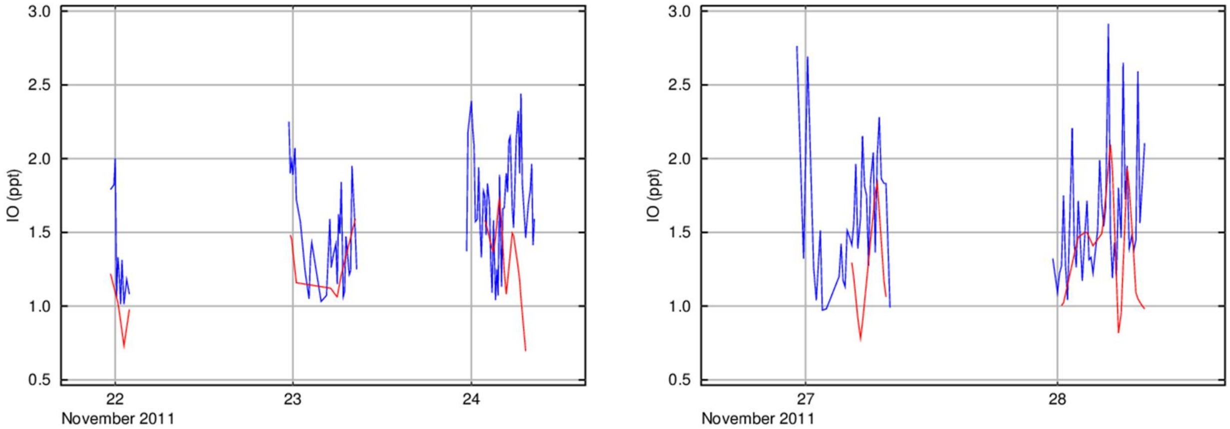

(c) Interpolated LIF and MAX-DOAS, Nov. 22–24

(d) Interpolated LIF and MAX-DOAS, Nov. 27–28

Figure 6.32.: IO volume mixing ratios retrieved from ship-based measurements during SHIVA (blue line) compared to LiF measurements of IO (red line). Figs. 6.32(c) and 6.32(d) are excerpts from Fig. 6.32(b).

above (differences ship - land etc.) applies to the volume mixing ratios as well.

In general, the ship-based volume mixing ratios range from 1–3 ppt (mostly between 1–2 ppt), the land based measurements from 1–4 ppt. No diurnal cycle was found in any of the data sets. The detection limit estimated above corresponds to ≈ 0.9 ppt. In comparison to TransBrom IO results (< 2 ppt), the volume mixing ratios during SHIVA are larger. As already mentioned, this is considered to be a consequence of biogenic iodine release in the coastal environment where SHIVA measurements were performed. During TransBrom (inorganic release from the interfacial surface layer), maximum IO concentrations were found close to the ground (see Fig. 6.24). As no profile retrieval is possible for SHIVA data, this cannot be verified. However, the obtained slant columns (Fig. 6.29) might be a hint that IO could be higher up in the atmosphere. Unfortunately, the performed simple retrieval of VMR estimates is not able to clarify this as all IO has been assumed to be confined in a block-profile.

During the SHIVA ship cruise, measurements of IO were performed also by the University of Leeds using a Laser-Induced Fluorescence (LIF) instrument which was installed onboard the RV Sonne. The IO volume mixing ratios derived from these measurements are shown in comparison to the

MAX-DOAS results in Fig. 6.32.[27]. For a better comparison and visibility, no error bars are plotted. In Fig. 6.32(a), all LIF data is plotted while in Fig. 6.32(b), the LIF data has been interpolated to the time of MAX-DOAS measurements.

In general, the LIF volume mixing ratios range from ≈ 0.5–2.5 ppt and are therefore slightly smaller than MAX-DOAS IO results. Especially in the first half of the cruise being in the South China Sea (see cruise track in Fig. 6.26) the LIF data is smaller and sometimes only half of the MAX-DOAS values. In contrast, MAX-DOAS and LIF values are comparable in the second half of the cruise. Here, both instruments suggest IO volume mixing ratios in the range of ≈ 0.8–2.5 ppt (Fig. 6.32(a)). In addition, MAX-DOAS and interpolated LIF data in Fig. 6.32(b) sometimes reproduce the same general shape, which is illustrated by Figs. 6.32(c) and 6.32(d) being a zoom-in of Fig.6.32(b). Reproducing the same shape by different instrument types is a strong hint that the retrieved IO is real. Nevertheless, even in the second half of the cruise the LIF IO is on the bottom end of MAX-DOAS IO values (most obvious in Fig. 6.32(b)). However, as only the 5° elevation angle has been used to convert slant columns into vertical columns and a simple approach assuming a block profile and an arbitrary mixing layer height was used to calculate volume mixing ratios, LIF and MAX-DOAS values cannot be expected to match precicely (for example, if the mixing layer height was doubled, the resulting volume mixing ratio according to Eq. 6.9 would be halved). Thus, the general agreement of both instrument types on a range of ≈ 1–2.5 ppt can be regarded as a success.

6.3. Summary

During the ship-based field campaign TransBrom, MAX-DOAS measurements of formaldehyde, nitrogen dioxide (both stratospheric as well as tropospheric) and iodine monoxide were performed in the western Pacific. This was motivated by addressing the problem of uncertain satellite-borne measurements of tropospheric trace gases over the remote ocean where a) the concentrations are usually very low and b) spectral impacts of liquid water potentially influence and disturb the DOAS fit (which appears to be especially problematic for the IO retrieval, see negative slant columns over the remote ocean in Fig. 1.1). While the impact of spectral structures of liquid water is subject of chapter 7, in this chapter, the performed MAX-DOAS measurements during TransBrom were used to retrieve background concentrations of trace gases over the remote ocean and (if possible) to validate corresponding measurements from the SCIAMACHY and GOME-2 satellite instruments. As a MAX-DOAS instrument is more sensitive for the lower troposphere than a satellite, its measurements are well-suited for this purpose. The nitrogen dioxide and formaldehyde satellite validation was published in (Peters et al., 2012), the measurements of IO were published in cooperation between IUP-Heidelberg and IUP-Bremen by (Großmann et al., 2013).

Stratospheric NO_2 columns obtained during TransBrom show a characteristic latitude-dependent U-shaped behaviour (Fig. 6.5). This shape is reproduced by both satellite instruments, SCIAMACHY as well as GOME-2. MAX-DOAS morning values of stratospheric NO_2 are lower than evening values because of the slow photolysis of N_2O_5 causing an increase of stratospheric NO_2 during the course of the day. In low latitudes an increase of $8.7 \pm 0.5 \cdot 10^{13}$ molec/cm^2/h was estimated. Stratospheric NO_2 columns from SCIAMACHY and GOME-2 differ by only ≈ 1% from each other and by an absolute value of $(0.45 - 0.68) \pm 1.3 \cdot 10^{14}$ molec/cm^2 from the MAX-DOAS

---

[27] For this data, many thanks to Hannah Walker, School of Chemistry, University of Leeds, UK.

morning values, which is a consequence of the satellite's overflight time (09:30 LT resp. 10:00 LT) and the stratospheric NO_2 diurnal cycle (Fig. 6.6).

Troposperhic NO_2 over the remote ocean was mostly below the estimated detection limit of ≈50 pptv or $1.3 \cdot 10^{14}$ molec/cm^2 for the vertical column, which can therefore be considered as an upper estimate for typical NO_2 levels in this remote area. The estimated limit is also in agreement with monthly averages from GOME-2. Events over the open ocean could assigned to passing of other ships or crossing of frequently used shipping routes (Figs. 6.7 and 6.2c). In the polluted marine environment close to Japan, NO_2 events were observed with peak concentrations of up to 0.8 ppbv close to the ground, whereas the background concentration did not exceed 0.2 ppbv (Fig. 6.10).

Formaldehyde was successfully detected for the whole campaign and considered to originate mainly from methane oxidation that requires daylight. This is supported by the characteristic diurnal cycle that was found for the HCHO vertical columns as well as profiles (most obvious at cloud-free conditions, see Fig. 6.15 and 6.16). Maximum values for the vertical column under cloud-free conditions were found to be $4 \cdot 10^{15}$ molec/cm^2 corresponding to a peak concentration of 1.1 ppbv (Fig. 6.16), which is slightly higher than earlier reported values ranging from 0.2–1 ppbv (e.g., Weller et al., 2000; Singh et al., 2001; Burkert et al., 2001), but by far lower than maximum values of 4.5 ppbv found by the DOAS technique in a tropical rain forest environment on Borneo, Malaysia (MacDonald et al., 2012). Furthermore, the maximum concentration of 1.1 ppbv found above the open ocean on 14 October could be caused by enhanced levels of precursor compounds other than methane (e.g., DMS, methanol) from oceanic sources. The diurnal cycle of formaldehyde is in good agreement with earlier reported observations from (Still et al., 2006) in the remote marine boundary layer. Additionally, a transport event of formaldehyde or its precursors was found ≈150 km away from the only possible source (island with rainforest vegetation) and calculated backward trajectories suggest that the formaldehyde or its precursors bridged this distance in 12–18 h before being detected by the MAX-DOAS instrument. Finally, GOME-2 and MAX-DOAS measurements agree on a typical vertical column about $3 \cdot 10^{15}$ molec/cm^2 for the remote ocean at the overpass time (Fig. 6.18).

The retrieved IO optical density during TransBrom is close to the detection limit and has a large uncertainty, i.e. the results have to be considered with care. However, IO levels retrieved from the IUP-Bremen and the IUP-Heidelberg MAX-DOAS instruments (both participating in TransBrom) agree within ≈50% and (even more important) show the same behaviour: 1) Maximum IO levels occured over the open ocean. 2) No correlation was found between IO retrieved from MAX-DOAS and organic precursors measured in situ (e.g., CH_2I_2). 3) No correlation was found between IO and the chlorophyll-a concentration. 4) An anti-correlation was found with O_3 in low altitudes, which was retrieved from ozone sondes. Therefore, an inorganic iodine release mechanism (from the ocean) is suggested. Because of the anti-correlation to O_3 this could be inorganic (ozone-depleting) reactions of aqueous iodide (I^-) with gaseous O_3 in the interfacial layer as proposed for example by Carpenter et al. (2013). Furthermore, model simulations (including only the atmosphere) require an *artificial* I_2 flux of $\approx 1.8 \cdot 10^8$ molec/cm^2/s to reproduce the observations (Großmann et al., 2013). This is in agreement with reported magnitudes of the I_2 release from iodine solutions in laboratory measurements by Carpenter et al. (2013, red line in Fig. 1a upper panel). It is suggested to include this release mechanism in chemical models to reproduce the observations (however, uncertainties exists, especially the influence of DOM). In general, over the open ocean - where satellites retrieve negative IO values - the MAX-DOAS measurements during TransBrom suggest IO concentrations of 0.5–2 ppt close to the surface or $1 - 3 \cdot 10^{12}$ molec/cm^2 for the vertical column, respectively.

In addition to TransBrom, IO in the tropical marine troposphere has been measured also during the SHIVA campaign in November 2011. The IUP-Bremen contributed to the campaign with two MAX-DOAS instruments. One instrument participated on the RV Sonne cruise from Singapore to Manila and the other instrument was installed at the island of Bohey Dulang in the Tun Sakaran Marine Park ≈ 20 km off the Malaysian coast of Borneo. From the ship-based measurements, IO vertical columns between $1 - 4 \cdot 10^{12}$ molec/cm^2 and volume mixing ratios between 1 and 3 ppt were retrieved. These levels are larger compared to the TransBrom results, most likely because the IO during TransBrom was measured above the open ocean and is supposed to originate from inorganic release only (see above). In contrast, the SHIVA campaign was carried out almost entirely in a coastal environment where more biogenic activity exists that is considered to produce precursors of IO. The IO levels measured from the land-based instrument on Bohey Dulang were occasionally even higher than ship-borne results and ranged between 1–4 ppt ($1 - 5 \cdot 10^{12}$ molec/cm^2 for the vertical columns). The reason is that these measurements were not only performed in a coastal environment but also close to a commercial seaweed field (≈ 12 km distance). Macro-algea (which were cultivated there) are known to produce organoiodines which are released to the atmosphere where they can be converted into IO.

7. Evaluation of the effects of absorption and scattering in liquid water on the DOAS analysis

7.1. Introduction and objectives

About 70% of the Earth's surface is covered by water giving the whole planet a blue shine as observed from space (first astronauts called it *the blue planet*). This demonstrates the importance of spectral impacts from liquid water for observations based on spectrometry over water surfaces. In the public, and sometimes even within the scientific community, it is a frequent misconception that the ocean is blue due to Rayleigh scattering or reflection of the blue sky. The sky is blue as a consequence of the preferred scattering of photons having short wavelengths (λ^{-4}-dependence). This effect is indeed present in liquid water as well giving rise to its bluish hint; but above this effect water has an intrinsic blue color as a result of its absorption coefficient, resp. its cross-section[28]. The light absorption of pure liquid water is relatively weak in the visible range. As a result, small amounts of water (i.e. a glass or bottle of water) appear to be transparent. Only when the light path through the water is at least in the range of meters, pure liquid water developes its intrinsic blue color. A famous example is the Blue Grotto on Capri, Italy. Its water is shining blue because almost all light enters the cave below the water surface, i.e. transmitted through

Figure 7.1.: Intense blue color of Pacific ocean water while being in a region of extremely low suspended particle content (during the TransBrom cruise).

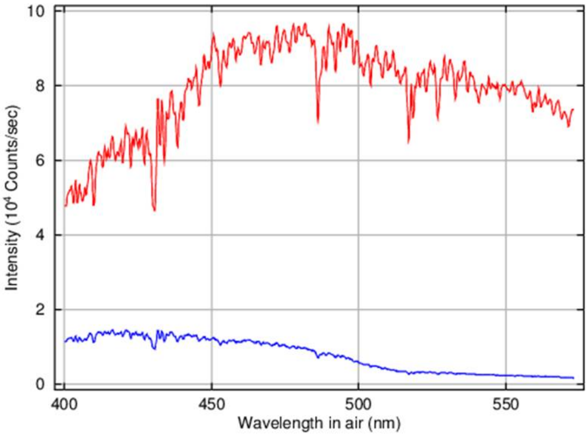

Figure 7.2.: Spectra recorded spectra towards the water surface for the scene shown in Fig. 7.1. Blue: Clear water (undisturbed view), red: Sea spray from ship's bow wave in the field of view.

---

[28] As differing only by the density (see Sect. 3.4.1), the terms *absorption coefficient* and *cross-section* are used synonymously for liquid water ($\rho \approx$ const.) in this section.

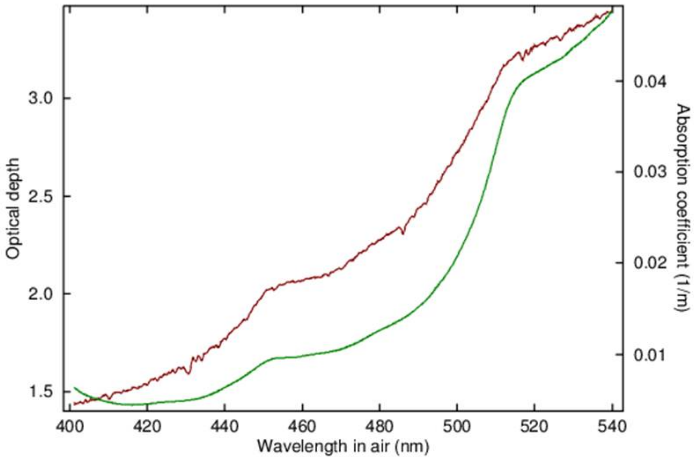

Figure 7.3.: Logarithm of the ratio of the spectra shown in Fig. 7.2 in brown and liquid water absorption coefficient from Pope and Fry (1997) in green.

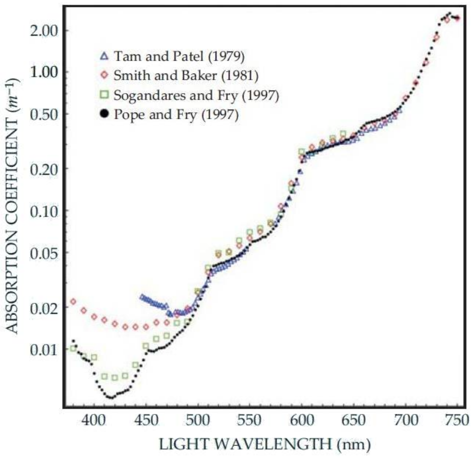

Figure 7.4.: Comparison of the liquid water absorption coefficient as measured by different groups, image taken from Dickey et al. (2011).

several meters of liquid water. In the same way, cracks and holes in ice glaciers have a blue shine because here photons escape that have passed through the ice (while the glacier surface is white as reflecting all wavelengths in the visible). Sunlight penetrating the ocean surface and travelling several meters under water before being backscattered into the atmosphere causes the blue color of the sea. However, the color of oceans, rivers and seas is mostly dominated by suspended particles or matter (i.e. phytoplancton, sediments). In general, the cleaner the water is, the more intense becomes its blue color (see Fig. 7.1).

For the scene in Fig. 7.1, taken on 14 October 2009 during the TransBrom cruise, spectra towards the water surface (-45° elevation angle) are shown in Fig. 7.2. The blue spectrum is a measurement towards the clear, *undisturbed* water surface and consists of photons that on average travelled several meters within the water before being scattered into the instrument's line of sight. Periodically (depending on the roughness of the sea), white sea spray from the ship's bow wave covered the scene that was observed by the small field of view of the instrument (red spectrum). The spectrum of this white sea spray can be regarded as the reflection of the incoming light before penetrating the water. As a consequence, almost no spectral effects of liquid water are present in this spectrum (in practice, the observed scene is not completely covered by sea spray and subsequently some influences from liquid water are present). Thus, the spectral impact of liquid water can be observed by comparing the blue and the red spectrum (this has been analysed in terms of a DOAS fit in Sect. 7.5).

If the difference between the red and the blue spectrum in Fig. 7.2 is considered to be the result of the light path under water (which is in the range of several tens of meters for these measurements, see Sect. 7.5), the slant optical density of liquid water can be calculated according to the Lambert-Beer law

$$I(\lambda) = I_0(\lambda) \cdot e^{-\tau_{water}(\lambda)} \tag{7.1}$$

$$\Leftrightarrow \ln\left(\frac{I_0(\lambda)}{I(\lambda)}\right) = \tau_{water}(\lambda) \tag{7.2}$$

where I_0 denotes the initial spectrum (red spectrum in Fig. 7.2) and I the attenuated spectrum after penetrating the water surface, passing through a water column of length s and being backscattered into the telescope (blue spectrum in Fig. 7.2). As the water density ρ is constant, the resulting slant optical density is proportional to the liquid water absorption coefficient (with the light path s being the scaling factor) as well as the liquid water absorption cross-section $\sigma(\lambda)$ (with the scaling factor $\rho \cdot s$).

The optical density $\tau_{water}(\lambda)$ is compared to the pure liquid water absorption coefficient as measured by Pope and Fry (1997) in Fig. 7.3. Both increase with wavelength in the visible range. As a result, the red part of the visible spectrum is suppressed in water leaving radiance and consequently water appears to be blue.

Although resulting from a single field measurement, the optical density shows remarkable similarity to the liquid water absorption coefficient measured in laboratory by Pope and Fry (1997), e.g. the shoulders around 450 nm and 515 nm (an explanation of the shoulders is given in Sect. 7.3). Note that the MAX-DOAS field measurements are observations of scattered light, i.e. the brown curve in Fig. 7.3 contains elastic and inelastic scattering effects. Nevertheless, the similarity to the water absorption is obvious demonstrating that these measurements are well-suited to study the liquid water absorption spectrum (after subtracting a polynomial accounting for elastic scattering, the two curves in Fig. 7.3 would agree even better). Nevertheless, discrepancies exist: For example, in the optical density derived from DOAS measurements leftover structures from Fraunhofer lines can be found indicating the presence of an effect similar to the Ring effect (as the Fraunhofer lines have not cancelled out completely according to Eq. 7.2). Two effects of inelastic scattering, the Vibrational Raman Scattering (VRS) in liquid water as well as the Brillouin Scattering are known to potentially cause leftover Fraunhofer structures.

Fig. 7.4 shows published pure water absorption coefficients as measured by different groups (Dickey et al., 2011). While good agreement is found at wavelengths > 500 nm, differences increase towards lower wavelengths (400-500 nm) as a result of weak absorption in this spectral range making measurements challenging. For the DOAS analysis, this is a critical region as many trace gases are fitted between 400 and 500 nm, i.e. iodine monoxide, nitrogen dioxide, glyoxal, or ozone, implying that the uncertainty of the liquid water absorption coefficient introduces problems to DOAS measurements above water surfaces (Sect. 7.2 gives an overview about previous studies focusing on this issue).

In general, the liquid water absorption spectra from laboratory measurements show only broad structures (Fig. 7.4). If the fit window is small enough, the broad liquid water spectrum is compensated by the polynomial of the DOAS fit and the problem reduces to the small structures from Fraunhofer lines. However, if the DOAS fit window is large, the fitted polynomial is unable to compensate even for the broad structures and a liquid water absorption cross-section has to be included in the fit (e.g., Richter and Burrows, 2000; Schönhardt, 2009).

Unfortunately, the absorption coefficient is provided by recent laboratory studies only at coarse resolution (e.g., Pope and Fry (1997) give the absorption coefficient for 2.5 nm spectral spacing, but state that the resolution is even lower, about 7 nm). Therefore, the exact position and shape of the observed shoulders is uncertain. For the DOAS analysis, such an uncertainty on the wavelength axis is a problem because trace gas absorption structures used to identify different species are often in the same range. Consequently, when strong liquid water absorption is present in the measurements, the uncertainties caused by the coarse resolution can dominate other trace gas absorption features and therefore decrease the fit quality.

In addition, literature values for the liquid water absorption coefficient correspond to standard conditions and pure water while real DOAS measurements encounter various water properties (temperature, salinity, suspended matter etc.). Thus, using an average cross-section for liquid water, resp. a correction spectrum for the existing pure water spectrum is desired.

To summarize, the study presented in this chapter aims at the investigation of liquid water effects with respect to the DOAS analysis, in particular:

- Retrieval of an average liquid water absorption cross-section (or a correction spectrum for existing cross-sections) under field conditions (averaging over true water properties) at a better spectral resolution than literature values in order to improve the DOAS fit quality over water surfaces.

- Sensitivity studies of the influence of inelastic scattering in the water (VRS and Brillouin) on the DOAS analysis and retrieval of an average VRS spectrum (or correction spectrum) to improve the fit quality.

This is achieved by using MAX-DOAS measurements towards the ocean's surface taken during the field campaign TransBrom (Sect. 6).

In Sect. 7.2, previous studies focussing on the liquid water spectral effects and their impact on remote sensing techniques are summarized. The theoretical background of the liquid water absorption spectrum (broad-band structure) as well as inelastic scattering effects in liquid water (broad- and narrow-band structures) is given in Sect. 7.3 and 7.4. In addition, theoretical limitations and errors in the DOAS analysis due to inelastic scattering effects are discussed in Sect. 7.4. In Sect. 7.5, the presence of liquid water spectral structures in MAX-DOAS field measurements from the TransBrom campaign is demonstrated and in Sect. 7.6, experimental cross-sections and correction spectra for existing literature cross-sections are derived from these observations. In Sect. 7.7, the impact of these empirically retrieved cross-sections, resp. correction spectra on the DOAS analysis is tested in satellite data.

7.2. Previous studies of the liquid water impact on remote sensing measurements

Several previous studies on the issue of liquid water impacts on remote sensing measurements exist. Most of them address effects of inelastic Raman scattering. In Sect. 3.3.1 and Sect. 3.3.3 it was already pointed out that inelastic Rotational Raman Scattering (RRS) on air molecules leads to a filling-in of Fraunhofer structures, which is known as the Ring effect and needs to be considered in the analysis (e.g., see Burrows et al., 1996, and references therein). In the ocean, molecular rotations are suppressed, but the inelastic Vibrational Raman Scattering (VRS) on H_2O molecules in the liquid phase leads to spectral shifts resulting in a similar Ring effect (see explanation in Sect. 7.4.1).

Spectral studies of the Raman effect in liquid water have been performed by Walrafen (1967) who also described the shape of the Raman band (see Sect. 7.4.1). Kattawar and Xu (1992) used a Monte Carlo method to model the filling-in of Fraunhofer lines caused by vibrational Raman scattering in the visible. Aiming on the application in satellite measurements, existing models (in the visible) have been extended into the UV region (Vasilkov et al., 2002, and references therein). In the UV, the filling-in of Fraunhofer lines by VRS in the ocean is decreased by chlorophyll and dissolved organic matter (DOM) as they absorb UV radiation. This was used to retrieve the oceanic chlorophyll content by Joiner et al. (2004).

Vountas et al. (2003) studied the impact of VRS on trace gas retrievals from satellite instruments (GOME) and found that neglecting VRS can cause significant errors, e.g. more than 30% for BrO slant columns over clear ocean scenarios.

In order to improve satellite DOAS measurements over water surfaces, Schönhardt (2009) tried to retrieve cross-sections linked to effects in liquid water from ground-based MAX-DOAS field measurements that were performed during a ship-borne campaign across the Atlantic ocean. Small-band structures were found, but they did unfortunately not improve the fit quality of satellite measurements.

Rozanov and Dinter (2013) modelled the effect of inelastic Raman scattering in ocean water using the radiative transfer model SCIATRAN. Spectra of vibrational Raman scattering simulated with this version of SCIATRAN are also used in Sect. 7.4.1 in order to estimate their impact on the DOAS analysis.

7.3. The absorption spectrum of the H_2O molecule

For most substances, the absorption cross-section (resulting in the typical color of a substance) is caused by photon induced electronic transitions. In contrast, the liquid water absorption cross-section is not caused by electronic transitions but by vibrational (in the gas phase also rotational) transitions of the molecule. Electromagnetic waves (photons) do not interact with the induced dipole moment but with the permanent dipole moment of the H_2O molecule (for theory, see Sect. 3.2), i.e. the photons excite vibrational modes. An interesting side-effect is that *heavy water* (D_2O instead of H_2O, where the hydrogen atoms are replaced by deuterium atoms resulting in a 10% increased mass due to the two additional neutrons) is colorless (Braun and Smirnov, 1993). This is, because the absorption bands in the red are shifted to the near infrared as a consequence of the higher moment of inertia (going along with the increased mass) which causes a shift of vibrational

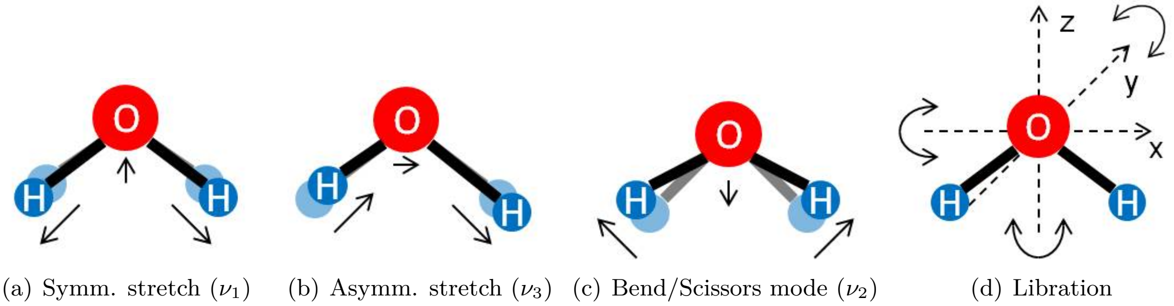

(a) Symm. stretch (ν_1) (b) Asymm. stretch (ν_3) (c) Bend/Scissors mode (ν_2) (d) Libration

Figure 7.5.: 7.5(a) - 7.5(c): Fundamental H_2O vibration modes, 7.5(d): Librations (around all three axes).

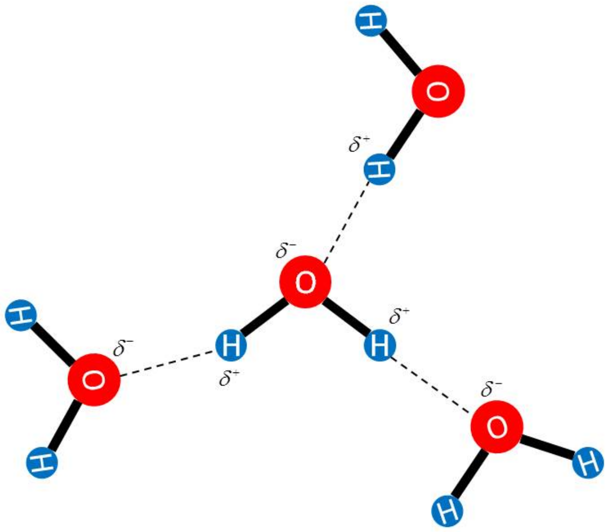

Figure 7.6: Hydrogen bonds between H_2O molecules in the liquid phase forming complexes (polymers). Due to the hydrogen bond length, the water density decreases with growing complex size (therefore ice is less dense than liquid water). With increasing temperatures, more hydrogen bonds break.

energy levels. If the absorption cross-section was caused by electronic transitions, no difference in absorption characteristics between different isotopes would be observed.

Fig. 7.5 shows the fundamental vibration modes of the H_2O molecule. In the absorption spectrum of liquid water, the stretch modes of the OH bond (Fig. 7.5(a), 7.5(b)) are dominant structures and occur at wavenumbers of ≈ 3400 cm^{-1}. The bend or scissors mode (Fig. 7.5(c)) appears at ≈ 1600 cm^{-1}. Consequently, the absorption due to excitation of fundamental vibration modes occurs in the infrared (≈ 3 μm for the OH-stretch modes and ≈ 6 μm for the scissors mode), not directly affecting the visible spectrum. The absorption in the visible range is caused by harmonics[29] and linear combinations of these fundamental modes and can be identified as shoulders in the absorption spectra in Fig. 7.4. E.g. the shoulder at ≈ 450 nm in Fig. 7.3 being visible in both, MAX-DOAS and literature values, corresponds to the seventh harmonic of the OH-stretch. Pope and Fry (1997) identify different shoulders in the absorption spectrum presented there.

The exact position of vibrational absorptions in the spectrum (and therefore the position of shoulders) is temperature dependent, as a consequence of hydrogen bonds in liquid water: In the H_2O molecule, oxygen is more electronegative than hydrogen resulting in a partial negative charge (δ^-) while the hydrogen atoms develop a partial positive charge (δ^+) as the binding electrons are located on average closer to the oxygen atom. Due to this structure of the H_2O molecule, an asymmetric charge distribution is formed (causing the permanent dipole moment) and intermolecular attractive forces develop, so called hydrogen bonds (Fig. 7.6). In liquid water, molecules arrange according to their asymmetric charge distribution and form clusters. The hydrogen bond's energy ranges from 5 - 30 kJ/mol (weaker than covalent or ionic bonds but stronger than Van-der-Vaals bonds). The hydrogen bonds decrease the vibrational energy levels for OH-stretches and thus cause a red-shift of vibrational transition energies by several hundred wavenumbers[30] (Braun and Smirnov, 1993, and references therein). With increasing temperature, hydrogen bonding decreases in importance, as a larger fraction of bonds is broken. As a result, the red-shift is temperature dependent (lower temperatures leading to a larger red-shift).

In the gas phase, H_2O exhibits a vast number of absorption lines resulting from many combined

---

[29] As the Schrödinger equation is a linear, homogeneous differential equation, each linear combination of fundamental solutions is again a solution. The integer multiple of a fundamental mode is called a harmonic.

[30] For example, for an initial wavelength of 400 nm, a shift of 100 cm^{-1} would correspond to 1.6 nm.

Figure 7.7: Illustration of a Raman band. The line shape was calculated according to (Walrafen, 1967) and (Kattawar and Xu, 1992) and is a superposition of different Gauss curves for monomers (single molecules) and polymers (H_2O complexes).

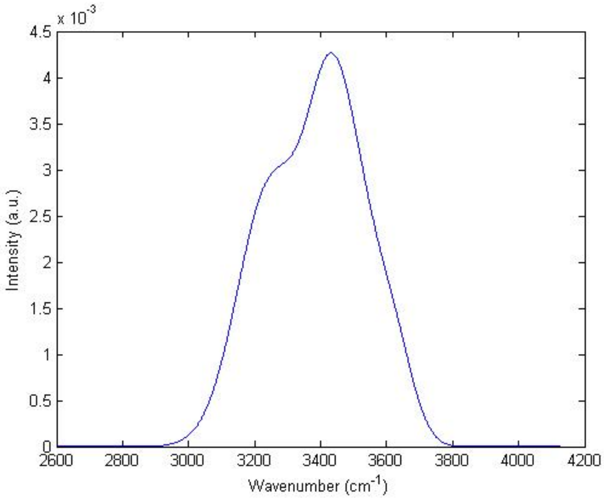

vibrational-rotational energy levels (as a consequence of H_2O's small moment of inertia of rotation). In the liquid phase, H_2O molecules are not free to rotate as a result of the intermolecular hydrogen bonding. Thus, these numerous absorption lines are suppressed. Instead of rotating, the molecules can only perform *Librations* around all three spatial axes 7.5(d) which are called *wagging*, *rocking* and *twist* (wavenumbers in the order of 1000 cm^{-1}). In liquid water, also intermolecular vibrations occur, corresponding to $\approx$ 500 cm^{-1}. However, these absorption structures are less intense and of minor importance for the absorption spectrum in the visible.

7.4. Inelastic scattering in water

Scattering processes of electromagnetic radiation (photons) in water can be either elastic or inelastic. Elastic scattering processes are Rayleigh and Tyndall (scattering on suspended particles, i.e. Mie-scattering under water). These processes cause no wavelength shifts, i.e. the only effect on the spectrum is the broad-banded λ^{-4}-dependence (resp. $\lambda^{-\kappa}$, see Sect. 3.3.2). As this changes the spectrum smoothly, it is compensated for by the polynomial in the DOAS analysis. Inelastic scattering processes are Vibrational Raman and Brillouin, both leading to wavelength shifts and therefore changes in the spectrum.

7.4.1. Vibrational Raman Scattering (VRS)

In the atmosphere, inelastic Rotational Raman Scattering (RSS) on (predominently) N_2 molecules leads to a filling-in of Fraunhofer structures which is known as the Ring effect (see. Sect. 3.3.1 and 3.3.3). In the DOAS analysis, a pseudo cross-section accounts for the Ring effect which was calculated by the Radiative Transfer Model SCIATRAN (Sect. 3.5.2).

In principle, inelastic Rotational Raman Scattering (RRS) occurs also on H_2O molecules, but in the atmosphere, the abundance of N_2 is much larger. In addition, the H_2O molecule is not linear (as N_2) and has a permanent dipole moment. As a consequence, vibrational modes can be excited (see Sect. 7.3). When the vibrational excited H_2O molecule decays into a final state different from the initial state, the scattered photon is wavelength shifted. As a result, Raman-Stokes and Anti-Raman-Stokes lines appear in the spectrum. This effect is known as Vibrational Raman Scattering (VRS). A qualitative description of Raman scattering was given in Sect. 3.3.1, Fig. 3.5 and 3.6

illustrate the Raman shift and the Raman spectrum, respectively. The VRS affects the spectrum in a similar way as the RRS and causes a Ring effect. However, this Ring effect due to VRS is smaller than the RRS caused Ring effect (an explanation for this is given below).

In the liquid phase, H_2O has no degrees of freedom of rotations as a result of the hydrogen bonds (see Sect. 7.3 and Fig. 7.6). Consequently, no Ring effect due to RRS occurs. In contrast, VRS becomes important due to the high density of H_2O molecules in water. Sect. 7.5 presents results showing that the VRS induced Ring signal is present in recorded spectra from MAX-DOAS during the ship-borne TransBrom campaign.

The RRS causes wavelength shifts which are in the range of Fraunhofer line widths. Therefore, relatively more intensity is shifted from the edge of a Fraunhofer line into its inside than from the inside to the outside. The consequence is the observed filling-in of Fraunhofer lines, known as the Ring effect. In comparison to RRS, the wavelength shift caused by VRS is much larger because the energy of the dominating stretch mode in liquid water is larger (> 3000 cm^{-1} corresponding to several tens of nanometers depending on the initial wavelength). For VRS, the filling-in of Fraunhofer lines is caused by the Raman band width which is explained in the following (see also Eq. 7.3-7.5).

In Fig. 7.7, the Raman band was calculated according to Walrafen (1967) and Kattawar and Xu (1992). This line shape differs from the Raman profiles shown in Fig. 3.6. The profiles in Fig. 3.6 apply to line shapes in the gas phase, they are Gauss-shaped and much sharper. In the liquid phase, the molecules are much closer and frequent collisions broaden the Raman line. Furthermore, hydrogen bonded H_2O complexes (sometimes called polymers) develop in the liquid phase (Fig. 7.6). The hydrogen bonds weaken the intramolecular, covalent O-H bonds and subsequently the vibrational excitation energy decreases. As a consequence, the resulting Raman band is a superposition of Gauss-profiles belonging to single H_2O molecules, resp. monomers (with undisturbed O-H bonds) and polymers (weakened O-H bonds). As the number of hydrogen-bonds in the water is temperature dependent (see Sect. 7.3), the shape of the Raman band is also temperature dependent. This has been used for remote sensing of the ocean temperature using LIDAR systems (e.g., Leonard et al., 1979).

If ΔE is the energy difference between an initial photon of wavelength λ_1 and an inelastically scattered photon of reduced energy (Stokes line) and wavelength λ_2, it is:

$$
\begin{aligned}
E_{\mathrm{ph,fin}} &= E_{\mathrm{ph,\ init}} - \Delta E && (7.3)\\
\Leftrightarrow \frac{hc}{\lambda_2} &= \frac{hc}{\lambda_1} - \Delta E && (7.4)\\
\Leftrightarrow \frac{1}{\lambda_2} &= \frac{1}{\lambda_1} - \tilde{\nu} && (7.5)
\end{aligned}
$$

($\Delta E = h \cdot c \cdot \tilde{\nu}$ with the wavenumber $\tilde{\nu}$ of the vibrational transition).

For an initial photon wavelength of $\lambda_1 = 400$ nm, Fig. 7.7 suggests a shift of ≈ 3200 cm^{-1} - 3600 cm^{-1} (wavenumbers for the FWHM of the Raman band). Eq. 7.5 then yields $\lambda_2 \approx 459$ nm - 467 nm, i.e. the VRS maps some intensity from the initial wavelength to a ≈ 8 nm (FWHM) wide band that is ≈ 65 nm shifted from the original wavelength. Because the wavelength is inversely proportional to the energy, with increasing initial wavelength both, the Raman shift as well as the Raman band width increase on the wavelength axis.

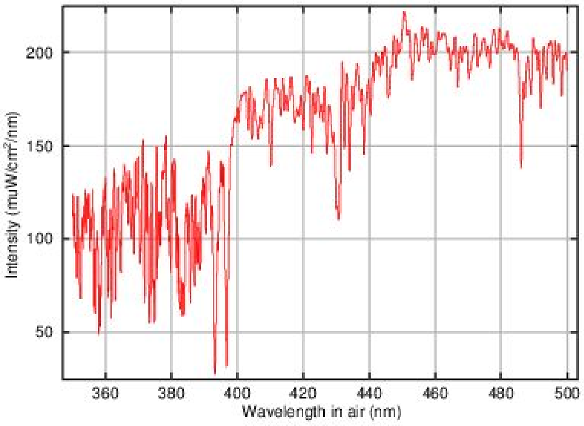

Figure 7.8.: Fraunhofer spectrum from 350 nm - 500 nm. Around 400 nm, the spectrum shows a sharp increase (*step* in intensity). Single Fraunhofer lines are much smaller than the Raman band width of ≈8 nm.

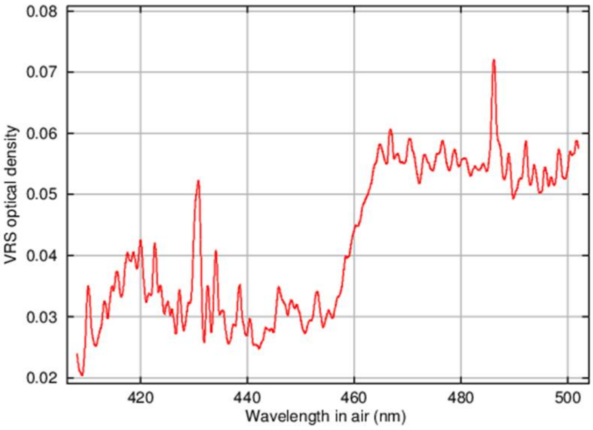

Figure 7.9.: Simulated VRS optical density in liquid water (from V. Rozanov, personal communication, 2012). Geometry: 30° SZA, -45° elevation angle, zenith direction as reference, scenario 2.

The VRS causes a Ring effect because the Raman band width (8 nm in the example above) is much larger than the width of Fraunhofer lines (see Fig. 7.8 and Fig. 7.15). Thus, almost the same intensity ΔI is shifted to the edge of a Fraunhofer line and into its minimum. Consequently, after the VRS, the Fraunhofer line is less deep (relatively to its edge), that is, a filling-in of Fraunhofer lines is observed.

Fig. 7.9 is a pseudo cross-section for the VRS effect calculated with the RTM SCIATRAN (V. Rozanov, personal communication, 2012) in the visible range (408 nm - 502 nm). The DOAS analysis is based on the optical depth, which is the logarithm of the ratio between a measured spectrum I_{meas} in a certain viewing direction and a reference spectrum I_{ref}. For ground-based MAX-DOAS, the reference spectrum is usually a zenith pointing spectrum taken close in time. The optical depth equals a polynomial plus the sum of all cross-sections multiplied with the respective slant columns of trace gases and other effects the photons encounter when travelling through the atmosphere (see DOAS equation 3.34). SCIATRAN simulates both, the recorded measurement spectrum $I_{\text{meas},+}$ and the reference spectrum $I_{\text{ref},+}$ taking into account all scattering and absorption processes including the effect of interest. In a second run, spectra in measurement and reference geometry are calculated again, but this time omitting the effect of interest yielding $I_{\text{meas,-}}$ and $I_{\text{ref,-}}$. Subtracting the optical depth excluding the effect of interest from the optical depth including it, i.e.:

$$\ln\left(\frac{I_{\text{meas},+}}{I_{\text{ref},+}}\right) - \ln\left(\frac{I_{\text{meas,-}}}{I_{\text{ref,-}}}\right) = -\tau_{\text{VRS}} \propto \sigma_{\text{VRS}} \qquad (7.6)$$

yields the (negative) optical density τ_{VRS} of the effect of interest (here: VRS). In first order (as shown below), the VRS optical density τ_{VRS} is proportional to a pseudo VRS cross-section σ_{VRS}. Consequently, it can be used in the DOAS analysis to account for the VRS effect in liquid water.

The narrow peaks in the VRS pseudo cross-section (Fig. 7.9) are caused by the filling-in of Fraunhofer lines resulting from VRS as explained above. For example, the prominent peak around 430-431 nm results from the filling-in of the Ca-Fe-Fraunhofer lines (consisting of close-by lines of Ca and Fe, respectively) at the same wavelength (compare Fig. 7.8). In addition to this high frequency structure, the VRS cross-section in Fig. 7.9 also shows broad structures. The most

Parameter	Scenario 1 (clean)	Scenario 2 (polluted & more chlorophyll)
AOT (337 nm)	0.1	0.19
AOT (550 nm)	0.08	0.15
NO_2	No	Yes ($2.5 \cdot 10^{15}$ molec/cm^2 VC)
Chlorophyll	0.05	0.15

Table 7.1: Different scenarios/SCIATRAN settings used for the simulation of VRS effects.

prominent feature is the *step* around 460 nm. This step is a consequence of the large Raman shift. The Fraunhofer spectrum in Fig. 7.8 exhibits a sharp increase (step) in intensity around 400 nm. According to the calculation given above, the Raman shift for an initial wavelength of 400 nm is ≈ 65 nm. Thus, the step in intensity in the Fraunhofer spectrum around 400 nm is shifted to ≈ 460 nm as a result of inelastic Vibrational Raman scattering. It should be noted, that this structure remains in the differential cross-section used for the DOAS analysis after subtracting a polynomial, when the applied DOAS fitting window is large enough (see Fig. 7.10, top picture).
One limitation of using a fixed VRS cross-section in the DOAS analysis to compensate for the VRS Ring effect is linearity. In the DOAS retrieval, a slant column is calculated for the VRS cross-section to fit the observations. This assumes a linear behaviour: If the light path under water increases or decreases (e.g. due to geometry), the assumption is that the VRS effect scales with a factor (the slant column). However, in practice, the VRS does not only attenuate the spectrum according to its cross-section, but it changes the spectrum in terms of intensity shifts. For example, if the light path doubles, the spectrum after the first half has already another shape than the initial one. In the second half, the VRS changes the spectrum again, this time in a slightly different way than before. In contrast, the way the VRS is implemented in the DOAS analysis assumes that the VRS will affect the spectrum in the same way as before.

A sensitivity study was performed to verify the resulting impact of this error source on the DOAS retrieval. Therefore, VRS optical densities were simulated using SCIATRAN for different scenarios and measurement geometries (resulting in a different length of light path under water).

In scenario 1, which can be referred to as *clean* or *unpolluted* scenario, input parameters for the SCIATRAN run were selected similar to realistic values from 14 October 2009 during TransBrom, namely a very low chlorophyll concentration in the ocean and a small aerosol optical thickness (AOT) as well as no NO_2 in the atmosphere (on 14 October 2009 during TransBrom, tropospheric NO_2 was found to be below the detection limit, see Sect. 6.1.3). The parameters are summarized in Tab. 7.1. The simulation was performed at a resolution of 0.01 nm and the resulting spectra were convolved with the MAX-DOAS instrument's slit function from 14 October 2009, before conversion to optical densities. In Fig. 7.10 (top picture), the red line is the simulated VRS optical density according to Eq. 7.6 for 30° SZA and a MAX-DOAS elevation angle of -45°. A 4th order polynomial was subtracted to create a differential optical density. The blue line is the same for a geometry of 80° SZA and a MAX-DOAS elevation angle of -45° as well. Obviously, the range (peak-to-peak) of the red line (30° SZA) is larger. This is due to a longer light path under water which was verified by a MAX-DOAS fit using measurements from the TransBrom campaign in an elevation angle of -45° (towards the water surface) on 14 October 2009 (for the reference I_0, the closest zenith spectrum was used). As the liquid water absorption coefficient from Pope and Fry (1997) used as

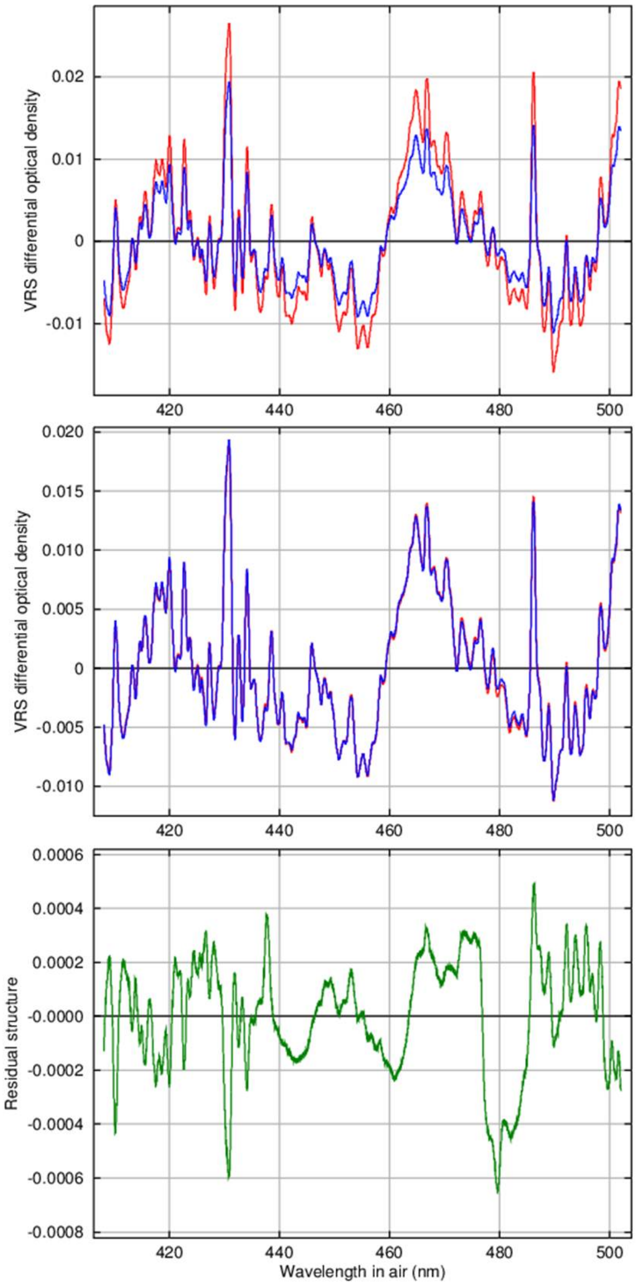

Figure 7.10: Simulation results for scenario 1 (clean scenario). Top: Differential VRS optical density (a 4th order polynomial was subtracted). Red line: 30° SZA and -45° elevation angle (≈ 55 m light path under water), blue line: 80° SZA and -45° elevation angle (≈ 40 m under water). Middle: The 30° SZA line is scaled to the 80° SZA line using a fixed scaling factor (resp. differential slant column) that has been calculated according to Eq. 7.7. Bottom: Difference of the lines in the middle picture or VRS residual. Peak-to-peak variations are ≈ 0.001, the RMS is $2.1 \cdot 10^{-4}$.

a cross-section in the DOAS fit is given in units of 1/m (see Fig. 7.4), the corresponding fitted water slant column is the light path under water in meters. The slant column suggests a light path of ≈55 m at 30° SZA and ≈40 m for 80° SZA. Thus, the ratio of the light paths under water for 80° and 30° is 40m/55m ≈ 0.7.

Due to the non-linearity, the VRS differential optical densities cannot be converted precisely into each other by using a fixed ratio. Thus, if the 30° SZA differential optical density $\tau_{30}(\lambda)$ was used as a pseudo cross-section in a DOAS fit, it could not be scaled to the 80° differential optical density $\tau_{80}(\lambda)$ without leaving a residual structure.

The optimal scaling factor a between the differential optical densities $\tau_{30}(\lambda)$ and $\tau_{80}(\lambda)$ is:

$$a = \frac{(\tau_{30}(\lambda), \tau_{80}(\lambda))}{(\tau_{30}(\lambda), \tau_{30}(\lambda))} = \frac{\sum_i \tau_{30}(\lambda_i) \cdot \tau_{80}(\lambda_i)}{\sum_i \tau_{30}(\lambda_i) \cdot \tau_{30}(\lambda_i)} = 0.70828 \tag{7.7}$$

where (,) denotes the scalar product. This is very close to the factor of 0.7 suggested by the ratio of liquid water absorption slant columns. Nevertheless, it is only a *mean* factor, i.e. if applied to the VRS optical densities, they will not match perfectly at all wavelengths.

To demonstrate this, the 30° SZA optical density was scaled by a and plotted together with the 80° SZA optical density in the middle picture of Fig. 7.10. The scaled 30° SZA optical density matches the 80° SZA optical density very well, but small differences are observed. In the bottom picture of Fig. 7.10, the difference of both optical densities from the middle picture is shown. This difference would result as residual spectrum in a DOAS fit. The maximum peak-to-peak variation of the residual is ≈ 0.001, the RMS $2.1 \cdot 10^{-4}$. This is in the same range (slightly higher) of a typical DOAS fit residual of tropospheric NO_2 during TransBrom (see Sect. 6.1).

It is important to note that this residual was derived assuming an elevation angle of -45°, i.e. measurements towards the water surface. This is appropriate for evaluating the spectral effects of liquid water, but for MAX-DOAS trace gas observations normally elevation angles of a few degrees above the horizon are used. The light collected in these directions contains some contribution from photons that have been under water and were backscattered into the atmosphere and then into the line of sight. However, the relative number of photons that have been under water is certainly lower than in the -45° elevation angle. As a result, the spectral impact of VRS in liquid water is much less in normal MAX-DOAS viewing directions and subsequently the residual due to the non-linearity of the VRS spectrum is smaller. To conclude, the calculations performed here can be regarded as upper estimate or worst case errors.

The above consideration was repeated for a different scenario 2, which can be referred to as *polluted* or *larger chlorophyll* scenario: In the atmosphere, NO_2 was included and the AOT was larger as in scenario 1. In the ocean, a larger chlorophyll concentration was assumed. The parameters are summarized in Tab. 7.1. Again, spectra for 30° and 80° SZA were simulated using SCIATRAN. For both SZAs, VRS optical densities have been calculated according to Eq. 7.6. The corresponding differential VRS optical densities (after subtracting a 4th order polynomial) are displayed in Fig. 7.11 (top picture). According to Eq. 7.7, the 30° SZA optical density was scaled to the 80° SZA optical density (Fig. 7.11, middle). The difference of these curves - the residual - is shown in the bottom picture of Fig. 7.11.

In comparison to scenario 1, the VRS optical density at 30° SZA fits better to the VRS optical density at 80° SZA and the residual is smaller. Peak-to-peak variations are in the order of 0.0006 and the RMS is $1.25 \cdot 10^{-4}$. Consequently, the DOAS fit quality would be affected to a lesser extent than in scenario 1. Most likely, the reason is that the light path under water in this scenario is shorter, which can be inferred from the differential optical densities that are larger in scenario 1 (Fig. 7.10, top picture) than in scenario 2 (Fig. 7.11, top picture). This gives further support to the assumption stated above that in real MAX-DOAS observations of trace gases performed a few degrees above the horizon the non-linearity of the VRS effect will introduce an error that is even smaller than the residuals given here.

So far, the error was evaluated arising when VRS spectra are used in the DOAS fit that were simulated for appropriate scenarios but *wrong* geometries and subsequently different light path lengths under water. In the following, the arising error is evaluated when using a VRS spectrum derived from a *wrong* scenario.

Therefore, Fig. 7.12 (top) shows the VRS differential optical density for 30° SZA and -45° elevation

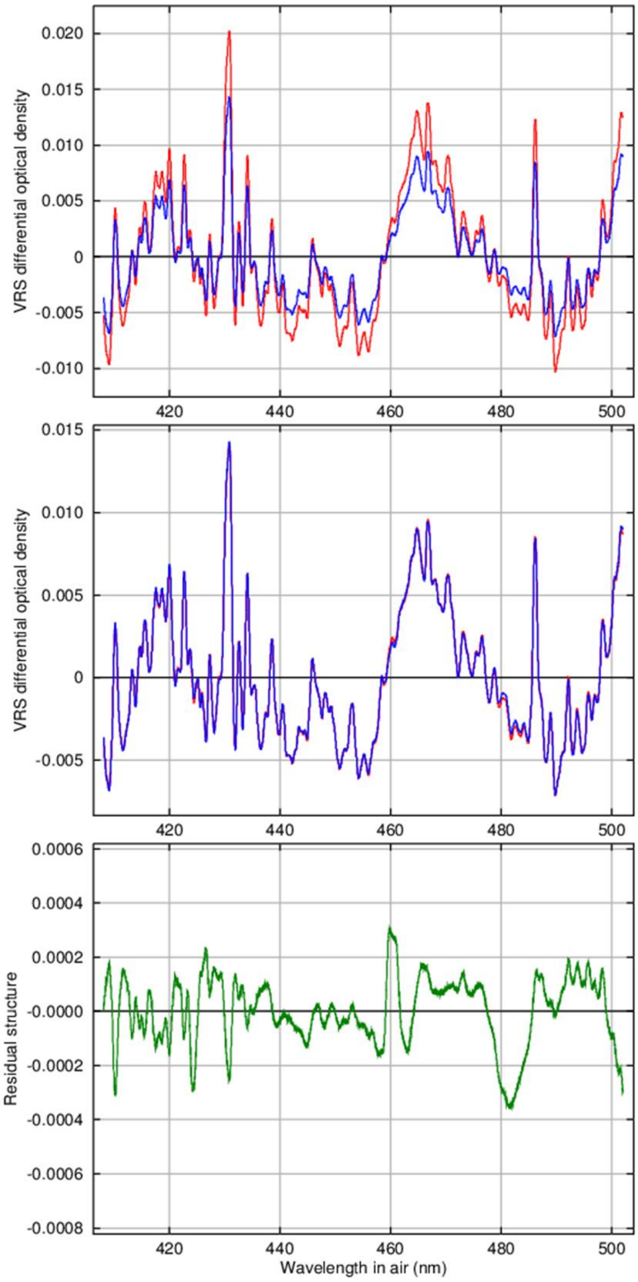

Figure 7.11: Simulation results for scenario 2 (polluted scenario). Top: Differential VRS optical density (a 4th order polynomial was subtracted). Red line: 30° SZA and -45° elevation angle, blue line: 80° SZA and -45° elevation angle. Middle: The 30° SZA line is scaled to the 80° SZA line. Bottom: Difference or VRS residual ($1.25 \cdot 10^{-4}$ RMS).

angle calculated for scenario 1 in red. The VRS differential optical density calculated for scenario 2 and the same geometry is displayed in blue. The scenario 1 line was scaled according to Eq. 7.7 to the scenario 2 line (middle picture) and the residual is shown in the bottom picture of Fig. 7.12. Here, the peak-to-peak variation is ≈ 0.0035 and the RMS $4.66 \cdot 10^{-4}$. In contrast to the results found before, this residual is larger than the residual of a typical DOAS fit and would subsequently decrease the fit quality.

In order to minimize the residual from VRS scaling, the 30° SZA differential optical densities from scenarios 1 and 2 (red and blue line in Fig. 7.12, top picture) have been orthonormalised. The two orthonormalised functions are displayed in Fig. 7.13. While the first orthonormal function looks like the diffential optical density, the second orthonormal function shows remarkable similarity to the (flipped) residual found before (compare to middle and bottom picture of Fig. 7.12).

According to Eq. 7.7, the optimal scaling factors were calculating for the first orthonormal function (Fig. 7.13(a)) to match the 30° SZA differential optical densities from scenario 1 and 2. The

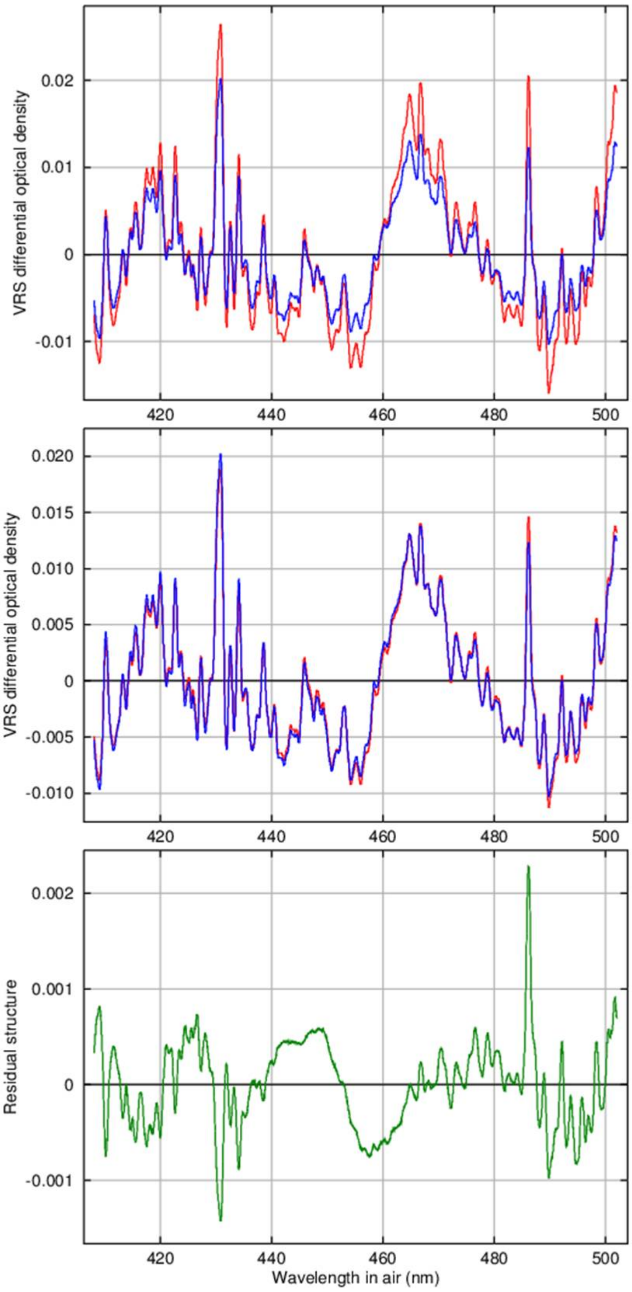

Figure 7.12: Simulation results for mixed scenarios. Top: Differential VRS optical density (a 4th order polynomial was subtracted). Red line: Scenario 1, 30° SZA and -45° elevation angle, blue line: Scenario 2, 30° SZA and -45° elevation angle. Middle: The 30° SZA scenario 1 line is scaled to the 30° SZA scenario 2 line. Bottom: Difference or VRS residual ($4.66 \cdot 10^{-4}$ RMS).

corresponding residuals are displayed in Fig. 7.14. Both residuals are smaller than the original residual and yield a peak-to-peak variation of ≈ 0.0015 and RMS $= 2.2 \cdot 10^{-4}$ for scenario 1, resp. ≈ 0.002 peak-to-peak and $3.1 \cdot 10^{-4}$ RMS for scenario 2. Thus, using this first orthonormal function (Fig. 7.13(a)) in the DOAS analysis would lead to smaller fit residuals than using a simulated VRS optical density (unless it is calculated for the true parameters). As the knowledge of the true parameters (chlorophyll, AOT etc.) is normally not given - and if, the calculation of VRS cross-sections would require large computational efforts - resp. the parameters vary over the measurement period, the use of such an *average* VRS cross-section in the DOAS analysis seems to be the best choice. This motivates to extract an approximate VRS cross-section from the TransBrom field campaign as real measurements towards the water surface have been performed with a MAX-DOAS instrument during the whole cruise which encountered various scenarios (e.g., polluted, unpolluted) and geometries (e.g., SZA).

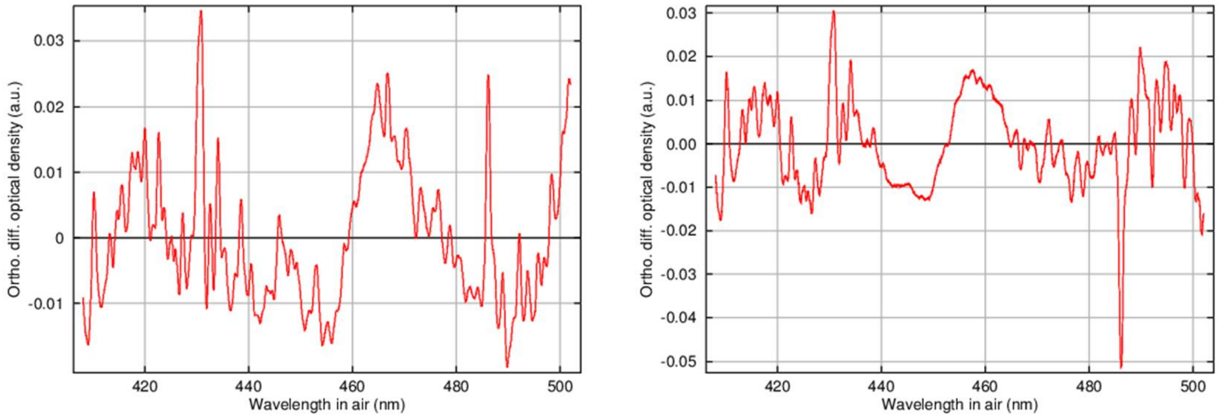

(a) 1st orthonormal function

(b) 2nd orthonormal function

Figure 7.13.: Orthonormal functions spanning the same space as the differential optical densities for 30° SZA and scenarios 1 and 2 (red and blue curves in the top picture of Fig. 7.12).

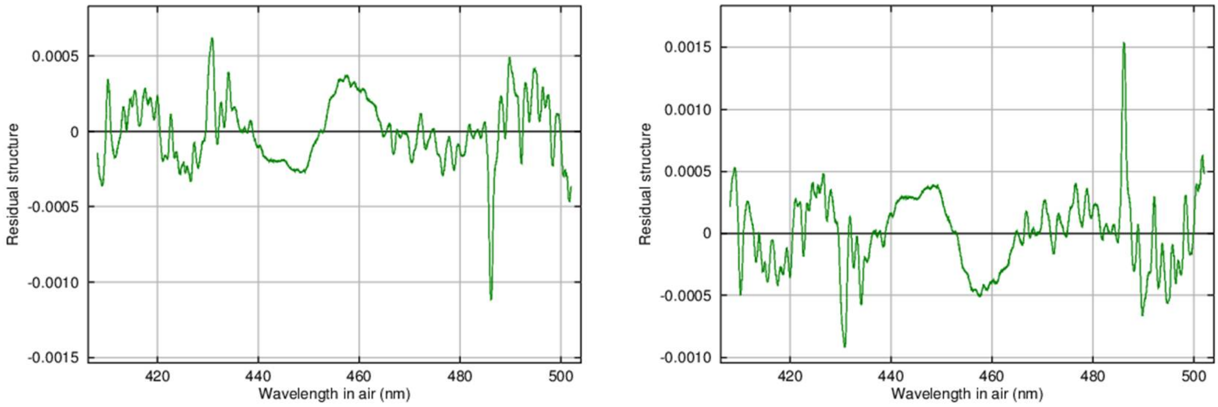

(a) Difference to scenario 1

(b) Difference to scenario 2

Figure 7.14.: Differences (residuals) between the scaled first orthonormal function (from Fig. 7.13(a)) and the 30° SZA differential optical densities of scenario 1 (left) and 2 (right).

To summarize:

- The VRS effect in liquid water changes the spectrum of scattered light observed above the water through spectral shifts. As a consequence, residual structures arise in the DOAS fit if the VRS effect is present but not compensated for.
- The VRS effect is similar to the RRS induced Ring effect, but the lengths of the shifts as well as the shape of the Raman band are different. Thus, the VRS cross-section is different from the RRS.
- Radiative transfer models can simulate VRS cross-sections for different scenarios (e.g., different length of light path under water). However, the cross-section is specific for a scenario (non-linearity of the VRS effect). Thus, residual structures are introduced when a VRS spectrum is used in the DOAS fit that corresponds to a *wrong* scenario.

- This error turned out to be the larger, the cleaner the scenario is (and the longer the light path under water).

- If the scenario the VRS spectrum was calculated for matches the true scenario (suspended matter, chlorophyll, etc.), the resulting residual structures arising from different lengths of light path under water are smaller or in the order of magnitude of typical DOAS fit residuals. Thus, in these cases, the introduced error will not much decrease the DOAS fit quality and can be neglected. This was shown for light paths of several tens of meters and an elevation angle of 45° towards the water surface. For realistic MAX-DOAS observations a few degrees above the horizon, the introduced error can be considered as being of even less importance since the fraction of photons having been under water is smaller.

- If the scenario the VRS spectrum was calculated for does not match the true scenario, the resulting residual structures are larger than typical DOAS fit residuals and would subsequently significantly decrease the fit quality. Using orthonormalised VRS cross-sections yields smaller residuals. This motivates the retrieval of an *average* VRS cross-section from real measurements during the field campaign TransBrom, which is described in Sect. 7.5. However, the above conclusions were drawn again from simulations of special viewing geometries in order to obtain average light paths under water of up to $\approx$ 55 m. For realistic measurements (e.g. $\leq$ 10 m light path under water for satellites, see Fig. 1.2 in chapter 1) the produced residual would be $\approx$ 5 times smaller than the one in Fig. 7.12 (bottom picture) and therefore smaller than typical DOAS residuals.

7.4.2. Brillouin Scattering

The inelastic scattering on density fluctuations is called Brillouin scattering and consists of two parts (Hickman et al., 1991; Dickey et al., 2011): 1) Scattering on isentropic pressure fluctuations (acoustic phonons). These propagate with the speed of sound in water in all directions. As a consequence, scattering on such phonons causes Doppler-shifts. The magnitude of the shift depends on the scattering angle, the refractive index and the speed of sound in water (see below). For an incident light beam of wavelength λ_0, the Brillouin scattering produces a pair of red- and blueshifted spectral lines called Mandelstam-Brillouin (MB) doublet, sometimes also referred to as Stokes and Anti-Stokes-lines, respectively, in analogy to Raman scattering. 2) Scattering on isobaric entropy fluctuations which are frozen and do not propagate. These processes cause an unshifted line (called Gross line) at the original wavelength.

The vectors of the incident light beam **k**, the scattered light beam **k'** as well as the phonon **q** have to fulfill the Bragg condition $\mathbf{q} = \mathbf{k'} - \mathbf{k}$. From this, the relation between the wavelength shift $\Delta\lambda$ and the original wavelength λ_0 can be derived (see e.g. Hickman et al., 1991):

$$\frac{\Delta\lambda}{\lambda_0} = \pm 2n\frac{v_s}{c}\sin\left(\frac{\theta}{2}\right) \tag{7.8}$$

Here, n is the refractive index, v_s the speed of sound in water, c the speed of light in vacuum and θ the scattering angle. Maximum wavelength shifts occur for $\theta = 180°$.

For typical values of liquid water, $n = 1.33$, $c \approx 3 \cdot 10^8$ m/s, $v_s \approx 1500$ m/s and an incident wavelength of 450 nm, Eq. 7.8 yields a wavelength shift of $\Delta\lambda \approx \pm$ 0.006 nm. This is far below the

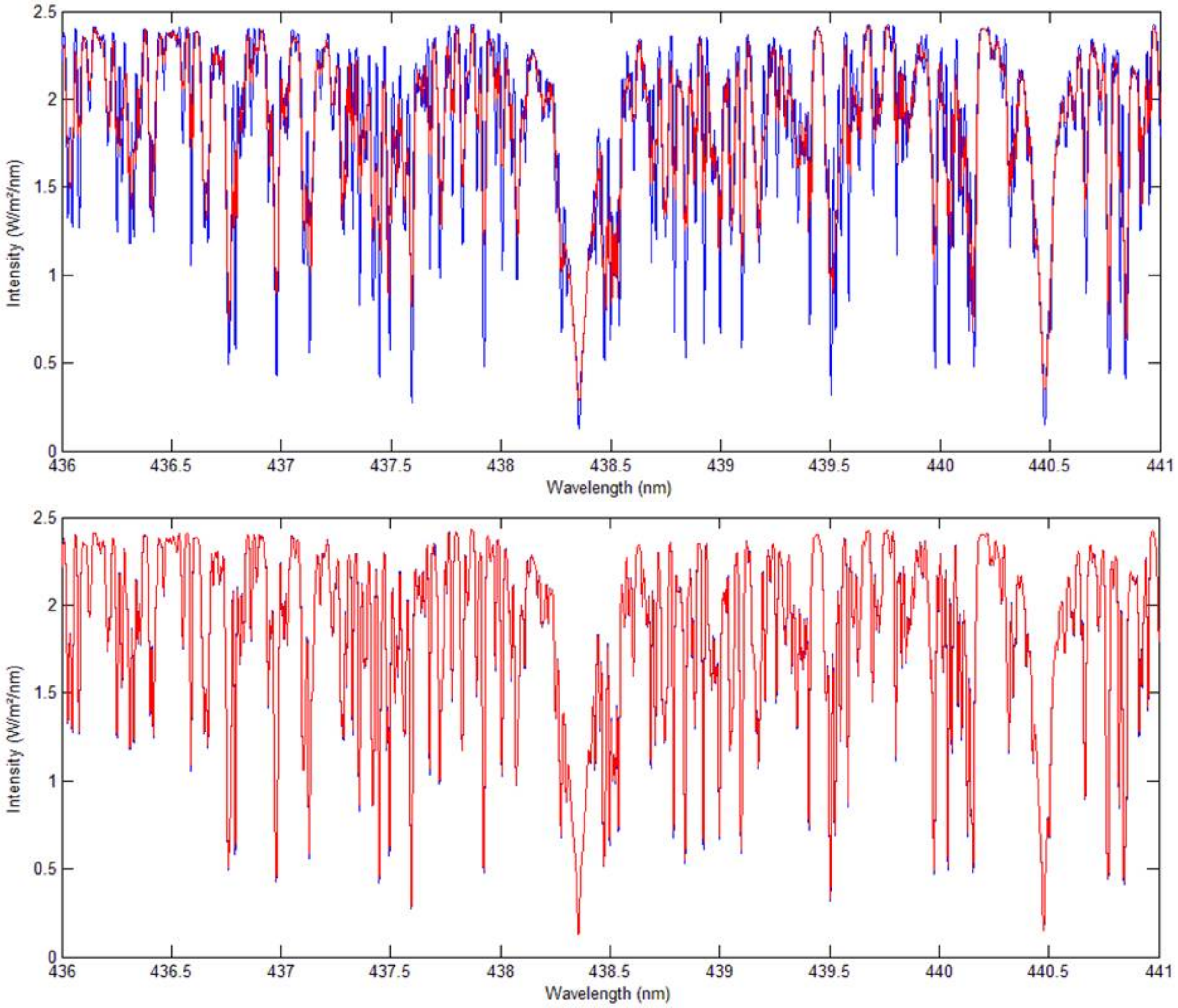

Figure 7.15.: Inelastic Brillouin scattering (Blue: Original Fraunhofer spectrum. Red: Spectrum after inelastic Brillouin scattering.). Top: Effect in liquid water. While broad-band structures are reproduced well (e.g. the Fe-line at 438.4 nm), narrow Fraunhofer structures are partly filled in, similar to the Ring effect. Bottom: Same calculation for air.

FWHM of the MAX-DOAS slit function, which is in the order of 0.5 nm. Nevertheless, the Brillouin scattering causes a partial filling-in of narrow Fraunhofer lines, which is illustrated in Fig. 7.15 and has been observed already by Xu and Kattawar (1994).

The ratio of the intensity of the Gross line to the intensity of the MB-doublet lines is called Landau-Placzek ratio and according to O'Connor and Schlupf (1967) it is given by:

$$\frac{I_G}{2I_{MB}} = \frac{C_p}{C_v} - 1 \tag{7.9}$$

With typical values for the specific heats C_p and C_v of water at 25°C and 1 bar, the ratio of the unshifted to the shifted intensity is about 1%, that is, almost all intensity is shifted to other wavelengths.

In the top picture of Fig. 7.15, a high-resolution Fraunhofer spectrum between 436 nm and 441 nm is displayed in blue. In addition, a spectrum affected by Brillouin scattering with $\theta = 180°$ (backscattering) and typical values for water (see above) was calculated according to Eq. 7.8 and

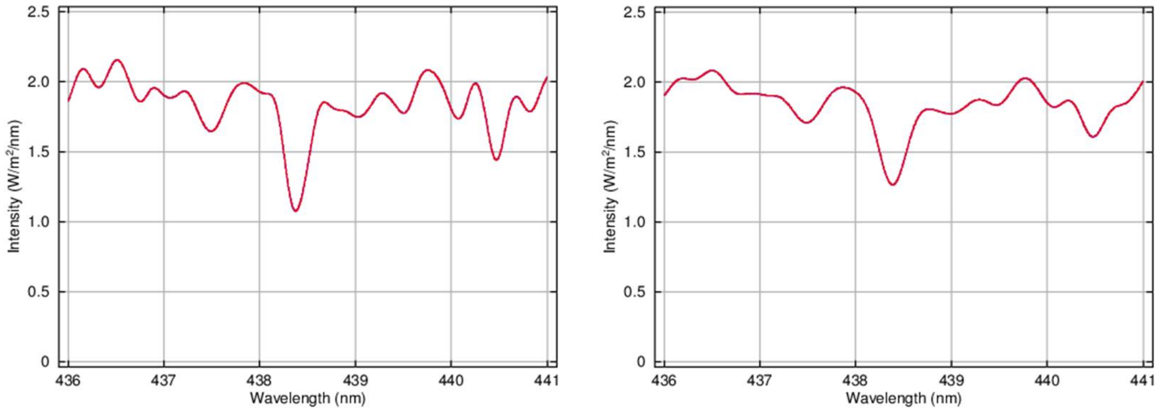

(a) Convolution: Gauss 0.2 nm FWHM

(b) Convolution: Gauss 0.3 nm FWHM

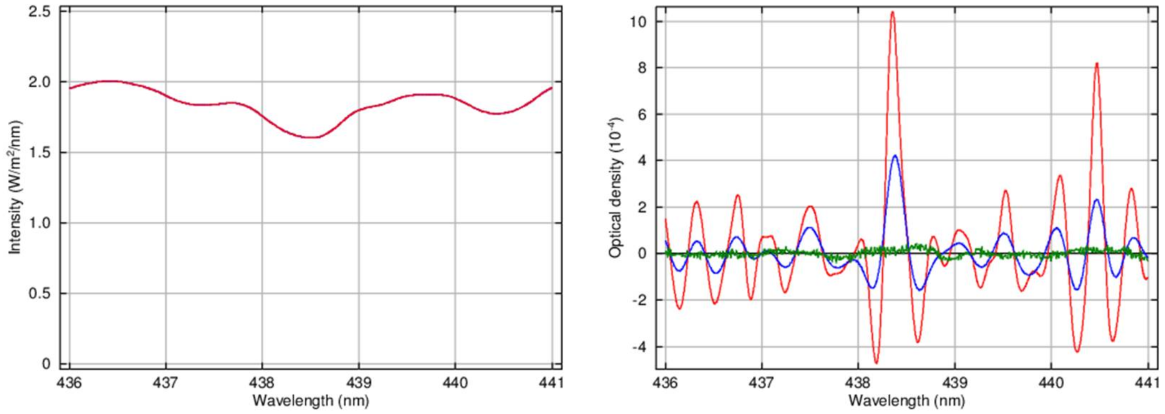

(c) Convolution: true slit function

(d) Brillouin optical density

Figure 7.16.: Figs. 7.16(a)-7.16(c): Highly resolved Fraunhofer spectrum and Brillouin affected spectrum from Fig. 7.15 (top picture) convolved with different slit functions. For Fig. 7.16(c), the true instrumental slit function from the MAX-DOAS campaign instrument's visible channel (FWHM $\approx$ 0.8 nm) was used. For all curves, no difference between the red (Brillouin affected) and blue (original Fraunhofer spectrum) can be observed. Fig. 7.16(d): Brillouin optical density ($\ln I_{\text{with}}/I_{\text{without}}$) calculated for all convolved spectra shown before: Red (Gauss slit function, 0.2 nm), blue (Gauss, 0.3 nm) and green (true instrument's slit function). For comparison: Largest structures in a high-quality DOAS fit residual are in the order of $\approx 5 \cdot 10^{-4}$.

Eq. 7.9 and is shown in red.

Due to the small wavelength shifts, broad structures as the Fe-line at $\approx$ 438.4 nm are almost identical in the incident and in the scattered spectrum. In contrast, narrow Fraunhofer lines show a clear *filling up effect*, similar to the Ring effect which is known from inelastic Raman scattering.

The bottom picture of Fig. 7.15 shows the same, but this time the calculations were performed for air. The incident and the scattered spectrum are almost identical. This is because the refractive index of air and the speed of sound in air are smaller than corresponding values for water ($n \approx 1$ and $v_s \approx 340$ m/s, respectively). As a result, according to Eq. 7.8, the wavelength shift in air is only $\approx$ 0.001 nm and therefore smaller than the shift in water. In addition, the ratio between unshifted and shifted intensity is higher, because for a two-atomic gas (N_2), $C_p = 7/2 \cdot R$ and $C_v = 5/2 \cdot R$, i.e. $C_p/C_v - 1 = 40\%$. Thus, in comparison to water, more light stays at the incident wavelength.

It has to be mentioned that this is a simplified calculation neglecting all effects of absorption and scattering in the atmosphere as well as in water except for Brillouin scattering. In addition, the calculated spectrum applies for a single scattering event ($\theta = 180°$) while in reality multiple scattering can occur. Thus, the effect is a function of the light path under water and a more sophisticated computation is needed to obtain accurate results (e.g., Xu and Kattawar, 1994, used a Monte Carlo Model). Nevertheless, the results of these calculations can be used to estimate the impact of the Brillouin effect on DOAS retrievals.

While the VRS produces large wavelength shifts and the RRS causes wavelength shifts which are in the range of strong Fraunhofer line widths, the Brillouin scattering causes very small shifts. As the filling-in of Fraunhofer lines increases if the line width is in the range of the shift (see discussion above and in Sect. 7.4.1 as well as Sect. 3.3.3), consequently, the Brillouin scattering causes predominantly a filling-in of very narrow Fraunhofer lines that are below the resolution of current DOAS instruments (and subsequently the filling-in of single lines is not directly measured as the Ring effect due to RRS). Thus, it has to be determined to what extent the filling-in of these narrow and not resolved lines impact the actual observed spectra, i.e. how much of the Brillouin induced Ring effect is still present if the high resolution spectra as displayed in Fig. 7.15 are convolved with the instrument's slit function.

In Figs. 7.16(a)-7.16(c), the spectra with and without taking into account Brillouin scattering in water from Fig. 7.15 (top picture) are convolved with different slit functions (Gaussian slit function of 0.2 nm, resp. 0.3 nm FWHM and the true slit function of the IUP-Bremen campaign instrument's visible channel, having a FWHM of ≈0.8 nm). By eye, no differences between the spectrum affected by Brillouin scattering and the unaffected Fraunhofer spectrum (red and blue lines) can be observed. However, the effect of Brillouin scattering in terms of optical depth can be calculated according to the Lambert-Beer law by taking the logarithm of the ratio of the Brillouin affected and the unaffected spectrum. This was performed for all convolved spectra shown in Figs. 7.16(a)-7.16(c) and plotted in Fig. 7.16(d).

The effect of Brillouin scattering can be neglected in the DOAS analysis if the resulting structures in terms of optical depth are smaller than a typical DOAS fit residual. Therefore, a threshold of $5 \cdot 10^{-4}$ was defined, which is the magnitude of largest structures in a typical high-quality DOAS fit residual. Corresponding RMS are usually lower and in the order of $1 \cdot 10^{-4}$ (e.g., see Sect. 6.1). As Fig. 7.16(d) shows, the Brillouin optical density is higher than this threshold when using a Gaussian slit function of 0.2 nm FWHM. For 0.3 nm, the resulting structures fall below this threshold and the corresponding RMS is about $1 \cdot 10^{-4}$. Using the instrument's true slit function causes a Brillouin optical density showing maximum structures of $4 \cdot 10^{-5}$ and $1.4 \cdot 10^{-5}$ RMS. This is below the residual's order of magnitude resulting from the best DOAS fits.

As a result, the Brillouin scattering can be neglected using the current MAX-DOAS campaign instrument. However, the structures of Brillouin optical density exceed the range of typical DOAS residuals using a Gauss slit function of 0.2 nm FWHM. Therefore, the Brillouin scattering has to be considered when future DOAS instrument slit functions (in the visible) reach the range of 0.2 nm FWHM or better. These conclusions apply to measurements in the visible (around 430 nm, see Fig. 7.16). For smaller wavelengths (UV) the effect is less strong as the wavelength shift $\Delta\lambda$ is proportional to λ_0 (Eq. 7.8).

7.5. Field measurements

In the following, the presence of liquid water spectral structures in the DOAS analysis of real measurements is demonstrated. Therefore, MAX-DOAS field measurements taken during the TransBrom campaign are used (for details about the campaign and the measurement geometry, see Sect. 6.1).

7.5.1. Preparation of the liquid water absorption cross-section

For considering the liquid water absorption, the cross-section published by Pope and Fry (1997) (e.g., see Fig. 7.3) was selected. This spectrum had to be prepared in order to allow the use in DOAS fits.

As the DOAS routine needs cross-sections in 0.1 nm (or 0.01 nm) spacing but the literature spectrum from Pope and Fry (1997) is provided only in 2.5 nm resolution, an interpolation was required to fill the gaps. A simple linear interpolation yields an absorption spectrum with sharp peaks (at the position of the original spectral points) which is unrealistic. Furthermore, despite the shoulders as explained in Sect. 7.3, small variances between adjacent (2.5 nm spaced) spectral points was observed in the 400-500 nm range, most likely due to mismeasurements/noise. As Pope and Fry (1997) state that the resolution of their spectrum is only ≈7 nm, before the interpolation a running mean over 3 adjacent spectral points (i.e., 7.5 nm) was applied to suppress noise yielding a smooth spectrum. Then, a spline interpolation was applied afterwards (this results in a smoother spectrum than using a linear interpolation) to obtain the required 0.1 nm spectrum.

The performed necessary changes may have good reasons, but return a high resolution liquid water absorption spectrum that is slightly different from the original one. However, the introduced differences are small: In Fig. 7.26, the difference between the obtained absorption spectrum and the original one is plotted in comparison to a retrieved liquid water correction spectrum. It has to be pointed out, that the correction spectra retrieved in the following sections were always calculated with the prepared liquid water absorption cross-section explained here and therefore describe corrections with respect to this specific cross-section.

7.5.2. Field measurements - Example 1

In a first example, only measurements in -45° and -60° elevation angles, i.e. measurements towards the ocean's surface, are used. As mentioned before, liquid water spectral effects are stronger in these viewing directions than in viewing directions above the horizon (which are normally used for the DOAS analysis). In Sect. 7.1 it was already pointed out that the scene observed by the instrument in the water viewing directions was sometimes (almost periodically, depending on the state of the sea) disturbed by white sea spray, when waves slapped against the ship or collided with its bow wave. As explained in Sect. 6.1, in every viewing direction a series of single spectra was recorded with an exposure time of 100 ms each (and integrated over 40 s in each viewing direction). Due to the short exposure time of 100 ms, these single measurements can be regarded as spectral *snapshots* without temporal evolution. Consequently, a color index (intensity at ≈ 400 nm divided by intensity at ≈ 570 nm) was defined to distinguish between measurements with (mostly) clear/undisturbed view inside the water and measurements whose view towards the water was (mostly) blocked by white sea spray: If the color index (CI) was > 2 (red parts suppressed), the corresponding spectrum was

Parameter	Settings	Remarks
	Measurements towards the water surface	
Elevation angles	-45°, -60°	towards water surface
Reference	Sea spray cover	closest, ΔSZA $\leq 2°$
Spectral range	412 - 498 nm	
Polynomial	4th order	
Straylight correction	Offset	
Liquid water absorption	(Pope and Fry, 1997)	Smoothed, interpolated
VRS	SCIATRAN simulation	30° SZA, -45° LOS, scenario 1 (Sect. 7.4.1) calculated by $\ln(I_{\text{meas},+}/I_{\text{meas},-})$
	Realistic DOAS Fit	
Elevation angles	-3° to 30°	(mostly) above the horizon
Reference	zenith	Fixed spectrum at 45° SZA
Spectral range	417.5 - 438.2 nm	IO fit window (Sect. 6.1)
Polynomial	2nd order	
Straylight correction	Offset	
VRS	SCIATRAN simulation	30° SZA, -45° LOS, scenario 1 (Sect. 7.4.1) calculated by Eq. 7.6
RRS (Ring)	CINDI Ring	
O_3	(Bogumil et al., 2003)	223 K
NO_2	(Vandaele et al., 1996)	295 K
IO	(Spietz et al., 2005)	
Water vapour	(Rothman et al., 2003), (Vandaele et al., 2005)	Using HITRAN 2009

Table 7.2.: DOAS test fit parameters to proof the presence of liquid water and VRS structures in field measurements.

considered to be dominated by water leaving radiation while a CI <= 1 was considered to indicate reflection of the incoming radiation (before penetrating the water surface) on the white sea spray. All single spectra within each 40 s - measurement that could be assigned to one or the other group (clear or sea spray covered) were averaged yielding two separate spectra for the same observation. Examples of both types of spectra can be found in Fig. 7.2.

The sea spray measurements have been used as reference $I_0(\lambda)$ in the DOAS fit (in reality however, these spectra will contain some liquid water structures, but these are suppressed compared to the undisturbed measurements). The undisturbed measurements collecting photons leaving the water have been used as measured spectra $I(\lambda)$. As both spectra correspond to the same viewing direction (and were taken for almost the same SZA as always the closest-in-time reference spectrum has been used), in first approximation, the difference is the light path under water. The optical depths $\ln(I_0/I)$ were analysed in a DOAS fit window that is large enough for the liquid water

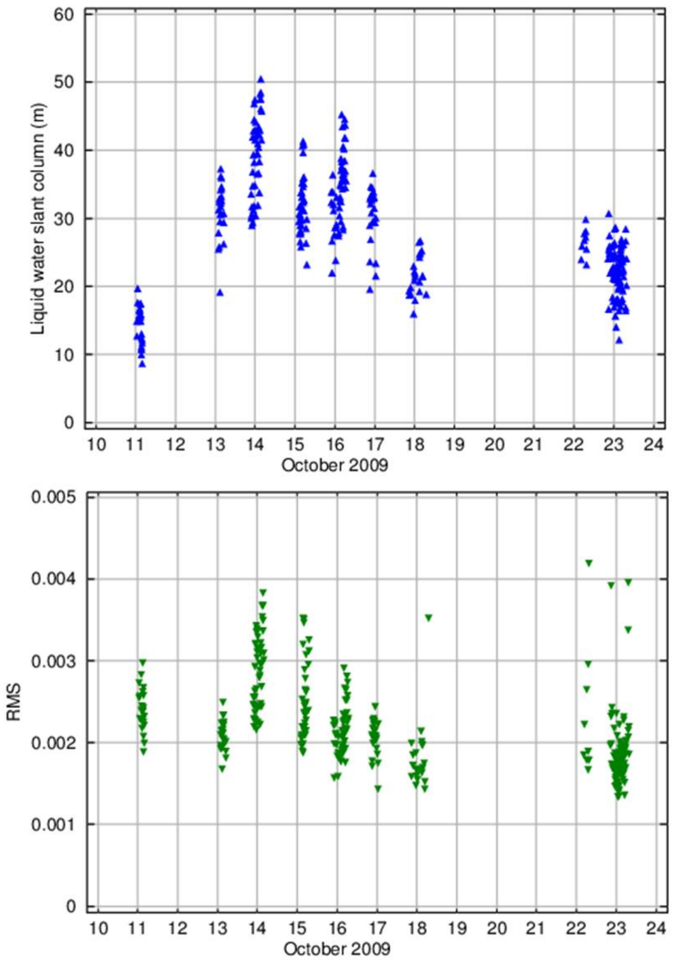

Figure 7.17: Top: Liquid water absorption slant columns resulting from the DOAS test fit in water viewing directions during TransBrom. The slant columns are of unit meters and have the meaning of underwater light path lengths. Bottom: Corresponding RMS of the fit residual.

absorption coefficient to exhibit structures that cannot be compensated by the DOAS polynomial. Consequently, the liquid water absorption coefficient from Pope and Fry (1997) that had to be prepared as described in Sect. 7.5.1 was used as cross-section in the DOAS fit.

For the VRS effect, in contrast to Eq. 7.6, an optical density has been calculated simply according to $\ln(I_{\text{meas},+}/I_{\text{meas},-})$ and included in the fit because the reference measurements have not been performed in zenith but in water viewing direction. However, the effect is marginal because there is almost no water leaving radiance collected in the zenith direction. Consequently, the resulting VRS optical density has almost the identical shape as the one used in Sect. 7.4.1 (e.g., shown in Fig. 7.10, top picture) and potential misfits due to a wrong scenario etc. (see discussion in Sect. 7.4.1) turned out to be larger than differences in the DOAS fit when using the VRS optical density with or without subtracting the zenith contribution. The fit parameters are summarized in Tab. 7.2.

As the liquid water absorption coefficient used as cross-section in the DOAS fit is given in $1/m$, the retrieved slant columns, which are shown in Fig. 7.17 (top picture) for the entire TransBrom cruise, are of unit meters and correspond to the mean photon path lengths under water. In this timeseries, some days are missing, e.g. 19-21 October. This is the result of the applied color index and a criterion for the maximum difference in terms of SZA (2°) between the measurement and the reference. This criterion was introduced to avoid atmospheric contamination of the measurements that would occur if the light path through the atmosphere was different in the measurement and in the reference.

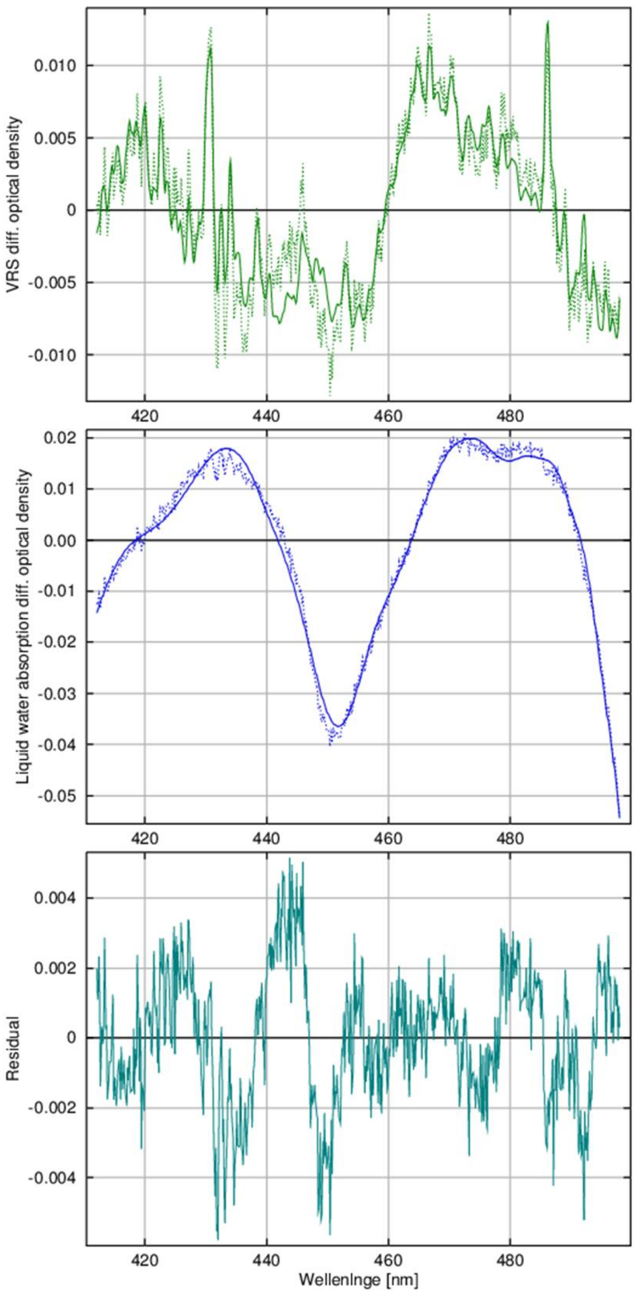

Figure 7.18: Exemplarily DOAS fit results of measurements towards the water surface (from measurements on 16 October, 05:09 UT $\approx$ 15 LT). Top: VRS fit (the dashed line is the fitted optical density, the solid line is the cross-section scaled by the slant column). Middle: Liquid water absorption fit. Bottom: Residual (RMS $= 2 \cdot 10^{-3}$).

Largest liquid water absorption slant columns, i.e. longest light paths under water occured on 14 October with values up to 50 metres. This behaviour was intuitively expected because on 14 October the ship encountered the clearest water that could be observed by eye throughout the whole cruise (see photo in Fig. 7.1). The bottom picture of Fig. 7.17 shows the corresponding fit's RMS for all measurements. The shape of the RMS timeseries reveals strong similarity to the retrieved length of light paths under water, e.g. on 14 October both, the liquid water absorption slant column as well as the RMS have a maximum. This is because errors due to uncertainties of the liquid water and VRS cross-sections scale with the light path under water. It is worth mentioning that liquid water absorption is the dominating effect in these measurements, which is demonstrated by Fig. 7.18 (explanation given below). Thus, even relatively small uncertainties of its cross-section can lead to large absolute residuals and subsequently the RMS follows the liquid water slant columns, as observed.

An exception of this behaviour is found for 11 October showing large RMS while corresponding liquid water slant columns are relatively low. Nevertheless, the residuals from this day clearly indicate that the large RMS values are caused by mismatches of the liquid water absorption. A possible explanation could be different water properties (temperature, salinity, suspended matter, etc.) influencing the shape of the absorption coefficient. However, also instrumental changes cannot be ruled out to cause these mismatches as, for example, the instrument slit function was optimized after 11 October.

In general, the RMS of these test fits are almost one order of magnitude larger than typical RMS values of proper DOAS fits, which are in the range of $5 \cdot 10^{-4}$ (e.g., see Sect. 6.1). Nevertheless, it has to be considered that these test fits of water-viewing measurements are extreme cases which were carried out for the purpose of detecting a strong liquid water signal in a broad fit window. In the MAX-DOAS analysis of atmospheric trace gases, which are not performed pointing towards the water surface but above the horizon, the impact of liquid water spectral structures and associated errors are smaller. In addition, the DOAS polynomial is supposed to compensate mismatches of the broad liquid water absorption better as the fit window for most trace gas retrievals is smaller than the test window used here (in small DOAS fit windows the polynomial is often considered to account entirely for the broad liquid water absorption).

In addition to the liquid water absorption, the structure of vibrational Raman scattering was detected in all water-viewing measurements as well. As an example, the fitted optical densities of VRS and liquid water absorption as well as the corresponding fit residual are shown in Fig. 7.18 for a measurement performed on 16 October (≈ 5 UT, corresponding to ≈ 15 LT and 54.5° SZA) in a viewing direction of -45° (towards the water surface). The liquid water absorption ranging from ≈ 0.02 to -0.05 (middle picture in Fig. 7.18) accounts for almost the entire differential optical depth and is much larger than the VRS differential optical density ranging from ≈ 0.01 to - 0.007 (top picture). Nevertheless, the VRS structure is clearly found and above the residual. The residual consists of narrow as well as broad-band structures (bottom picture). The broad-band structures result from misfits of the large liquid water absorption (e.g., see the slope when decreasing around 445 nm). The narrow-band structures are either caused by misfits of the VRS effect or by another effect, which is not included in the fit. For example, this could be rotational Raman scattering in the atmosphere if the reference spectrum is not exactly the radiance before penetrating the water. Misfits of the VRS effect could arise if a cross-section derived for an inappropriate scenario is used (see Sect. 7.4.1). This indicates the need for an average VRS as well as an average absorption spectrum for liquid water derived from field measurements.

7.5.3. Field measurements - Example 2

In the second example, the presence of VRS structures in realistic measurements performed in viewing directions above the horizon is demonstrated. Therefore, parameters taken from the IO-fit (see Sect. 6.1) are used. Trace gases having absorption bands in the fitting window of 417.5-438.2 nm (ozone, NO_2, water vapour) are considered as well as a pseudo cross-section for rotational Raman and vibrational Raman scattering. No liquid water absorption is included because the applied DOAS polynomial compensates very efficiently for the broad liquid water structures in the relatively narrow window of ≈ 20 nm (this was tested, but is not presented here). The DOAS analysis is performed for all scan directions from -3° (slightly towards the water surface) to 10° (above the horizon) elevation angle. A daily zenith measurement at ≈ 45° SZA is used as fixed reference

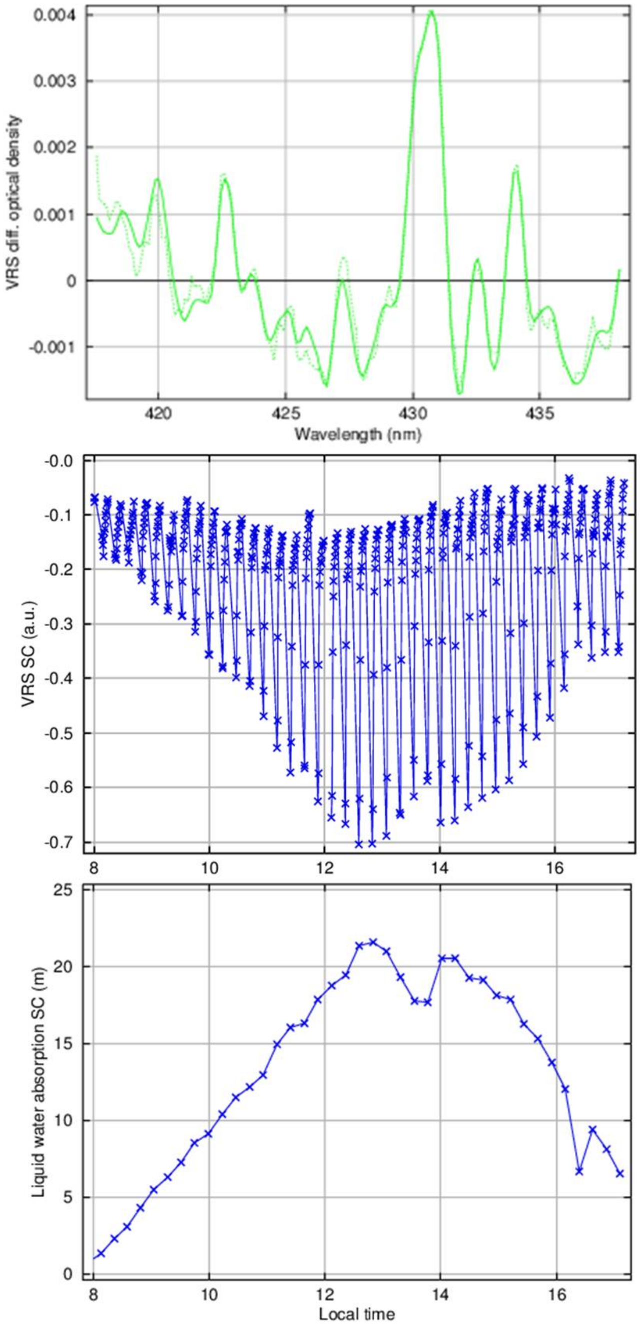

Figure 7.19: DOAS fit results of measurements performed on 14 October. Top: Exemplarily VRS structure found in a measurement in 2° elevation angle at 00:42 UT ≈ 10:30 LT (dashed: Fit, solid: Scaled reference). Middle: Corresponding VRS slant columns for the whole day (elevation angles: -3° to 10°). Bottom: Liquid water absorption slant columns (in a larger fitting window of 412-498 nm) in an elevation angle of -3°.

spectrum [31]. The applied fit parameters are summarized in Tab. 7.2.

The top picture in Fig. 7.19 shows exemplarily the fitted VRS differential optical density for a measurement performed on 14 October (clearest water, best viewing conditions) at ≈10:30 LT. In this example, the VRS structure is clearly found although the measurement has been performed not towards the water surface but in an elevation angle of 2° above the horizon, i.e. also observations in these viewing directions contain some contributions from water leaving radiance. The residual's RMS of the example shown here is $2.3 \cdot 10^{-4}$, which is smaller than in the previous example and in the range of typical DOAS residuals. The timeseries of VRS slant columns for the whole day (14 October) is presented in the middle picture of Fig. 7.19. All values are negative because

---

[31] As mentioned in Sect. 6.1, artificial structures were introduced when using zenith reference spectra at small SZA in the tropics, probably due to saturation effects or direct sunlight in the telescope. To avoid this, fixed reference spectra at 45° SZA were used.

the filling-in of Fraunhofer lines acts effectively like an emission. The sawtooth-shaped timeseries reflects the scanning sequence, which begins with elevation angles of -3° and increases up to 10° (the 15° and 30° elevation angles are not displayed here as the VRS signal was too small). The -3° direction points slightly towards the ocean surface and corresponding values are the most negative (absolute values are highest) as the contribution of water leaving radiance is highest. Afterwards, an increase of slant columns (or decrease of their absolute values) is observed in each scanning sequence because of the decreasing contributions of photons having been in the water. A broader variation is overlaying the scanning sequences leading to maximum values around noon/afternoon, most likely simply because the average light path under water is longest then. To verify this, the liquid water absorption coefficient was fitted for the -3° observations (because these measurements have the strongest liquid water impact of all scanning directions) in a larger fitting window from 412-498 nm (the range from the previous example). In this larger fitting window the liquid water absorption coefficient's broad structures are not compensated by the DOAS polynomial. The resulting slant columns resp. light paths under water are shown in the bottom picture of Fig. 7.19 and reveal the same diurnal cycle as the VRS slant columns. (Note, that even the small dips shortly before 14 LT and after 16 LT are found in both, the VRS as well as the liquid water slant columns). The observed extension of the average underwater light path around noon and in the afternoon may be a combination of different reasons, e.g. real *cleanliness* of the sea, roughness of the sea surface and position of the sun.

7.5.4. Field measurements - Conclusions

To conclude, the first example was designed to observe a maximal spectral impact of liquid water while at the same time suppressing almost all atmospheric influences. This example demonstrated the presence of liquid water absorption structures as well as VRS structures in water leaving radiance in the visible range (≈ 400-500 nm) where literature values of the absorption coefficient differ from each other (Fig. 7.4). The fit quality was dominated by misfits of the liquid water absorption, which were small in relation to the fitted optical density but large on an absolute scale as the absorption signal was strong. Thus, these measurements are well suited to retrieve an average liquid water absorption (as well as VRS) signal for the DOAS analysis under field conditions.

In the second example, realistic measurements (mostly) above the horizon were analysed using fit parameters similar to the IO fit. In this example, the DOAS polynomial compensated the liquid water absorption structures and consequently, it was not included in the fit. In contrast, the VRS structure is narrow-banded and was succesfully detected. As expected, strongest VRS signals were found in viewing directions slightly pointing towards the water surface (-3° direction) and decrease rapidly towards the horizon (Fig. 7.19, middle picture). Nevertheless, also in viewing directions a few degrees above the horizon a VRS signal was observed (Fig. 7.19, top and bottom pictures).

7.6. Experimentally derived cross-sections

A sytematical study comprising several approaches was performed in order to improve DOAS measurements over water surfaces and especially to retrieve empirical *average* cross-sections for liquid water absorption as well as VRS or correction spectra for currently available cross-sections. The filling-in of Fraunhofer structures by Brillouin scattering can be neglected when using current DOAS

instruments, as demonstrated in Sect. 7.4.2.
For the following study, the observations in water viewing directions (-45° and -60° elevation angle)[32] and sea spray measurements as reference I_0 were used, as suggested in Sect. 7.5. The challenge is that the optical depth calculated from these measurements is a superposition of a) liquid water absorption, b) VRS effect, and c) other effects (e.g. straylight in the spectrometer). Further complications arise due to the fact that the VRS spectrum is both, narrow-banded as well as broad-banded, meaning that no separation between absorption spectrum and VRS spectrum is possible for example by simply applying a high-pass, resp. low-pass filter. In detail, the following approaches were tested:

1. First, DOAS fits are performed similar to the fit in example 1 (Sect. 7.5) but **excluding** cross-sections of liquid water absorption and VRS. As explained in Sect. 7.5 (first fit example), these measurements were performed in a way that the resulting optical depth contains in principle only effects in the water and subsequently no atmospheric trace gases are fitted. As a result, this approach avoids possible correlations between liquid water effects and trace gas absorptions (resulting in errors of the retrieved trace gas). The resulting fit residuals, which are a superposition of all effects that have not been considered in the DOAS fit, are analysed in terms of a Principal Component Analysis (PCA) in order to distinguish between independent components the residuals are composed of.
   In principle, the precondition of this approach is that the different effects produce variance in the residuals in a different way (see explanation of the PCA in Sect. 7.6.1). This is a simplification as both effects (liquid water absorption as well as VRS) probably depend in a similar way on various parameters (water properties, length of light path under water). In addition, as mentioned before, VRS is narrow- as well as broad-banded. The straylight correction (additive polynomial to $I(\lambda)$, see Sect. 3.4.4) in the DOAS analysis can compensate partly for narrow-band structures that originate in reality from VRS (e.g., see Vountas et al., 2003). The same is true for the DOAS polynomial and broad-band structures. Therefore, several sets of DOAS parameters were tested (different fitting windows, different orders of the DOAS polynomial, including or excluding a straylight correction) before the PCA was performed.

2. In the second attempt, either VRS or liquid water absorption are included in the DOAS fit. This overcomes the problem of separating both effects in a simultaneous retrieval. The resulting residuals are analysed in order to retrieve an improved cross-section for the effect that was not included in the DOAS fit. The disadvantage is that a cross-section is included in the fit that was initially intended to be improved. However, the second (retrieved and improved) cross-section possibly compensates at least partially for the uncertainties of the first one.

3. In the third approach both liquid water as well as VRS cross-sections are included in the DOAS fit. The resulting residuals are then analysed in order to retrieve an *average* residual structure containing the error due to the uncertainty of both cross-sections.

---

[32] The measurements in $-3°$ elevation angle showing liquid water structures as well (see Sect. 7.5) have not been used since a) they contain considerable influences of atmospheric contributions and b) a separation into clear water and sea spray cover is not possible.

4. Additional approaches and ideas potentially arising from observations during the first three approaches.

7.6.1. Principal component analysis (PCA)

High-dimensional data sets are spanned by many vectors forming a generating system (or coordinate system) for the data set space, i.e. each data point can be expressed as a linear combination of these vectors (for illustration, see Fig. 7.20 of the example given below). These vectors are not necessarily linearly independent from each other, meaning that they are not necessarily a basis system[33]. In addition, the variance of data in one direction can be much less than in other directions, i.e. the corresponding generating vector spanning this direction (the corresponding axis of the coordinate system) can be neglected without loosing a lot of information about the data set.

The Principal Component Analysis (PCA) is a method to reduce the large number of generating vectors (axes of the coordinate system) while finding a new, smaller set of so called principal components that characterise the data sufficiently, that is, without loss of too much information. The principal components are linear combinations of the original vectors (i.e. expressed in the old coordinates), orthogonal and spanning the same space, i.e. they are basis vectors for the data set space. Often a limited number of these new basis vectors (principal components) is enough to describe the major information content of the data. Therefore, the PCA is normally used to either compress data or to analyse data in terms of identifying general patterns.

In the following, the PCA is illustrated by a simple two-dimensional example: A set or *cloud* of data points is described by the vectors (axes) v_1 and v_2 (Fig. 7.20). These vectors are not perpendicular, i.e. they describe partly the same behaviour (there is some redundance). The PCA uses the variance in the data to derive new vectors (principal components) w_1 and w_2. The first principal component w_1 is in the direction of largest scatter in the data. The second principal component is in the direction of largest variance orthogonal to the first one etc.. Since w_1 and w_2 are perpendicular, there is no redundancy left. It is obvious from Fig. 7.20 that the principal components span the

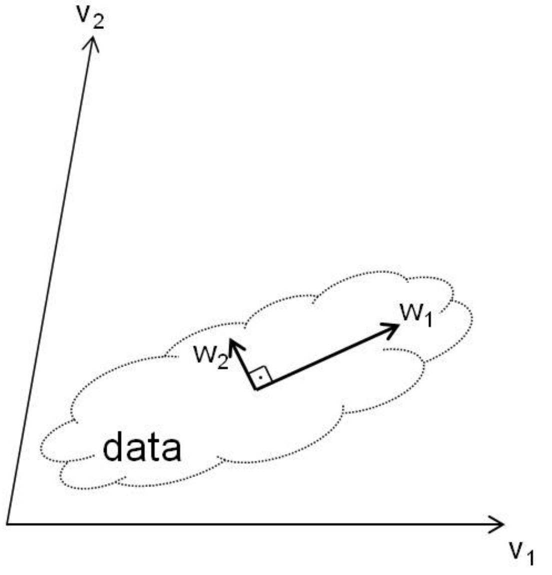

Figure 7.20: Simple example illustrating the idea of the Principal Component Analysis (PCA). A data set (cloud) is expressed by non-orthogonal vectors v_1 and v_2. The PCA creates a new set of orthogonal basis vectors w_1 and w_2 spanning the same data set space. However, w_1 alone may sufficiently describe the data.

---

[33] In linear algebra, a basis is a set of linearly independent vectors that, in a linear combination, can represent every vector in a given vector space.

same space as the original vectors. Furthermore, the first principal component alone accounts for the major information content of the data set while the second component is of minor importance and subsequently only a limited amount of information is lost when neglecting w_2.

Mathematically, the principal components are retrieved as eigenvectors of the data's covariance matrix $\boldsymbol{C}$. In general, a data set comprising m elements $\{\boldsymbol{r}_1, \ldots, \boldsymbol{r}_i, \ldots, \boldsymbol{r}_m\}$ may be of dimension n, i.e. each element has n coordinates λ_j: $\boldsymbol{r}_i = (r_i(\lambda_1), \ldots r_i(\lambda_j), \ldots r_i(\lambda_n))$. In the analysis performed in this chapter, the data set comprised m DOAS residuals $\boldsymbol{r_i}$ (each consisting of some residual optical depth at the different wavelengths λ_j). This input data may be aligned in a $m \times n$ - matrix (each row is a residual $\boldsymbol{r}_i$). Then, the covariances are calculated between each two dimensions (the covariance is always measured between two dimensions), for example between λ_1 and λ_2

$$cov(\lambda_1, \lambda_2) = \frac{\sum_{i=1}^{m} \left[(r_i(\lambda_1) - \bar{r}(\lambda_1)) \cdot (r_i(\lambda_2) - \bar{r}(\lambda_2)) \right]}{m-1} \tag{7.10}$$

and composed in the covariance matrix $\boldsymbol{C}$:

$$\boldsymbol{C} = \begin{pmatrix} cov(\lambda_1, \lambda_1) & cov(\lambda_1, \lambda_2) & & \cdots \\ cov(\lambda_2, \lambda_1) & cov(\lambda_2, \lambda_2) & & \\ & & \ddots & \\ \vdots & & & cov(\lambda_n, \lambda_n) \end{pmatrix} \tag{7.11}$$

Thus, $\boldsymbol{C}$ is a $n \times n$ square matrix and symmetrical about the main diagonal. It might either have none or n (but nothing in between) eigenvectors $\boldsymbol{w}_j$ and eigenvalues c_j (which are real numbers, because $\boldsymbol{C}$ is symmetric) fulfilling the equation

$$\boldsymbol{C} \cdot \boldsymbol{w}_j = c_j \cdot \boldsymbol{w}_j \tag{7.12}$$

All eigenvectors or principal components are orthogonal (meaning no redundancy) and of dimension n, as $\boldsymbol{C}$ is a $n \times n$ - matrix. They are expressed as linear combinations of the original vectors, resp. coordinates λ_j. As a result, they can be interpreted again as a spectrum, which is of major importance for the purpose here. In addition, they span the same data set space (for illustration, see Fig. 7.20). Thus, the data can be completely expressed in the principal components instead of the original coordinates (this is of minor importance for the purpose here). The eigenvalues give the weighting of scatter or variance (or information) in the data that is in the direction of the corresponding eigenvector. The first principal component (the most significant one) is the eigenvector with highest eigenvalue. The relative percentage P of variance or information, which is explained by the eigenvector $\boldsymbol{w}_j$ can be calculated by

$$P(\boldsymbol{w}_j) = \frac{|c_j|}{\sum_{k=1}^{n} |c_k|} \cdot 100\% \tag{7.13}$$

In the analysis performed in this section, often $> 95\%$ of the variance is explained by the first one or two principal components alone. However, the retrieved principal components are abstract parameters that describe the variance in the data most effectively, but do not necessarily have a physical meaning. In addition, as Fig. 7.20 illustrates, the PCA retrieves components that produce scatter totally intependently from each other. As VRS and liquid water absorption both scale with

Parameter	Settings	Remarks
Elevation angle	-45°, -60°	
SZA	<85°	
Measurements	Clear water	100 ms individual as well as integrated
Reference	Closest sea spray	ΔSZA $\leq 2°$
Fit windows	408 - 502 nm, 412 - 498 nm, 410 - 470 nm, 410 - 455 nm	
DOAS polynomial	2nd order, 4th order	for all fit windows
Straylight correction	with/without offset	for all fit windows and polynomials
Liquid water	not included	to be retrieved
VRS	not included	to be retrieved
analysis of residuals	PCA and (exemplarily) factor analysis	
further restrictions tested	only afternoons of 10-18 October	observed scene is in the shadow (no reflections)

Table 7.3.: Different settings tested for approach 1.

the length of light path under water, most likely they produce scatter (or variance) in a very similar way. Therefore, many different approaches and settings were tested (see Sect. 7.6) in order to find principal components that can be identified as liquid water absorption and VRS effect, respectively.

7.6.2. Results of approach 1

For the simultaneous retrieval of liquid water absorption and VRS cross-sections, 16 sets of DOAS residuals were produced for the whole cruise differing in fitting window, applied DOAS polynomial, and straylight correction. Afterwards, each set of residuals was analysed in terms of a Principal Component Analysis (exemplarily, also a factor analysis was tested). In addition, further restrictions were tested by using either all available residuals or only residuals from measurements in the afternoon and evening of 10-18 October. During this time, the ship was moving straight southwards (see Fig. 6.2) so that the observed scene was in the shadow of the ship for measurements in the afternoon (the instrument was measuring to the east). This avoids reflections on the sea surface and subsequently saturation effects or direct sunlight in the telescope. Each analysis was performed on averaged spectra (all individual 100 ms spectra within the integration time of one measurement that could be assigned to clear water or sea spray were averaged, respectively) as well as directly on the individual 100 ms spectra (before averaging). The number of analysed residuals in the first case is $\approx$ 330 (without restrictions) and the number of individual residuals $\approx$ 5100. The applied settings that have been tested are summarized in Tab. 7.3.
Unfortunately, a complete separation into one principle component representing liquid water and one component representing the VRS effect (and other components for all remaining structures,

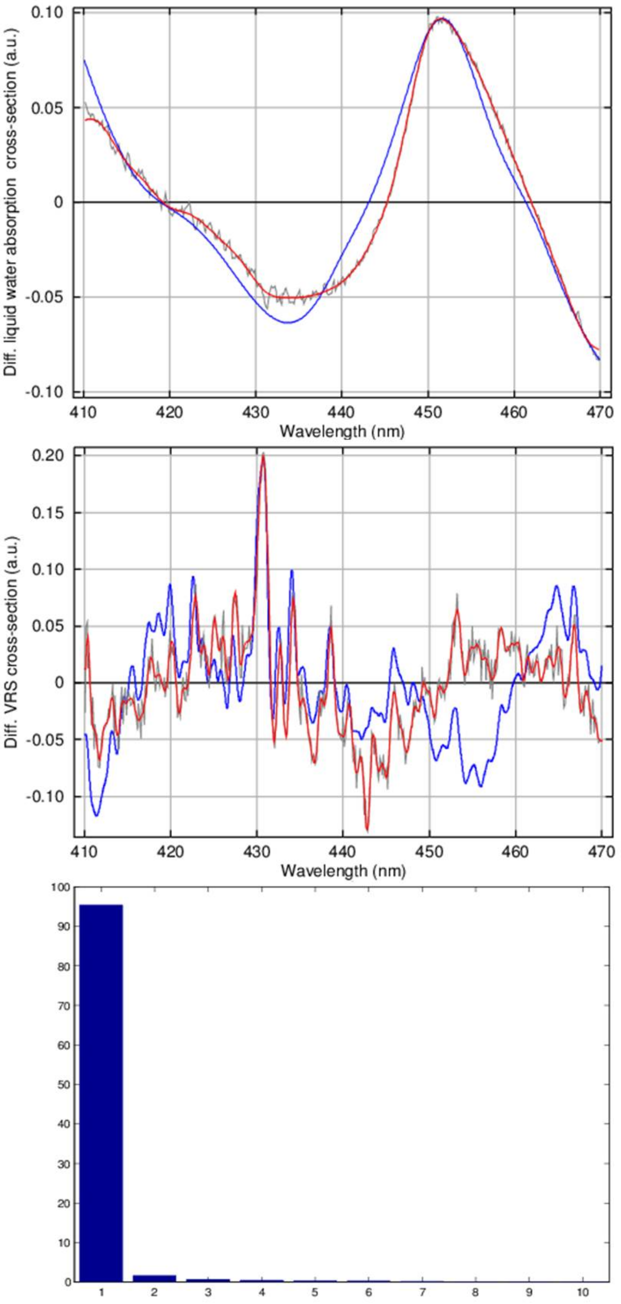

Figure 7.21: Best results of the PCA following approach 1. Top: Normalised 1st principal component in grey (and in red after applying a low-pass filter). Blue: Differential (i.e. subtraction of a 2nd order polynomial) liquid water absorption coefficient from Pope and Fry (1997) scaled to the 1st principal component. Middle: Normalised 2nd principal component (in the same color coding). In blue is the differential simulated VRS optical density for 30° SZA and scenario 1 which has been taken from the first example fit in Sect. 7.5 and that was scaled to the 2nd principal component. Bottom: Diagram of the amount of variance explained by the corresponding principal component, calculated according to Eq. 7.13.

such as straylight and noise) was not obtained by any of the performed retrievals. Mostly, the first two principal components were similar to VRS and liquid water absorption, but exposed features indicating that the respective component is neither VRS nor liquid water absorption alone. For example, the step in the VRS was often not existing and the liquid water absorption structure was always mixed with high-frequency components. Thus, the PCA seems to have difficulties to distinguish between high- and low-frequency contributions, as was expected (Sect. 7.6). Sometimes the retrieved principal components were even completely different from VRS and liquid water absorption. The reason is, as mentioned before, that the principal components do not necessarily have physical meanings. The PCA retrieves unobservable *causes* (the principle components) that produce orthogonal variance of the observables (the residuals). In contrast, VRS and liquid water absorption can be expected to produce variance quite linearly or proportionally because the larger the liquid water absorption signal is in the optical depth the larger also the VRS signal is, as both

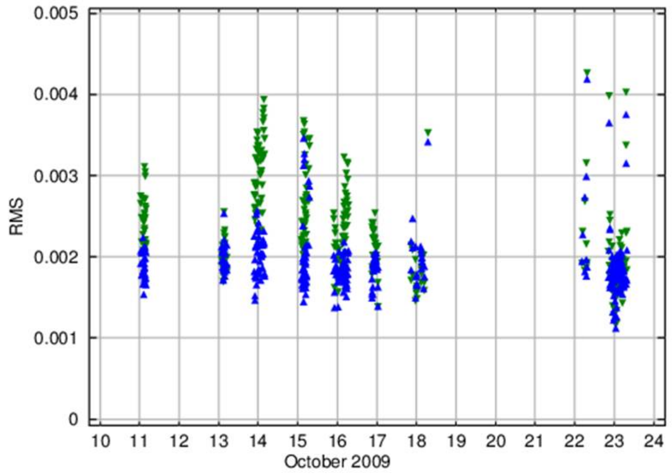

Figure 7.22: Approach 1: RMS of DOAS test fits using measurements towards the water surface. Blue: Using the retrieved 1st and 2nd principal component from Fig. 7.21. Green: Using the liquid water absorption coefficient from Pope and Fry (1997) and the simulated VRS spectrum for 30° SZA and scenario 1 used in the first example in Sect. 7.5.

depend on the length of light path under water.

However, the results from the PCA were much more reasonable than that of a factor analysis. Factor analysis is famous in social sciences where it was originally invented to analyse intelligence tests in order to derive unobserved factors (e.g., mathematical skills etc.) from the test results. Thus, the factor analysis is similar to PCA as it searches for patterns and attempts to effectively explain the observed data with help of non-observable factors. The advantage of this method is, that the retrieved factors do not have to be orthogonal. The factor analysis was tested exemplarily on almost all DOAS fits from Tab. 7.3 (as requiring much more computational effort, it was not used as systematically as the PCA). However, none of the performed retrievals returned factors showing similarity to liquid water absorption and VRS cross-sections simultaneously and subsequently this method was not pursued.

Best PCA results for separated VRS and liquid water structures were retrieved from the DOAS analysis using only measurements in the shadow, i.e. in the afternoons of 10-18 October, applying a fitting window of 410-470 nm, a 2nd order polynomial and omitting straylight effects (i.e., the offset polynomial in the DOAS fit). The retrieved first and second principal components from the PCA are shown as grey lines in the top and middle picture of Fig. 7.21. They can be identified with the liquid water absorption and VRS cross-sections (blue lines), respectively. Note, that the principal components are basis vectors of length 1 (i.e., the squared *intensity* integrated over the wavelength axis is 1) meaning that the numbers on the y-axis (or *intensity* axis) have no meaning in terms of strength of the corresponding component. The amount of information or variance that is accounted for by a certain principle component has been calculated from the associated eigenvalues according to Eq. 7.13. The results are shown for the first ten principle components in the bottom picture of Fig. 7.21. The first principle component alone accounts for ≈ 95% of the information in the DOAS residuals. The first two principle components together describe the data almost entirely. Obviously, residual Fraunhofer structures superpose the first principal component identified with liquid water absorption, i.e. it is contaminated by influences of VRS (or other effects, e.g. straylight, noise, atmospheric RRS contributions). As a result, the obtained principal components cannot be assigned uniquely to one or the other physical process. In order to force a separation of broad-band structures, a low-pass filter was applied on the first principal component (red line in top picture). Accordingly, the second principal component was low-pass filtered to cut off higher frequencies (noise).

In general, the filtered first principle component shows remarkable similarity to the differential liquid water absorption coefficient from Pope and Fry (1997). Note, that small discrepancies are introduced by the filtering process in the beginning and end of the fitting window. For example, even the shoulder at ≈ 425 nm is present in both curves, but it is slightly more distinct in the first principle component. Also the exact position and depth of the minimum around 430-440 nm is different in both data sets. These differences could be either mismatches caused by the PCA and compensated for by other, less important principal components, or they could be real and improve the DOAS fit if the first principal component is used as cross-section.

For the (filtered) second principal component, the maxima and minima appear at the same positions as in the simulated VRS cross-section (as resulting from Fraunhofer lines). Especially in the first half of the fitting window until 440 nm a good agreement with the simulated line is found. At larger wavelengths, both lines tend to disagree in terms of the underlying, broad-band structure: In the VRS cross-section, a *step* appears around ≈ 460 nm (see Sect. 7.4.1), which appears in the second principle component around 450 nm. On the other hand, some structures seem to be more reasonable in the second principle component. For example, the two minima immediately after the strong peak at 430 nm are deeper than in the simulated VRS cross-section. In the example fit in Sect. 7.5, these structures were too small causing large residuals at the corresponding spectral positions (compare Fig. 7.18). As a result, the larger structures retrieved by the PCA could be realistic.

Two DOAS fits were performed in order to verify whether the retrieved principal components improve the fit quality or not. Therefore, again the measurements towards the sea surface ($-45°$ and $-60°$ elevation angle) and corresponding sea spray measurements as reference were used. A fitting window from 412 nm to 468 nm was selected, which is the spectral range where the principal components were retrieved minus a margin of 2 nm on each side to avoid misfits due to the discrepancies caused by the filtering (see Fig. 7.21). In addition, a second order polynomial and an offset-straylight correction was applied in both fits. In the first fit, the liquid water absorption coefficient from Pope and Fry (1997) and the simulated VRS spectrum for 30° SZA and scenario 1 from the first example in Sect. 7.5 were used. In the second fit, the retrieved principle components from Fig. 7.21 were used instead. The RMS of both fits are shown in Fig. 7.22 demonstrating that the fit using the principle components yields smaller RMS. However, it has to be mentioned that the validation performed here has only limited significance, since the principle components are tested on the same data set they were retrieved from, i.e. they are expected to give a good result. This is most likely the reason why the improvement in terms of RMS is largest for 10-18 October, as this is the period from which the principle components are derived. However, also on 22 and 23 October, which were not included in the retrieval, the RMS values are slightly smaller in the fit with principle components (most obvious when comparing the position of high RMS values).

However, the PCA was not able to achieve a complete separation of the two effects (VRS and liquid water absorption) that were present in the residuals. This is most likely due to the fact that the PCA retrieves orthogonal components. If two components produced variance in the residuals independently from each other (i.e. they would produce variance in a very different way), the PCA would be able to retrieve them. But this is not the case for VRS and liquid water absorption. Both optical densities scale with the light path under water and - if excluded in the DOAS fit - the respective left-over signals in the residuals behave in a very similar way.

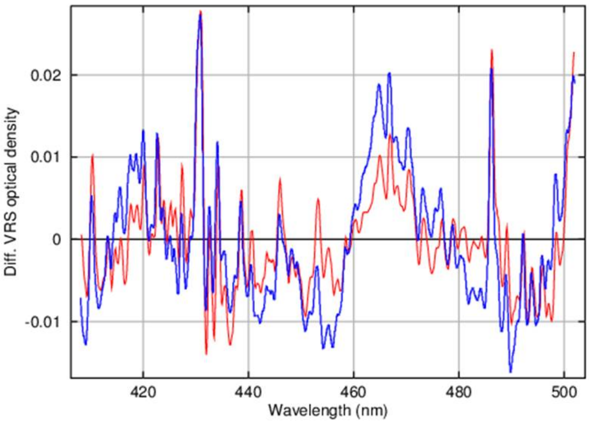

Figure 7.23.: Approach 2 result: Average of the performed DOAS fit (excluding VRS) residuals in red. In blue is the simulated differential VRS spectrum (a 4th order polynomial has been subtracted) for 30° SZA and scenario 1 also used in the first example of Sect. 7.5.

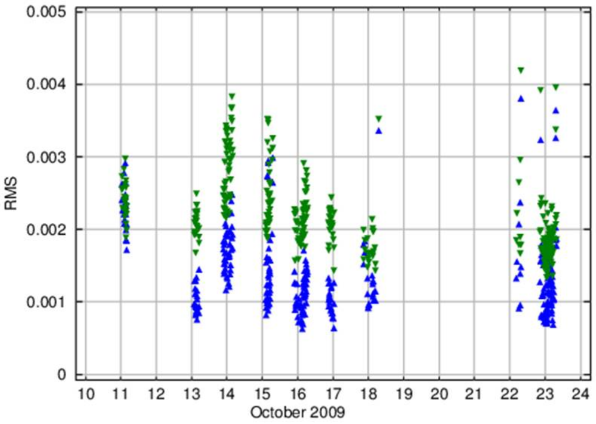

Figure 7.24.: Approach 2: RMS of DOAS test fits using measurements towards the water surface (fit settings: Tab. 7.2). Blue: Using the liquid water absorption coefficient from Pope and Fry (1997) and the retrieved spectrum from Fig. 7.23. Green: Using the simulated VRS spectrum for 30° SZA and scenario 1.

7.6.3. Results of approach 2

To overcome the problem of approach 1 (features that are present in the residuals appeared in the wrong cross-section, i.e. the separation was always incomplete), approach 2 was not aiming at the simultaneous retrieval of VRS and liquid water absorption spectra. Instead, it was tested to include either the liquid water absorption or the VRS cross-section in the DOAS fit and analyse the residuals afterwards in order to retrieve the respective other cross-section from it.

As VRS consists of both, high- and low-frequency components whereas liquid water absorption is only broad-banded, it was first tested to include VRS and straylight correction to obtain residuals in which only broad structures are left. However, it turned out that this approach does not work. The reason is, that a) the dominating structures in the differential optical depth are those of the broad-banded liquid water and b) the DOAS fit (as being a least-squares method) attempts to minimize the residuals. Consequently, the DOAS fit tries to compensate for the dominating broad structures with help of the VRS effect's broad structures (in combination with the fitted polynomial), resulting in oversized fitted VRS optical densities. As a result of the over-correction, the fit residuals suffer artifacts of the small-band VRS structure. Therefore, the liquid water absorption from Pope and Fry (1997) was used as cross-section in the fit while the VRS effect was excluded. Again, several DOAS fits were performed using the same fit parameters as in the first approach (see Tab. 7.3) with the only difference that liquid water was included this time. Also restrictions according to approach one (Tab. 7.3) were tested, i.e. using not the entire data but only measurements in the shadow.

The residuals resulting from different DOAS fits were averaged, revealing large similarity to the VRS structure. Figure 7.23 shows the simulated VRS spectrum from the first example in Sect. 7.5 in blue (30° SZA, scenario 1, see Sect. 7.4.1). The red line is the average residual of the DOAS fit from 408-502 nm, using a 4th order polynomial and no straylight correction. The main features are present in both spectra, especially the step around 460 nm giving rise to the assumption that it is at the right spectral position (in approach one, the step was retrieved at ≈ 450 nm), although it is larger in the simulated VRS spectrum. In general, the broad structures appear to be more distinct in the simulated VRS spectrum. The reason is most likely that the DOAS fit - similar to the explanation given above - used the broad structures of the liquid water absorption (in combination with the DOAS polynomial) to compensate partially for the broad-band structures of VRS in order to minimize the overall residual structure. However, this is not necessarily a disadvantage. Under the condition that VRS and liquid water absorption scale in the same way (which can be assumed as both depend on the length of the light path under water), for the DOAS fit it does not matter if broad structures that are present in the optical depth are compensated by VRS or liquid water (see also discussion in Sect. 7.6.5).

In order to test the improvement of the fit quality, the DOAS fit from Sect. 7.5 (the parameters are summarized in Tab. 7.2) was repeated, but the VRS cross-section used there was replaced by the average residual structure from Fig. 7.23. The RMS of the original fit (which was already displayed in Fig. 7.17, bottom picture) is shown in Fig. 7.24 in green, the RMS of the new fit using the average residual structure instead of VRS in blue. Obviously, the fit using the average residual structure yields lower RMS. However, this has again only limited significance since the residual structure is fitted in the same data from which it is derived.

An advantage of this retrieval is that the problem using the PCA - the principal components are orthogonal while the physical processes are not - is not existing any more. The disadvantage of this retrieval is that only one cross-section is *improved* (here: VRS). However, possible uncertainties of the non-improved cross-section (here: Liquid water absorption) leading to misfits may be compensated by the retrieved cross-section under the condition that both effects scale in the same way (for VRS and liquid water absorption this can be assumed, as explained above).

A further limitation is that the corresponding DOAS fit was performed without straylight correction. This was necessary because the straylight correction compensated almost entirely for high-frequency (Fraunhofer) structures in the optical depth, which are caused either by VRS or straylight. Consequently, from these residuals it was not possible to retrieve any VRS spectrum. On the other hand, the residual structures are certainly caused by straylight to some extent. As the DOAS fit was performed without correction for it, the retrieved spectrum contains some structures that are potentially not due to VRS but straylight, i.e. the *improved* spectrum here is an instrumental- and measurement condition-sensitive solution. However, the straylight contribution is typically small for the MAX-DOAS instrument, i.e. in first approximation the retrieved spectrum can be assumed to be caused by the VRS effect.

7.6.4. Results of approach 3

The most obvious approach attempts not to retrieve improved cross-sections of VRS and liquid water absorption. In contrast to the previous approaches, realistic DOAS fits, i.e. including liquid water absorption, VRS as well as a straylight correction, have been performed using measurements towards the water surface and sea spray measurements as reference. The resulting fit residuals have been analysed in order to retrieve an average correction spectrum that accounts for uncertainties in the existing VRS and liquid water spectra (as well as possible additional influences).

Several sets of realistic DOAS residuals were performed, which are summarized in Tab. 7.4. The small fitting window of 410-455 nm from approach one (see Tab. 7.3) has not been used since the broad-band liquid water cross-section was included.

Parameter	Settings	Remarks
Elevation angle	-45°, -60°	
SZA	<85°	
Measurements	Clear water	100 ms individual as well as integrated
Reference	Closest sea spray	ΔSZA $\leq 2°$
Fit window	408 - 502 nm, 412 - 498 nm, 412 - 470 nm	
DOAS polynomial	2nd order, 4th order	for all fit windows
Straylight correction	first order (offset)	
Liquid water	included	(Pope and Fry, 1997)
VRS	included	First example in Sect. 7.5

Table 7.4: Different DOAS settings used for approach 3.

The resulting residuals have been averaged for each DOAS fit. Averaged residuals corresponding to different DOAS fits reveal the same general structures, even if retrieved in another fit window or applying another DOAS polynomial, i.e. the observed residual pattern seems to be stable. For illustration, some average residuals are exemplarily shown in Fig. 7.25 (note also the similarity between the lines in Fig. 7.25 and the residual structure of the test fit in Fig. 7.18).

These average residual spectra have been retrieved using a smoothed and spline interpolated version of the literature water absorption coefficient from Pope and Fry (1997) in order to adopt it for use in DOAS fits (see explanation in Sect. 7.5). For completeness, it has to be ruled out that the retrieved systematic structures are caused by these changes (this would imply that the published literature spectrum is already correct). Therefore, from the used absorption cross-section the original one (as it is published in literature) was subtracted. For comparison to the retrieved residual spectrum which is differential, a 2nd order polynomial was subtracted and the resulting line is plotted in red in Fig. 7.26 together with the corresponding residual spectrum from Fig. 7.25 (green line). Obviously, the structures due to the changes applied to the liquid water absorption spectrum (i.e. the red line) are much smaller than the retrieved residual spectrum (green). The red line was scaled by 10 (brown line) so that the last peak is of the same size as the corresponding peak of the green line. Apart from the last two maxima and minima, only the minimum around 450 nm coincide to some extent, but it is twice the size in the retrieved residual spectrum. Overall, the two curves show almost no agreement with each other and the correlation was calculated as $\approx$0.18. Consequently, the retrieved spectrum can be assumed not to result from the changes applied to the liquid water absorption spectrum. However, at this point it should be mentioned again that the residual spectrum was retrieved using a specific liquid water absorption spectrum (for the uncertainty of which it corrects) and subsequently it should be used only in combination with this in later DOAS fits.

To verify the effect (and possible improvement) of the retrieved average residual structure, the DOAS fit from the first example in Sect. 7.5 was repeated (for settings, see Tab. 7.2), but in addition the blue line from Fig. 7.25 was included as a cross-section. The resulting RMS are shown in Fig. 7.27 as green points for the original fit and as blue points for the fit including the

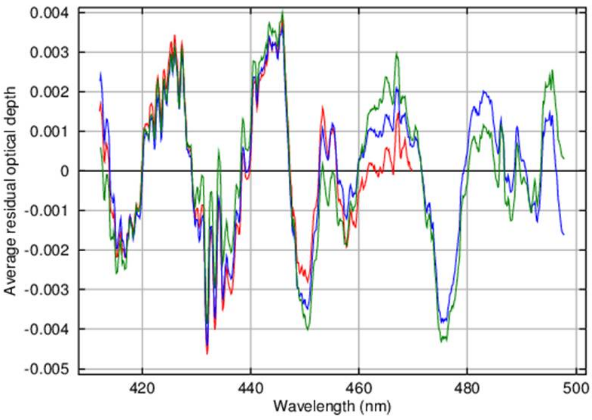

Figure 7.25.: Approach 3: Averaged residuals of different DOAS fits. Red: 412-470 nm and 2nd order polynomial, blue: 412-498 nm and 4th order polynomial, green: 412-498 nm and 2nd order polynomial.

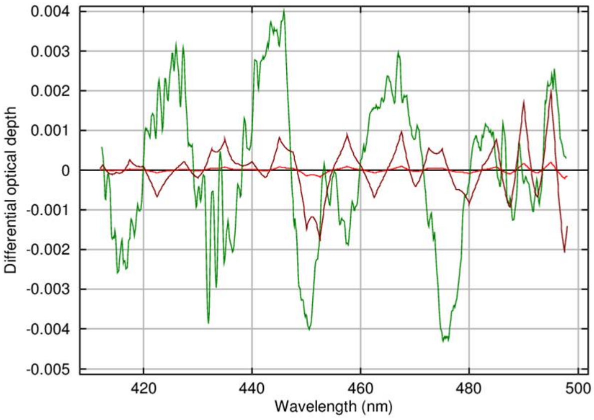

Figure 7.26.: Average residual structure in green (corresponding to the green line in Fig. 7.25) and difference between applied liquid water spectrum and (linear interpolated) spectrum from (Pope and Fry, 1997) in red (multiplied by 10 in brown).

retrieved structure. Obviously, the fit quality improves by a factor of 2-3 when including the average residual structure, with the exception of 11 October. On this day, almost no improvement is observed. Figure 7.17 indicates that the liquid water absorption is small compared to other days, but at the same time the RMS is high. The residuals of this day reveal strong mismatches of the liquid water absorption. The reason for this is unknown, conditions of the sea (strong groundswell at this day, suspended matter etc.) could be a possible explanation as well as instrumental effects (the slit function was optimized in the night between 11 and 12 October). However, the residuals of this day show differences to the other days and subsequently the average residual structure improve the fit quality only slightly as the relative contribution of a single day is low. Nevertheless, in general, the improvement demonstrated by Fig. 7.27 is large, but again, this has only limited significance because the residual structure is used for the same spectra from which it is derived, so an improvement is to be expected.

It is worth mentioning that the (absolute values of) the slant columns of the retrieved residual spectrum (Fig. 7.25) follow the shape of the liquid water absorption slant columns and therefore the length of the light path under water. This is demonstrated by a correlation plot shown in Fig. 7.28. A linear regression yields a correlation of $\approx 94\%$. This is strong evidence for the assumption that the average residual structure compensates misfits of liquid water absorption (most likely in combination with VRS misfits) and not compensating for any potential instrumental artifacts or systematic noise as these would hardly show a linear relationship to the length of the underwater light path (the possibility of an instrumental effect is ruled out in Sect. 7.7.2).

7.6.5. Additional approach (approach 4)

During the DOAS test fits for approach 2, it became obvious that if straylight is included but VRS is excluded then the straylight correction compensates very efficiently for Fraunhofer structures. This is consistent with previous findings of Vountas et al. (2003). As a consequence, the retrieval of a VRS spectrum from fits including a straylight correction was not possible in approach two (Sect. 7.6.3).

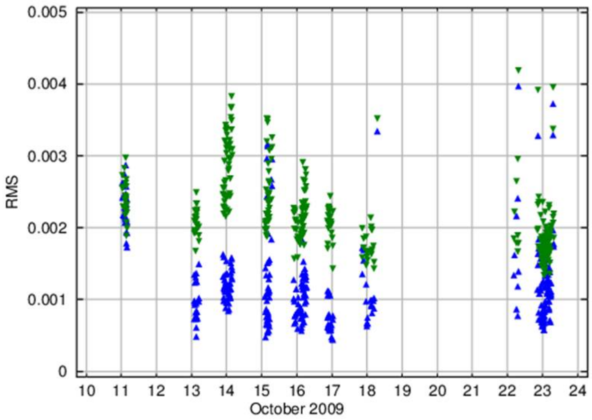

Figure 7.27.: Approach 3: Improvement of the DOAS fit quality (fit settings taken from Tab. 7.2) by introducing the retrieved average residual derived in approach three. Green: Original fit RMS without average residual (see bottom picture of Fig. 7.17), blue: RMS of the same fit but including the average residual structure.

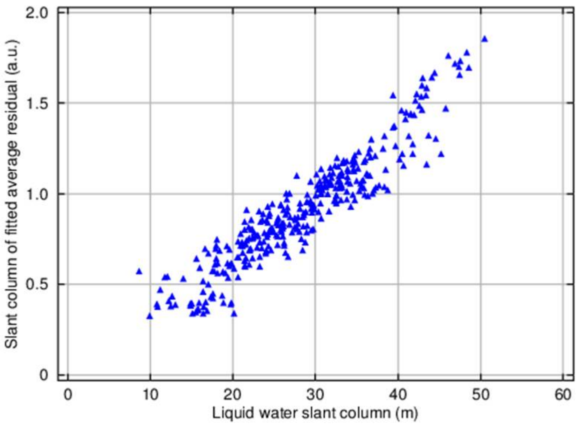

Figure 7.28.: Approach 3: Correlation plot between the fitted slant columns of liquid water absorption and the derived average residual structure (for the latter one, absolute values are shown as the slant columns of the fitted average residual structure were negative). Linear regression: Slope ≈ 0.03, offset ≈ −0.05, correlation ≈ 0.94.

However, if the straylight correction is able to compensate for the high-frequency components of VRS, then only its broad structures remain in the optical depth. Therefore, a set of DOAS fits including liquid water absorption and straylight but excluding VRS have been performed (for settings, see Tab. 7.5).

Note, that the DOAS fit arranges the polynomial and the liquid water absorption in a way that compensates as far as possible for the broad VRS structures even if this introduces misfits of the liquid water absorption at other spectral positions as long as the sum of squared residual points decreases (see Eq. 3.36). As a result, the DOAS fit residuals do not necessarily look like the broad-band structures of VRS.

The resulting residuals have been averaged for each DOAS fit. Averaged residuals corresponding to different fit parameters reveal the same general structures, as the examples in Fig. 7.29 show. Almost no difference is observed whether an offset and a linear straylight correction or only an offset straylight correction is applied. Instead, small differences occur between different fitting windows and applied degree of the DOAS polynomial. Most likely the reason for this behaviour is that in each fit another combination of DOAS polynomial and liquid water absorption yields minimal overall residual structures as explained above. However, the differences are small except for the beginning and end of the fitted spectral range. Note that although a straylight correction was applied that was found to correct efficiently for Fraunhofer structures, some small-band structures persist in the averaged residuals. Some of these features were also found in the retrieved spectra in approach 3 (Fig. 7.25), e.g. the small-band structures at ≈ 430-435 nm. Obviously, these structures are neither completely accounted for by the simulated VRS spectrum alone (approach 3) nor by the straylight correction alone (this approach). As it was also found for approach 3, the retrieved spectra show no similarity to the line accounting for the changes applied to the liquid water absorption cross-section (brown line in Fig. 7.26), i.e. these spectra are not caused by the changes that were made in order to adopt the liquid water cross-section for use in DOAS fits.

Table 7.5: Different DOAS settings used in approach 4.

Parameter	Settings	Remarks
Elevation angle	-45°, -60°	
SZA	<85°	
Measurements	Clear water	100 ms individual as well as integrated
Reference	Closest sea spray	$\Delta SZA \leq 2°$
Fit window	408 - 502 nm, 412 - 498 nm, 410 - 470 nm	
DOAS polynomial	2nd order, 4th order	for all fit windows
Straylight correction	offset and linear	for all combinations
Liquid water	included	(Pope and Fry, 1997)
VRS	not included	

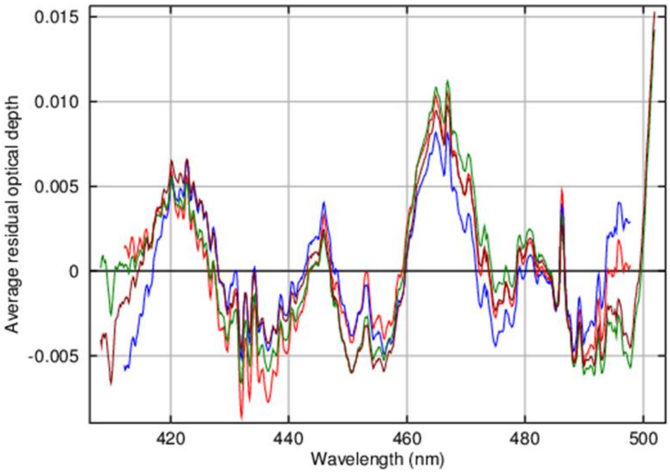

Figure 7.29: Approach 4: Averaged residuals of different DOAS fits (using an offset straylight correction). Red: 412-498 nm and 2nd order polynomial, blue: 412-498 nm and 4th order polynomial, green: 408-502 nm and 2nd order polynomial, brown: 408-502 nm and 4th order polynomial.

The potential improvement due to the retrieved residual structure was tested using the fit parameters from the first example in Sect. 7.5 (settings are summarized in Tab. 7.2) with the difference that no VRS structure but the residual structure retrieved in this approach is included. For the residual structure, the spectrum retrieved in a fitting window of 412-498 nm and applying a 4th order polynomial has been selected (which is the blue line in Fig. 7.29), as these are the parameters of the test fit. The resulting RMS timeseries is shown in Fig. 7.30, green denotes the original fit, blue the fit using the average residual structure instead of VRS. The fit quality increases by a factor of ≈ 2 (apart from 11 October, similar to the previous approach) when using the retrieved spectrum.

In contrast to approach 3, this has some significance, although again an average residual is fitted in the same data from which it is derived. The difference is that in approach 3 the average residual was used as an additional cross-section. Here, two fits are compared, one of them using a VRS cross-section, the other the retrieved spectrum. The result is that using the retrieved spectrum instead of VRS is producing smaller RMS.

The disadvantage is that the average spectrum has been retrieved from fits where the DOAS polynomial in combination with liquid water absorption (and straylight) is arranged in a way that

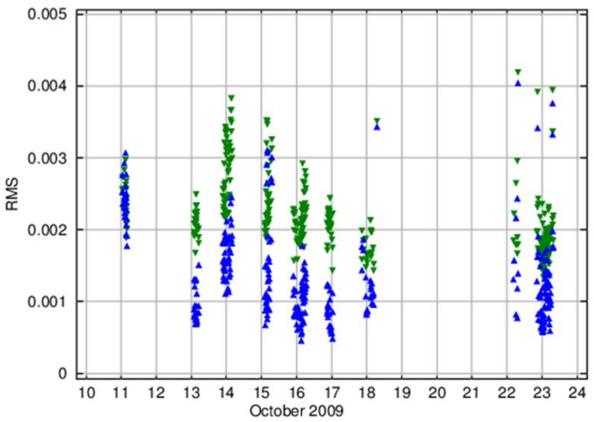

Figure 7.30.: Approach 4: Improvement of the DOAS fit quality using settings from the first example fit in Sect. 7.5 (the settings are summarized in Tab. 7.2). Green: Original fit RMS, blue: RMS when excluding VRS and including the retrieved structure (blue line in Fig. 7.29).

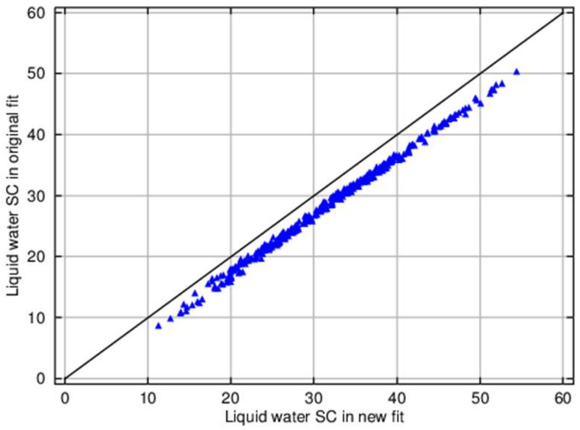

Figure 7.31.: Approach 4: Correlation plot of liquid water slant columns. On the y-axis are values of the original fit (using VRS), on the x-axis values of the new fit (using the average spectrum instead of VRS). In black is the 1:1 line. A linear regression yields: Slope ≈ 0.96, offset ≈ -1.97, correlation ≈ 0.998.

minimizes the overall residual, as explained above. As a result, a) the average residual does not exactly look like VRS's broad-band structures and b) the fitted optical density of liquid water (and therefore its slant columns) might be slightly different from the corresponding values of a fit using VRS. This means the liquid water slant columns are also potentially different in a fit when using the retrieved average spectrum instead of VRS. This is demonstrated by Fig. 7.31 showing a correlation plot between liquid water slant columns resulting from the two fits performed to verify the RMS improvement (including VRS on the y-axis and including the average spectrum instead of VRS on the x-axis). Obviously, the slant columns are not the same in the fits, but reveal a linear dependance and a large correlation of 99.8%. Consequently, care must be taken with respect on the interpretation of liquid water slant columns when using the retrieved average spectrum.

7.6.6. Overview of the different approaches

Approach 1 aimed at the simultaneous retrieval of VRS and liquid water absorption structures from DOAS fits excluding these effects and further analysis using a PCA. Best case results show similarities with literature resp. simulated cross-sections of VRS and liquid water absorption. Nevertheless, it turned out that the PCA was not able to separate the two effects completely (see Fig. 7.21), most likely because it retrieves components that vary independently from each other, which is not true for VRS and liquid water absorption (both scaling with the underwater light path). In addition, using the results of approach 1 in a DOAS test fit yields the smallest improvement (Fig. 7.22).

In approach 2, liquid water absorption was included in different DOAS fits while VRS was excluded. From the fit residuals, an average structure was retrieved that shows large similarity to the simulated VRS spectrum from SCIATRAN (Fig. 7.23). Nevertheless, the broad structures, especially the step around 460 nm are expressed to a lesser extent in the retrieved spectrum compared to the simulated one. The reason is most likely that the DOAS fit arranged the polynomial and the broad-band liquid water cross-section in a way to compensate partially for the VRS broad structures (in order to minimize the fit residual). In addition, no straylight correction was applied because it compensates partially for Fraunhofer structures as it is an additive polynomial in $I(\lambda)$. Thus, residual structures caused by straylight effects might remain in the retrieved VRS structure. However, an improvement of the fit quality was observed when using the retrieved VRS structure instead of the simulated one in a DOAS test fit (Fig. 7.24).

The most obvious approach 3, simply retrieving an average residual spectrum (Fig. 7.25) from fits including literature cross-sections for liquid water and VRS, yields the largest improvement (Fig. 7.27). Slant columns of the retrieved average residual (when included in the fit) scale with the length of light path under water (Fig. 7.28), which is reasonable under the condition that the average residual accounts for uncertainties of the liquid water absorption and/or VRS. However, an improvement when applying in the same data from which the spectrum is derived is expected, so tests in other data sets (satellite data) are required.

Approach 4 uses the fact that a straylight correction is able to compensate for Fraunhofer structures from VRS to some extent, which was also found in a previous study (Vountas et al., 2003). An average residual spectrum was retrieved from DOAS fits including liquid water absorption and straylight correction (Fig. 7.29) accounting for those VRS structures that are not compensated by the straylight correction (as well as potential uncertainties of liquid water absorption). Application of this average spectrum avoids the need of a VRS cross-section and yields smaller RMS than fits using a simulated VRS spectrum (Fig. 7.30), but at the price that the liquid water absorption slant columns are not the same as in the original fit (Fig. 7.31).

7.7. Verification of retrieved structures

In this section, the retrieved liquid water spectral structures from Sect. 7.6 are tested on satellite data. The results of approach 1 were not pursued further for the reasons mentioned above (Sect. 7.6.6).

7.7.1. Verification of approach 2

The experimentally retrieved VRS spectrum from approach 2 was tested in a DOAS fit on OMI satellite data from August 2007 (which is 2 years earlier than the ground-based measurements from which the cross-section was retrieved). For the DOAS fit, a fitting window from 410–495 nm was selected, which is broad enough to obtain structures from liquid water absorption and the broad VRS structures. An offset straylight correction and a polynomial of degree 4 were applied as well as cross-sections of O_3, NO_2, O_4, water vapour, the Ring effect (RRS), liquid water absorption, and the retrieved (empirical) VRS spectrum.

Figure 7.32(a) shows exemplarily the fitted VRS differential optical density for a measurement at $\approx$ 11°N and $\approx$ 155°E on 1 August 2007. Obviously, the structure of the retrieved VRS spectrum is clearly detected in the satellite data. Figure 7.32(b) shows the corresponding fit residual which looks unstructured. The only two larger misfits, which appear in the residual around $\approx$433 nm and $\approx$475 nm, are most likely caused by the fact that the satellite's resolution is better than the MAX-DOAS instrument's resolution, which is a limiting factor for the potential use of the retrieved VRS spectrum.

Figure 7.33 shows the results of the performed DOAS test fit on a global scale. For the maps

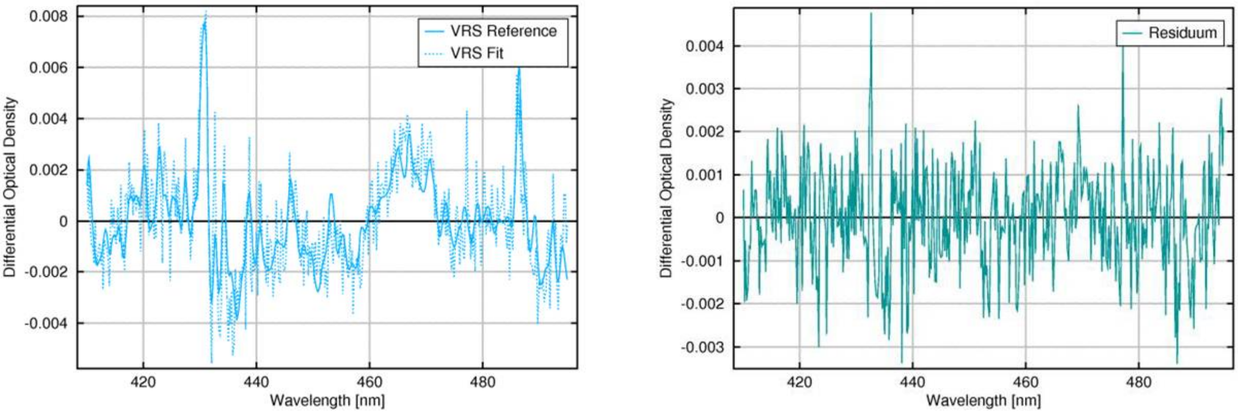

(a) VRS diff. optical density

(b) Residual

Figure 7.32.: The retrieved VRS spectrum from approach 2 is fitted in OMI data over the remote Pacific (1 Aug 2007, ≈ 11°N and ≈ 155°E, orbit 70801227).

shown here, which are a monthly average (August 2007), only cloud-free pixels (cf ≤ 0.2) have been used. The empirical VRS slant column is plotted in Fig. 7.33(a). Obviously, the retrieved VRS spectrum is clearly linked to liquid water and areas of highest slant columns coincide with regions of highest liquid water absorption slant columns, which are plotted in Fig. 7.33(c) for comparison. Note, that the VRS effect is effectively an emission as describing the filling-in of Fraunhofer structures and subsequently strongest VRS slant columns are most negative[34]. The values of the VRS slant columns are given in a.u. because these slant columns are the scaling factors of the retrieved average VRS structure from approach 2, which is obviously not calibrated.

The corresponding VRS fit errors for the slant columns shown in Fig. 7.33(a) are plotted in Fig. 7.33(b). While smallest errors occur over clear water surfaces, the fit error over land is mostly in the order of 100%, i.e. no reliable VRS structure is found here (the contrast between sea and land can be nicely seen on the example of Madagascar).

A clear exception of this can be found in the southeast of the Arabian peninsula where VRS fit errors reach the same values as over the ocean. Also over Australia (Simpson desert) and on some spots over the northern Sahara, the same behaviour is found. Furthermore, the VRS slant columns (Fig. 7.33(a)) at these locations tend to negative values as over the ocean although this is not as obviously to see as in the VRS error due to the color-coding. By comparing to satellite images (photos) it was found that these areas are desert regions with yellow-reddish sand dunes. For example, over the Arabian peninsula it was found by zooming-in that the shape of the region of small VRS errors follows exactly the sand dunes region. However, even if the VRS fit errors are small in this region, when evaluating the fitted VRS optical densities it turned out that not the small-band structures (Fraunhofer lines) of the VRS spectrum but predominantly the broad-band structures (e.g. the step around 460 nm) are fitted well. The most likely explanation is that these regions of sand dunes have a broad-band structure in the spectral reflectance that is not included in the fit.

---

[34] This physical explanation is true for VRS. However, if a retrieved residual spectrum is used again in DOAS fits (see also the following sections), always negative slant columns are obtained if the spectrum is successfully detected over water surfaces. The reason is simply that the residual spectrum is included as an absorption structure in the fitting routine. (Normally, a positive cross-section's value means a large absorption. In contrast, if the residual is positive, this means less absorption. If the residual is included in the fitting routine as a cross-section, the result is the obtained negative fit factors or slant columns, respectively.)

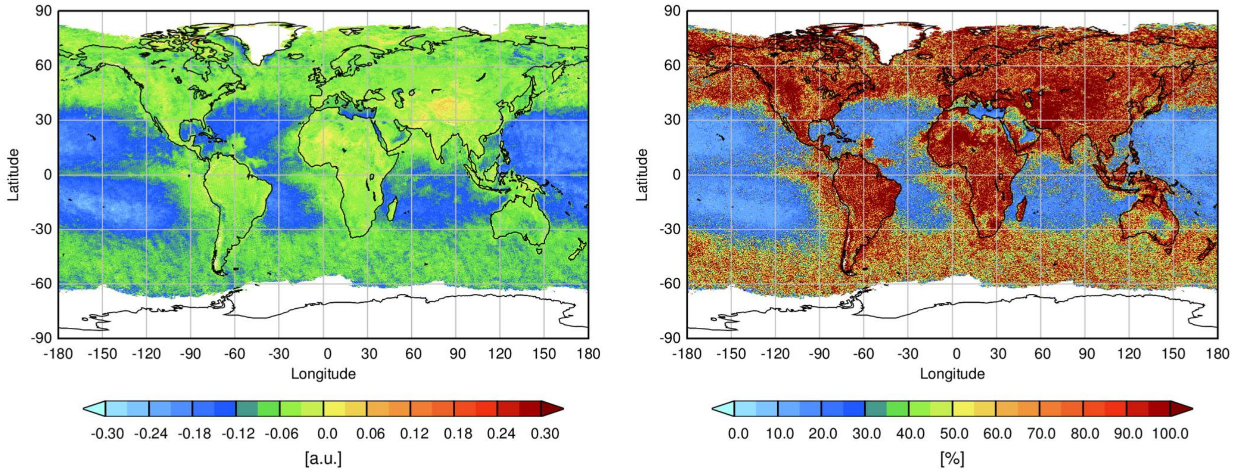

(a) Empirical VRS slant column

(b) Empirical VRS error

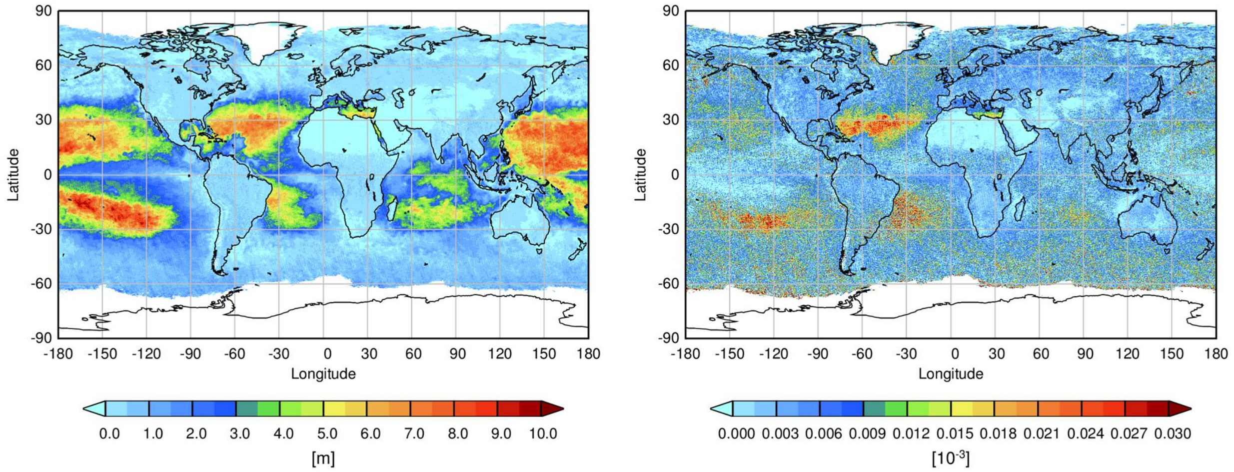

(c) Liquid water slant column

(d) $\text{Chisquare}_{\text{simul\_VRS}}$ - $\text{Chisquare}_{\text{empirical\_VRS}}$

Figure 7.33.: Performance of the retrieved VRS spectrum in OMI satellite data for August 2007 (Figs. 7.33(a)–7.33(b)). For comparison, Fig. 7.33(c) shows the retrieved liquid water absorption slant column for the same fit. Fig. 7.33(d) shows the difference of the chisquare between two fits using the same parameters except for VRS: First, using a simulated VRS cross-section and second, using the retrieved VRS spectrum. The plots have been prepared by L. Alvarado, IUP Bremen (personal communication, 2013).

For example, such spectral structures from soil in satellite data have been also found by Richter et al. (2011). In order to minimize the residual, the fitting routine then compensates for the sand structure with the broad-band VRS structure (that is in principle not present over these regions) most likely in combination with the DOAS fit and/or the liquid water structure. The result of this compensation is then enhanced VRS slant columns and small corresponding errors over these regions.

To verify the potential of improving DOAS fits using the retrieved VRS spectrum, a second run of DOAS fits on OMI data was performed. Therefore, the same fit parameters were applied with the only difference that not the retrieved (empirical) VRS spectrum but a VRS spectrum that was calculated by SCIATRAN (T. Dinter, IUP Bremen, personal communication 2013) for satellite geometry was used (this VRS spectrum for satellite observations has been simulated with the same

SCIATRAN version used before in this chapter). The chisquare[35] of the fit using the retrieved VRS spectrum was subtracted from the chisquare of the fit using the simulated spectrum and the difference is plotted in Fig. 7.33(d). Thus, positive numbers indicate that the fit with the retrieved VRS spectrum yields smaller chisquares and therefore a better fit quality.

Obviously, the DOAS fit using the empirical VRS structure leads to clearly smaller chisquare values predominantly over the northern Atlantic, the southeast Pacific and over the southern Atlantic in the region of the South Atlantic Anomaly (SAA). It should be mentioned that on some parts over the east central Pacific the simulated VRS spectrum performs slightly better than the retrieved one, but overall, the empirical VRS spectrum leads to a better fit quality over water surfaces. Also over desert regions (e.g. Sahara) the simulated VRS spectrum leads to smaller chisquare values, obviously because the interference with sand structures is stronger and they are compensated to a larger extent. Over the ocean, maximum values for the chisquare difference are in the order of $0.3 \cdot 10^{-3}$ (Fig. 7.33(d)) while the chisquare of both the fit with empirical VRS as well as simulated VRS is typically in the range of $0.6 \cdot 10^{-3}$ (Fig. 7.36(d)) gives an impression of the chisquare in the fits performed here). Thus, an improvement of up to 5% over water surfaces is achieved by using the empirical VRS spectrum.

To conclude, the empirically retrieved VRS spectrum from approach 2 is successfully detected in satellite data. Over water surfaces, the DOAS fit improved (in terms of the chisquare) by a few percent compared to the fit using a simulated VRS spectrum. However, the empirical VRS spectrum is differential as resulting from DOAS fit residuals and also it may partially correct for uncertainties of the liquid water absorption that was used in the retrieval fit window (see Sect. 7.5.1), which might be the main reason why it performs better. As a consequence, the empirical VRS spectrum is case-sensitive and should be used a) only together with the liquid water cross-section used in the retrieval fit and b) only in DOAS fits that are similar to the retrieval fit (same order of polynomial, similar spectral range). However, the potential of improving DOAS fits over water surfaces by using empirical VRS spectra was demonstrated and theoretically, empirical VRS spectra could be retrieved from the TransBrom water measurements for various desired fit windows.

7.7.2. Verification of approach 3

The retrieved average residual structure found in approach 3 (for simplicity called the approach-3-spectrum in the following) is considered to correct for uncertainties of the liquid water absorption and the VRS cross-sections used in the retrieval fit. However, the approach-3-spectrum could have several possible reasons, which are described in detail and verified below:

- Instrumental effects
- An input solar spectrum for the SCIATRAN calculation of VRS that is different from the true solar spectrum
- Real misfits of currently available liquid water and/or VRS cross-sections

It is unlikely that the approach-3-spectrum is caused by instrumental effects for various reasons: 1) Instrumental effects (e.g., wavelength-dependent efficiency of grating spectrometers, wavelength-

---

[35] The squareroot of chisquare divided by the number of wavelengths (pixel columns of the CCD) in the fit window yields the RMS. Thus, both values describe the fit quality but the Chisquare increases with the fit window while the RMS is *normalised*.

Figure 7.34: Approach 3 verification: Average residuals retrieved with different input spectra for the SCIATRAN VRS simulation. The blue line corresponds to the blue line in Fig. 7.25 (retrieval window 412–498 nm, 4th order polynomial, VRS simulation: Scenario 1, Kurucz solar spectrum). Red line: VRS simulation for scenario 2 and Kurucz solar spectrum. Green: Scenario 2 and solar spectrum from SCIAMACHY.

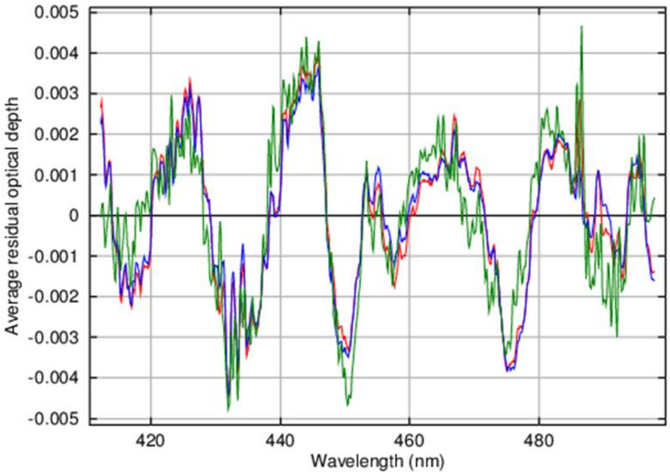

dependent quantum efficiency of the CCD) should cancel out by taking the ratio of I and I_0 in the DOAS analysis. 2) Instrumental effects would not scale with the light path under water, but this behaviour was observed (Fig. 7.28). 3) If it were instrumental effects, the resulting structures should remain also in the residuals of off-axis and zenith measurement (i.e. in the normal trace gas retrievals as described in Sect. 6.1), which is not observed. 4) Finally, if tested in satellite data, a spectrum caused by instrumental effects should not be linked to oceanic regions. However, as can be seen below (Fig. 7.36), this is observed and subsequently the retrieved approach-3-spectrum is not caused by instrumental effects (but correct for liquid water structures that are not completely accounted for by existing cross-sections).

The VRS cross-section has been simulated using a solar spectrum from literature (Kurucz solar spectrum). However, the sun activity is known to undergo changes, for example the 11-year cycle, meaning that the true solar spectrum at the time of the retrieval (the TransBrom campaign) is potentially different from the one used in the retrieval fit. This could possibly cause a residual structure. To verify this error source, the calculations of approach 3 were repeated using different solar spectra for the SCIATRAN simulation of a VRS spectrum (that is used then in the retrieval fit). Figure 7.34 shows some resulting average residual structures (different approach-3-spectra). The blue line was retrieved in a window from 412–498 nm using a 4th order DOAS polynomial and corresponds to the blue line in Fig. 7.25. In the retrieval of this structure, the VRS spectrum for scenario 1 was used. As input for the SCIATRAN VRS calculation, the Kurucz solar spectrum was used. The red line in Fig. 7.34 was obtained from the same retrieval parameters, but using the SCIATRAN VRS simulation for scenario 2. Almost no difference is observed demonstrating that the scenario has only a marginal influence on the retrieved approach-3-spectrum. (Consequently, if the approach-3-spectrum corrects not only for misfits of the liquid water absorption but also for misfits of the VRS spectrum, these misfits are systematical. Unfortunately, it cannot be distinguished if the approach-3-spectrum is caused by misfits of liquid water absorption alone, by VRS alone, or by a combination of both, but the latter is most probable).

The green line in Fig. 7.34 was obtained by using the same fit parameters and a SCIATRAN simulated VRS spectrum for scenario 2. The difference to the red line is that this time a solar spectrum recorded by the SCIAMACHY instrument was used as input for the SCIATRAN VRS simulation. Obviously, this leads to small changes in the retrieved approach-3-spectrum, but the overall structure stays the same. As a result, the assumption that the solar spectrum used for the

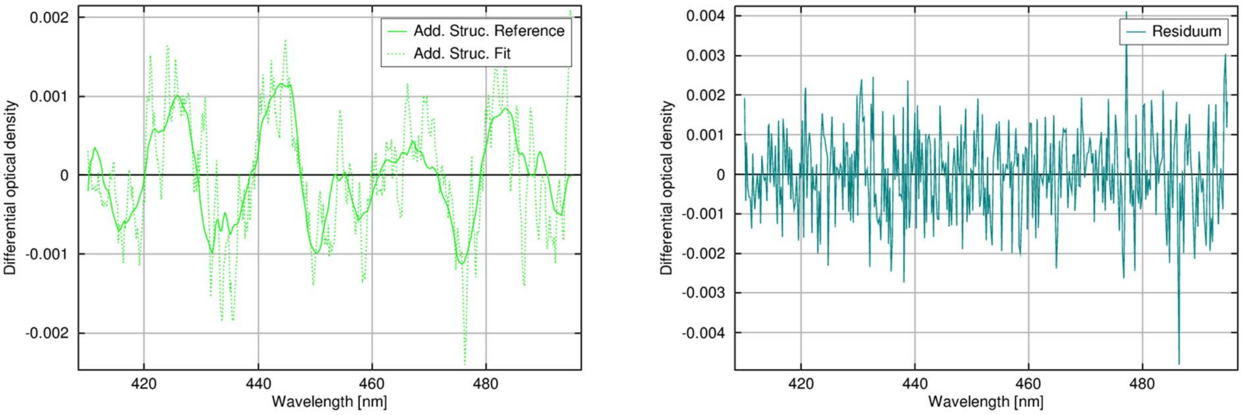

(a) Fitted Approach-3-spectrum (b) Residual

Figure 7.35.: The retrieved spectrum from approach 3 is fitted in OMI data over the remote Pacific (1 Aug 2007, ≈ 11°N and ≈ 155°E). To reduce pixel-to-pixel variation and improve visualisation, a running mean over 5 pixels was applied to the fitted spectrum in Fig. 7.35(a).

SCIATRAN VRS simulation causes the observed approach-3-spectrum could be ruled out.[36]

The most likely explanation for the approach-3-spectrum is that it is caused by misfits of liquid water absorption and VRS. This would allow using it in DOAS fits as a correction spectrum for uncertainties of liquid water spectral effects.

To verify this, the approach-3-spectrum was fitted in OMI data (again, one month - August 2007 - was used for these tests). The same fit parameters as in Sect. 7.7.1 were used: A fit window from 410–495 nm, a 4th order polynomial, an offset straylight correction and cross-sections of O_3, NO_2, O_4, water vapour, the Ring effect (RRS) as well as liquid water absorption. In addition, a SCIATRAN VRS spectrum was calculated for satellite geometry and the retrieved approach-3-spectrum was used as an additional absorber.

Figure 7.35 shows exemplarily the fitted approach-3-spectrum in OMI data. The retrieved structure is clearly found although the fitted optical density is small. This is because it is a correction spectrum accounting for uncertainties of existing cross-sections (therefore, a running mean was applied for better visualisation of the fitted optical density). On a global scale, the results are shown in Fig. 7.36.

In Fig. 7.36(a), the slant columns of the approach-3-spectrum used as an additional absorber are plotted. Clearly, this structure is linked to the ocean and it reveals the same pattern as the liquid water absorption (e.g., compare to Fig. 7.33(c)) or VRS (Fig. 7.33(a)) with largest (most negative) values over clear ocean surfaces in the tropics. In contrast, positive slant columns occur over desert areas, but in larger regions as found in Sect. 7.7.1 (see Fig. 7.33(a)). Moreover, the fit error of the approach-3-spectrum (Fig. 7.36(b)) indicate that the slant columns over land are >= 100% (almost) everywhere and the positive values over the desert are subsequently not reliable. However, the most likely explanation is again possible interference between the approach-3-spectrum and spectral structures of the surface that are unaccounted for in the fit.

The chisquare of the fit is plotted in Fig. 7.36(c). It increases to higher latitudes in the south because

---

[36] Note, that the solar spectrum from SCIAMACHY has a worse resolution (≈0.5 nm between 400 and 500 nm) than the Kurucz spectrum. Consequently, the SCIATRAN simulation using the Kurucz spectrum are more accurate and as the resulting structures are (almost) invariant against the input solar spectrum (Fig. 7.34), it is recommended to use the Kurucz spectrum for calculation of the VRS effect.

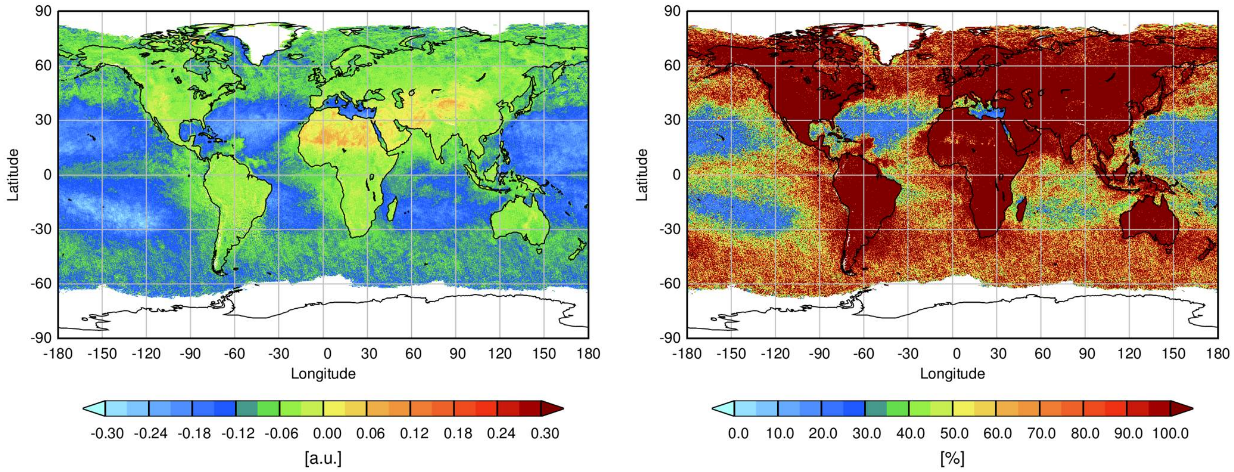

(a) Approach 3 structure: Slant column

(b) Approach 3 structure: Fit error

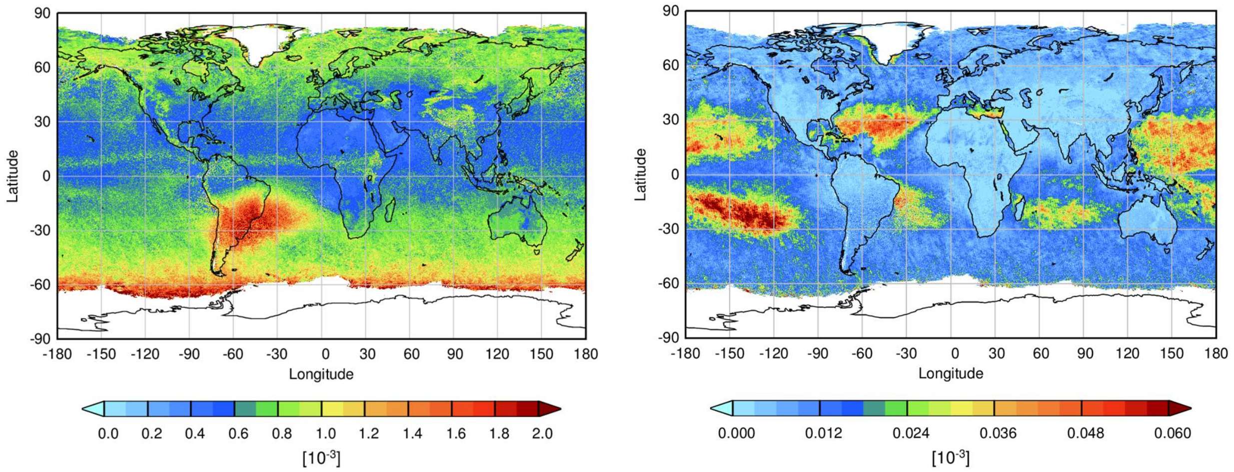

(c) $\text{Chisquare}_{\text{including}}$

(d) $\text{Chisquare}_{\text{excluding}}$ - $\text{Chisquare}_{\text{including}}$

Figure 7.36.: Fit factor, resp. Slant column of the retrieved approach-3-spectrum in OMI satellite data for August 2007 (Fig. 7.36(a)). The corresponding fit error is plotted in Fig. 7.36(b). The Chisquare of the fit including the approach-3-spectrum is shown in Fig. 7.36(c). Figure 7.36(d) is the difference of the chisquare of a DOAS fit excluding the approach-3-spectrum and the chisquare of the same fit including it (the latter fit is the one shown in Figs 7.36(a)–7.36(c)). The plots have been prepared by L. Alvarado, IUP Bremen (personal communication, 2013).

of less light (August is antarctic winter). Typical values for the chisquare of this fit are $\approx 0.6 \cdot 10^{-3}$, in the region of the South Atlantic Anomaly the chisquare reaches $\approx 1.8 \cdot 10^{-3}$. The chisquare difference between two fits, first excluding and afterwards including the approach-3-spectrum (the latter fit is the one shown in Figs. 7.36(a)–7.36(c)) is plotted in Fig. 7.36(d). Positive values indicate larger chisquares in the fit without the approach-3-spectrum. Obviously, the consideration of the spectrum leads to smaller chisquare values and therefore better fit qualities predominantly over the ocean. The resulting pattern of the chisquare difference agrees again with the pattern of liquid water absorption. While the fit quality over continents remains the same (whether including or excluding the approach-3-spectrum), highest differences over clear ocean surfaces are $0.06 \cdot 10^{-3}$ corresponding to an increase of the fit quality in the order of 10% (and up to 20–30% in the region of the SAA).

To conclude, the retrieved approach-3-spectrum is a correction spectrum accounting for uncertain-

Parameter	Ap4a fit	Ap4b fit
Range	410-495 nm	410-495 nm
Polynomial	4th order	4th order
VRS	yes	no
Approach-4-spectrum	no	yes
Offset (Straylight)	yes	yes
Other	O_3, NO_2, O_4, water vapour, liq. water, Ring (RRS)	O_3, NO_2, O_4, water vapour, liq. water, Ring (RRS)

Table 7.6: Parameters for the verification fits (called Ap4a and Ap4b) of the retrieved approach-4-spectrum in OMI satellite data (August 2007).

ties of the liquid water absorption and VRS. However, it is a differential correction spectrum as resulting from DOAS fit residuals. Following the conclusions in the previous section, it is recommended to use the approach-3-spectrum only for fit parameters similar to the parameters of the retrieval fit. Furthermore (even more important), it should be used only in combination with the specific cross-sections used in the retrieval fit.

7.7.3. Verification of approach 4

In order to verify the retrieved approach-4-spectrum (considered to account for broad-band VRS structures as well as uncertainties of the liquid water absorption) in satellite data, two test fits were performed using OMI data from August 2007. In the first fit (Ap4a), a simulated VRS cross-section for satellite geometry was used whereas in the second fit (Ap4b), the approach-4-spectrum was included and VRS was excluded. An offset straylight correction was included in both fits. The fit parameters are summarized in Tab. 7.6.

Figure 7.37 shows exemplarily the fitted optical density of the approach-4-spectrum and the corresponding residual for a measurement over the remote ocean. The structure is clearly found and the fit seems even better than the approach-3-structure in the previous section (compare to Fig. 7.35(a)). However, this is because the approach-3-structure was only a correction spectrum for liquid water and VRS and subsequently the differential optical density is smaller compared to the optical density of the approach-4-spectrum: The latter spectrum does not only correct for uncertainties of liquid water but contains also entire broad-band structures of VRS (e.g. the increase around 460 nm) and yields therefore a larger optical density.

The performance of both, the Ap4a as well as the Ap4b fit on a global scale is shown in Fig. 7.38. In Fig. 7.38(a), the VRS slant columns of the Ap4a fit are plotted. The regions of largest (most negative) VRS slant columns are the well-known regions of clear ocean water that were already seen in the previous sections. Note, here again VRS slant columns over desert regions are found with similar values as over the ocean, which was in Sect. 7.7.1 identified as compensation of spectral structures from the ground by broad-band VRS structures.

The slant columns of the approach-4-spectrum which replaced the VRS cross-section in the Ap4b fit are plotted in Fig. 7.38(b). In general, the same pattern is found as for the VRS slant columns in Fig. 7.38(a) (the values are absolutely smaller, but the approach-4-spectrum is not calibrated

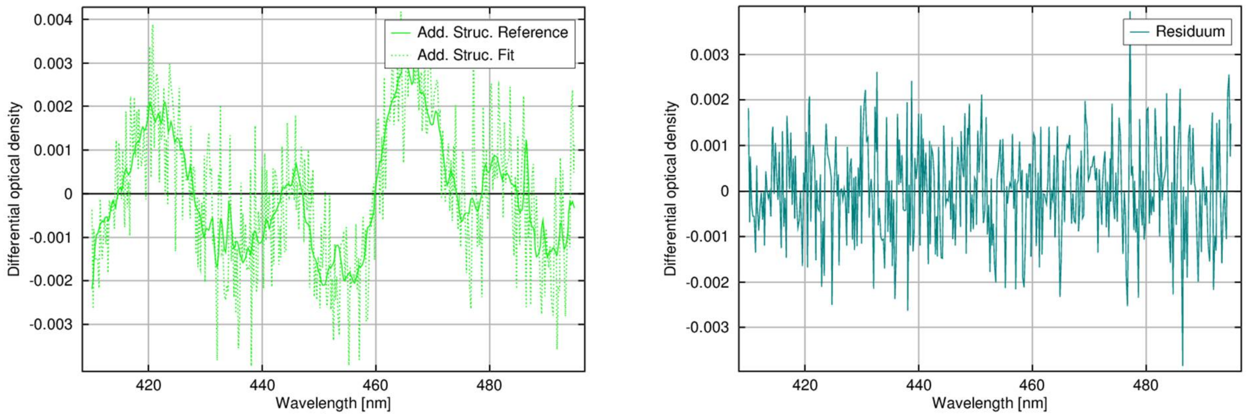

(a) Fitted Approach-4-spectrum (Ap4b fit)

(b) Residual (Ap4b fit)

Figure 7.37.: The retrieved approach-4-spectrum is fitted in OMI data over the remote Pacific (Ap4b fit, see Tab: 7.6, example from 1 Aug 2007, ≈ 11°N and ≈ 155°E).

as resulting from field measurements and thus, absolute values cannot be expected to agree). This is reasonable as the approach-4-spectrum is considered to compensate broad-band VRS structures (and uncertainties of liquid water absorption). Even the desert (sand dunes) regions at the Arabian peninsula and Australia are reproduced, giving rise to the assumption that spectral surface structures here are compensated by broad-band VRS structures.

Figures 7.38(c) and 7.38(d) show the slant columns of the offset straylight correction of the Ap4a and Ap4b fits, respectively. In comparison to the Ap4a fit, the offset slant columns of the Ap4b fit (Fig. 7.38(d)) show a strong sea-land contrast. While the values over continents stay relatively stable, the values over the ocean change and the pattern of VRS, resp. approach-4-spectrum seems to be added. The obvious reason is that VRS is not included in the AP4b fit (in contrast to the AP4a fit) and subsequently the offset straylight correction compensates for small-band structures of VRS as it was intended in the motivation of approach 4.

The chisquare of the Ap4a fit is plotted in Fig. 7.38(e). The chisquare increases to the south (Antarctic winter, almost no light) as well as in the region of the South Atlantic Anomaly. Over the remote ocean, typical values are $\approx 0.6 \cdot 10^{-3}$ (consistent to findings in Sect. 7.7.2).

In Fig. 7.38(f), the difference between the chisquare in fit Ap4a and Ap4b is plotted. Positive values mean larger chisquares in the Ap4a fit and therefore a better fit quality of Ap4b. In general, both fits perform with almost the same quality over continents, but over the ocean the Ap4b fit performs better in the regions where liquid water, resp. VRS, resp. the approach-4-spectrum is found in largest extents. It is remarkable that in these regions the fit without VRS is better. The conclusion is either a) the combination of the approach-4-spectrum and the offset straylight correction is able to compensate VRS structures even better than a simulated VRS spectrum or b) the Ap4b fit performs better over clear water surfaces because the approach-4-spectrum compensates not only for broad-band VRS structures, but also for uncertainties of the liquid water absorption cross-section.

However, the fit quality over water surfaces is improved and this was achieved not by applying an additional correction spectrum (as in approach 3) but by replacing one cross-section (VRS) by another one (approach-4-structure), i.e. the number of included cross-sections is constant. The largest improvement of chisquare in the order of $\approx 0.06 \cdot 10^{-3}$ is found over the southern Pacific.

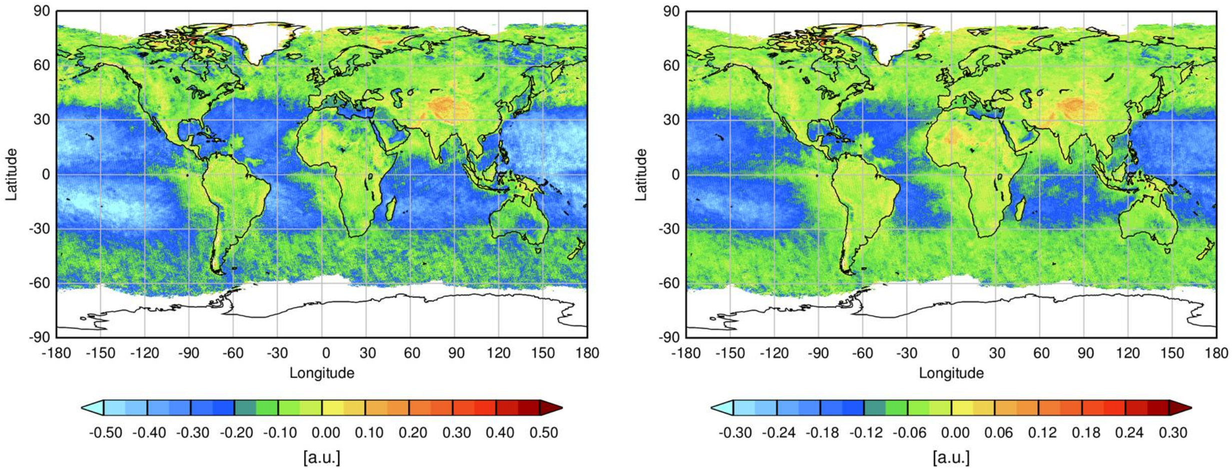

(a) Ap4a VRS slant column

(b) Ap4b Approach-4-spectrum slant column

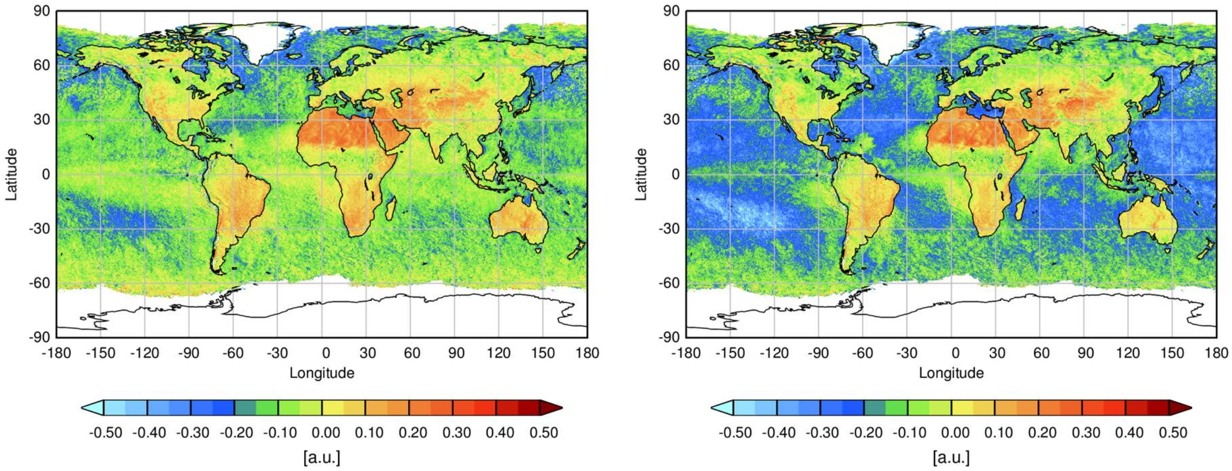

(c) Ap4a Offset slant column

(d) Ap4b Offset slant column

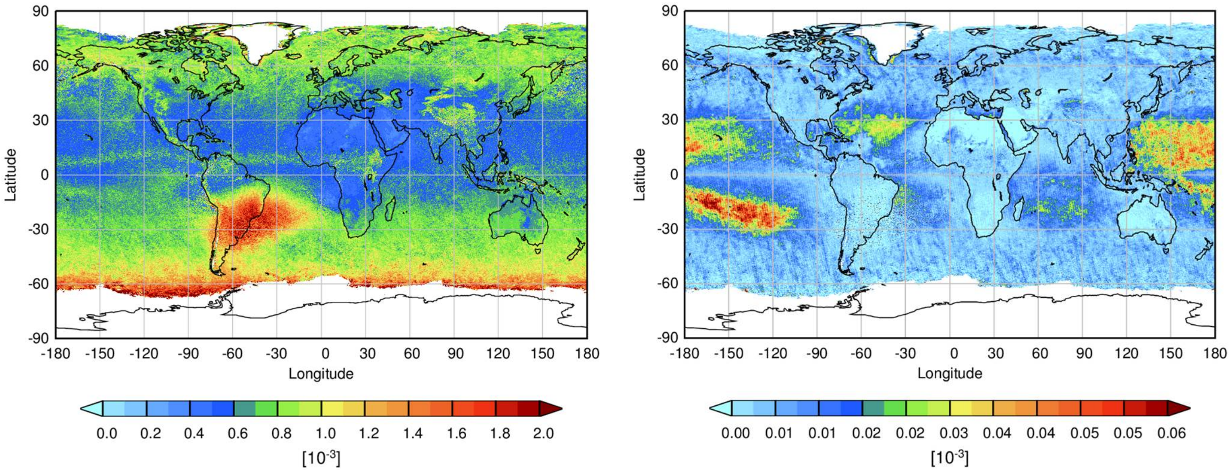

(e) Ap4a Chisquare

(f) Chisquare$_{\mathrm{Ap4a}}$ - Chisquare$_{\mathrm{Ap4b}}$

Figure 7.38.: Verification of approach 4 in OMI satellite data (August 2007 average).

Table 7.7: Parameters for the SCIAMACHY IO standard fit (Schönhardt et al., 2012) and the performed test fit using the retrieved residual water spectrum.

Parameter	standard fit	test fit
Range	416–430 nm	416–430 nm
Polynomial	2nd order	2nd order
Reference	solar spectrum (normally Earthshine)	solar spectrum
Residual water spectrum	no	yes
Straylight	Offset and Slope	Offset
Other	O_3, NO_2, IO, Ring (RRS)	O_3, NO_2, IO, Ring (RRS)

This corresponds to a maximum improvement of ≈10% and is therefore comparable with the result of approach 3. However, apart from this maximum value over the southern Pacific, the improvement of approach 3 is on average larger (compare Figs. 7.38(f) and 7.36(d)). Another limitation is that the offset straylight correction is used to compensate for both, small-band VRS structures as well as straylight (its original purpose). As VRS and straylight do not behave linearly, this might introduce new errors. Thus, despite of the success of approach 4, the approach 3 appears to be the preferred alternative.

7.7.4. Application in the satellite IO window

The previous sections demonstrate the general potential of the different retrieved experimental spectra to improve DOAS fits over water surfaces. However, these tests were performed in a large fitting window (encompassing the IO, NO_2 and CHOCHO DOAS fit ranges in the visible) in which the liquid water absorption's broad structures (as well as broad structures of VRS) are present.

In contrast, the IUP-Bremen SCIAMACHY satellite IO fit window is quite small. It ranges from 416-430 nm and neither VRS nor liquid water absorption is included (Schönhardt et al., 2012) because the applied 2nd order polynomial is considered to compensate for any broad-band structures (e.g., due to liquid water) in this small window and an applied offset and first order (slope) straylight correction is considered to account for narrow-band VRS structures.

Nevertheless, all retrieved spectra of the previous approaches were tested in the satellite IO window but unfortunately did not lead to immediate improvements, i.e. the chisquare (resp. RMS) did not decrease and the negative IO values over the ocean (compare to Fig. 1.1) persist. The reason is that the retrieved spectra were designed for very different fit parameters, e.g. they correct for VRS and liquid water absorption cross-sections that are not included in the IO fit.

However, the obtained results and conclusions of the previous sections motivated a further attempt: Using the TransBrom water measurements, the retrieval of a residual spectrum caused by water-related effects was repeated, but this time the exact settings of the satellite IO fit were applied (apart from any trace gases because they are assumed to be absent in the TransBrom measurements if using sea spray measurements as reference). The retrieval fit was performed from 416–430 nm and a 2nd order DOAS polynomial was used. In addition, only the offset straylight correction was applied. This is slightly different from the settings in the SCIAMACHY IO standard fit that also

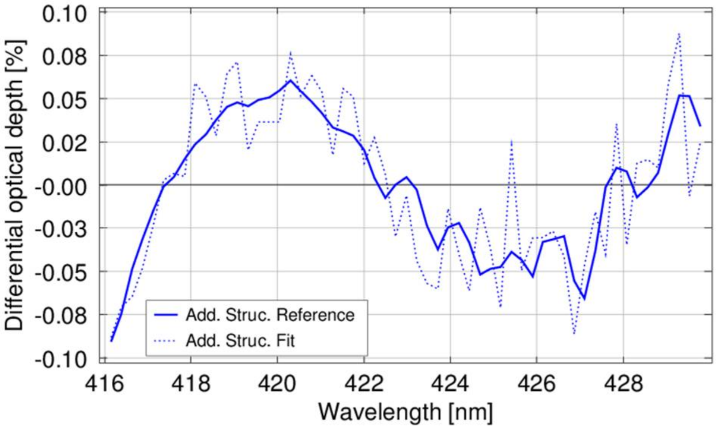

Figure 7.39: Average residual water spectrum from MAX-DOAS measurements (retrieved using the settings of the IO standard fit) fitted in SCIAMACHY data (here: Over the southern Pacific, 120° E, 27° S).

uses a first order (slope) straylight correction. However, this was tested in the ground-based water viewing measurements and the slope was not reliably found. The residuals showing systematic structures were then averaged and the resulting spectrum is considered to be a correction spectrum describing liquid water effects (absorption, VRS and possible further unknown effects) in the IO fit window that are not compensated by the applied 2nd order DOAS polynomial and the offset straylight correction.

In the next step, the retrieved residual water spectrum was included in the standard SCIAMACHY IO fit for test purpose (Tab. 7.7). In addition, the slope straylight correction was excluded because it was not used in the retrieval fit. This also keeps the number of applied cross-sections constant which is important as the fit window is small (and therefore contains only a small number of independent pieces of information). Also, the IO standard fit is normally performed using an Earthshine spectrum over the southeast Pacific as reference spectrum, i.e. a reference spectrum containing water structures. For this test, a solar spectrum was used as reference instead, because the influence of the retrieved residual water spectrum is to be investigated. The fit settings are summarized in Tab. 7.7.

Figure 7.39 shows the retrieved residual water spectrum which is successfully found here in SCIAMACHY data over the southern Pacific. In general, the retrieved spectrum consists only of a rather smooth change with wavelength, i.e. it is a relatively broad-band structure. Of course, this has also to do with the very small fit window encompassing only a few nanometers.

On a global scale, the fitted slant columns of the residual water spectrum are plotted in Fig. 7.40(a) (this is a 10 days average without cloud screening). In the previous sections, if the different residual spectra were used again in (ground-based as well as satellite) DOAS fits, they were found reliably always with negative slant columns (for example, see the approach-3 fit and the corresponding error in Figs. 7.36(a) and 7.36(b)). This is simply because they are interpreted as absorptions by the fitting routine (see footnote 34 in Sect. 7.7.1). Obviously, in Fig. 7.40(a) only the slant columns over very clear water surfaces are negative and the observed pattern is similar to the well-known pattern of VRS or liquid water absorption (in addition, an ice-edge artifact is observed close to the Antarctic). For better visualisation, all positive slant columns are plotted in grey in Fig. 7.40(a). However, in practice, all grey pixels hold positive slant columns of the residual water spectrum, which are by magnitude in the same range or even larger than the negative slant columns over clear water surfaces. The reason is most likely the weakly structured shape of the residual water spectrum in the small IO fitting window. The criterion for the DOAS fit is to minimize the chisquare

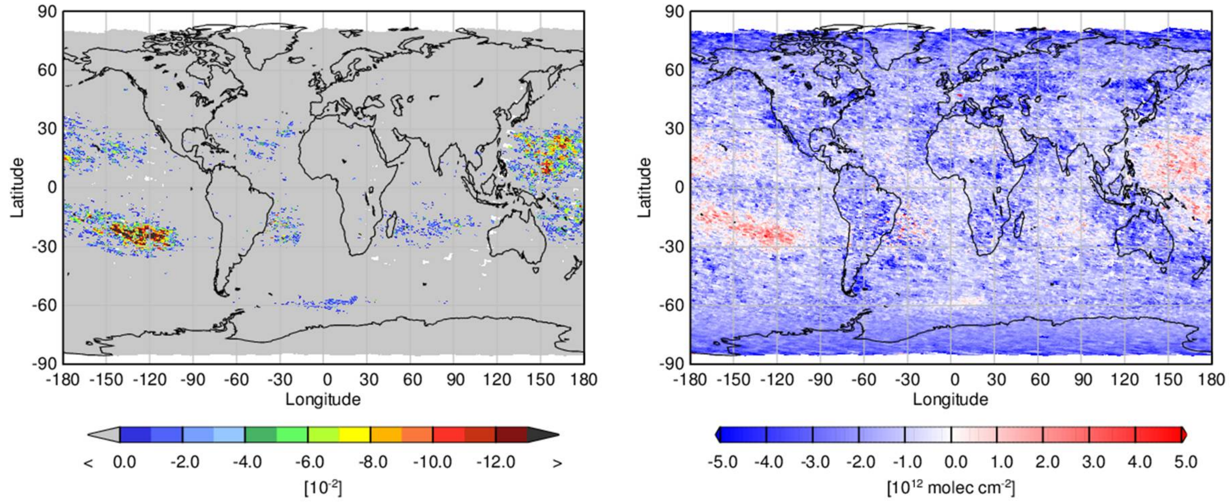

(a) SC of the retrieved water spectrum

(b) SC IO(test fit) - SC IO(standard fit)

Figure 7.40.: Verification of the residual water spectrum from MAX-DOAS measurements (retrieved using the settings of the IO standard fit) in SCIAMACHY data (01.10.2007-10.10.2007).

(resp. RMS), i.e. all included cross-sections are scaled with certain factors (slant columns) so that the overall residual is minimized. Because the residual water spectrum is rather smooth it may for example (in combination with the DOAS polynomial or another broad-band cross-section) compensate for smooth spectral surface structures. This is supported by the observation that the residual water spectrum improves the chisquare of the satellite IO fit predominantly not over water surfaces, but over continents or regions of unclear water, respectively. To conclude, the problem arising from the smooth shape of the residual water structure is that it is only found correctly in regions of specifically strong liquid water structures and - even more important - easily misfitted in other regions without clear water surfaces.

The effect of including the residual water spectrum on the fitted IO slant columns is shown in Fig. 7.40(b) where the difference between the IO slant columns of the test fit including the residual water spectrum and the IO slant columns of the standard fit are plotted. Consequently, positive numbers indicate larger IO slant columns in the fit including the residual water spectrum (and vice versa). Obviously, in the regions of strong liquid water structures where the residual water spectrum is found correctly, the fit using this spectrum instead of the slope yields larger IO values than the standard fit. Therefore, using the residual water structure reduces the problem of negative IO slant columns over the ocean (compare to Fig. 1.1). However, it has to be admitted that the increase is in the range of $1 - 2 \cdot 10^{12}$ molec/cm^2 and does therefore not entirely compensate the negative values over the ocean (less than $-3 \cdot 10^{12}$ molec/cm^2) in the standard fit (Fig. 1.1).

The limiting factor for using the test fit is that it does not only increase the IO in regions where the residual water spectrum is correctly found, but it also decreases the IO in regions where it is found incorrectly (blue values in Fig. 7.40(b)), which demonstrates the interference between IO and the retrieved structure.

The above observations support the assumption that the observed negative IO over the ocean is caused by liquid water effects. As a result, using the residual water spectrum leads to more realistic IO values in regions of strong liquid water structures but at the same time to possibly incorrect IO values elsewhere.

Therefore, at the moment the standard IO fit is recommended and the test fit including the residual water spectrum should be only used if one is interested in IO over regions of very strong liquid water influences (e.g. parts of the southeast Pacific). Nevertheless, if the standard IO fit may improve in the future using a larger fit window, the retrieval of a water-related residual spectrum could be repeated with the new parameters and possibly - as being more structured - this residual water spectrum is then found more reliable over water surfaces only (and increasing the IO there) and not found over other regions (i.e. not changing the IO there).

7.8. Summary

This chapter comprises the analysis of MAX-DOAS measurements during TransBrom in order to study spectral effects of liquid water and to improve the consideration of these effects in (satellite-borne) DOAS measurements over water surfaces.

For the inelastic VRS and Brillouin scattering in liquid water a sensitivity study was performed: VRS optical densities were simulated using the radiative transfer model SCIATRAN for different geometries and scenarios, e.g. chlorophyll content etc. (V. Rozanov, personal communication, 2012) and the introduced error in terms of optical depth when using a wrong VRS spectrum in a DOAS analysis was estimated. The introduced error is only larger than residual optical depths of $5 \cdot 10^{-4}$ (high-quality DOAS fits) if both, the geometry as well as the scenario (AOT, pollution, chlorophyll etc.) do not match the real conditions. However, this sensitivity study was performed for MAX-DOAS measurements pointing directly towards the water surface yielding light paths of ≈ 50 m under water. As a) the VRS optical density and therefore the introduced error scales with the light path under water and b) MAX-DOAS measurements are normally performed in angles above the horizon (where the contribution of water leaving radiance is smaller) and maximum values for the underwater light path in satellite measurements is in the order of only 10 m (e.g., Fig. 7.33(c)), consequently, using a VRS cross-section that was calculated for parameters that do not match entirely the real conditions will not introduce residual structures above the limit of high-quality DOAS fits.
In addition to the VRS sensitivity study, the filling-in of narrow Fraunhofer lines due to inelastic Brillouin scattering was evaluated and it was found that measurements which are performed with the typical resolution of current DOAS instruments are not disturbed by them.

Four different approaches were made aiming at the retrieval of empirical spectra of liquid water absorption and VRS, or correction spectra for currently available literature cross-sections of these effects:

- Approach 1: The simultaneous retrieval of an empirical VRS and liquid water absorption spectrum from DOAS fit residuals using a Principal Component Analysis was not successful because the PCA was not able to separate the two effects. The reason is, that VRS and liquid water absorption scale linearly and subsequently in the DOAS residuals, they produce variance in a similar way.
- Approach 2: An empirical (differential) VRS spectrum was obtained when including the liquid water absorption cross-section (but excluding VRS) in DOAS fits towards the water surface.

The retrieved VRS spectrum shows strong similarity to the SCIATRAN simulated VRS cross-section (Fig.7.23). However, some differences predominantly concerning the broad-band VRS structures are observed, most likely because a) the DOAS fit arranged the polynomial and the broad-band liquid water cross-section in the retrieval fit in a way to compensate partially for the VRS broad-band structures (in order to minimize the fit residual) and b) the retrieved VRS spectrum may compensate for uncertainties of the applied broad-banded liquid water absorption cross-section. However, when applied in a satellite (OMI) DOAS fit which is similar to the retrieval fit, the empirical spectrum performs up to 5% better than the simulated spectrum over water surfaces (Fig. 7.33(d)). Thus, it can be recommended to use an empirical VRS spectrum if a) it is used together with the liquid water cross-section that was applied in the retrieval fit (Sect. 7.5.1) and b) it is used in DOAS fits that are similar to the retrieval fit (same order of polynomial, similar spectral range).

- Approach 3: When including both, a SCIATRAN simulated VRS spectrum as well as the liquid water absorption cross-section in MAX-DOAS fits towards the water surface, the resulting residuals showed systematic structures and an average residual has been retrieved (approach-3-spectrum). The structures of the approach-3-spectrum are relatively stable against changes of the applied VRS spectrum in the retrieval fit and the solar spectrum used as input for the SCIATRAN VRS calculation (Fig. 7.34). When fitted in OMI satellite data, the approach-3-spectrum is successfully found over water surfaces (Fig. 7.35(a)) and the resulting slant columns reproduce the pattern of the liquid water absorption slant columns very well (Fig. 7.36(a)). Thus, retrieved spectrum is not an instrumental artifact of the MAX-DOAS instrument. In addition, the chisquare of the satellite DOAS test fit decreased by 10%–30% over regions of clear water (Fig. 7.36(d)). To conclude, the approach-3-spectrum can be regarded as a correction spectrum for uncertainties of the cross-section of either liquid water absorption, VRS or both.

- Approach 4: The offset straylight correction of the DOAS fit effectively compensates for small-band structures of VRS. Thus, a residual spectrum (approach-4-spectrum) was retrieved from MAX-DOAS fits during TransBrom that included liquid water absorption and offset straylight correction, but no VRS cross-section. The resulting approach-4-spectrum is considered to compensate for broad-band structures from VRS and uncertainties of the applied liquid water absorption cross-section. In satellite data the approach-4-spectrum is successfully found when used instead of VRS (Fig. 7.37(a)) and its slant columns reproduce the global pattern of VRS and liquid water (Fig. 7.38(b)). The same pattern is also introduced in the fitted slant columns of the offset straylight correction as it accounts for small-band VRS structures in this fit (Fig. 7.38(d)). When comparing two fits, one with VRS (and offset straylight correction) and the other with approach-4-spectrum (instead of VRS) and offset straylight correction, the chisquare of the latter fit decreased by up to 10% over regions of clear water (Fig. 7.38(f)). This is remarkable because no VRS cross-section is used for this fit demonstrating that the VRS structures can be compensated very efficiently by a combination of offset straylight correction (small-band structures) and approach-4-spectrum (broad-band structures).

To conclude, the retrieved empirical spectra in approaches 2, 3 and 4 improve DOAS test fits (large fitting windows of 410–495 nm) over the ocean, i.e. leading to smaller chisquares: Approach 2:

5%, Approach 3: 10%–30%, Approach 4: 10%. The retrieved spectra should be used only in combination with the same cross-sections included in the retrieval fit. In addition, all retrieved empirical spectra are differential and should be used only for parameters - fitting range and order of polynomial - similar to the parameters in the retrieval fit. The fact that even these rather simple field measurements are able to increase the satellite fit quality by ≈10% over clear water surfaces demonstrates that (most likely) predominantly the liquid water absorption has considerable uncertainties and an accurate laboratory measurement of this cross-section at a finer resolution (0.1 nm or better) for DOAS applications is strongly recommended.

The SCIAMACHY satellite IO standard fit is substantially different from the large test fitting windows studied before. Thus, a residual water spectrum (Fig. 7.39) was retrieved specifically for the IO fit. The shape of the retrieved spectrum turned out to be rather smooth. As a consequence, it is only found correctly over regions of very strong liquid water structures while it is easily misfitted elsewhere. However, if the residual water spectrum is found correctly in satellite data over clear water surfaces, the IO increases (Figs. 7.40(a) and 7.40(b)) validating the assumption that effects of liquid water lead to the observed negative IO slant columns over the ocean (Fig. 1.1). Unfortunately, over different regions where the residual water spectrum is misfitted, the IO decreases. Therefore, the potential improvement of the retrieved residual water spectrum is limited and using the standard IO fit is recommended unless the focus is explicitly on regions of strongest liquid water influences (e.g. parts of the tropical southeast Pacific).

8. Summary and conclusions

This thesis is about measurements of atmospheric trace gases using the ground-based **M**ulti-**AX**is **D**ifferential **O**ptical **A**bsorption **S**pectroscopy (MAX-DOAS) technique. In particular, the initial objectives and main results of this thesis are (see also introduction in chapter 1):

- The improvement of the existing IUP-Bremen MAX-DOAS instrument, predominantly to avoid an internal mirror (producing artificial optical effects often disturbing the trace gas retrieval) and to allow pointing in any viewing direction, especially towards the water surface (measurements of water leaving radiance) which was performed during a ship-borne campaign (TransBrom). In total, the improved instrument participated at three campaigns and is installed at several sites within the IUP-Bremen BREDOM network of permanent MAX-DOAS ground stations.

- The retrieval of tropospheric trace gas (profiles) in the marine boundary layer over the remote ocean. Here, satellite instruments often have problems to detect trace gases because the concentrations are small and spectral structures from liquid water disturb the measurements. The MAX-DOAS instrument has a higher sensitivity for the lower atmosphere and subsequently background concentrations in the marine troposphere are estimated with higher accuracy and used to validate corresponding satellite measurements.

- The investigation of spectral structures from liquid water and their impact on the DOAS analysis. It was observed that over the remote ocean trace gases are often misfitted and tend to negative values. Correction spectra for currently available liquid water cross-sections were retrieved from ground-based measurements during a ship campaign and it was demonstrated that these correction spectra have the potential to improve space-borne DOAS measurements over the ocean.

Improvement and installations of the MAX-DOAS instrument

The existing (old) IUP-Bremen MAX-DOAS instrument had the disadvantage of two different viewing ports (including and excluding a motorised mirror) for zenith and off-axis measurements, respectively. As a result, offsets were sometimes observed between the two types of observations, most likely caused by a degradation effect of the mirror.

As part of this thesis, an improved MAX-DOAS telescope unit was designed. The new telescope is smaller and lighter in weight allowing to mount it on a commercial Pan-Tilt-Head (for security cameras) that moves the whole telescope unit in the pointing direction. Therefore, it needs only one viewing port (and no mirror) for both, zenith as well as off-axis measurements. As a result, offsets between the two observation types are no longer present. Furthermore, the improved instrument is not only free in pointing in any elevation angle but also in any azimuthal direction. This allows to use it very easily for TargetDOAS measurements.

In addition, the new telescope was equipped with an inclinometer for quality-control of the applied elevation angle and recording of the actual viewing direction when used in ship-borne set-ups. A video camera (pointing exactly in the viewing direction) was included in the telescope unit for scene documentation. Using a gravity-driven shutter (pointing straight downwards), dark measurements can be easily performed. Like the old telescope, it is equipped with a HgCd line lamp for calibration measurements.

The new telescope unit was manufactured by an external workshop, the wiring and electrics are self-made. In addition, Delphi units for the operation of the new instrument (Pan-Tilt-Head, video camera, inclinometer) were created and included in the program code of the existing MAX-DOAS measurement software AMAX-OMA.

In total, four instruments have been built. Three stations within the BREDOM-network have been updated to the new system and the additional (4th) instrument participated in three field campaigns in the context of this PhD thesis.

Instrument performance during an intercomparison campaign

The improved MAX-DOAS instrument participated in the Cabauw Intercomparison Campaign of Nitrogen Dioxide measuring Instruments (CINDI) in Cabauw, Netherlands, in June-July 2009 where it showed excellent performance (Roscoe et al., 2010; Piters et al., 2012; Pinardi et al., 2013). During the 15 days period of formal semi-blind intercomparison of NO_2 and O_4 using standardized DOAS settings, all 22 participating DOAS instruments agreed within 15%, most within 5%. The IUP-Bremen instrument was selected as one of the reference instruments because of its complete time coverage of observations (good reliability) and consistent results in comparison to other reference instruments. For the intercomparison of HCHO slant columns in the UV, differences of <15% were found between most of the 9 participating instruments and again the IUP-Bremen system was selected as one of the reference instruments.

Apart from the intercomparison, tropospheric NO_2 profiles were retrieved from the IUP-Bremen MAX-DOAS measurements. For days with very good viewing conditions, it was demonstrated that the MAX-DOAS measurements are capable to close the gap between satellite measurements averaging over a large area on the one hand and continuous in situ observations at a specific location on the other hand, i.e. the retrieved vertical column is consistent to the satellite observation while at the same time the retrieved ground VMR coincides in shape and absolute value with in situ observations.

Monthly averages of the GOME-2 satellite instrument suggest an NO_2 vertical column of $1-1.5\cdot10^{16}$ molec/cm^2 for the location of the measurement site, which is in general in agreement with MAX-DOAS observations. On days with good viewing conditions (golden days), the agreement between satellite values and coinciding MAX-DOAS values is often almost perfect. Nevertheless, occasionally differences of up to ≈50% are observed even on days with good weather and clear viewing conditions, most likely due to pollution that is within the satellite pixel but not in the MAX-DOAS instrument's line of sight.

Trace gas retrieval in the tropical marine troposphere

In October 2009, the instrument participated in the ship-borne field campaign TransBrom across the remote western Pacific ocean, where background columns and concentrations of HCHO, NO_2 as well as IO in the marine boundary layer were retrieved and - if possible - compared to corresponding satellite measurements (Peters et al., 2012; Großmann et al., 2013). In addition, SCIAMACHY and GOME-2 observations of stratospheric NO_2 were validated.

As expected, the satellite columns of stratospheric NO_2 are on average slightly lower than MAX-DOAS a.m. values which is a consequence of the NO_2 diurnal cycle. During the day, a linear increase of $8.7 \pm 0.5 \cdot 10^{13}$ molec/cm^2/h was estimated at low latitudes. Both, the satellites as well as the MAX-DOAS measurements reproduce the same characteristic latitude-dependent shape of stratospheric NO_2.

For the remote ocean, an upper limit of the tropospheric NO_2 concentration of ≈50 ppt or $1.3 \cdot 10^{14}$ molec/cm^2 for the vertical column was estimated which is in agreement with the GOME-2 monthly average. Sparse NO_2 enhancement events could be assigned to passing of other ships or crossing of frequently used shipping routes.

Formaldehyde was successfully detected above the detection limit during the whole cruise and revealed a clear diurnal cycle with maxima around noon. This is expected since the HCHO background concentration is considered to result mainly from methane oxidation (that requires daylight) over the remote ocean. Maximum values at best weather conditions and strong sun irradiance reached up to 1.1 ppb or $4 \cdot 10^{15}$ molec/cm^2 (this value is possibly influenced by additional precursors other than methane). A transport event of formaldehyde or its precursors was found ≈150 km away from the only possible source (island with rainforest vegetation) and calculated backward trajectories suggest that the HCHO or its precursors bridged this distance in 12–18 h before being detected by the MAX-DOAS instrument. GOME-2 and MAX-DOAS measurements agree on a typical vertical column of $\approx 3 \cdot 10^{15}$ molec/cm^2 for the remote ocean at the overpass time (≈9:30 LT).

Over the tropical remote ocean - where satellites often retrieve negative IO values - the MAX-DOAS measurements during TransBrom suggest IO concentrations of 0.5–2 ppt close to the surface or $1 - 3 \cdot 10^{12}$ molec/cm^2 for the vertical column, respectively. From comparison to complimentary data, inorganic pathways for the iodine to reach the atmosphere are suggested, most likely the reaction of gaseous ozone with iodide in the interfacial layer.

In addition, ship- and land-based measurements of IO in the tropical marine boundary layer have been performed during the SHIVA campaign in November 2011. The ship-based measurements carried out predominantly in the coastal environment around the Malaysian peninsula and Borneo suggest IO levels of 1–3 ppt (vertical columns $\approx 1 - 4 \cdot 10^{12}$ molec/cm^2) which is slightly higher than observed values during TransBrom. The reason is most likely the release of organoiodines (IO precursor species) resulting from biogenic activity that is much larger in coastal waters than in the remote tropical ocean. Land-based measurements from an island ≈ 20 km off the coast of Malaysian Borneo yield occasionally even larger IO levels of 1–4 ppt (vertical columns $\approx 1 - 5 \cdot 10^{12}$ molec/cm^2) due to the measurement's site proximity to a commercial seaweed field (macro-algea are known to produce various types of organoiodines).

Evaluation of the effects of absorption and scattering in liquid water on the DOAS analysis

During the TransBrom cruise, MAX-DOAS measurements have been performed pointing towards the sea surface in order to study spectral effects of liquid water and to improve the consideration of these effects in (space-borne) DOAS measurements over water surfaces. In addition, a sensitivity study of VRS spectra simulated for different scenarios and their impact on the DOAS analysis was performed. The uncertainty (error) introduced by using a VRS spectrum that is simulated for a *wrong* scenario (i.e. a scenario that does not match the real conditions) is often below the typical residual optical density of a high-quality DOAS fit even assuming the geometry of a ground-based instrument pointing directly into the water (up to 50 m light path under water). In practice, MAX-DOAS measurements of atmospheric trace gases are not performed into the water and the underwater light path in satellite measurements is normally $\leq$ 10 m. Thus, the introduced error if applying a wrong VRS spectrum can be neglected. In another estimation, the filling-in of narrow Fraunhofer lines due to inelastic Brillouin scattering was found not to disturb measurements that are performed with the typical resolution of current DOAS instruments.

Using the MAX-DOAS measurements towards the sea surface, different approaches were evaluated aiming at the retrieval of experimental correction spectra for currently available literature cross-sections of liquid water absorption and/or VRS. When applied in independent measurements of the OMI satellite instrument, the retrieved spectra are successfully found reproducing the global pattern of liquid water absorption and VRS. In addition, they improve DOAS test fits (large fitting window of 410–495 nm) over the ocean by typically ≈10% (an even more in the region of the South Atlantic Anomaly). However, the limitation for potential use in future DOAS fits is that the experimental spectra are already differential as resulting from fit residuals.

For the IUP-Bremen standard IO fit (only 14 nm wide and neither VRS nor liquid water absorption are included at all), a residual water spectrum had to be retrieved exclusively using the exact IO fit parameters. The resulting spectrum is very smooth and unstructured. Consequently, it is only detected correctly over regions of strongest liquid water structures where it increases the IO (and thus reduces the problem of negative IO over the ocean) while it is misfitted elsewhere and subsequently descreases the IO there. As a result, the potential use of the retrieved residual water spectrum is limited. However, the interference between residual water structures and IO was demonstrated. Furthermore, if the satellite IO fit may improve to a larger fit window in the future, the residual water spectrum could be found more reliably thus helping the IO fit.

Conclusions

This work could contribute to recent scientific questions and improve the instrumental MAX-DOAS capabilities of the IUP-Bremen. In particular, this work meets the three initial objectives it was focused on:

First, the existing IUP-Bremen MAX-DOAS instrument was improved and thereby successfully overcomes the limitations of the old instrument (only one azimuthal viewing direction, offsets in the trace gas retrieval due to optical effects inside the telescope). This was a precondition for the DOAS measurements on which this thesis reports. The new instrument shows excellent performance (selected as reference instrument during an NO_2 intercomparison campaign). Meanwhile, this instrument type is also installed at several sites within the IUP-Bremen BREDOM network of MAX-DOAS measurement sites.

Second, this thesis was successful in that it provides new information about trace gases (NO_2, HCHO and IO) in the marine boundary layer over the remote ocean where only a limited number of observations exist so far. SCIAMACHY and GOME-2 satellite measurements of NO_2 and HCHO were validated using the MAX-DOAS observations performed in this thesis. The results of IO contribute to an ongoing discussion about the ocean being a non-biogenic source for iodine release, which is supported by the findings of this thesis.

Third, the impact of liquid water spectral effects on the DOAS analysis was investigated and correction spectra for currently available cross-sections of liquid water absorption and Vibrational Raman Scattering were retrieved. It was demonstrated that the consideration of these residual correction spectra in MAX-DOAS and satellite DOAS measurements improves the fit quality (up to 20% for satellite measurements) over clear water surfaces. This result implies the need for better laboratory measurements of liquid water spectra for use in DOAS applications. It could also be shown that the negative IO slant columns over clean ocean surfaces derived from satellite measurements are caused by insufficiently removed liquid water structures, which was expected but speculative before.

Outlook and Recommendations

The instrumental improvement is an ongoing process (e.g. sun shading plates after TransBrom etc.). A further advantage would be a filter wheel inside the telescope unit that could be equipped with attenuating plates or foils of different thickness allowing direct sun measurements. Also, a synthetic (plastic) housing could be tested for the telescope unit making it lighter in weight. In any case, the telescope housing should be stiffening (because of wind-driven movements), which requires thicker walls and therefore a lighter, presumably also stiffer material. Also it should be tested to arrange the components inside the telescope more compact aiming at a smaller housing and thus reducing the wind impacted surface.

The profile retrieval BREAM running in the context of this thesis was using the SCIATRAN version 2.2 and needs to be updated to the actual SCIATRAN version. Also the retrieval of an aerosol extinction in the first step of BREAM should be optimized. At the moment, the shape of the aerosol profile is selected by the user (and only scaled by the program). The retrieval of an optimal aerosol extinction profile should be automated.

The MAX-DOAS measurements of IO in the marine boundary layer are clearly at the detection limit. Misfits of the Ring effect were observed to have the largest impact on the fit quality (and often dominate the fit). The pseudo cross-section for the Ring effect is calculated with radiative transfer models, in this case SCIATRAN. Thus, larger efforts on the simulation of the Ring effect could increase the reliability of MAX-DOAS IO results.

Finally, it is strongly recommended to perform an accurate laboratory measurement of the liquid water absorption cross-section at a fine resolution (0.1 nm or better) in the range of 400–500 nm as the retrieved residual correction spectra demonstrate a potential improvement in terms of fit quality in this spectral range and also the interference between incompletely removed liquid water structures with IO structures.

A. Appendix

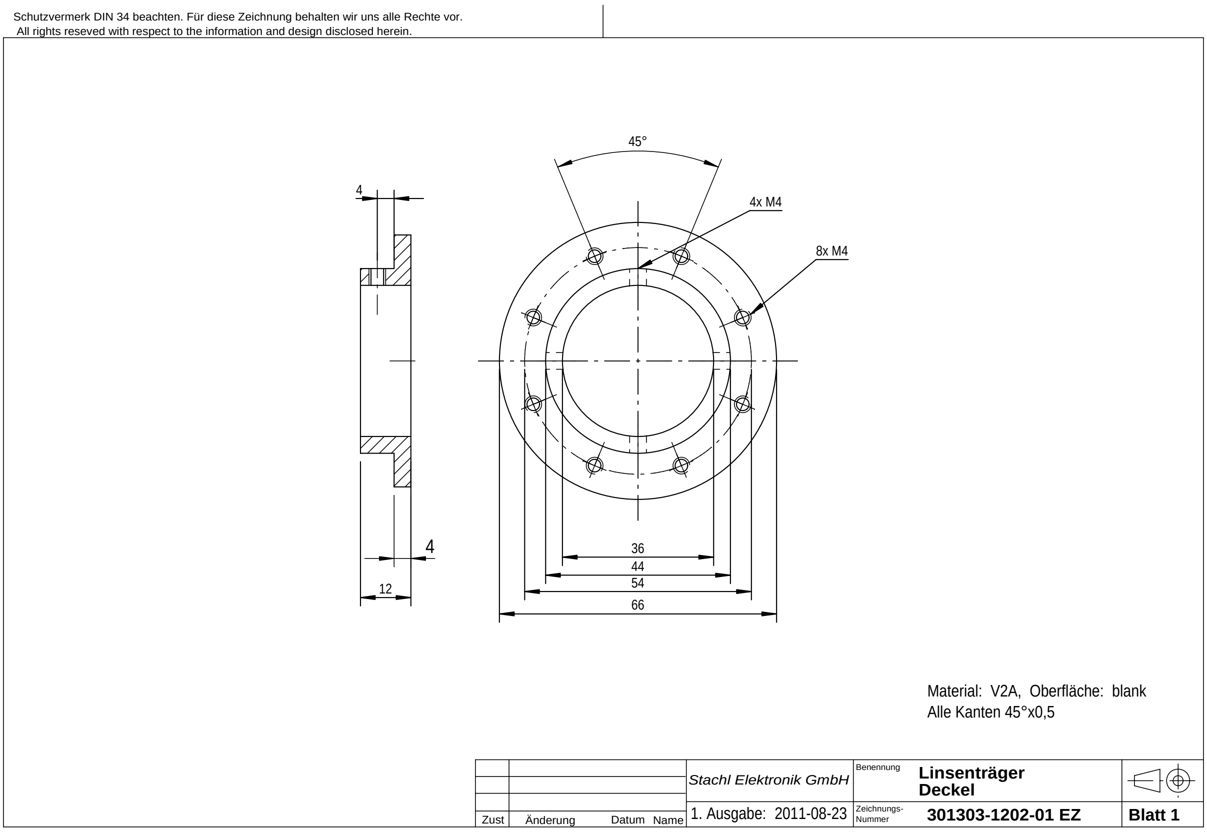

Figure A.1.: Blueprint of the telescope: Entrance window's outer cap. The actual window has a diameter of 36 cm. The outer cap is fixed with screws to its mount (Fig. A.2). For measurements in the tropics, a cylindrical visual cover can be fixed to the cap to avoid direct sunlight in the telescope. Construction design drawn by A. Stachl (see footnote 6 on page 52).

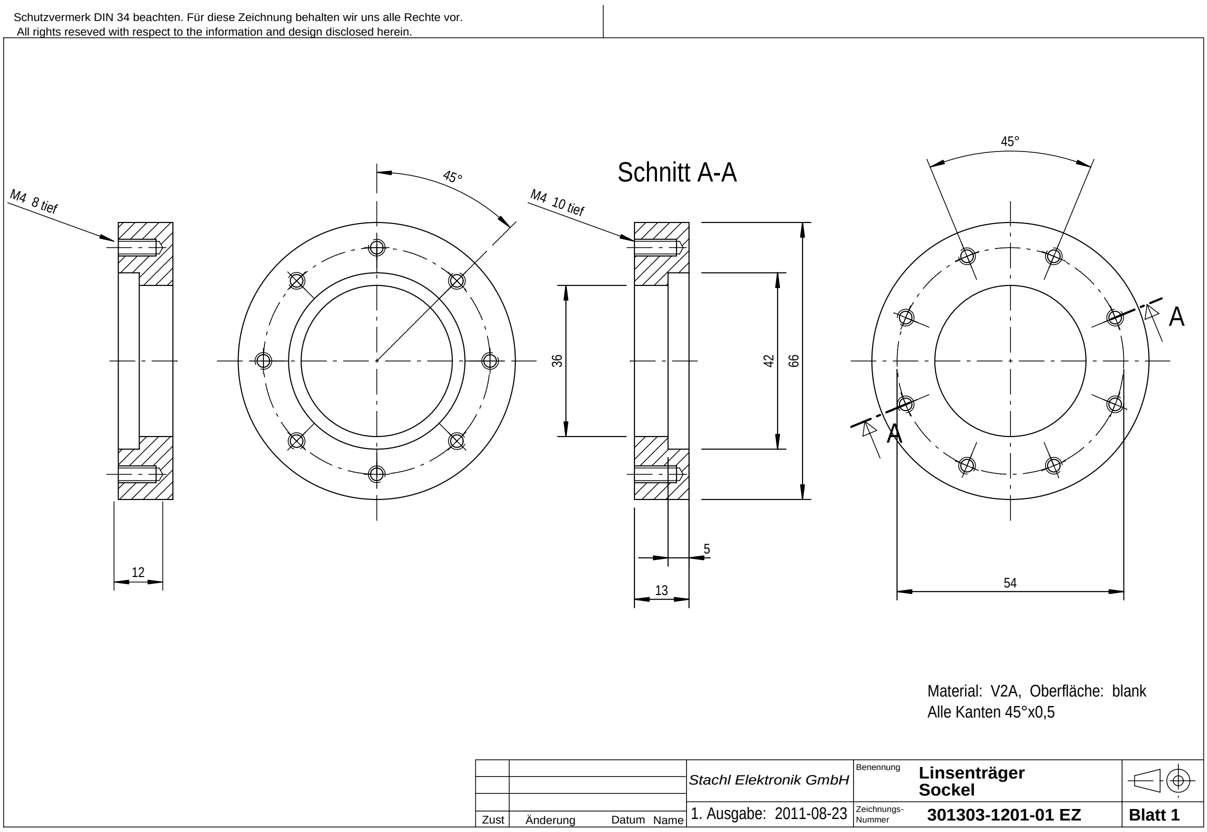

Figure A.2.: Blueprint of the telescope: Entrance window mount. The actual window has a diameter of 36 cm. The outer cap (Fig. A.1) presses on the fused silica plate (42 mm diameter) and two circular buffer pads, which are located in the indentation of 42 mm diameter. Construction design drawn by A. Stachl (see footnote 6 on page 52).

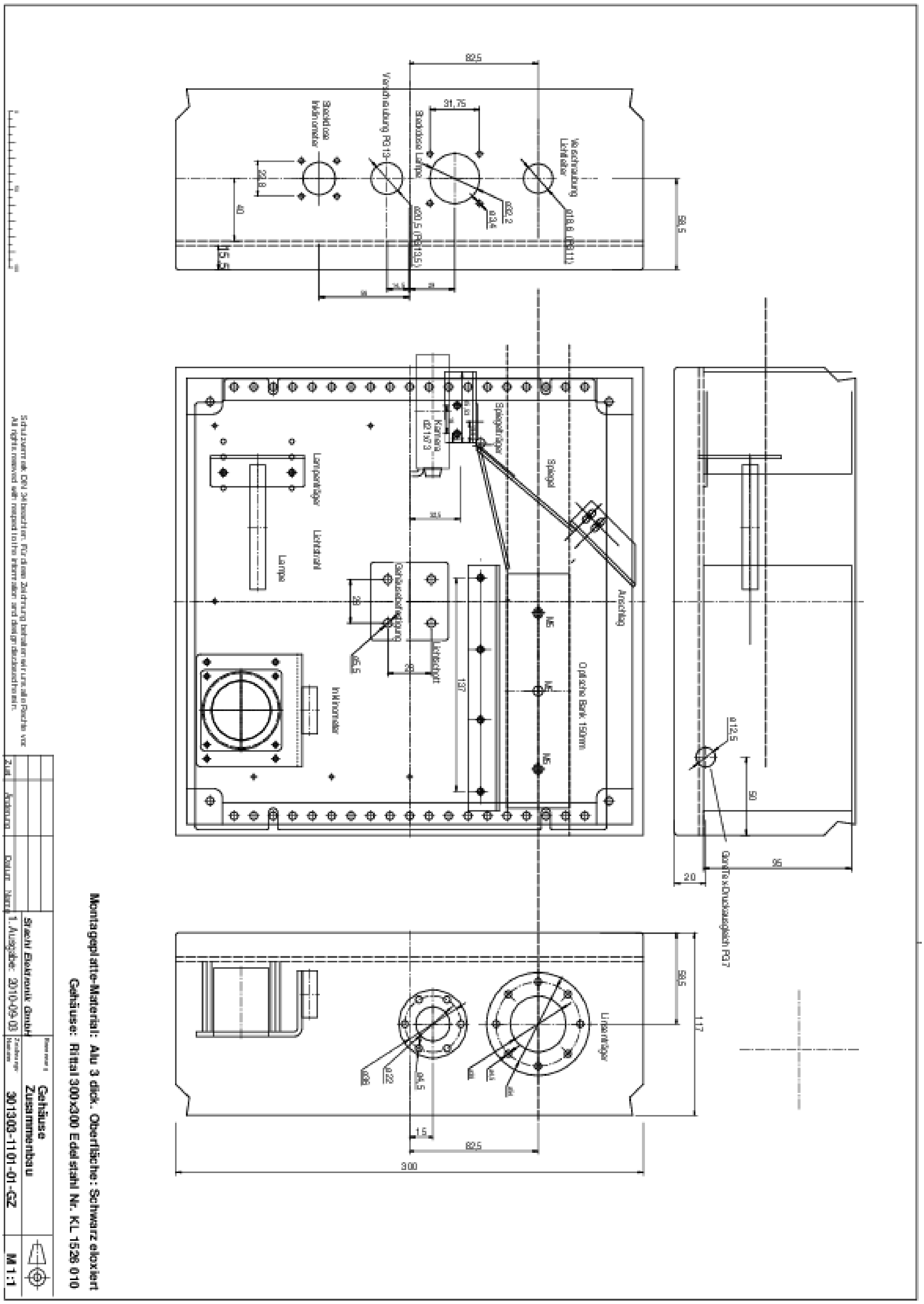

Figure A.3.: Blueprint of the telescope box and arrangement of interior components. Construction design drawn by A. Stachl (see footnote 6 on page 52).

List of abbreviations

AMF	Air Mass Factor
AOD	Aerosol Optical Depth
a.u.	arbitrary units
BAMF	Block Air Mass Factor
BREAM	BREmian Advanced MAX-DOAS Retrieval Algorithm
BREDOM	BREmian DOAS network for atmospheric Measurements
CCD	Charge-Couple Device
CINDI	Cabauw Intercomparison Campaign of Nitrogen Dioxide measuring Instruments
DOAS	Differential Optical Absorption Spectroscopy
ENVISAT	ENVIronmental SATellite
ERS-2	Second European Remote-Sensing Satellite
ESA	European Space Agency
GOME-2	Global Ozone Monitoring Instrument-2
HITRAN	HIgh Resolution TRANsmission
ITCZ	InterTropical Convergence Zone
IUP	Institut für Umweltphysik (Institute of Environmental Physics)
LIDAR	LIght Detection And Ranging
LOS	Line of Sight
MAX-DOAS	Multi-AXis DOAS
MBL	Marine Boundary Layer
NASA	National Aeronautics and Space Administration
OMI	Ozone Monitoring Instrument
RMS	Root Mean Square
RRS	Rotational Raman Scattering
RTM	Radiative Transfer Model
SCIAMACHY	SCanning Imaging Absorption spectroMeter for Atmospheric CHartographY
SAA	Solar Azimuth Angle, also Southern Atlantic Anomaly
SC	Slant Column
SCIATRAN	Radiative Transfer Model for SCIAMACHY
SZA	Solar Zenith Angle
UV	UltraViolett
VC	Vertical Column
Vis	visible
VOC	Volatile Organic Compound
VRS	Vibrational Raman Scattering

Bibliography

Aliwell, S. R., Van Roozendael, M., Johnston, P. V., Richter, A., Wagner, T., Arlander, D. W., Burrows, J. P., Fish, D. J., Jones, R. L., Tørnkvist, K. K., Lambert, J. C., Pfeilsticker, K., and Pundt, I.: Analysis for BrO in zenith-sky spectra: An intercomparison exercise for analysis improvement, Journal of Geophysical Research-Atmospheres, 107, 2002.

Anderson, L. G., Lanning, J. A., Barrell, R., Miyagishima, J., Jones, R. H., and Wolfe, P.: Sources and Sinks of Formaldehyde and Acetaldehyde: An Analysis of Denver's Ambient Concentration Data, Atmospheric Environment, 30, 2113–2123, 1996.

Arlander, D. W., Brüning, D., Schmidt, U., and Ehhalt, D. H.: The Tropospheric Distribution of Formaldehyde During TROPOZ II, J. Atmos. Chem., 22, 251–268, 1995.

Barrie, L. A., Bottenheim, J. W., Schnell, R. C., Crutzen, P. J., and Rasmussen, R. A.: Ozone Destruction and Photochemical-Reactions at Polar Sunrise in the Lower Arctic Atmosphere, Nature, 334, 138–141, 1988.

Bates, D. R. and Hays, P. B.: Atmospheric nitrous oxide, Panet. Space Sci., 15, 189–197, 1967.

Bates, D. R. and Nicolet, M.: The Photochemistry of Atmospheric Water Vapor, Journal of Geophysical Research, 55, 301–327, 1950.

Beirle, S., Platt, U., Wenig, M., and Wagner, T.: Weekly cycle of NO2 by GOME measurements: a signature of anthropogenic sources, Atmospheric Chemistry and Physics, 3, 2225–2232, 2003.

Beirle, S., Platt, U., von Glasow, R., Wenig, M., and Wagner, T.: Estimate of nitrogen oxide emissions from shipping by satellite remote sensing, Geophysical Research Letters, 31, 2004.

Boersma, K. F., Eskes, H. J., and Brinksma, E. J.: Error analysis for tropospheric NO_2 retrieval from space, J. Geophys. Res., 109, 2004.

Bogumil, K., Orphal, J., Homann, T., Voigt, S., Spietz, P., Fleischmann, O. C., Vogel, A., Hartmann, M., Kromminga, H., Bovensmann, H., Frerick, J., and Burrows, J. P.: Measurements of molecular absorption spectra with the SCIAMACHY pre-flight model: instrument characterization and reference data for atmospheric remote-sensing in the 230–2380 nm region, J. Photochem. Photobiol. A., 157, 167–184, 2003.

Bovensmann, H., Burrows, J. P., Buchwitz, M., Frerick, J., Noël, S., Rozanov, V. V., Chance, K. V., and Goede, A. P. H.: SCIAMACHY: Mission Objectives and Measurement Modes, Journal of the Atmospheric Sciences, 56, 127–150, 1999.

Brasseur, G. P., Orlando, J. J., and Tyndall, G. S.: Atmospheric Chemistry and Global Change, Oxford University Press, New York, 1999.

Braun, C. L. and Smirnov, S. N.: Why Is Water Blue?, Journal of Chemical Education, 70, 612–614, 1993.

Brinkmann, R. T.: Rotational Raman scattering in planetary atmospheres, The Astrophysical Journal, 154, 1087–1093, 1968.

Burkert, J., Andres-Hernandez, M. D., Stobener, D., Burrows, J. P., Weissenmayer, M., and Kraus, A.: Peroxy radical and related trace gas measurements in the boundary layer above the Atlantic Ocean, Journal of Geophysical Research-Atmospheres, 106, 5457–5477, 2001.

Burrows, J. P., Hölzle, E., Goede, A. P. H., Visser, H., and Fricke, W.: SCIAMACHY - Scanning Imaging Absorption Spectrometer for Atmospheric Chartography, Acta Astronautica, 35, 445–451, 1995.

Burrows, J. P., Vountas, M., Rozanov, V., Richter, A., Platt, U., Haug, H., Marquard, L., and Chance, K.: Study of the Ring effect, Tech. rep., ESA Study No 10996/94/NL/CN, SERCO, 1996.

Burrows, J. P., Weber, M., Buchwitz, M., Rozanov, V., Ladstatter-Weissenmayer, A., Richter, A., DeBeek, R., Hoogen, R., Bramstedt, K., Eichmann, K. U., and Eisinger, M.: The global ozone monitoring experiment (GOME): Mission concept and first scientific results, Journal of the Atmospheric Sciences, 56, 151–175, 1999.

Callies, J., Corpaccioli, E., Eisinger, M., Hahne, A., and Lefebvre, A.: GOME-2 – Metop's Second-Generation Sensor for Operational Ozone Monitoring, ESA Bulletin-European Space Agency, 102, 28–36, 2000.

Carpenter, L. J.: Iodine in the marine boundary layer, Chemical Reviews, 103, 4953–4962, 2003.

Carpenter, L. J., MacDonald, S. M., Shaw, M. D., Kumar, R., Saunders, R. W., Parthipan, R., Wilson, J., and Plane, J. M. C.: Atmospheric iodine levels influenced by sea surface emissions of inorganic iodine, Nature Geosci, 6, 108–111, 10.1038/ngeo1687, 2013.

Chance, K. V. and Spurr, R. J. D.: Ring effect studies: Rayleigh scattering, including molecular parameters for rotational Raman scattering, and the Fraunhofer spectrum, Applied Optics, 36, 5224–5230, 1997.

Chapman, S.: On ozone and atomic oxygen in the upper atmosphere, Philosophical Magazine, 10, 369–383, 1930.

Crutzen, P. J.: The influence of nitrogen oxides on the atmospheric ozone content, Quart. J. R. Met. Soc., 96, 320–325, 1970.

De Smedt, I., Muller, J. F., Stavrakou, T., van der A, R., Eskes, H., and Van Roozendael, M.: Twelve years of global observations of formaldehyde in the troposphere using GOME and SCIAMACHY sensors, Atmospheric Chemistry and Physics, 8, 4947–4963, 2008.

Demtröder, W.: Experimentalphysik 2 - Elektrizität und Optik, 4. Auflage, Springer-Verlag Berlin Heidelberg New York, 2006.

Demtröder, W.: Experimentalphysik 3 - Atome, Moleküle und Festkörper, 4. Auflage, 2010.

Dickey, T. D., Kattawar, G. W., and Voss, K. J.: Shedding new light on light in the ocean, Physics Today, 64, 44–49, 2011.

Dinter, T.: Modellierung ozeanischer Rückstreuung unter Einbeziehung von Vibrations-Raman-Streuung und die Auswertung anhand von Satellitendaten, Diploma thesis, University of Bremen, 2005.

Dobson, G. M. B. and Harrison, D. N.: Measurements of the amount of ozone in the Earth's atmosphere and its relation to other geophysical conditions, in: Proc. R. Soc. Lond. A, pp. 660–693, London, 1926.

Draxler, R. R. and Rolph, G. D.: HYSPLIT (HYbrid Single-Particle Lagrangian Integrated Trajectory) Model access via NOAA ARL READY Website (http://ready.arl.noaa.gov/HYSPLIT.php), 2011.

Farman, J. C., Gardiner, B. G., and Shanklin, J. D.: Large Losses of Total Ozone in Antarctica Reveal Seasonal ClO_x/NO_x Interaction, Nature, 315, 207–210, 1985.

Fleischmann, O. C., Hartmann, M., Burrows, J. P., and Orphal, J.: New ultraviolet absorption cross-sections of BrO at atmospheric temperatures measured by time-windowing Fourier transform spectroscopy, J. Photochem. Photobiol. A., 168, 117–132, 2004.

Franke, K., Richter, A., Bovensmann, H., Eyring, V., Jöckel, P., Hoor, P., and Burrows, J. P.: Ship emitted NO_2 in the Indian Ocean: comparison of model results with satellite data, Atmos. Chem. Phys., 9, 7289–7301, 2009.

Frieß, U., Sihler, H., Sander, R., Pöhler, D., Yilmaz, S., and Platt, U.: The vertical distribution of BrO and aerosols in the Arctic: Measurements by active and passive differential optical absorption spectroscopy, J. Geophys. Res., 116, 2011.

Garland, J. A. and Curtis, H.: Emission of Iodine from the Sea-Surface in the Presence of Ozone, Journal of Geophysical Research-Oceans and Atmospheres, 86, 3183–3186, 1981.

Gil, M., Yela, M., Gunn, L. N., Richter, A., Alonso, I., Chipperfield, M. P., Cuevas, E., Iglesias, J., Navarro, M., Puentedura, O., and Rodríguez, S.: NO_2 climatology in the northern subtropical region: diurnal, seasonal and interannual variability, Atmos. Chem. Phys., 8, 1635–1648, 2008.

Gottwald, M., Bovensmann, H., Lichtenberg, G., Noël, S., von Bargen, A., Slijkhuis, S., Piters, A., Hoogeveen, R., von Savigny, C., Buchwitz, M., Kokhanovsky, A., Richter, A., Rozanov, A., Holzer-Popp, T., Bramstedt, K., Lambert, J.-C., Skupin, J., Wittrock, F., Schrijver, H., and Burrows, J. P.: SCIAMACHY, Monitoring the Changing Earth's Atmosphere, DLR, Institut für Methodik der Fernerkundung (IMF), 2006.

Grainger, J. F. and Ring, J.: Anomalous Fraunhofer Line Profiles, Nature, 193, 762, 1962.

Großmann, K., Frieß, U., Peters, E., Wittrock, F., Lampel, J., Yilmaz, S., Tschritter, J., Sommariva, R., Glasow, R. v., Quack, B., Krüger, K., Pfeilsticker, K., and Platt, U.: Iodine monoxide in the Western Pacific marine boundary layer, Atmos. Chem. Phys., 13, 3363–3378, 2013.

Heckel, A., Richter, A., Tarsu, T., Wittrock, F., Hak, C., Pundt, I., Junkermann, W., and Burrows, J. P.: MAX-DOAS measurements of formaldehyde in the Po-Valley, Atmos. Chem. Phys., 5, 909–918, 2005.

Hellwege, K. H.: Einführung in die Physik der Molekeln, 2. Auflage, Heidelberger Tachenbücher, Springer Verlag, 1990.

Hendrick, F., Van Roozendael, M., Kylling, A., Petritoli, A., Rozanov, A., Sanghavi, S., Schofield, R., von Friedeburg, C., Wagner, T., Wittrock, F., Fonteyn, D., and De Maziere, M.: Intercomparison exercise between different radiative transfer models used for the interpretation of ground-based zenith-sky and multi-axis DOAS observations, Atmospheric Chemistry and Physics, 6, 93–108, 2006.

Hickman, G. D., Harding, J. M., Carnes, M., Pressman, A., Kattawar, G. W., and Fry, E. S.: Aircraft Laser Sensing of Sound-Velocity in Water - Brillouin-Scattering, Remote Sensing of Environment, 36, 165–178, ga805 Times Cited:34 Cited References Count:33, 1991.

Hönninger, G., Friedeburg, C. v., and Platt, U.: Multi axis differential optical absorption spectroscopy (MAX-DOAS), Atmos. Chem. Phys., 4, 231–254, 2004.

Johnston, H.: Reduction of Stratospheric Ozone by Nitrogen Oxide Catalysts from Supersonic Transport Exhaust, Science, 173, 517–522, 1971.

Joiner, J., Vasilkov, A. P., Flittner, D. E., Gleason, J. F., and Bhartia, P. K.: Retrieval of cloud pressure and oceanic chlorophyll content using Raman scattering in GOME ultraviolet spectra, Journal of Geophysical Research-Atmospheres, 109, 2004.

Kattawar, G. W. and Xu, X.: Filling in of Fraunhofer Lines in the Ocean by Raman-Scattering, Applied Optics, 31, 6491–6500, 1992.

Kattawar, G. W., Young, A. T., and Humphreys, T. J.: Inelastic scattering in planetary atmospheres. I. The Ring effect, without aerosols, The Astrophysical Journal, 243, 1049–1057, 1981.

Konovalov, I. B., Beekmann, M., Richter, A., Burrows, J. P., and Hilboll, A.: Multi-annual changes of NO_x emissions in megacity regions: nonlinear trend analysis of satellite measurement based estimates, Atmos. Chem. Phys., 10, 8481–8498, 2010.

Kreher, K., Fiedler, M., Gomer, T., Stutz, J., and Platt, U.: The latitudinal distribution (50°N-50°S) of NO_2 and O_3 in October/November 1990, Geophysical Research Letters, 22, 1217–1220, 1995.

Krüger, K. and Quack, B.: Introduction to special issue: the TransBrom Sonne expedition in the tropical West Pacific, Atmos. Chem. Phys. Discuss., 12, 1401–1418, 2012.

Kurucz, R. L., Furenlid, I., Brault, J., and Testerman, L.: Solar Flux Atlas from 296 to 1300 nm, National Solar Observatory, 1984.

Leonard, D. A., Caputo, B., and Hoge, F. E.: Remote-Sensing of Subsurface Water Temperature by Raman-Scattering, Applied Optics, 18, 1732–1745, 1979.

Leue, C., Wenig, M., Wagner, T., Klimm, O., Platt, U., and Jahne, B.: Quantitative analysis of NO_x emissions from Global Ozone Monitoring Experiment satellite image sequences, Journal of Geophysical Research-Atmospheres, 106, 5493–5505, 2001.

Levelt, P. F., Hilsenrath, E., Leppelmeier, G. W., van den Oord, G. H. J., Bhartia, P. K., Tamminen, J., de Haan, J. F., and Veefkind, J. P.: Science objectives of the Ozone Monitoring Instrument, Ieee Transactions on Geoscience and Remote Sensing, 44, 1199–1208, 2006a.

Levelt, P. F., Van den Oord, G. H. J., Dobber, M. R., Malkki, A., Visser, H., de Vries, J., Stammes, P., Lundell, J. O. V., and Saari, H.: The Ozone Monitoring Instrument, Ieee Transactions on Geoscience and Remote Sensing, 44, 1093–1101, 2006b.

Löhnert, U., Crewell, S., and Simmer, C.: An integrated approach toward retrieving physically consistent profiles of temperature, humidity, and cloud liquid water, Journal of Applied Meteorology, 43, 1295–1307, 2004.

Löhnert, U., Turner, D. D., and Crewell, S.: Ground-Based Temperature and Humidity Profiling Using Spectral Infrared and Microwave Observations. Part I: Simulated Retrieval Performance in Clear-Sky Conditions, Journal of Applied Meteorology and Climatology, 48, 1017–1032, 2009.

MacDonald, S. M., Oetjen, H., Mahajan, A. S., Whalley, L. K., Edwards, P. M., Heard, D. E., Jones, C. E., and Plane, J. M. C.: DOAS measurements of formaldehyde and glyoxal above a south-east Asian tropical rainforest, Atmospheric Chemistry and Physics, 12, 5949–5962, 2012.

Marbach, T., Beirle, S., Platt, U., Hoor, P., Wittrock, F., Richter, A., Vrekoussis, M., Grzegorski, M., Burrows, J. P., and Wagner, T.: Satellite measurements of formaldehyde linked to shipping emissions, Atmos. Chem. Phys., 9, 8223–8234, 2009.

Mayer-Kuckuck, T.: Atomphysik: Eine Einführung, Teubner Studienbücher Physik, Teubner, 1997.

McFiggans, G., Coe, H., Burgess, R., Allan, J., Cubison, M., Alfarra, M. R., Saunders, R., Saiz-Lopez, A., Plane, J. M. C., Wevill, D. J., Carpenter, L. J., Rickard, A. R., and Monks, P. S.: Direct evidence for coastal iodine particles from Laminaria macroalgae - linkage to emissions of molecular iodine, Atmospheric Chemistry and Physics, 4, 701–713, 2004.

Meller, R. and Moortgat, G. K.: Temperature dependence of the absorption cross sections of formaldehyde between 223 and 323 K in the wavelength range 225-375 nm, J. Geophys. Res., 105, 7089–7101, 2000.

Möller, A., Lovric, M., and Scholz, F.: Evidence for the occasional appearance of molecular iodine in sea water, International Journal of Environmental Analytical Chemistry, 63, 99–106, 1996.

Molina, M. J. and Rowland, F. S.: Stratospheric Sink for Chlorofluoromethanes - Chlorine Atom Catalyzed Destruction of Ozone, Bulletin of the American Meteorological Society, 55, 491–491, 1974.

Noxon, J. F.: Nitrogen-Dioxide in Stratosphere and Troposphere Measured by Ground-Based Absorption Spectroscopy, Science, 189, 547–549, 1975.

O'Connor, C. L. and Schlupf, J. P.: Brillouin Scattering in Water - Landau-Placzek Ratio, Journal of Chemical Physics, 47, 31–38, 1967.

O'Dowd, C. D., Jimenez, J. L., Bahreini, R., Flagan, R. C., Seinfeld, J. H., Hameri, K., Pirjola, L., Kulmala, M., Jennings, S. G., and Hoffmann, T.: Marine aerosol formation from biogenic iodine emissions, Nature, 417, 632–636, 2002.

Oetjen, H.: Messungen atmosphärischer Spurengase in Ny-Ålesund - Aufbau und Inbetriebnahme eines neuen DOAS Meßsystems, Diploma thesis, University of Bremen, 2002.

Peters, E., Wittrock, F., Grossmann, K., Friess, U., Richter, A., and Burrows, J. P.: Formaldehyde and nitrogen dioxide over the remote western Pacific Ocean: SCIAMACHY and GOME-2 validation using ship-based MAX-DOAS observations, Atmospheric Chemistry and Physics, 12, 11 179–11 197, 2012.

Pfeilsticker, K. et al.: The SHIVA Western Pacific campaign in November and December 2011 - Post-campaign Activity Report (`http://shiva.iup.uni-heidelberg.de/dl/SHIVA_campaign_report.pdf`), Tech. rep., University of Heidelberg, 2012.

Pinardi, G., Roozendael, M. V., Abuhassan, N., Adams, C., Cede, A., Clémer, K., Fayt, C., Frieß, U., Gil, M., Herman, J., Hermans, C., Hendrick, F., Irie, H., Merlaud, A., Comas, M. N., Peters, E., Piters, A. J. M., Puentedura, O., Richter, A., Schönhardt, A., Shaiganfar, R., Spinei, E., Strong, K., Takashima, H., Vrekoussis, M., Wagner, T., Wittrock, F., and Yilmaz, S.: MAXDOAS formaldehyde slant column measurements during CINDI: intercomparison and analysis improvement, Atmos. Meas. Tech., 6, 167–185, 2013.

Piters, A. J. M., Boersma, K. F., Kroon, M., Hains, J. C., Roozendael, M. V., Wittrock, F., Abuhassan, N., Adams, C., Akrami, M., Allaart, M. A. F., Apituley, A., Beirle, S., Bergwerff, J. B., Berkhout, A. J. C., Brunner, D., Cede, A., Chong, J., Clémer, K., Fayt, C., Frieß, U., Gast, L. F. L., Gil-Ojeda, M., Goutail, F., Graves, R., Griesfeller, A., Großmann, K., Hemerijckx, G., Hendrick, F., Henzing, B., Herman, J., Hermans, C., Hoexum, M., Hoff, G. R. v. d., Irie, H., Johnston, P. V., Kanaya, Y., Kim, Y. J., Baltink, H. K., Kreher, K., Leeuw, G. d., Leigh, R., Merlaud, A., Moerman, M. M., Monks, P. S., Mount, G. H., Navarro-Comas, M., Oetjen, H., Pazmino, A., Perez-Camacho, M., Peters, E., Piesanie, A. d., Pinardi, G., Puentedura, O., Richter, A., Roscoe, H. K., Schönhardt, A., Schwarzenbach, B., Shaiganfar, R., Sluis, W., Spinei, E., Stolk, A. P., Strong, K., Swart, D. P. J., Takashima, H., Vlemmix, T., Vrekoussis, M., Wagner, T., Whyte, C., Wilson, K. M., Yela, M., Yilmaz, S., Zieger, P., and Zhou, Y.: The Cabauw Intercomparison campaign for Nitrogen Dioxide measuring Instruments (CINDI): design, execution, and early results, Atmos. Meas. Tech., 5, 457–485, 2012.

Platt, U. and Perner, D.: Direct Measurements of Atmospheric CH_2O, HNO_2, O_3, NO_2, and SO_2 by Differential Optical-Absorption in the near UV, Journal of Geophysical Research-Oceans and Atmospheres, 85, 7453–7458, 1980.

Platt, U. and Stutz, J.: Differential Optical Absorption Spectroscopy: Principles and Applications, Physics of Earth and Space Environments, Springer Verlag, 2008.

Pope, R. M. and Fry, E. S.: Absorption spectrum (380-700 nm) of pure water. II. Integrating cavity measurements, Applied Optics, 36, 8710–8723, 1997.

Read, K. A., Mahajan, A. S., Carpenter, L. J., Evans, M. J., Faria, B. V. E., Heard, D. E., Hopkins, J. R., Lee, J. D., Moller, S. J., Lewis, A. C., Mendes, L., McQuaid, J. B., Oetjen, H., Saiz-Lopez, A., Pilling, M. J., and Plane, J. M. C.: Extensive halogen-mediated ozone destruction over the tropical Atlantic Ocean, Nature, 453, 1232–1235, 2008.

Richter, A.: Absorptionsspektroskopische Messungen stratosphärischer Spurengase über Bremen, 53° N, Phd thesis, University of Bremen, 1997.

Richter, A. and Burrows, J. P.: A multi wavelength approach for the retrieval of tropospheric NO_2 from GOME measurements (`http://www.doas-bremen.de/paper/esa_00_richter.pdf`), in: proceedings of the ERS-ENVISAT symposium, ESA publication SP-461, 2000.

Richter, A., Eyring, V., Burrows, J. P., Bovensmann, H., Lauer, A., Sierk, B., and Crutzen, P. J.: Satellite measurements of NO_2 from international shipping emissions, Geophysical Research Letters, 31, 2004.

Richter, A., Burrows, J. P., Nüß, H., Granier, C., and Niemeier, U.: Increase in tropospheric nitrogen dioxide over China observed from space, Nature, 437, 129–132, 2005.

Richter, A., Begoin, M., Hilboll, A., and Burrows, J. P.: An improved NO_2 retrieval for the GOME-2 satellite instrument, Atmos. Meas. Tech., 4, 1147–1159, 2011.

Rodgers, C. D.: Inverse Methods for Atmospheric Sounding - Theory and Practice, Series on Atmospheric, Oceanic and Planetary Physics, World Scientific, 2000.

Rolph, G. D.: Real-time Environmental Applications and Display sYstem (READY) Website (http://ready.arl.noaa.gov), 2011.

Roscoe, H. K., Roozendael, M. V., Fayt, C., Piesanie, A. d., Abuhassan, N., Adams, C., Akrami, M., Cede, A., Chong, J., Clémer, K., Friess, U., Ojeda, M. G., Goutail, F., Graves, R., Griesfeller, A., Grossmann, K., Hemerijckx, G., Hendrick, F., Herman, J., Hermans, C., Irie, H., Johnston, P. V., Kanaya, Y., Kreher, K., Leigh, R., Merlaud, A., Mount, G. H., Navarro, M., Oetjen, H., Pazmino, A., Perez-Camacho, M., Peters, E., Pinardi, G., Puentedura, O., Richter, A., Schönhardt, A., Shaiganfar, R., Spinei, E., Strong, K., Takashima, H., Vlemmix, T., Vrekoussis, M., Wagner, T., Wittrock, F., Yela, M., Yilmaz, S., Boersma, F., Hains, J., Kroon, M., Piters, A., and Kim, Y. J.: Intercomparison of slant column measurements of NO_2 and O_4 by MAX-DOAS and zenith-sky UV and visible spectrometers, Atmos. Meas. Tech., 3, 1629–1646, 2010.

Rothman, L. S., Barbe, A., Benner, D. C., Brown, L. R., Camy-Peyret, C., Carleer, M. R., Chance, K., Clerbaux, C., Dana, V., Devi, V. M., Fayt, A., Flaud, J. M., Gamache, R. R., Goldman, A., Jacquemart, D., Jucks, K. W., Lafferty, W. J., Mandin, J. Y., Massie, S. T., Nemtchinov, V., Newnham, D. A., Perrin, A., Rinsland, C. P., Schroeder, J., Smith, K. M., Smith, M. A. H., Tang, K., Toth, R. A., Vander Auwera, J., Varanasi, P., and Yoshino, K.: The HITRAN molecular spectroscopic database: edition of 2000 including updates through 2001, Journal of Quantitative Spectroscopy & Radiative Transfer, 82, 5–44, 2003.

Rozanov, A., Rozanov, V., and Burrows, J. P.: A numerical radiative transfer model for a spherical planetary atmosphere: combined differential-integral approach involving the Picard iterative approximation, Journal of Quantitative Spectroscopy & Radiative Transfer, 69, 491–512, 2001.

Rozanov, A., Rozanov, V., Buchwitz, M., Kokhanovsky, A., and Burrows, J. P.: SCIATRAN 2.0 – A new radiative transfer model for geophysical applications in the 175–2400 nm spectral region, Adv. Space Res., 36, 1015–1019, 2005.

Rozanov, V. V. and Dinter, T.: Modeling of radiative transfer in the coupled ocean-atmosphere system including inelastic processes (in prep.), 2013.

Rozanov, V. V. and Rozanov, A. V.: Differential optical absorption spectroscopy (DOAS) and air mass factor concept for a multiply scattering vertically inhomogeneous medium: theoretical consideration, Atmos. Meas. Tech., 3, 751–780, 2010.

Saiz-Lopez, A., Plane, J. M., Baker, A. R., Carpenter, L. J., von Glasow, R., Martin, J. C., McFiggans, G., and Saunders, R. W.: Atmospheric chemistry of iodine, Chemical Reviews, 112, 1773–804, 2012.

Schönhardt, A.: DOAS measurements of iodine monoxide from satellite, Phd thesis, University of Bremen, 2009.

Schönhardt, A., Richter, A., Wittrock, F., Kirk, H., Oetjen, H., Roscoe, H. K., and Burrows, J. P.: Observations of iodine monoxide columns from satellite, Atmospheric Chemistry and Physics, 8, 637–653, 2008.

Schönhardt, A., Begoin, M., Richter, A., Wittrock, F., Kaleschke, L., Martin, J. C. G., and Burrows, J. P.: Simultaneous satellite observations of IO and BrO over Antarctica, Atmospheric Chemistry and Physics, 12, 6565–6580, 2012.

Seyler, A.: Implementierung und Charakterisierung eines Inklinometers in einem MAX-DOAS, Bachelor thesis, University of Bremen, 2011.

Simpson, W. R., Carlson, D., Honninger, G., Douglas, T. A., Sturm, M., Perovich, D., and Platt, U.: First-year sea-ice contact predicts bromine monoxide (BrO) levels at Barrow, Alaska better than potential frost flower contact, Atmospheric Chemistry and Physics, 7, 621–627, 2007a.

Simpson, W. R., von Glasow, R., Riedel, K., Anderson, P., Ariya, P., Bottenheim, J., Burrows, J., Carpenter, L. J., Friess, U., Goodsite, M. E., Heard, D., Hutterli, M., Jacobi, H. W., Kaleschke, L., Neff, B., Plane, J., Platt, U., Richter, A., Roscoe, H., Sander, R., Shepson, P., Sodeau, J., Steffen, A., Wagner, T., and Wolff, E.: Halogens and their role in polar boundary-layer ozone depletion, Atmospheric Chemistry and Physics, 7, 4375–4418, 2007b.

Singh, H., Chen, Y., Staudt, A., Jacob, D., Blake, D., Heikes, B., and Snow, J.: Evidence from the Pacific troposphere for large global sources of oxygenated organic compounds, Nature, 410, 1078–1081, 2001.

Solomon, S., Schmeltekopf, A. L., and Sanders, R. W.: On the Interpretation of Zenith Sky Absorption Measurements, J. Geophys. Res., 92, 8311–8319, 1987.

Solomon, S., Garcia, R. R., and Ravishankara, A. R.: On the Role of Iodine in Ozone Depletion, Journal of Geophysical Research-Atmospheres, 99, 20 491–20 499, 1994.

Spietz, P., Martin, J. C. G., and Burrows, J. P.: Spectroscopic studies of the I_2/O_3 photochemistry - Part 2. Improved spectra of iodine oxides and analysis of the IO absorption spectrum, Journal of Photochemistry and Photobiology a-Chemistry, 176, 50–67, 2005.

Stavrakou, T., Müller, J.-F., Smedt, I. D., Roozendael, M. V., Werf, G. R. v. d., Giglio, L., and Guenther, A.: Global emissions of non-methane hydrocarbons deduced from SCIAMACHY formaldehyde columns through 2003–2006, Atmos. Chem. Phys., 9, 3663–3679, 2009.

Still, T. J., Al-Haider, S., Seakins, P. W., Sommariva, R., Stanton, J. C., Mills, G., and Penkett, S. A.: Ambient formaldehyde measurements made at a remote marine boundary layer site during the NAMBLEX campaign - a comparison of data from chromatographic and modified Hantzsch techniques, Atmospheric Chemistry and Physics, 6, 2711–2726, 2006.

Stolarski, R. S. and Cicerone, R. J.: Stratospheric Chlorine - Possible Sink for Ozone, Canadian Journal of Chemistry-Revue Canadienne De Chimie, 52, 1610–1615, 1974.

Takashima, H., Irie, H., Kanaya, Y., and Syamsudin, F.: NO_2 observations over the western Pacific and Indian Ocean by MAX-DOAS on *Kaiyo*, a Japanese research vessel, Atmos. Meas. Tech. Discuss., 4, 6069–6095, 2011.

Theys, N., Van Roozendael, M., Hendrick, F., Yang, X., De Smedt, I., Richter, A., Begoin, M., Errera, Q., Johnston, P. V., Kreher, K., and De Maziere, M.: Global observations of tropospheric BrO columns using GOME-2 satellite data, Atmospheric Chemistry and Physics, 11, 1791–1811, 2011.

Thompson, A. M. and Zafiriou, O. C.: Air-Sea Fluxes of Transient Atmospheric Species, Journal of Geophysical Research-Oceans and Atmospheres, 88, 6696–6708, 1983.

Vandaele, A. C., Hermans, C., Simon, P. C., Roozendael, M. V., Guilmot, J. M., Carleer, M., and Colin, R.: Fourier Transform Measurement of NO_2 Absorption Cross-Section in the Visible Range at Room Temperature, J. Atmos. Chem., 25, 289–305, 1996.

Vandaele, A. C., Hermans, C., Simon, P. C., Carleer, M., Colin, R., Fally, S., Mérienne, M. F., Jenouvrier, A., and Coquart, B.: Measurements of the NO_2 absorption cross-section from 42 000 cm-1 to 10 000 cm-1 (238–1000 nm) at 220 K and 294 K, J. Quant. Spectrosc. Radiat. Transfer, 59, 171–184, 1998.

Vandaele, A. C., Fayt, C., Hendrick, F., Hermans, C., Humbled, F., Van Roozendael, M., Gil, M., Navarro, M., Puentedura, O., Yela, M., Braathen, G., Stebel, K., Tornkvist, K., Johnston, P., Kreher, K., Goutail, F., Mieville, A., Pommereau, J. P., Khaikine, S., Richter, A., Oetjen, H., Wittrock, F., Bugarski, S., Friess, U., Pfeilsticker, K., Sinreich, R., Wagner, T., Corlett, G., and Leigh, R.: An intercomparison campaign of ground-based UV-visible measurements of NO_2, BrO, and OClO slant columns: Methods of analysis and results for NO_2, Journal of Geophysical Research-Atmospheres, 110, 2005.

Vasilkov, A. P., Joiner, J., Gleason, J., and Bhartia, P. K.: Ocean Raman scattering in satellite backscatter UV measurements, Geophysical Research Letters, 29, 2002.

von Glasow, R., Sander, R., Bott, A., and Crutzen, P. J.: Modeling halogen chemistry in the marine boundary layer - 1. Cloud-free MBL, Journal of Geophysical Research-Atmospheres, 107, 2002.

Vountas, M., Rozanov, V. V., and Burrows, J. P.: Ring effect: Impact of Rotational Raman scattering on radiative transfer in earth's atmosphere, J. Quant. Spectrosc. Radiat. Transfer, 60, 943–961, 1998.

Vountas, M., Richter, A., Wittrock, F., and Burrows, J. P.: Inelastic scattering in ocean water and its impact on trace gas retrievals from satellite data, Atmos. Chem. Phys., 3, 1365–1375, 2003.

Vrekoussis, M., Wittrock, F., Richter, A., and Burrows, J. P.: GOME-2 observations of oxygenated VOCs: what can we learn from the ratio glyoxal to formaldehyde on a global scale?, Atmos. Chem. Phys., 10, 10 145–10 160, 2010.

Wagner, T., Chance, K., Frieß, U., Gil, M., Goutail, F., Hönninger, G., Johnston, P. V., Karlsen-Tørnkvist, K., Kostadinov, I., Leser, H., Petritoli, A., Richter, A., Roozendael, M. V., and Platt, U.: Correction of the Ring effect and I_0-effect for DOAS observations of scattered sunlight, in: Proc. of the 1st DOAS Workshop, 2001.

Wagner, T., Dix, B., von Friedeburg, C., Friess, U., Sanghavi, S., Sinreich, R., and Platt, U.: MAX-DOAS O_4 measurements: A new technique to derive information on atmospheric aerosols - Principles and information content, Journal of Geophysical Research-Atmospheres, 109, 2004.

Wagner, T., Burrows, J. P., Deutschmann, T., Dix, B., von Friedeburg, C., Friess, U., Hendrick, F., Heue, K. P., Irie, H., Iwabuchi, H., Kanaya, Y., Keller, J., McLinden, C. A., Oetjen, H., Palazzi, E., Petritoli, A., Platt, U., Postylyakov, O., Pukite, J., Richter, A., van Roozendael, M., Rozanov, A., Rozanov, V., Sinreich, R., Sanghavi, S., and Wittrock, F.: Comparison of box-air-mass-factors and radiances for Multiple-Axis Differential Optical Absorption Spectroscopy (MAX-DOAS) geometries calculated from different UV/visible radiative transfer models, Atmospheric Chemistry and Physics, 7, 1809–1833, 2007.

Walrafen, G. E.: Raman Spectral Studies of Effects of Temperature on Water Structure, Journal of Chemical Physics, 47, 114ff, 1967.

Wang, P., Stammes, P., A, R. v. d., Pinardi, G., and Roozendael, M. v.: FRESCO+: an improved O_2 A-band cloud retrieval algorithm for tropospheric trace gas retrievals, Atmos. Chem. Phys., 8, 6565–6576, 2008.

Wayne, R. P.: Chemistry of Atmospheres, 3rd edition, Oxford University Press, 2000.

Weigert, A. and Wendker, H. J.: Astronomie und Astrophysik: Ein Grundkurs, 3. Auflage, Wiley-VCH, 1996.

Weller, R., Schrems, O., Boddenberg, A., Gäb, S., and Gautrois, M.: Meridional distribution of hydroperoxides and formaldehyde in the marine boundary layer of the Atlantic (48° N - 35° S) measured during the Albatross campaign, J. Geophys. Res., 105, 14.401–14.412, 2000.

Wittrock, F.: The retrieval of oxygenated volatile organic compounds by remote sensing techniques (`http://www.doas-bremen.de/paper/diss_wittrock_06.pdf`), Phd thesis, University of Bremen, 2006.

Wittrock, F., Oetjen, H., Richter, A., Fietkau, S., Medeke, T., Rozanov, A., and Burrows, J. P.: MAX-DOAS measurements of atmospheric trace gases in Ny-Ålesund - Radiative transfer studies and their application, Atmos. Chem. Phys., 4, 955–966, 2004.

Wittrock, F. et al.: Measurements of NO_2 profiles with MAX-DOAS: Theoretical and practical case studies as part of the Cabauw Intercomparison campaign for Nitrogen Dioxide Measuring Instruments (CINDI), in prep. for AMTD.

Wofsy, S. C., McElroy, M. B., and Yung, Y. L.: The Chemistry of Atmospheric Bromine, Geophysical Research Letters, 2, 215–218, 1975.

Xu, X. and Kattawar, G. W.: Filling in of Fraunhofer Lines in the Ocean by Brillouin-Scattering, Applied Optics, 33, 4835–+, 1994.

Erklärung

Hiermit erkläre ich, dass ich die Arbeit ohne unerlaubte fremde Hilfe angefertigt habe, dass ich weiterhin keine anderen als die angegebenen Quellen und Hilfsmittel benutzt und die den benutzten Werken wörtlich oder inhaltlich entnommenen Stellen als solche kenntlich gemacht habe.

Bremen, 25.06.2013

Enno Peters

Acknowledgements / Danksagung

An dieser Stelle möchte ich mich bei all denjenigen bedanken, die zum Gelingen dieser Arbeit beigetragen haben. Leider sind das insbesondere durch die vielen Kampagnen viel zu viele Menschen und ich entschuldige mich jetzt schon bei all den Zu-kurz-Gekommenen.

Prof. John P. Burrows danke ich ganz besonders dafür, dass er mir die Möglichkeit gegeben hat, in einem ebenso interessanten wie anspruchsvollen Fachgebiet von in meinen Augen herausragender Relevanz, der Umweltphysik, zu forschen und arbeiten. Ich war des Öfteren beeindruckt, dass jemand, der so viel zu tun hat, trotzdem eine so klare Vorstellung davon hat, was die wesentlichen Punkte meiner Arbeit sind - manchmal sogar klarer als ich selbst.

Prof. Justus Notholt danke ich für die freundliche Übernahme des Zweitgutachtens, trotz aller zeitlichen Engpässe!

Mein größter Dank gilt Folkard Wittrock und Andreas Richter.
Andreas, ich war immer wieder beeindruckt von deinem enormen (Fach-)Wissen, genauso wie von der Gabe, es jedem Neuling immer wieder geduldig von Null angefangen zu erklären. Ich glaube, ich habe in den letzten Jahren von niemandem so viel gelernt wie von dir.
Folkard, tausend Dank für deine gute Betreuung, dafür, dass du immer ein offenes Ohr hattest, mir jederzeit mit Rat und Tat zur Seite standest und vor allem für unser freundschaftliches Verhältnis. Und natürlich auch für die Erkenntnis, dass mysteriöserweise immer alles irgendwie auf den letzten Drücker doch noch gut geht...

Many thanks to the Dutch KNMI for hosting the CINDI campaign and all the colleagues I met there. I learned a lot during that time (which was my first campaign experience). And I will always remember Mihalis finding the little creatures in his breakfast!

Ein großer Dank gebührt Birgit Quack und Kirstin Krüger vom GEOMAR Kiel für die Organisation der TransBrom Kampagne. Auf einem Forschungsschiff über den Pazifik zu fahren, ist ganz sicher eine der Erfahrungen, die man noch seinen Enkeln erzählen kann. Vielen Dank auch an die Besatzung des Forschungsschiffs Sonne, die uns gut über den Teich gebracht haben! Bei Katja Großmann vom IUP-Heidelberg bedanke ich mich für die gute Zusammenarbeit, nicht nur während der TransBrom-Kampagne an Bord der Sonne, sondern auch während der Zeit der Datenauswertung und Veröffentlichungen danach.

Many thanks also to the IUP-Heidelberg for organizing the SHIVA campaign, especially Johannes Lampel who operated our instrument onboard the RV Sonne. This campaign would have been impossible without the support and help of our Malaysian colleagues and students, thank you! For me, it was not the easiest campaign and thanks a million to Mihalis who jumped in and came along with me to Borneo!

Especially many thanks to the entire DOAS group! There is really a warm and pleasant atmosphere in the group that I realized right from the beginning and that never changed. I always felt comfortable. Thank you!! And although it may be unfair to pick out a single member, I have in particular to thank Anja who helped me a lot and answered a thousand questions! Thanks!

Zwölf Punkte des Dankes gehen an die wichtigsten Menschen in meinem Leben, meine Familie, und insbesondere meine Mutter, meinen Bruder und Isa. Von euch kommt die unbezahlbare Unterstützung, ohne die gar nichts geht! Fühlt euch gedrückt!